UNIVERSITÄT BAYREUTH

From Fibers to 3D Architectures: How Structural Hierarchies Affect Heat Transport

Dissertation

to be awarded the degree of
Doctor of Natural Sciences (Dr. rer. nat.)

at the Faculty of Biology, Chemistry & Earth Sciences
University of Bayreuth

submitted by
Ina Klein
born in Réduit, Mauritius

Bayreuth, 2025

The work for this thesis was carried out from November 2020 to September 2025 at the Chair of Physical Chemistry I - Colloidal Structures and Energy Materials at the University of Bayreuth under the supervision of Prof. Dr. Markus Retsch.

This is a full reprint of the dissertation submitted to obtain the academic degree Doctor of Natural Sciences (Dr. rer. nat.) and approved by the Faculty of Biology, Chemistry & Earth Sciences of the University of Bayreuth.

Type of Dissertation:	Cumulative Dissertation
Thesis submitted:	October 21, 2025
Acceptance by the Exam Commission:	October 29, 2025
Date of Scientific Colloquium:	April 20, 2026

Acting Dean:
Prof. Dr. Janosch Hennig

Doctoral Committee:

Prof. Dr. Markus Retsch	(Reviewer)
Prof. Dr. Johannes C. Brendel	(Reviewer)
Prof. Dr. Josef Breu	(Chairman)
Prof. Dr. Johannes Margraf	(Examiner)

Time won't wait, give it all today.

BEARTOOTH

Acknowledgement

Throughout my Ph.D., I was supported by many people to whom I owe my sincere thanks.

First, I would like to thank my Doctoral Committee for giving their time as examiners of my thesis.

Especially, I want to thank my supervisor, Prof. Dr. Markus Retsch, for giving me the chance to pursue my Ph.D. in his group, for the balance of freedom and guidance in my research, and for his support throughout these years. I also want to thank him and the whole PCI team for the friendly atmosphere in our group. I really valued working with everyone of them, as well as spending time together outside of work. I do not take it for granted that so many of my colleagues, from the Retsch group and beyond, became friends. They made my Ph.D. a time I will always enjoy looking back on.

Stefan, I want to thank you for all the laughs, adventures, and for being there for me throughout this journey. I am grateful for all the great times we've shared and look forward to many more to come.

I am also very thankful for my longtime friends. Even though life has taken us in different directions, it always feels as if no time has passed when we see each other again. The friends I made during my studies have filled my time in Ulm and beyond with countless great memories, and it means a lot to know that I can always count on them.

Finally, I want to thank those who have supported me throughout my whole life: my family. I feel very lucky to have had the chance to pursue what I wanted, and I could not have done this without the support of my parents, Karin and Josef, who I know will always have my back. A big thank you also goes to my brother Philip for his encouragement, and to my grandparents Christine, Sigmar, Gerti, and Sepp, who have believed in me for as long as I can remember.

Publications and Contributions

This thesis is written as a cumulative dissertation. It is based on the following peer-reviewed publications:

[1] Ina Klein*, Melina Weber, Hans-Werner Schmidt, Markus Retsch „Thermal Transport Across Supramolecular Bonds in Self-Assembled BTA Fibers“, **2025**, *Manuscript*.

[2] Ina Klein*, Sophie E. Fritze*, Alexander Berger, Holger Schmalz, Andreas Greiner, Markus Retsch „Thermal Transport in Polystyrene Nonwovens: Influence of Anisotropy, Structural Modification, and Functionalization“, *ACS Applied Polymer Materials*, **2026**, *8*, 1954–1963, DOI 10.1021/acsapm.5c03952.
**These authors contributed equally to this work.*

[3] Ina Klein*, Maria Ester Marroquin Lacayo, Thomas Blesch, Sabine Rosenfeldt, Patrick Länger, Klaus Kreger, Stefan Rettinger, Jürgen Senker, Hans-Werner Schmidt, Markus Retsch „Do Nucleating Agents or Processing Methods Affect the Thermal Transport in RacoPP?“, *Journal of Polymer Science*, **2025**, *63*, 4516-4524, DOI 10.1002/pol.20241079.

[4] Ina Klein*, Thomas Tran, Réne Reiser, Maximilian Theis, Sabine Rosenfeldt, Marius Schöttle, Carl Schirmeister, Peter Bösecke, Stefan Rettinger, Rolf Mülhaupt, Markus Retsch „High and tuneable anisotropic thermal conductivity controls the temperature distribution of 3D printed all-polyethylene objects“, *Journal of Materials Chemistry A*, **2023**, *11*, 22492-22502, DOI 10.1039/d3ta04483a.

This thesis does not include the results of the following peer reviewed publications and manuscripts:

[5] Aileen Keutgen, Ina Klein, Feng Shi, Alexander J. C. Kuehne „Mesoscopic Supramolecular Assembly of Stereolithographically Printed Microgels“, *Advanced Functional Materials*, **2023**, *34*, 2310835, DOI 10.1002/adfm.202310835

[6] Sophie E. Fritze*, Marius Schmidt*, Ina Klein, Andreas Greiner, Markus Retsch „Combining Bead-on-String Fiber Architecture and Homogeneous Silver Nanowire Integration: A Synergistic Approach to Functional 3D Electrospun Sponges“, **2025**, *Manuscript*.
**These authors contributed equally to this work.*

[7] Max Stevenson, Michael König, Ina Klein, Radha Boya, Jürgen Senker, Markus Retsch, Josef Breu „A Practical Approach to Thickness-Dependent Cell Constant Correction for Coplanar or Interdigitated Electrodes“, *Electrochimica Acta*, **2025**, 147985, DOI `10.1016/j.electacta.2025.147985`.

The following conference presentations and miscellaneous scientific contributions were part of my PhD:

[1] **Poster Presentation:** „Anisotropic Thermal Conductivity of 3D Printed All-PE Composite“, *Freiburg Macromolecular Colloquium*, **2023**, Freiburg (GER).

[2] **Oral Presentation:** „Tuneable Anisotropic Thermal Conductivity Controls the Temperature Distribution in 3D Prints“, *Nanoscale and Microscale Heat Transfer*, **2024**, Girona (ESP).

[3] **Poster Presentation:** „Do Nucleators or Processing Methods Affect the Thermal Transport in RacoPP?“, *MRS Fall Meeting & Exhibit*, **2024**, Boston (USA).

[4] **Oral Presentation:** „Controlling the Temperature Distribution of 3D Printed All-PE Material“, *MRS Fall Meeting & Exhibit*, **2024**, Boston (USA).

[5] **Poster Presentation:** „Anisotropic Thermal Transport in 3D Printed All-PE Material“, *Collaborative Symposium and Workshop on Advanced and Living Materials*, **2024**, Amherst (USA).

Summary

The transport of heat is part of our everyday life, whether we warm our hands at a bonfire, blow dry our hair, or fry an egg for breakfast. However, in many cases heat does not voluntarily go where it is needed. Instead, thermal energy is often even a harmful byproduct. Considering current trends, such as global warming and miniaturization of electronic devices, it is evident that we must expand our knowledge of thermal transport and improve our skills in controlling it. Excess heat must be efficiently dissipated, for example from the human body or from localized hot spots in electronics.

The analysis of hierarchically structured materials is of great interest in this context, as the different size scales of structural features decouple the heat transport from the overarching macroscopic architecture. Therefore, this thesis focuses on harnessing such structural hierarchies to better understand and better tune heat transport. While the sample geometries in the four projects comprising this work vary from one-dimensional fibers to two-dimensional membranes and films to three dimensional architectures, they are all linked by establishing a relationship between the structural hierarchies and thermal transport properties.

In the first of the four projects, self-assembled fibers of benzene-1,3,5-tricarboxamide (BTA) molecules were investigated. By successfully determining their thermal diffusivity along the fiber axis, this work provided an excellent opportunity to examine how heat propagates through purely non-covalent interactions. Based on the systematic study of a series of BTAs with varying side groups, the thermal transport properties were set into context of the BTA molecular structures. Moreover, an initial assessment of the intermolecular bonding strengths within the fibers provided valuable insight into the factors that govern supramolecular thermal transport.

The second project transitions from individual fibers to fiber networks, examining the effects of anisotropy, post-processing treatments, and functionalization on thermal transport in non-wovens. By comparing the thermal diffusivity of cold-pressed and annealed membranes with different degrees of fiber alignment, we determined that increasing structural anisotropy enhances thermal anisotropy only to a certain extent. Our results highlight the crucial role of the size and quality of fiber–fiber contacts. Furthermore, we demonstrated that incorporating highly conductive fillers is ineffective when other conduction bottlenecks remain, and uncovered an intriguing contrast in the response of electrical and thermal transport to structural anisotropy.

Shifting from the fundamentally oriented studies to more applied systems, the third project investigates thermal transport in a copolymer of propylene and ethylene (racoPP), a material widely used in industry. The influence of injection- and compression-molding, as well as BTA additives, on the structural and thermal transport properties was analyzed. During processing, the BTA molecules self-assemble, and the resulting fibrils can align with the flow direction, providing oriented nucleation sites for anisotropic crystal growth of the polymer. Despite these structural dependencies, the thermal transport properties proved highly resilient to both nucleating agents and processing conditions.

In contrast to this resilience, the fourth project explores a system where thermal transport is deliberately governed by structure. We achieved macroscopic control of crystallite orientation in a fully recyclable all-PE material, enabling tunable, directional thermal transport. During extrusion-based 3D printing, extended-chain nanocrystals were formed. These fiber-like shish structures enable continuous thermal transport along the print direction. We found that the resulting anisotropy in thermal diffusivity depends on the printing parameters and can be used to control temperature distributions in two- and three-dimensional specimens by defining the print directions accordingly. This project therefore offers a promising contribution to sustainable thermal management applications.

Overall, this thesis examines thermal transport from multiple perspectives. While the projects span different sample geometries and range in focus from fundamental questions to application-oriented investigations, they consistently center on the crucial role of structural hierarchies in governing heat transport.

Zusammenfassung

Der Transport von Wärme ist Teil unseres Alltags, ob wir uns an einem Lagerfeuer die Hände wärmen, uns die Haare föhnen oder ein Ei zum Frühstück braten. Jedoch gelangt Wärme in vielen Fällen nicht freiwillig dorthin, wo sie benötigt wird. Vielmehr stellt thermische Energie oft sogar ein schädliches Nebenprodukt dar. Angesichts aktueller Entwicklungen wie der globalen Erderwärmung und der Miniaturisierung elektronischer Geräte ist es offensichtlich, dass wir unser Wissen über den Wärmetransport erweitern und unsere Fähigkeiten zu dessen Steuerung verbessern müssen. Überschüssige Wärme muss effizient abgeführt werden, etwa aus dem menschlichen Körper oder aus lokalisierten Hot Spots in elektronischen Geräten.

Die Analyse hierarchisch aufgebauter Materialien ist in diesem Kontext von großem Interesse, da die unterschiedlichen Größenskalen der strukturellen Einheiten den Wärmetransport von der übergeordneten makroskopischen Architektur entkoppeln. Aus diesem Grund konzentriert sich diese Arbeit darauf, solche strukturellen Hierarchien zu nutzen, um den Wärmetransport besser zu verstehen und gezielter zu steuern. Während die Probengeometrien in den vier Projekte dieser Arbeit von eindimensionalen Fasern über zweidimensionale Membranen und Folien bis hin zu dreidimensionalen Architekturen variieren, sind sie alle miteinander verbunden, indem sie die strukturellen Hierarchien mit den Eigenschaften des Wärmetransports in Beziehung setzen.

Im ersten der vier Projekte wurden selbstassemblierte Fasern aus Benzol-1,3,5-tricarboxamid (BTA) Molekülen untersucht. Durch die erfolgreiche Bestimmung ihrer thermischen Diffusivität entlang der Faserachse bot diese Arbeit eine ausgezeichnete Gelegenheit, zu untersuchen, wie sich Wärme durch rein nicht-kovalente Wechselwirkungen ausbreitet. Basierend auf der systematischen Untersuchung einer Reihe von BTAs mit unterschiedlichen Seitengruppen wurden die Wärmetransporteigenschaften in den Kontext der molekularen BTA-Strukturen gesetzt. Darüber hinaus lieferte eine erste Einschätzung der intermolekularen Bindungsstärken innerhalb der Fasern wertvolle Einblicke in die Faktoren, die den supramolekularen Wärmetransport bestimmen.

Das zweite Projekt geht vom Studium einzelner Fasern zu Fasernetzwerken über und untersucht die Auswirkungen von Anisotropie, Nachbehandlungen und Funktionalisierung auf den Wärmetransport in Vliesstoffen. Durch den Vergleich der thermischen Diffusivität von kaltgepressten und getemperten Membranen mit unterschiedlichen Faserorientierungen stellten wir fest, dass eine zunehmende strukturelle Anisotropie die thermische Anisotropie nur bis zu einem gewissen Grad verstärkt. Unsere Ergebnisse betonen die entscheidende Rolle der Größe und Qualität der Faser-Faser-Kontakte. Des Weiteren zeigten wir, dass die Einarbeitung von hochleitfähigen Füllstoffen ineffektiv ist, solange andere Limitierungen für die Wärmeleitung bestehen und deckten einen interessanten Kontrast im Verhalten des elektrischen und thermischen Transports bei struktureller Anisotropie auf.

Übergehend von den grundlagenorientierten Studien zu stärker anwendungsorientierten Systemen, untersucht das dritte Projekt den Wärmetransport in einem Copolymer aus Propylen und Ethylen (racoPP), einem Material, das in der Industrie weit verbreitet ist. Die Einflüsse von Spritzguss- und Formpress-Prozessen sowie von BTA-Additiven auf die strukturellen Eigenschaften und die thermischen Transporteigenschaften wurden analysiert. Während der Verarbeitung assemblieren sich die BTA-Moleküle, und die entstehenden Fibrillen können sich mit der Flussrichtung ausrichten, was orientierte Keime für das anisotrope Kristallwachstum des Polymers liefert. Trotz dieser strukturellen Abhängigkeiten erwiesen sich die Wärmetransporteigenschaften als sehr widerstandsfähig sowohl gegenüber den Keimbildnern, als auch gegenüber den Verarbeitungsbedingungen.

Im Gegensatz zu dieser Widerstandsfähigkeit untersucht das vierte Projekt ein System, in dem der Wärmetransport gezielt durch die Struktur gesteuert wird. Wir erreichten makroskopische Kontrolle der Kristallitorientierung in einem vollständig recycelbaren PE-Material und konnten so einen gerichteten, steuerbaren Wärmetransport realisieren. Während des extrusionsbasierten 3D-Drucks entstanden Nanokristalle aus gestreckten Polymerketten. Diese faserähnlichen Shish-Strukturen ermöglichen einen kontinuierlichen Wärmetransport entlang der Druckrichtung. Wir stellten fest, dass die resultierende Anisotropie der thermischen Diffusivität von den Druckparametern abhängt und zur Steuerung von Temperaturverteilungen in zwei- und dreidimensionalen Proben genutzt werden kann, indem die Druckrichtungen entsprechend festgelegt werden. Dieses Projekt leistet somit einen vielversprechenden Beitrag zu nachhaltigen Wärmemanagement-Anwendungen.

Insgesamt untersucht diese Arbeit den Wärmetransport aus verschiedenen Blickwinkeln. Während die Projekte unterschiedliche Probengeometrien umfassen und sich im Fokus von grundlegenden Fragen bis hin zu anwendungsorientierten Untersuchungen erstrecken, stellen sie konsequent die entscheidende Rolle von strukturellen Hierarchien für den Wärmetransport in den Mittelpunkt.

Contents

I Fundamentals 1

1 Introduction 3
- 1.1 Motivation . . . 3
- 1.2 Basic Concepts of Thermal Transport . . . 4
- 1.3 Enhancing and Understanding Thermal Transport in Polymers . . . 12

2 Methods 17
- 2.1 Structural Characterization . . . 17
  - 2.1.1 Polarized Infrared Spectroscopy . . . 17
  - 2.1.2 Wide Angle X-Ray Scattering . . . 18
  - 2.1.3 Small Angle X-Ray Scattering . . . 20
  - 2.1.4 Scanning Electron Microscopy . . . 22
  - 2.1.5 Laser Scanning Confocal Microscopy . . . 24
- 2.2 Thermal Diffusivity Analysis . . . 25
  - 2.2.1 Light Flash Analysis . . . 25
  - 2.2.2 Lock-In Thermography . . . 27

3 References 29

II Outline 35

4 Synopsis 37

5 Individual Contributions to Joint Publications 53

6 References 55

III Publications 57

7 Thermal Transport Across Supramolecular Bonds in Self-Assembled BTA Fibers 59

8 Thermal Transport in Polystyrene Nonwovens: Influence of Anisotropy, Structural Modification, and Functionalization 71

9 Do Nucleating Agents or Processing Methods Affect the Thermal Transport in RacoPP? 89

10 High and Tuneable Anisotropic Thermal Conductivity Controls the Temperature Distribution of 3D Printed All-Polyethylene Objects 105

Part I

Fundamentals

1 Introduction

1.1 Motivation

Heat is underrated - and I am not just saying this because I often feel cold. Sure, in contrast to other energy transfer mechanisms, it doesn't launch rockets, power the laptop I am working on, or send us flying down a slide. But it's always there, whether we ask for it or not. Maybe not the hero of the story, but certainly the inevitable byproduct. This is based on the second law of thermodynamics, which states that heat can never flow from a colder to a warmer body without some other associated change, typically external work, occurring at the same time.[1] This innocent-sounding law both challenges humankind and illustrates the universality of heat. It cannot be avoided, so we have to deal with it. More specifically, this means we must learn how to transport thermal energy efficiently away from places where it may cause harm toward places where it is indifferent or desired.

A very current example are electronic devices. Inefficient conversion between chemical and electrical energy leads to thermal energy. This energy needs to be transferred away from the heat source and dissipated into the device's surroundings to ensure high performance, reliability, and safety.[2,3] The issue becomes increasingly pressing with ongoing miniaturization of electronic devices, as heat generation becomes even more concentrated.[2,4] Efficient thermal management systems are required. A key to this challenge are suitable materials that efficiently conduct heat without conducting electrons.[5] Beyond electronics, controlled thermal transport is also a key concern in many other prominent fields, including aerospace, renewable energy systems or fabrics.[6–8] Depending on the application, the material must meet various criteria, ranging from specific shape requirements and mechanical characteristics to anisotropic transport properties. To meet the numerous and specific demands simple homogeneous materials are insufficient. In contrast, hierarchical structures inherently introduce the complexity that is sometimes necessary, making them particularly interesting for thermal management applications.

Their structural levels across multiple length scales implies significant variability. This is undoubtedly a great advantage, but also means that a try-and-error approach is nonviable for research. Instead, we must focus on understanding the complex transport processes. It is essential to identify not only the key parameters that influence thermal transport but also to grasp why they are crucial and why other factors can be disregarded. Knowledge is the basis for rational material design. This principle stayed with me throughout my Ph.D. I investigated thermal transport in hierarchical systems of different dimensionalities, placing particular emphasis on structure-property relationships. While my work spans both fundamental and applied research, an overarching aim has always been to contribute new insights into thermal transport processes.

Certainly, all research on this topic is grounded in theoretical principles. Therefore, I will introduce basic concepts of thermal energy transport in the following section (Section 1.2), followed by a discussion of selected relevant work in the field (Section 1.2). Chapter 2 outlines the techniques used for structural and thermal characterization, concluding Part I. In Part II I give an overview of all projects in this thesis and describe my contributions to each. Finally, the publications discussed in this work are presented in Part III.

1.2 Basic Concepts of Thermal Transport

Thermal energy refers to the random motion of atoms and molecules within a material. It is closely linked to the material's temperature, which is a measure of the average kinetic energy of the moving particles.[9] According to the second law of thermodynamics, thermal energy is spontaneously transferred from regions of higher temperature to those of lower temperature, increasing the overall entropy of the universe in the process.[1] This transfer can occur through three fundamental mechanisms: radiation, convection, and conduction (Figure 1.1). In the following pages, I will provide a concise overview of key concepts and laws related to these forms of heat transport, beginning with radiation.

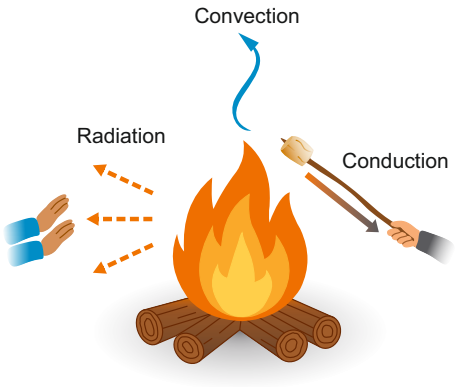

Figure 1.1: Schematic illustration of the three heat transfer mechanisms: radiation, convection, and conduction, depicted in a campfire scenario.

Radiative heat transfer is the emission or absorption of electromagnetic waves. It allows heat transfer even through vacuum. Although the spectrum of thermal radiation lies mainly in the infrared range, it can also include shorter wavelengths, as displayed by the energy emitted by the sun. When a radiant heat flux, commonly measured in watts per square meter, impinges on the surface of a body, a fraction of the incident energy is transmitted through the material, a fraction is reflected, and the remainder is absorbed. These fractions are referred to as transmittance τ, reflectance ρ and absorptance α, respectively[10]

$$1 = \tau + \rho + \alpha \tag{1.1}$$

A theoretical material that absorbs all incident radiation, and neither reflects or transmits any of it, regardless of wavelength or angle of incidence, is called a black body.[11] The radiative power B_b emitted by a black body at a certain temperature T per unit solid angle, per unit surface area, and per unit wavelength λ is called spectral radiance. It is given by Planck's law, where c is the speed of light, k_B is Boltzmann's constant, and h is Planck's constant.[12]

$$B_b(\lambda, T) = \frac{2hc^2}{\lambda^5} \frac{1}{\exp(\frac{hc}{k_B T \lambda}) - 1} \tag{1.2}$$

The spectral emissive power is obtained by integrating Planck's Law over all solid angles, resulting in the power emitted per unit surface area, per unit wavelength. A black body defines the theoretical upper limit for this quantity. No macroscopic material can emit more power per unit area in the far-field regime at a given wavelength than a black body at the same temperature.[10,13] As temperature increases, the wavelength corresponding to the peak spectral

emissive power shifts to shorter wavelengths. Therefore, the maximum spectral emissive power of a black body at room temperature lies in the far-infrared range, while the Sun, which can be approximated as a black body, emits most strongly in the visible range (Figure 1.2). This temperature dependence of the peak wavelength is described by Wien's displacement law.[14]

$$\lambda_{max} = \frac{b}{T} \tag{1.3}$$

where:

$$b = 2.898 \cdot 10^{-3}\, m\, K \tag{1.4}$$

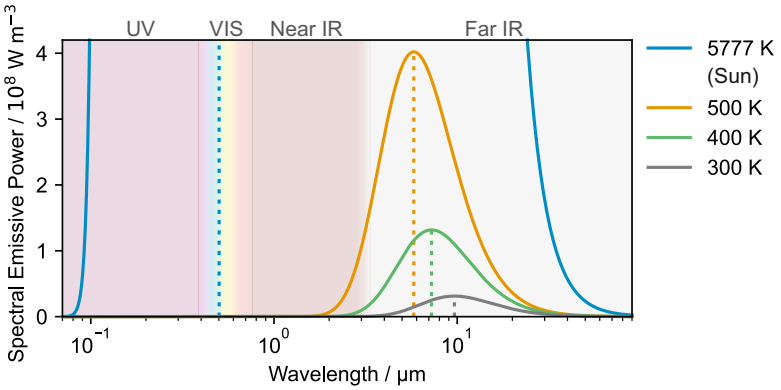

Figure 1.2: Spectral emissive power of a black body at various temperatures. Dotted lines indicate the wavelengths corresponding to the maximum spectral emissive power for each temperature.

Integrating the spectral emissive power over all wavelengths results in the black body's total emissive power $P_b(T)$, which strongly increases with temperature as given by the Stefan-Boltzmann law.[15–17]

$$P_b(T) = \sigma\, T^4 \tag{1.5}$$

where:

$$\sigma = \frac{2\pi^5 k_B^4}{15 h^3 c^2} \approx 5.67 \cdot 10^{-8}\, W m^{-2} K^{-4} \tag{1.6}$$

In reality, we do not encounter perfect absorbers or emitters. Instead, all materials absorb and emit less radiation than an ideal black body. The radiative behavior of such real-world materials is described by the spectral emittance ϵ_λ. Since black bodies define the upper limit of emissive power, the spectral emittance of any actual material must lie between zero and one.

$$\epsilon_\lambda = \frac{P(T,\lambda)}{P_b(T,\lambda)} \tag{1.7}$$

As mentioned earlier, black bodies are ideal emitters as well as ideal absorbers of radiation. Kirchhoff's law explains that this isn't just a coincidence. In its general form, the law states that a material in thermal equilibrium emits as much radiation as it absorbs, at every wavelength and in every direction.[11] For the case where emission and absorption are independent of direction, Kirchhoff's law is expressed as:

$$\epsilon_\lambda(T) = \alpha_\lambda(T) \tag{1.8}$$

Importantly, this relation holds at each individual wavelength but does not imply that the total emittance ϵ equals to the total absorptance α. These are only equal when the incident

radiation P_{inc} matches the black body spectrum or when the emittance and absorptance are constant across wavelengths. Although some real materials, copper for instance, nearly exhibit wavelength-independent emittance and absorptance, this is not generally the case, and the total emittance and total absorptance typically differ.[10]

$$\epsilon(T) = \frac{\int \epsilon_\lambda \, P_{b,\lambda}(T) \, d\lambda}{\int P_{b,\lambda}(T) \, d\lambda} \neq \frac{\int \alpha_\lambda \, P_{inc,\lambda}(T) \, d\lambda}{\int P_{inc,\lambda}(T) \, d\lambda} = \alpha(T) \tag{1.9}$$

In practice radiative exchange often takes place under non-equilibrium conditions. A familiar example is sitting near a campfire on a cool evening. Your skin and clothes feel warm because they absorb more infrared radiation from the fire than they emit themselves (Figure 1.1). In this case, radiative exchange is clearly unbalanced. Yet radiation is only part of the story. When holding your hands above the flames, rising hot air makes convective heat transfer obvious, a heat transfer mechanism I will now turn my attention to.

Convection is the process of heat transfer through bulk movement of fluid, which may be in the form of a liquid or gas. The macroscopic motion of fluid particles carries the thermal energy across distances.[10] For example, the hot air above a bonfire has a lower density than the surrounding cooler air and rises, transporting the kinetic energy of the gas molecules with it (Figure 1.1). When fluid motion arises from temperature-induced density gradients, the process is called natural or free convection.[18,19] In contrast, forced convection occurs when external forces, such as fans or pumps, drive the fluid motion.[19] When a solid body is placed in the fluid, the rate of heat transfer per unit area, termed heat flux q, is approximated by Newton's law of cooling:

$$q = h \, \Delta T \tag{1.10}$$

Here, h denotes the convective heat transfer coefficient, and ΔT is the temperature difference between the surface of the body and the undisturbed fluid far away from it.[10,20] Although Newton's law of cooling often provides reasonable approximations for convective heat transfer, it is only valid when the fluid temperature remains nearly constant and radiative heat transfer can be neglected.[21] The heat transfer coefficient is not a universal constant. It varies significantly depending on several factors, including the temperature difference between the body and the fluid, surface roughness, geometry, and the nature and velocity of the fluid.[10,21]

Finally, I will focus on the thermal transport mechanism that is most relevant to my work: thermal conduction. Conduction occurs in solids, liquids, and gases, but unlike convection, it does not rely on the bulk movement of the material. Instead, thermal energy is transferred through interactions between the energy carriers, such as molecular collisions or vibrations of atoms in a lattice. The rate at which heat is conducted by a material is described by Fourier's law of heat conduction, which relates the heat flux $\vec{q}$ to the corresponding temperature gradient ∇T.[10,22]

$$\vec{q} = -k \, \nabla T \tag{1.11}$$

The equation can be simplified to its scalar form when considering steady-state, one dimensional heat transfer[10]:

$$q = k \frac{\Delta T}{L} \tag{1.12}$$

Here, ΔT is the temperature difference between the warm and the cold side of the medium and L is the corresponding distance over which heat is conducted. The coefficient k is the thermal conductivity, a material-specific property that quantifies the efficiency with which heat

is conducted.[10,22] Returning to the bonfire example, thermal conductivity is the reason we prefer a wooden stick over a steel one when roasting marshmallows. Wood, with its lower thermal conductivity, transfers less energy per second from the hot fire to our cooler hand (Figure 1.1).

However, the rate at which a material responds to a temperature change is not directly determined by its thermal conductivity. Instead, it is governed by the thermal diffusivity α, which is related to the thermal conductivity by the following expression.[23]

$$\alpha = \frac{k}{\rho\, C_p} \tag{1.13}$$

Here, ρ is the density and C_p is the specific heat capacity. While thermal conductivity tells us how much heat is conducted, thermal diffusivity describes how fast that heat spreads through a material. In the bonfire example, diffusivity determines how fast the heat, once transferred into the stick, travels to your hand. Although the two properties are related, their physical meanings are distinct. Air, for instance, has a very low thermal conductivity ($0.026\,\mathrm{W\,m^{-1}\,K^{-1}}$), but its low density and heat capacity result in a thermal diffusivity of about $22 \cdot 10^6\,\mathrm{m^2\,s^{-1}}$, which is surprisingly comparable to that of nickel ($23 \cdot 10^6\,\mathrm{m^2\,s^{-1}}$).[23] As visualized in Figure 1.3, both properties vary widely among materials, reflecting differences in the fundamental mechanisms by which materials conduct heat. These mechanisms are explored across different material classes in the following sections.

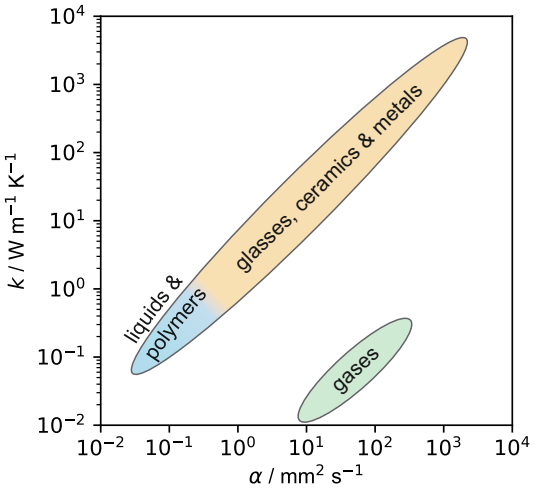

Figure 1.3: Thermal conductivity k versus thermal diffusivity α for a wide variety of homogeneous materials. Adapted with permission from[23].

When a gas is heated, for example by a radiator, the kinetic energy of nearby molecules increases, causing them to move more rapidly. These faster-moving molecules collide with neighboring ones, transferring energy and increasing their velocity. As this chain of collisions continues, heat propagates through the gas.[10] Importantly, this process of conduction must be distinguished from the convection mechanism discussed earlier, where energy is transported by the bulk motion of the gas rather than passed between individual molecules.

The efficiency of conductive energy transfer depends not only on the nature of the molecules but also on factors such as the average molecular velocity $\bar{\nu}$, volumetric specific heat capacity C_V, and mean free path λ_M, which is the average distance a molecule travels between collisions.

Assuming the gas behaves ideally and that collisions are purely elastic, the kinetic theory yields an expression for its thermal conductivity.[24]

$$k = \frac{1}{3}\,\bar{\nu}\,C_V\,\lambda_M \tag{1.14}$$

Heat transfer in liquids is often described as similar to that in gases, driven by the transfer of kinetic energy during molecular collisions. However, the significantly closer molecular spacing in liquids leads to higher thermal conductivity values. The dominant role of intermolecular interactions makes the situation more complex, and some approaches draw parallels between thermal conduction in liquids and in non-metallic solids. In the latter the atomic cores have fixed relative positions and the heat transfer is governed primarily by vibrations of the lattice around equilibrium.[25]

The quantized modes of lattice vibrations in a solid are called phonons.[25,26] They can be grouped into two main branches: acoustic phonons, where atoms in the lattice vibrate in phase, and optical phonons, where the atoms vibrate out of phase. Acoustic phonons are associated with low-frequency, long-wavelength vibrations, while optical phonons exhibit higher frequencies and can interact with light.[27,28] Each of these branches can further be divided into longitudinal and transverse modes, depending on the polarization: in longitudinal modes the atomic displacement is parallel to the phonon wave vector, whereas in transverse modes it is perpendicular (Figure 1.4).[27]

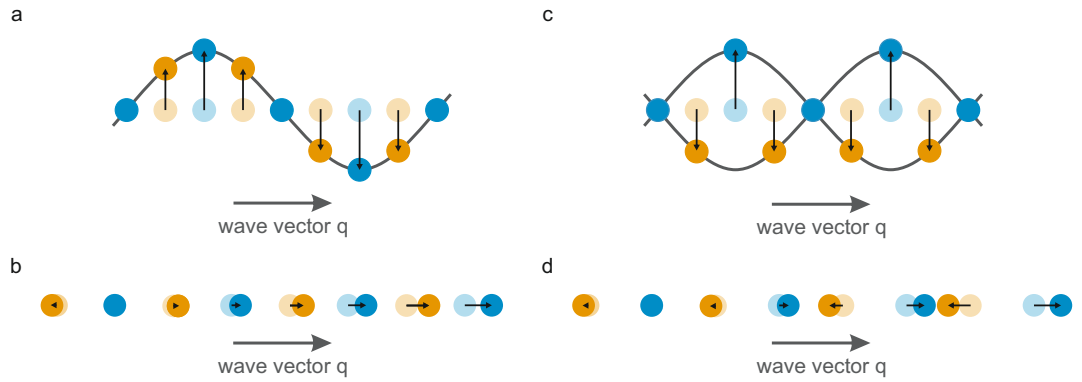

Figure 1.4: Scheme of phonons in a diatomic linear lattice, displayed by the particle displacements for a a) transverse acoustic mode, b) longitudinal acoustic mode, c) transverse optical mode, and d) longitudinal optical mode.

In crystalline electrically insulating solids phonons dominate heat conduction, and their frequencies span a broad spectrum, with an upper limit defined by the material-specific Debye frequency ν_D. This frequency is related to the Debye temperature, an important parameter for comparing the thermal behavior of different solid materials.[24,29]

$$\theta_D = \frac{h\,\nu_D}{k_B} \tag{1.15}$$

Above the Debye temperature the molar phonon heat capacity $C_{V,m,p}$ approaches a constant value of $3\,R$, where R is the ideal gas constant. This occurs because each atom effectively contributes three vibrational degrees of freedom, all of which are thermally excited. Below the Debye temperature, however, not all phonon modes are active, resulting in a heat capacity that scales with T^3. This characteristic behavior is known as the Debye law and successfully captures the behavior of many crystalline solids.[9,24]

To better understand phonon thermal conductivity, it is essential to consider the group velocity ν_g, which describes the speed at which vibrational energy is carried by a specific phonon mode. Physically, it represents the transmission velocity of a wave packet and is defined by the gradient of the phonon frequency ω with respect to the phonon wave vector q.[27]

$$\nu_g = \frac{d\omega}{dq} \tag{1.16}$$

The group velocity is influenced by the bonding strength in the material. It is related to the force constant C between neighboring planes in the crystal lattice, the atomic mass m, and the lattice spacing a.[27] Stronger bonding leads to higher phonon group velocities, underlining the importance of interatomic interactions for thermal transport properties.

$$\nu_g = a\sqrt{\frac{C}{m}}\, cos\left(\frac{q\,a}{2}\right) \tag{1.17}$$

Drawing an analogy to the kinetic theory of gases the thermal conductivity of phonons k_p can be estimated by following equation.[25,30]

$$k_p = \frac{1}{3}\,\bar{\nu}_g\, C_{Vp}\,\bar{\lambda}_{Mp} \tag{1.18}$$

Here, $\bar{\nu}_g$ is the average group velocity, C_{Vp} is the volumetric heat capacity, and $\bar{\lambda}_{Mp}$ is the phonon mean free path before scattering. When using the Debye-derived volumetric heat capacities C_{Vp}, this equation leads to a T^3 dependence of thermal conductivity at very low temperatures, where phonon–phonon interactions are negligible, and the mean free path is approximately temperature-independent. At higher temperatures, the heat capacity becomes nearly constant, but as the temperature approaches the Debye temperature, phonon-phonon interactions begin to dominate. These interactions reduce the mean free path of phonons, which becomes inversely proportional to temperature. As a result, thermal conductivity declines accordingly.[9,25,26]

Despite its usefulness, this expression (1.18) is a simplification. In real materials heat capacity, group velocity and phonon mean free path vary with phonon frequency. A more accurate description therefore requires summing over the contributions of all individual phonon modes i.[31]

$$k_p = \frac{1}{3}\sum_i \nu_{g,i}\, C_{V,i}\, \lambda_{p,i} \tag{1.19}$$

While the basic nature of phonons and their role in heat conduction has now been introduced, the processes that limit their propagation remain to be discussed. The following section will therefore focus on the various scattering mechanisms that influence phonon transport in materials.

Phonon-phonon scattering arises from the anharmonicity of lattice potentials, meaning the potential energy is not a quadratic function of atomic displacements but includes higher-order terms. These anharmonic contributions enable interactions between lattice vibrations, a process referred to as phonon-phonon scattering.[26,30] Such scattering events are commonly classified into Normal (N-) and Umklapp (U-) processes. In a simplified but accessible description, N-processes do not contribute to the thermal resistance, as the crystal momentum is conserved. In contrast, U-processes involve a momentum transfer to the lattice, thereby causing thermal resistance.[30,32] Figure 1.5 a schematically shows that for U-processes to occur, the phonon

wave vectors q must be large enough that their sum exceeds the first Brillouin zone. This zone represents a primitive cell in reciprocal space defined by the crystal's symmetry. Any wave vector exceeding the first Brillouin zone can be mapped back into it by subtracting an appropriate reciprocal lattice vector G. For acoustic modes the wave vector generally increases with phonon frequency, so higher-frequency phonons are more likely to undergo U-processes.[27] Mathematically the N- and U- process are described as follows.[33]

$$q_1 + q_2 - q_3 = \begin{cases} 0 & N - process \\ G & U - process \end{cases} \tag{1.20}$$

So far an ideal, defect-free crystal was assumed, where phonon–phonon interactions are the only scattering mechanism. While this is a valid approximation for many materials, real materials often exhibit additional phonon scattering mechanisms. At low temperatures, when the phonon mean free path becomes comparable to the dimensions of the material, boundary scattering becomes dominant and the thermal conductivity becomes dependent on the size of the crystal.[27] This is also true at room temperature in nanostructures and thin films, where the dimensions are sufficiently small. Similarly, grain boundaries can limit thermal transport. Moreover, lattice defects and atomic impurities serve as scattering sites, particularly affecting high-frequency phonons.[34] Figure 1.5 b provides a summary of these extrinsic scattering mechanisms.

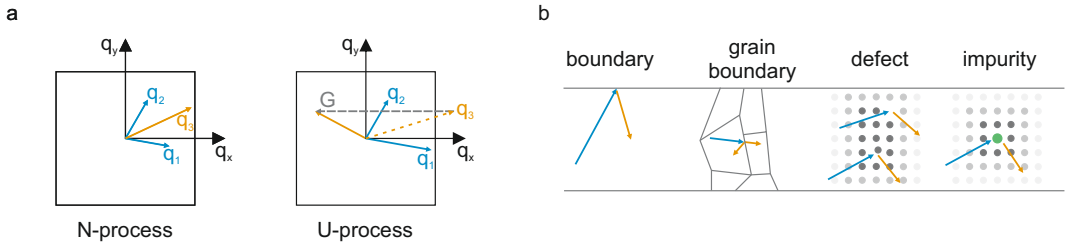

Figure 1.5: Schematic illustration of phonon scattering mechanisms. a) Normal- and Umklapp- phonon collision process. The square represents the first Brillouin zone. b) Scattering of phonons at boundaries, grain boundaries, defects or impurities.

In contrast to crystalline solids, amorphous materials lack long-range order. This raises the question of how heat is transported through such disordered structures, given that phonons with their well-defined wave vectors are not applicable in the absence of translational symmetry. Instead the normal modes of vibration can be categorized into diffusons, locons and propagons.[30,35]

Among these, propagons most closely resemble phonons. They are delocalized low-frequency modes that can propagate ballistically over several atom distances before scattering. Like phonons, propagons can be characterized by well-defined wave vectors and wavelengths. In contrast, diffusons are non-propagating delocalized modes, typically associated with intermediate frequencies. They contribute to thermal transport via a diffusion-like mechanism, and often dominate heat conduction in amorphous materials. Finally, locons are localized non-propagating modes, commonly associated with high frequencies and often present where there is a strong deviation in the local atomic coordination. Their contributions to thermal transport are usually negligible.[30,35–37]

Moreover, the temperature dependence of thermal conductivity in amorphous materials differs from that observed in crystals. At very low temperatures, it scales approximately with T^2. As

temperature increases, the rise in thermal conductivity becomes more gradual and eventually reaches a plateau between $5\,\mathrm{K}$ and $15\,\mathrm{K}$. At higher temperatures, it increases again and becomes roughly proportional to the specific heat capacity.[38]

As a result of the less efficient transport mechanisms, amorphous materials typically exhibit a lower thermal conductivity than crystalline structures. For example, diamond at $300\,\mathrm{K}$ has a thermal conductivity of $2300\,\mathrm{W\,m^{-1}\,K^{-1}}$, whereas its counterpart, amorphous carbon, exhibits a thermal conductivity of only $1.6\,\mathrm{W\,m^{-1}\,K^{-1}}$.[39]

Although the differences in thermal conductivity between dielectric crystals and amorphous materials can be substantial, heat transport in both cases is governed by atomic vibrations. In contrast, thermal conduction in pure metals is primarily dominated by mobile electrons. The valence electrons of the metal atoms are free to move throughout the lattice, forming an electron gas. Unlike phonons, these delocalized electrons serve not only as the primary heat carriers in metals but also the carriers of electrical current.[25,27] As a result, there is a strong link between thermal and electrical transport in metals, which can be quantified by the Wiedemann-Franz law.[27,40]

$$L = \frac{k}{\sigma\, T} \tag{1.21}$$

Here, L is the Lorenz number and σ is the electrical conductivity. The Lorenz number reflects the degree to which heat and electrical conduction are coupled in a given material. For an ideal metal, in which electrons are the only heat carriers, the Lorenz number becomes a material-independent constant, known as the ideal Lorenz number L_0.[41]

$$L_0 = \frac{k_e}{\sigma\, T} = \frac{\pi\, {k_B}^2}{3\, e^2} = 2.44 \cdot 10^{-8}\, \frac{W\,\Omega}{K^2} \tag{1.22}$$

However, impurities and structural disorder reduce the electron mean free path, and the contribution of phonons to the thermal conductivity becomes non-negligible.

$$k = k_e + k_{ph} \tag{1.23}$$

These additional phonon contributions and the resulting electron-phonon scattering are the primary reasons why real metals deviate from the ideal Lorenz number.[41] Nonetheless, the theoretical value agrees remarkably well with experimental measurements for many pure metals.[27,41]

With this, the primary thermal transport mechanisms have been introduced: radiation, convection, and conduction in dielectric solids, both crystalline and amorphous, as well as in metals. However, the mechanisms are not always strictly separable. In many systems such as polymers, composites, and hybrid materials multiple conductive transport pathways coexist. Crystalline and amorphous regions, metallic fillers, strength of intra- or intermolecular interactions, and interfaces can all influence heat transport. Current research focuses on deepening the understanding of these complex mechanisms and correlations, leveraging this knowledge to design materials with targeted thermal performance.[42,43]

1.3 Enhancing and Understanding Thermal Transport in Polymers

Polymers combine low weight, corrosion resistance, low cost, and easy processability, which has led to their widespread use across industries. Their inherently low thermal conductivity, especially in the amorphous state, renders them effective thermal insulators. At the same time, their electrical insulation is highly beneficial for thermal management applications in electronics. In this context, however, low thermal conductivity represents a major limitation. The need to combine the favorable properties of polymers with efficient heat dissipation has therefore driven substantial efforts to better understand and enhance their thermal transport performance.[42–44]

As early as 1950, it was observed that stretching of elastomeric polymers could significantly influence the thermal conductivity, although no clear explanation was given at the time.[45] In 1963, it was demonstrated that amorphous polyvinyl chloride, polycarbonate, polymethyl methacrylate and polystyrene all exhibit increased thermal conductivity along the stretching direction, accompanied by a decrease in the perpendicular direction. Moreover, the degree of thermal anisotropy was found to increase with draw ratio.[46] Not long after, the anisotropy was attributed to two main factors. One is the relative strength of intermolecular versus intramolecular bonding. The lower this ratio the higher the thermal anisotropy, based on the correlation between group velocity and bonding strength (equation 1.17). The second factor is the molecular orientation induced by stretching. This orientation depends on the effective molecular segment length, the length of polymer chain segments that are free to align without being hindered by entanglements or by other structural constraints.[47]

In semicrystalline polymers, the thermal conductivity at room temperature increases with crystallinity because crystalline regions provide more efficient pathways for heat transport (see Section 1.2). These materials, which consist of crystalline and amorphous domains, also permit greater thermal anisotropy than purely amorphous polymers.[38] The crystalline regions are typically organized into spherulites or lamellar stacks. Within these regions polymer chains fold into lamellae that are separated by amorphous material (Figure 1.6). When a semicrystalline polymer is stretched or extruded, the lamellae reorient toward the tensile axis, crystalline domains fragment, and at high strains the chains align along the draw direction to form fibrillar structures.[38,48,49] The strong covalent backbone bonds allow for highly efficient heat conduction along the orientation direction.[38]

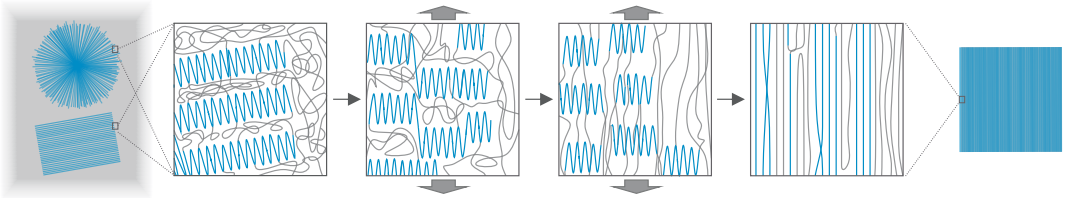

Figure 1.6: Schematic illustration of a semicrystalline polymer, with crystalline regions organized into spherulites (left top) or lamellar stacks (left bottom). Upon stretching, the crystalline domains fragment and the chains realign along the tensile axis, ultimately forming fibrillar structures.

Since these early discoveries, the role of structural anisotropy in enhancing thermal transport has been an active area of research, with computational findings supporting and motivating experimental efforts. Computational phonon calculations for polymethylenimine, polyamide

and poly(methylene oxide) predict low thermal conductivities in the inter-chain directions, where bonding relies on Van der Waals forces. In contrast, very high values are predicted along the chain direction, reaching $21.81\,\mathrm{W\,m^{-1}\,K^{-1}}$, $65.27\,\mathrm{W\,m^{-1}\,K^{-1}}$ and $94.95\,\mathrm{W\,m^{-1}\,K^{-1}}$, respectively. However, the relative contributions of phonon lifetime, group velocity, and modal heat capacity to these high values differ significantly among the polymers. This highlights the independence of these factors, which all play a key role in achieving high thermal conductivity.[50] Notably, these three systems do not represent the upper limit of achievable thermal conductivity and anisotropy in polymers. Molecular dynamics simulations of single extended polymer chains have shown that mass disorder reduces thermal conductivity by creating localized vibrational modes that hinder the energy transport by long-wavelength, delocalized modes. Consequently, higher thermal conductivities are predicted for polymers that do not incorporate heteroatoms or functional groups with different masses into the chain.[51]

Using first-principles-based anharmonic calculations, single-chain polyethylene (PE) was predicted to reach a thermal conductivity of $1400\,\mathrm{W\,m^{-1}\,K^{-1}}$. In bulk PE, anharmonic inter-chain Van der Waals forces increase the number of allowed scattering events. Nevertheless, a high thermal conductivity of $237\,\mathrm{W\,m^{-1}\,K^{-1}}$ was predicted along the chain direction. In contrast, strong anharmonic scattering and low group velocities reduce the conductivity in the cross direction by nearly three orders of magnitude, resulting in extreme anisotropy.[52] Although reported thermal conductivities of bulk PE in the chain direction vary widely across theoretical studies, they all confirm the strong potential of PE for thermal management applications.[52–55]

Experimental measurements typically yield lower values than predicted by theory.[52,56] Single fibers of high density PE (HDPE) and ultra high molecular weight PE (UHMWPE) with high crystalline alignment exhibit thermal conductivities between $10\,\mathrm{W\,m^{-1}\,K^{-1}}$ and $20\,\mathrm{W\,m^{-1}\,K^{-1}}$ along the fiber axis, where longitudinal acoustic phonons are the primary heat carriers. The characteristic T^{-1} decay near room temperature suggests that anharmonic scattering, rather than structural disorder, limits the heat transport.[56] However, even higher thermal conductivities were achieved with ultra-drawn UHMWPE nanofibers, tens of millimeters in length, which reached about $104\,\mathrm{W\,m^{-1}\,K^{-1}}$ when fiber quality approached that of an ideal crystal.[57] This value exceeds the thermal conductivities of several metals, including platinum, iron and nickel, highlighting the remarkable potential of polymers when optimally processed.[39,57]

Drawing is also crucial for achieving high conductivity in films. Uniaxially stretched UHMWPE films have reached $65\,\mathrm{W\,m^{-1}\,K^{-1}}$, and even biaxially stretched films achieved $18\,\mathrm{W\,m^{-1}\,K^{-1}}$. Increasing the draw ratio induces structural changes that lead to chain extension, crystal growth, and a considerable degree of orientation in the amorphous regions.[58,59] Additionally, the high thermal conductivities were attributed to the disentanglement of polymer chains and the increase in molecular weight, which reduces the relative number of chain ends acting as defects.[58]

The theoretical and experimental achievements show that the typically low thermal conductivity values reported for polymers arise from structural features that can be significantly modified. Strong covalent bonds along the polymer chains enable high group velocities in crystalline polymer structures, and when mass or structural defects are minimized, thermal conductivities comparable to those of metals become accessible.

So far, the weak intermolecular interactions responsible for low thermal conductivity perpendicular to the polymer chains have been discussed only as a limiting factor. However, this perspective is incomplete. Research shows that π-π stacking and hydrogen bonding, which are

relatively strong compared to conventional Van der Waals forces, can be harnessed to enhance thermal conductivity. By deliberately incorporating motifs that form supramolecular bonds, chains in amorphous or semi-crystalline polymers can be bridged. These bridges stiffen the lattice, constrain the chain rotation and improve the lattice order – all factors that reduce phonon scattering and consequently enhance thermal transport. Moreover, they establish continuous thermal pathways through the material, further improving heat conduction.[60–63]

Despite their use in enhancing thermal conductivity, the transport mechanisms across such supramolecular bonds remain largely unexplored. Experimental studies present a significant challenge, as they require a stable and measurable system where heat is transferred solely via intermolecular interactions. Nevertheless, a few studies have managed to investigate such systems and provide valuable insights.[64–66] For instance, analysis of self-assembled supramolecular polymer fibers formed from melamine and various hydroxybenzoic acid isomers revealed that hydrogen bond strength influences phonon transport, specifically stronger bonds lead to higher thermal conductivity. Additionally, a correlation was found in these systems between hydrogen bond strength and π-stacking efficiency perpendicular to the fiber axis.[64] The results reinforce the significant influence of bonding strength on phonon transport, both directly, and indirectly by affecting the defect and thermal pathway density. However, the study does not provide a detailed investigation of the underlying phonon propagation processes.

While hydrogen bonds generally form stronger interactions, single-crystalline π-stacked triphenylene columns exhibit a thermal diffusivity of approximately $0.21\,\mathrm{mm^2\,s^{-1}}$ along the stacking direction.[65,67] This value surpasses many covalently bound polymers and highlights the potential relevance of π-π interactions. The temperature-dependent thermal conductivity in this direction resembles that of crystalline dielectric solids, and mean free path calculations identify acoustic phonons as the primary heat carriers across π-stacked molecules. Although localized intramolecular vibrations play a key role in the heat capacity, they hardly carry thermal energy. Only below the Debye temperature are their energies sufficiently low to enable coupling with acoustic phonons, allowing stored vibrational energy to participate in heat conduction. Perpendicular to the stacking axis, where molecules are linked by weak, nondirectional Van der Waals forces, short phonon mean free paths indicate minimal acoustic phonon transport and an amorphous-like transport behavior.[65]

A direct comparison between thermal transport by π-π interactions and covalent bonding was made possible using an organic molecule that undergoes reversible single-crystal-to-single-crystal topochemical polymerization upon light exposure. At room temperature, the thermal conductivity of the polymerized structure was only about 1.4 times higher than that of the depolymerized form, in which heat transfer occurred exclusively via supramolecular interactions. The group velocities differed similarly modestly, by a factor of 1.2, and both systems appear to be dominated by U-scattering.[66] These results indicate that in systems with significant intermolecular interactions, identical composition, and nearly identical structures, the presence of covalent bonds is not as decisive for thermal transport as one might expect. However, covalent bonding raises the Debye temperature, and below this threshold, phonon mean free paths and scattering times increase exponentially. As a result, at lower temperatures, the polymerized material exhibits substantially higher thermal conductivity than its supramolecular counterpart, with the difference becoming more pronounced as temperature decreases.[66]

Based on the current state of research, thermal transport across supramolecular interactions appears to resemble that of crystalline materials, with acoustic phonons acting as the dominant

heat carriers. While the strength of individual bonds has some direct influence on phonon transport, its indirect effect by shaping molecular packing and reducing defect density emerges as the more decisive factor for overall thermal conductivity. Nevertheless, in my view, our understanding of heat transport via supramolecular interactions is still in its early stages, and each newly studied system continues to reveal further aspects of the complex mechanisms involved.

While the discussed strategies for enhancing thermal transport focus on tailoring the polymer structure itself, a widely explored approach involves embedding highly conductive fillers into the matrix to form a composite. Various fillers have been used for this purpose, ranging from metals such as nickel, copper and silver, to ceramics including boron nitride and silicon carbide, to carbon based materials like graphene or carbon nanotubes.[68] The choice of filler from the vast number of available options depends on the priorities of the specific application.

The thermal percolation threshold is a relevant parameter for all composites. It describes the filler volume fraction necessary for the formation of a continuous network that enables efficient heat conduction. This point is characterized by a sudden increase in thermal conductivity as a function of filler volume fraction.[68,69] Achieving percolation, and thus high thermal conductivity, typically requires high filler loadings. These high loadings are often associated with increased costs and processing challenges.[68] However, increasing the filler aspect ratio and optimizing their orientation and distribution can lower the percolation threshold. Platelet-shaped fillers, for instance, naturally align parallel to each other, promoting the formation of thermal pathways.[68,69] Processing methods such as injection molding or additive manufacturing can reinforce this alignment, leading to particularly high in-plane thermal conductivity.[68,70,71] Nanowires have an even higher aspect ratio, which favors the formation of stable conductive paths. For example, the thermal percolation threshold in an epoxy-silver composite dropped from 38 vol% for nanocubes to 28 vol% for nanorods with an aspect ratio of 15, and to about 26 vol% for nanowires with an aspect ratio of 33 (Figure 1.7).[69]

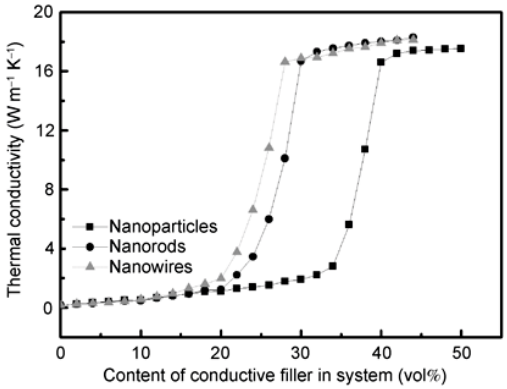

Figure 1.7: Relationship between filler content and thermal conductivity in isotropic epoxy–silver composites with varying silver filler aspect ratios. Reproduced with permission from[69].

Independent of the percolation threshold, the thermal resistance at the polymer-filler interface is a key factor governing filler effectiveness. However, disorder, multiple phases, and heterogeneities across different length scales complicate predicting and controlling interfacial transport in composites.[72] Nevertheless, various strategies have been developed to improve interfacial interactions between the filler and the polymer matrix. For example, coating highly conductive fillers with an intermediate layer can reduce the modulus mismatch between the stiff filler and the soft polymer, thereby decreasing their difference in acoustic impedance.

Lowering this impedance contrast reduces phonon scattering and thereby enhances thermal conductivity.[73,74] Another approach is to leverage intermolecular interactions by choosing appropriate polymer and filler materials. For instance, strong π-π interactions between the aromatic rings in polyaniline and graphite fillers effectively increase the thermal conductivity.[75] Furthermore, oxygen-containing defects on the surface of a graphite filler raise the cross-plane thermal conductivity in polyvinyl alcohol more than a defect-free graphite filler, even though the latter has intrinsically higher thermal conductivity. The enhancement is suggested to arise from atomic defects that promote intermolecular interactions between the filler and polymer, induce distinct vibrational modes, and thereby enable strong vibrational coupling at the polymer–filler interface.[72]

Yarns, nonwovens and woven fabrics receive significant interest for thermo-regulating textiles and other heat spreading applications. While composites contain interfaces between two different materials, such fiber assemblies contain interfaces of the same material. These contact areas, however, are rarely ideal. Structural defects, disorder, variations in structural orientation, and surface roughness all impact thermal transport across the boundaries.[76] These imperfections manifest as contact resistance, a central factor in several theoretical simulations that model the thermal conductivity of fiber networks. The suitability of these models depends on the specific fiber and network parameters. Nevertheless, they consistently identify fiber volume fraction, orientation distribution, fiber length, diameter, conductivity, and contact resistance as key parameters.[77–79] Moreover, in fibrous systems comparable to glass wool, increasing contact resistance changes the impact of the inter-fiber contacts. This, in turn, renders the enhancing effect of higher density and longer fibers, as well as the reducing effect of larger diameters, more pronounced. However, the mean fiber orientation does not appear to correlate with the contacts' influence. Instead, the thermal conductivity consistently decreases as the mean angle with respect to the heat flux direction increases.[79]

A dependence of thermal transport on fiber orientation was also observed experimentally in fibrous polyurethane membranes, where stretching introduced not only structural anisotropy but also anisotropic thermal transport properties.[80] In another experimental study, UHMWPE fibers were first twisted into yarns and then woven into fabrics, enabling direct assessment of the effect of each hierarchical step on thermal conductivity. The reduction in effective thermal conductivity from fiber to yarn to fabric was mainly attributed to the packing density of fibers within the yarn and the packing density of yarns within the fabric.[81] This indicates that thermal transport across the fibers plays a negligible role compared to the transport along the highly conductive fibers. Nevertheless, the fabric showed a notably high thermal conductivity of about $10\,\mathrm{W\,m^{-1}\,K^{-1}}$, highlighting the potential of such flexible textiles in thermal management applications.[81]

In summary, a diverse range of theoretical and experimental approaches has demonstrated that the thermal conductivity of polymers can be significantly enhanced and controlled by tuning structural alignment, engineering supramolecular interactions and introducing highly conductive fillers. Moreover, the role of interfacial interactions, in both composites and fibrous systems, is an important aspect of this research area. However, the overview also reveals the need for further progress in understanding thermal transport in hierarchical systems. Open questions remain regarding heat transport across non-covalent interactions as well as in complex fibrous systems. Furthermore, the variability and tunability of hierarchical polymeric systems provide immense potential for thermal management applications that has yet to be fully harnessed.

Methods

2

2.1 Structural Characterization

A sound investigation of how hierarchical structures affect thermal transport requires detailed structural analysis from the molecular to the microscopic level. To meet this requirement, various methods providing complementary information across different length scales were applied. The most important techniques will be briefly introduced in the following sections.

2.1.1 Polarized Infrared Spectroscopy

In several contributions to this thesis, I assessed the alignment of polymer chains qualitatively via polarized infrared (IR) spectroscopy. This technique is based on the core concept of Fourier-transform IR spectroscopy, where infrared light illuminates the sample and the transmitted or reflected light is detected. To obtain wavelength-resolved data, the detected signal is Fourier transformed and processed against a reference measurement. In contrast to this classical approach, polarized IR spectroscopy uses linearly polarized incident radiation. Therefore, a polarizer is included in the setup to filter the radiation from the light source, transmitting only components with an electric field oscillating in a specific plane (Figure 2.1).

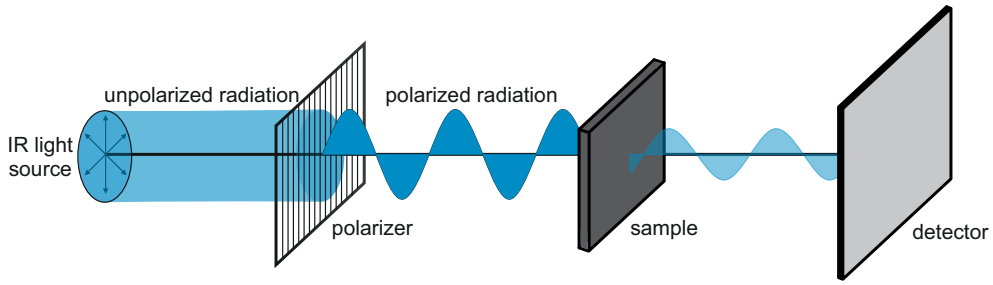

Figure 2.1: Schematic illustration of polarized infrared (IR) spectroscopy.

By rotating the polarizer around the beam propagation axis, a qualitative assessment of in-plane molecular orientations is enabled. Depending on their symmetry, vibrational modes of polymers exhibit parallel or perpendicular transition moments relative to the polymer chain, or no specific polarization at all. Modes with a parallel transition moment are termed parallel or π polarized modes. Consequently, they are most efficiently excited by light that is polarized in the corresponding direction. Conversely, perpendicular or σ polarized modes are most efficiently excited by light polarized at 90° relative to the polymer chain.[82] In an ideal case, the absorptance would be proportional to $\cos^2\theta$, where θ is the angle between the polarized light's orientation and the transition moment of the vibrational mode (Malus' Law); thus a 90° angle would result in zero absorptance.[83]

Spectra measured with different polarization angles of the incident radiation, combined with knowledge of a sample's polarized modes, therefore allow determining whether the polymer chains in the probed area exhibit a preferred orientation.

2.1.2 Wide Angle X-Ray Scattering

Wide angle X-ray scattering (WAXS), also often referred to as wide angle X-ray diffraction, is a powerful technique for analyzing molecular-scale structural properties, typically in the range of $0.1\,\mathrm{nm}$ to $10\,\mathrm{nm}$. A collimated, monochromatic X-ray beam illuminates the sample, and the X-rays are elastically scattered by the electron clouds of the atoms (Figure 2.2 a).[84] The periodic arrangement of atoms in a crystal creates intrinsic variations in electron density, so interference of the scattered waves produces a characteristic diffraction pattern on the detector. A beam stop prevents the unscattered primary beam from saturating the detector. Constructive interference occurs when the path difference between scattered X-rays is an integer multiple of the wavelength. In all other cases, destructive interference dominates (Figure 2.2 b). Bragg's Law relates the X-ray wavelength λ, the spacing between lattice planes d and the angle of diffraction θ, providing the basis for extracting structural information from the diffraction pattern. The integer n denotes the diffraction order and is typically one for the most intense reflections.[85]

$$n\,\lambda = 2\,d\,\sin\theta \tag{2.1}$$

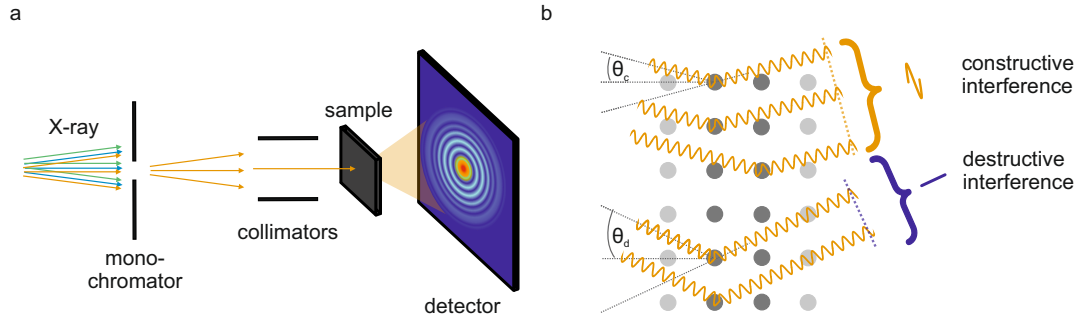

Figure 2.2: Schematic illustration of wide angle X-ray scattering (WAXS). a) Basic experimental setup. b) Illustration of Bragg's law showing constructive and destructive interference depending on the scattering angle.

For a given WAXS setup, the X-ray wavelength is fixed, and structural analysis is performed by evaluating the diffraction signals as function of 2θ.[86] Since lattice spacings are generally on the same order of magnitude as the X-ray wavelength, the relevant 2θ angles tend to be relatively large, usually above $10°$. Copper K_α radiation, with a wavelength of approximately $0.1541\,\mathrm{nm}$, is a common choice in WAXS measurements. However, other sources like silver anodes or synchrotron facilities are also employed, providing different X-ray wavelengths. For a wavelength-independent description of the diffraction patterns, the scattering vector q is employed.[84]

$$q = \frac{4\,\pi}{\lambda}\,\sin\theta \tag{2.2}$$

The setup used in this thesis includes a 2D area detector. The resulting 2D diffraction pattern can be azimuthally integrated to obtain a 1D intensity profile as a function of 2θ or the scattering vector q. The positions of the diffraction peaks provide the crystal lattice parameters, while the peak widths offer an approximation of the crystallite size.

Although lacking long-range order, atoms and bonds in amorphous materials still have fixed sizes and local arrangements. This short-range order causes fluctuations in the electron density, resulting in broad diffuse halos rather than sharp Bragg peaks characteristic of crystals. The degree of crystallinity can be estimated from the ratio of the integrated intensity of crystalline peaks to the total scattering intensity, including contributions from the amorphous halo.[84,87]

For anisotropic samples, the 2D data provides additional information. Intensity variations as a function of the scattering vector q and the azimuthal angle ψ qualitatively reveal orientation-dependent spacings on the atomic scale. These 2D patterns allow for identification of a preferred orientation of unit cells. Furthermore, a Hermans orientation factor f_H can be calculated from the intensity distribution $I(\psi)$ to quantify the anisotropy. Here, ϕ represents the angles formed by the crystallographic axes (a, b, and c), and θ denotes the Bragg angle for the respective hkl plane.[88,89]

$$\overline{\sin^2\psi} = \frac{\int_0^{2\pi} I(\psi)\,\sin^2\psi\, cos\psi\, d\psi}{\int_0^{2\pi} I(\psi)\, cos\psi\, d\psi} \tag{2.3}$$

$$\overline{\cos^2\phi} = \cos^2\theta\,\overline{\sin^2\psi} \tag{2.4}$$

$$f_H = f_c = 0.5\left(3\,\overline{\cos^2\phi}_c - 1\right) \tag{2.5}$$

For orthorhombic unit cells, the Hermans factor can also be determined from the values obtained for f_a and f_b.

$$f_a = 0.5\left(3\,\overline{\cos^2\phi}_a - 1\right) \tag{2.6}$$

$$f_b = 0.5\left(3\,\overline{\cos^2\phi}_b - 1\right) \tag{2.7}$$

$$f_H = f_c = -f_a - f_b \tag{2.8}$$

A Hermans orientation factor of 0 indicates an isotropic structure, whereas a value of 1 represents perfect uniaxial alignment. Hence, intermediate values reflect the extent of structural orientation, allowing the anisotropy of different samples to be quantitatively compared.

Overall, WAXS offers rich structural insight into crystalline and semi-crystalline, isotropic and anisotropic materials. As shown in Equation 2.1, decreasing Bragg angles probe increasing lattice spacings. The relatively large angles accessible in WAXS are therefore well suited for analyzing structural features on the Ånström to few-nanometer scale. However, larger structures, on the order of tens of nanometers, require smaller scattering angles.

2.1.3 Small Angle X-Ray Scattering

Small angle X-ray scattering (SAXS) is an ideal complement to WAXS. Most parts of the setup are identical, and some instruments can perform both techniques. However, in SAXS the distance between sample and detector is much larger, enabling the detection of small scattering angles, typically with 2θ below $10°$. This allows the analysis of features ranging from roughly $1\,\mathrm{nm}$ to $100\,\mathrm{nm}$, and in some cases even up to $1000\,\mathrm{nm}$ (Figure 2.3). Surfactant assemblies, colloids, proteins and domains in soft matter are common examples.[84]

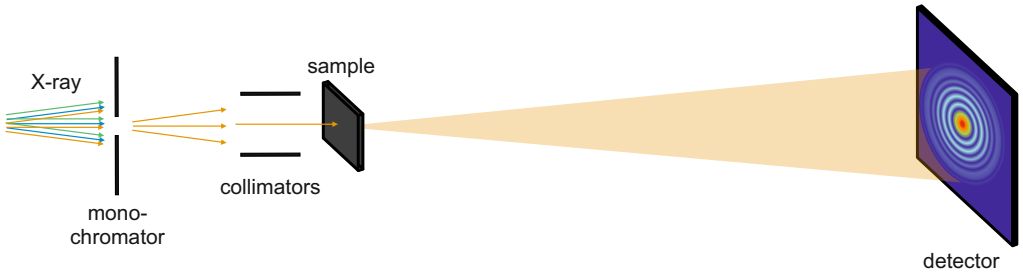

Figure 2.3: Schematic illustration of a basic small angle X-ray scattering (SAXS) setup.

Like WAXS, SAXS relies on the elastic scattering of monochromatic X-rays by the sample's electrons. In contrast to WAXS, where electron density contrast in crystals is intrinsically provided by the periodic arrangement of atoms, SAXS requires sufficient electron density contrast between nano- to mesoscale features of interest and their surrounding medium. When such contrast exists, constructive and destructive interference produces a measurable scattering pattern on the detector.[90]

For isotropic samples, the 2D scattering pattern can be radially averaged to obtain a 1D intensity profile. The scatterers probed by SAXS are often not as uniformly spaced as lattice planes in a crystal. Consequently, the superposition of their scattering contributions can broaden or smear out the minima and maxima in the scattering curve. Nevertheless, for structures with sufficiently low dispersity, the detected intensity as a function of the scattering vector q encodes valuable information about the distance, size and shape of the sample features. To extract the information, appropriate models are fitted to the experimental intensity distribution, and their parameters are optimized to best reproduce the measured data. These models are expressed in terms of the form factor $P(q)$ and the structure factor $S(q)$, which are related to the intensity distribution $I(q)$ as follows:[90]

$$I(q) \propto P(q)\, S(q) \tag{2.9}$$

In essence, the form factor represents the sum of individual scattering waves arising from within the volume of a single average scattering feature. In contrast, the structure factor accounts for the interference of waves scattered by different, neighboring features in the sample. Consequently, the form factor obtained from fitting, combined with prior knowledge of the sample, reveals structural details about the features themselves, whereas the structure factor provides insight into their mutual interactions and spacial arrangement within the sample.[90]

For anisotropic samples, reducing the 2D scattering data to a 1D curve, leads to a loss of information. 2D Azimuthal representations or intensity maps plotted with respect to detector coordinates (q_x, q_y) directly reveal anisotropy on the nano- to mesoscale. Furthermore, specific

anisotropic intensity patterns can be directly linked to certain structural features, such as fibers or lamellae, revealing their shape and orientation. Their alignment typically goes hand in hand with a preferred orientation on smaller length scales, highlighting the synergy of WAXS and SAXS. The complementary use of both methods provides a full picture from the atomic to the nano- and mesoscale.

2.1.4 Scanning Electron Microscopy

Depending on the size of relevant structures, the sample area of interest, and surface properties, different microscopy techniques vary in suitability. For the samples studied in this thesis, either scanning electron microscopy (SEM) or laser scanning confocal microscopy (LSCM) was employed. While both methods provide direct visualization of appropriately sized features, the underlying principles differ strongly.

For SEM, an electron beam is generated by an electron gun and the electrons are accelerated by a high voltage, typically between $1\,\mathrm{kV}$ and $20\,\mathrm{kV}$. The condenser lens system adjusts the current and diameter of the beam and the objective lens system focuses it on the sample surface (Figure 2.4). The electrons interact with the sample surface either by elastically scattering from atomic nuclei or by inelastically scattering with atomic shells. The elastically backscattered electrons (BSE) preserve their kinetic energy and are collected by the BSE detector, which is positioned above the sample in line with the electron beam. Secondary electrons (SE) stem from the outer shells of atoms and are ejected by the incident electrons (SE1) or by backscattered electrons (SE2). The latter are attracted by a positive potential at the SE2 detector, which is too weak to affect the trajectory of the high-energetic BSE. As the sample surface is scanned by the electron beam, its position can be correlated with the number of electrons collected by the detectors. While the BSE mode provides high composition contrast, the SE2 detector offers a clear 3D impression of the sample surface.[91]

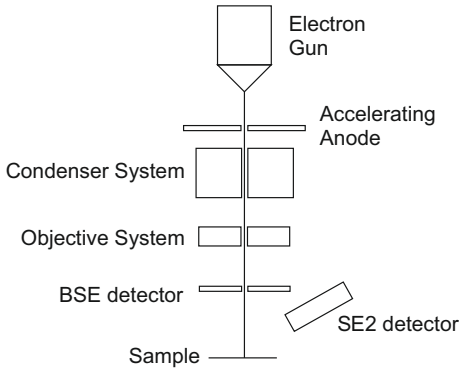

Figure 2.4: Schematic illustration of a scanning electron microscopy (SEM) setup.

The advantage of using accelerated electrons instead of light for imaging lies in their significantly lower wavelengths. According to the Abbe limit, a lower wavelength λ reduces the minimum distance between two distinguishable points d, thereby increasing the resolution. Here, n is the refractive index of the medium surrounding the lens and δ is the half-angle of the light or electron cone collected by a lens.[92]

$$d = \frac{\lambda}{2\,n\,\sin\delta} \tag{2.10}$$

Therefore, with sufficient acceleration, SEM achieves a resolution on the order of nanometers and a significantly better depth of field compared to classical optical microscopy techniques.[91] However, charging effects or sample degradation at excessive voltages make it necessary to optimize the acceleration voltage based on the sample composition, preparation, and required resolution.[93] Depending on the desired information, the detection strategies can be used individually or combined, and comparison of their results may offer insights into the spatial

distribution of different materials. Moreover, the acquired images can be processed and analyzed, for example through Fourier transformation to identify repeating patterns, or by determining particle sizes, fiber or nanowire diameters and orientations, as well as their respective distributions.[94–97] Since each image captures only a local region, reliable evaluation typically requires a statistically meaningful number of micrographs.

2.1.5 Laser Scanning Confocal Microscopy

Despite its lower resolution compared to SEM, the optical technique LSCM is highly practical, as it operates under atmospheric pressure and requires no special sample preparation. It enables fast and easy acquisition of sharp, high-contrast images of large sample areas.

The specific LSCM device used for this thesis features two separate optical imaging modes. The first mode functions similarly to a conventional microscope: an objective lens focuses white light onto the sample, and the reflected light is directed back through the objective to a detector, resulting in a color image. The second mode is the key component for the LSCM technique and provides significantly enhanced axial resolution compared to standard optical microscopy. A laser at $405\,\mathrm{nm}$ is used to obtain a high lateral resolution compared to longer-wavelength light. This light is focused onto the sample by the objective lens. The reflected light passes through a pinhole aperture before being detected by a photomultiplier. By blocking light reflected from above or below the focal plane, the pinhole strongly reduces out-of-focus haze (Figure 2.5).[98] Similar to SEM, the focused laser beam scans the sample surface using Piezo elements, imaging the area point-by-point.

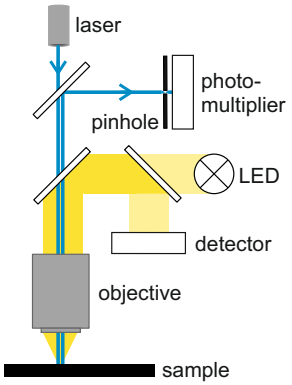

Figure 2.5: Schematic illustration of laser scanning confocal microcopy (LSCM).

LSCM not only provides high-resolution images but, owing to its shallow depth of field, also enables the acquisition of detailed topographic information.[98] By automatically shifting the focal plane, precise height profiles of the surface can be reconstructed. In addition, the accessible analysis area can be extended well beyond the native field of view of the objective lens through stitching, in which multiple fields of view are combined into a single large image. The acquired images can be processed and evaluated in various ways, for instance to quantify surface roughness, sample thickness, plateau or cavity dimensions, height variations, and fiber orientation.[99]

2.2 Thermal Diffusivity Analysis

The characterization of thermal transport properties was the core of my research throughout this thesis. Light flash analysis (LFA) and lock-in thermography (LIT) were used to obtain the thermal diffusivity values for various materials. LFA was particularly suited to assessing through-plane transport in 3D architectures, while LIT provided in-plane values of thin films and fibers. In the following section, I will introduce these two methods and explain their underlying principles.

2.2.1 Light Flash Analysis

To achieve optimal absorption and emission properties, the surface of samples with an insufficiently dark color is coated with a thin carbon layer several micrometers thick. The sample is positioned in the sample holder, above the light source and below the nitrogen-cooled IR detector (Figure 2.6). When the predefined temperature in the sample chamber is reached, the light source applies a thermal pulse. The heat is absorbed by the sample surface, conducted through the sample, and the time-dependent temperature rise on the opposite side is monitored by the detector.

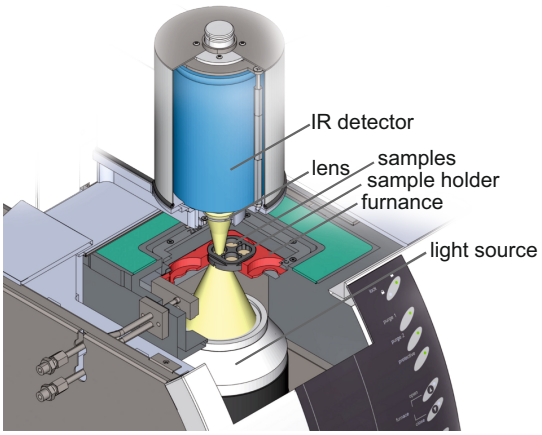

Figure 2.6: Schematic illustration of a light flash analysis (LFA) setup. Adapted with permission from[100] copyright NETZSCH-Gerätebau GmbH.

Knowing the sample thickness l, the thermal diffusivity α can be calculated from the half-rise time $t_{1/2}$.[101]

$$\alpha = 1.38 \frac{l^2}{\pi^2 \, t_{1/2}} \tag{2.11}$$

This equation, however, assumes ideal conditions with opaque samples, an infinitely short pulse, and no heat losses. To account for non-ideal conditions, various extended models have been developed.[102] For the analysis of samples in this thesis, the improved Cape–Lehman model, as implemented in the instrument software, was used. This model accounts for heat losses and a finite pulse duration in the calculation of thermal diffusivity.[103] If the density and specific heat capacity are known, the obtained thermal diffusivity can be used to calculate the through-plane thermal conductivity according to the relation given in Equation 1.13.

LFA is a fast, robust, and non-destructive thermal analysis method, ideally suited for samples with a homogeneous thickness in the millimeter range and an even surface topography. The technique also enables temperature-dependent studies and measurements under vacuum or controlled gas atmospheres, providing reliable thermal diffusivity values across a wide range of sample shapes and sizes.[102]

2.2.2 Lock-In Thermography

Unlike the commercial LFA device, the LIT setup used in this work is custom-built, consisting of a point laser, a vacuum chamber, and an IR camera. To enhance the absorption and emission, samples of light surface color are coated with a thin carbon layer only several nanometers thick. The measurements are performed at low pressure to minimize convective and conductive heat losses of the sample to its surroundings.[104] The point laser is focused onto the sample surface. An optically transparent and an IR transparent window in the vacuum chamber allows periodic heating of the sample from one side and monitoring the thermal response from the opposite side. The time-dependent signal is then converted to the frequency domain by Fourier transform, yielding amplitude and phase data at the excitation frequency (Figure 2.7). This conversion is crucial for the method, as most noise detected in the time-domain is constant or occurs at frequencies different from the measurement frequency. Therefore, LIT enables measurements even when the noise floor is larger than the excitation response signal.[105]

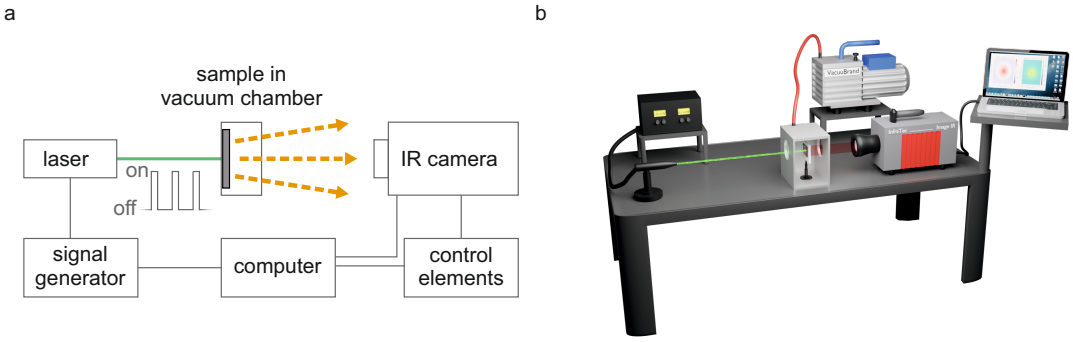

Figure 2.7: Illustration of the custom-built lock-in thermography (LIT) setup. a) Schematic of the main components and their interconnections. b) 3D Visualization of the experimental setup.

A *Python* script developed by my former colleague Thomas Q. V. Tran for thin film evaluation calculates the thermal diffusivity from the amplitude and phase data. The script first determines the coordinates of the excitation point. For thermally isotropic samples, the distance r from this point to each pixel is computed, and the amplitude and phase data are converted from 2D spatial data to a 1D functions of r. For anisotropic samples, only data points along two orthogonal directions are evaluated: the preferred thermal transport direction and the cross-direction. In both cases, the amplitude data is multiplied by $\sqrt{r}$ and the natural logarithm is applied to linearize its relationship with r.[104] In contrast, for fiber measurements, where heat transport is considered one-dimensional the amplitude data is log-transformed directly, without multiplication by $\sqrt{r}$.[106]

In all cases, the linearized amplitude and phase data as a function of r are fitted and the respective slopes m_{Amp} and m_{ϕ} are directly related to the thermal diffusivity values α_{Amp} and α_{ϕ}. Here, $f_{lock-in}$ is the excitation frequency.[104]

$$m_{Amp} = -\sqrt{\frac{\pi\, f_{lock-in}}{\alpha_{\ln Amp}}} \tag{2.12}$$

$$m_{\phi} = -\sqrt{\frac{\pi\, f_{lock-in}}{\alpha_{\phi}}} \tag{2.13}$$

In the ideal case of no thermal losses, the thermal diffusivity could be determined from either of the two slopes. To optimize accuracy under real conditions, we reduced the pressure in the vacuum chamber to below $1 \cdot 10^{-5}\,\mathrm{bar}$ and used the product of both slopes to calculate the thermal diffusivity.[104]

$$\alpha = \frac{\pi\, f_{lock-in}}{m_{Amp}\; m_{\phi}} \tag{2.14}$$

The lock-in frequency is a crucial experimental parameter and is typically determined from a frequency sweep at a single sample position. On the one hand, low frequencies increase the thermal penetration depth μ. To prevent boundary effects, the lateral extensions of a thin film or the length of a fiber must be significantly larger than the thermal penetration depth. Therefore, excessively low lock-in frequencies can lead to inaccurate values of the thermal diffusivity.[104]

$$\mu = \sqrt{\frac{\alpha}{\pi\, f_{lock-in}}} \tag{2.15}$$

On the other hand, excessively high frequencies can lead to diffraction effects from the detection optics and diffusivity overestimation.[104] They also reduce the thermal penetration depth, an important consideration for the samples investigated in this thesis. To ensure reliable results the thermal penetration depth must remain well above the sample thickness. A frequency sweep typically exhibits a plateau region where the thermal diffusivity values are independent of frequency (Figure 2.8). To obtain accurate thermal diffusivity values a frequency within this plateau must be selected.

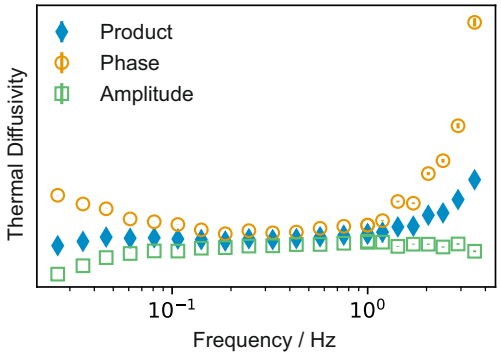

Figure 2.8: Exemplary frequency sweep demonstrating the the deviation of thermal diffusivity values at high and low frequencies, and the plateau region in between.

Additionally, and particularly important for fiber measurements, a suitable laser power is required. High powers can distort results by excessively heating the sample, whereas low powers lead to poor signal-to-noise ratios.[107] Therefore, a balanced power must be identified.

Although LIT requires specific sample conditions and often preliminary frequency sweeps, it enables the determination of thermal diffusivity across a wide range of materials. The key advantages of LIT include its high sensitivity, the ability to selectively probe in-plane thermal transport, and its suitability for characterizing thin films and fibers. With known density and specific heat capacity, the measured diffusivity can also be converted into in-plane thermal conductivity using Equation 1.13.

References

[1] R. Clausius, *Annalen der Physik* **1854**, *169*, 481–506, DOI 10.1002/andp.18541691202.

[2] A. R. Dhumal, A. P. Kulkarni, N. H. Ambhore, *Journal of Engineering and Applied Science* **2023**, *70*, 140, DOI 10.1186/s44147-023-00309-2.

[3] R. Bahru, M. F. M. A. Zamri, A. H. Shamsuddin, N. Shaari, M. A. Mohamed, *International Journal of Energy Research* **2020**, *45*, 3548–3568, DOI 10.1002/er.6078.

[4] A. L. Moore, L. Shi, *Materials Today* **2014**, *17*, 163–174, DOI 10.1016/j.mattod.2014.04.003.

[5] C. Zhao, Y. Li, Y. Liu, H. Xie, W. Yu, *Advanced Composites and Hybrid Materials* **2023**, *6*, 27, DOI 10.1007/s42114-022-00584-2.

[6] F. Jiang, S. Zhao, L. Wang, S. Yu, H. Guan, J. Liu, *Frontiers in Materials* **2022**, *9*, 907858, DOI 10.3389/fmats.2022.907858.

[7] S. Y. Khan, S. Rauf, S. Liu, W. Chen, Y. Shen, M. Kumar, *Energy & Environmental Science* **2025**, *18*, 1130–1175, DOI 10.1039/d4ee03525a.

[8] L. Peng, B. Su, A. Yu, X. Jiang, *Cellulose* **2019**, *26*, 6415–6448, DOI 10.1007/s10570-019-02534-6.

[9] G. Wedler, *Lehrbuch der Physikalischen Chemie*, 5. vollst. überarb. und aktualisierte Aufl., WILEY-VCH, Weinheim, **2004**.

[10] I. Lienhard, J. H., V. Lienhard, J. H., *A Heat Transfer Textbook*, 5. ed, Dover Publications, Mineola, NY, **2019**.

[11] G. Kirchhoff, *Annalen der Physik* **1860**, *185*, 193–215, DOI 10.1002/andp.18601850205.

[12] M. Planck, *Verhandlungen der Deutschen Physikalischen Gesellschaft* **1900**, *2*, 237–245.

[13] J. C. Cuevas, F. J. García-Vidal, *ACS Photonics* **2018**, *5*, 3896–3915, DOI 10.1021/acsphotonics.8b01031.

[14] W. Wien, *Sitzungsberichte der Königlich Preußischen Akademie der Wissenschaften zu Berlin* **1893**, *Erster Halbband*, 55–62.

[15] J. Stefan, *Sitzungsberichte der Kaiserlichen Akademie der Wissenschaften in Wien Mathematisch-Naturwissenschaftliche Classe* **1879**, *79*, 391–428.

[16] L. Boltzmann, *Annalen der Physik* **1884**, *258*, 291–294, DOI 10.1002/andp.18842580616.

[17] V. K. Bityukov, Y. I. Khudak, N. G. Gusein-zade, *Bulletin of the Lebedev Physics Institute* **2018**, *45*, 46–50, DOI 10.3103/s1068335618020033.

[18] W. Prout, *Chemistry, Meteorology, and the Function of Digestion Considered with Reference to Natural Theology*, William Pickering, London, **1834**.

[19] W. Nusselt, *Gesundheits-Ingenieur* **1915**, *38*, Translated from German: Das Grundgesetz des Wärmeüberganges., 477–482, DOI 10.4224/20331615.

[20] I. Newton, *Philosophical Transactions of the Royal Society of London* **1701**, *22*, 824–829, DOI 10.1098/rstl.1700.0082.

[21] M. Vollmer, *European Journal of Physics* **2009**, *30*, 1063–1084, DOI 10.1088/0143-0807/30/5/014.

[22] J. Fourier, *The Analytical Theory of Heat*, Translated from French: Théorie de la Chaleur., Didot, Paris, **1822**.

[23] A. Salazar, *European Journal of Physics* **2003**, *24*, 351–358, DOI 10.1088/0143-0807/24/4/353.
[24] P. Atkins, J. De Paula, *Atkins' Physical Chemistry*, 8., W. H. Freeman, New York, NY, **2006**.
[25] Z. Xian, Z. Ping, C. Xiao, Y. Wang, X. Ding, X. Liu, X. Tian, *Thermal Management Materials for Electronic Packaging*, 1., WILEY-VCH, Weinheim, **2024**.
[26] R. Peierls, *Annalen der Physik* **1929**, *395*, 1055–1101, DOI 10.1002/andp.19293950803.
[27] C. Kittel, *Introduction to Solid State Physics*, 8., John Wiley & Sons, New York, NY, **2005**.
[28] D. Wright, D. H. Mudiyanselage, E. Guzman, X. Fu, J. Teeter, B. Da, F. Kargar, H. Fu, A. A. Balandin, *Applied Physics Letters* **2024**, *125*, DOI 10.1063/5.0233163.
[29] P. Debye, *Annalen der Physik* **1912**, *344*, 789–839, DOI 10.1002/andp.19123441404.
[30] G. Zhao, Q. Yan, *Functional Materials from Colloidal Self-Assembly*, 1., WILEY-VCH, Weinheim, **2022**, pp. 493–538, DOI 10.1002/9783527828722.
[31] Z. Tong, S. H. Li, X. L. Ruan, H. Bao, *Physical Review B* **2019**, *100*, 144306, DOI 10.1103/PhysRevB.100.144306.
[32] A. A. Maznev, O. B. Wright, *American Journal of Physics* **2014**, *82*, 1062–1066, DOI 10.1119/1.4892612.
[33] G. J. Chaplain, J. M. De Ponti, A. Colombi, R. Fuentes-Dominguez, P. Dryburg, D. Pieris, R. J. Smith, A. Clare, M. Clark, R. V. Craster, *Nature Communications* **2020**, *11*, 3267, DOI 10.1038/s41467-020-17021-x.
[34] X. Qian, J. Zhou, G. Chen, *Nature Materials* **2021**, *20*, 1188–1202, DOI 10.1038/s41563-021-00918-3.
[35] P. B. Allen, J. L. Feldman, J. Fabian, F. Wooten, *Philosophical Magazine B* **1999**, *79*, 1715–1731, DOI 10.1080/13642819908223054.
[36] H. R. Seyf, A. Henry, *Journal of Applied Physics* **2016**, *120*, 025101, DOI 10.1063/1.4955420.
[37] W.-X. Zhou, Y. Cheng, K.-Q. Chen, G. Xie, T. Wang, G. Zhang, *Advanced Functional Materials* **2019**, *30*, 1903829, DOI 10.1002/adfm.201903829.
[38] C. L. Choy, *Polymer* **1977**, *18*, 984–1004, DOI 10.1016/0032-3861(77)90002-7.
[39] C. Y. Ho, R. W. Powell, P. E. Liley, *Journal of Physical and Chemical Reference Data* **1972**, *1*, 279–421, DOI 10.1063/1.3253100.
[40] L. Lorenz, *Annalen der Physik* **1872**, *223*, 429–452, DOI 10.1002/andp.18722231107.
[41] N. Stojanovic, D. H. S. Maithripala, J. M. Berg, M. Holtz, *Physical Review B* **2010**, *82*, 075418, DOI 10.1103/PhysRevB.82.075418.
[42] Z. Wang, Z. Wu, L. Weng, S. Ge, D. Jiang, M. Huang, D. M. Mulvihill, Q. Chen, Z. Guo, A. Jazzar, X. He, X. Zhang, B. B. Xu, *Advanced Functional Materials* **2023**, *33*, 2301549, DOI 10.1002/adfm.202301549.
[43] Z. Li, Y. Sun, F. Hu, D. Liu, X. Zhang, J. Ren, H. Guo, M. Shalash, M. He, H. Hou, S. M. El-Bahy, D. Pan, Z. M. El-Bahy, Z. Guo, *Journal of Materials Science & Technology* **2025**, *218*, 191–210, DOI 10.1016/j.jmst.2024.07.053.
[44] Q. Chen, K. Yang, Y. Feng, L. Liang, M. Chi, Z. Zhang, X. Chen, *Composites Part A: Applied Science and Manufacturing* **2024**, *178*, 107998, DOI 10.1016/j.compositesa.2023.107998.
[45] T. M. Dauphinee, D. G. Ivey, H. D. Smith, *Canadian Journal of Research* **1950**, *28A*, 596–615, DOI 10.1139/cjr50a-050.
[46] K. H. Hellwege, J. Hennig, W. Knappe, *Kolloid-Zeitschrift & Zeitschrift für Polymere* **1963**, *188*, 121–127, DOI 10.1007/bf01499903.

[47] B. D. Washo, D. Hansen, *Journal of Applied Physics* **1969**, *40*, 2423–2427, DOI 10.1063/1.1658009.
[48] C. L. Choy, Y. Fei, T. G. Xi, *Journal of Polymer Science Part B: Polymer Physics* **1993**, *31*, 365–370, DOI 10.1002/polb.1993.090310315.
[49] S. Jabbari-Farouji, J. Rottler, O. Lame, A. Makke, M. Perez, J. L. Barrat, *ACS Macro Letters* **2015**, *4*, 147–150, DOI 10.1021/mz500754b.
[50] R. Dahule, K. Oqmhula, R. Maezono, K. Hongo, *ACS Applied Polymer Materials* **2025**, *7*, 1431–1439, DOI 10.1021/acsapm.4c03165.
[51] J. Liu, R. Yang, *Physical Review B* **2012**, *86*, 104307, DOI 10.1103/PhysRevB.86.104307.
[52] X. Wang, M. Kaviany, B. Huang, *Nanoscale* **2017**, *9*, 18022–18031, DOI 10.1039/c7nr06216h.
[53] B. Ni, T. Watanabe, S. R. Phillpot, *Journal of Physics: Condensed Matter* **2009**, *21*, 084219, DOI 10.1088/0953-8984/21/8/084219.
[54] A. Henry, G. Chen, S. J. Plimpton, A. Thompson, *Physical Review B* **2010**, *82*, 144308, DOI 10.1103/PhysRevB.82.144308.
[55] A. Henry, G. Chen, *Physical Review Letters* **2008**, *101*, 235502, DOI 10.1103/PhysRevLett.101.235502.
[56] X. Wang, V. Ho, R. A. Segalman, D. G. Cahill, *Macromolecules* **2013**, *46*, 4937–4943, DOI 10.1021/ma400612y.
[57] S. Shen, A. Henry, J. Tong, R. Zheng, G. Chen, *Nature Nanotechnology* **2010**, *5*, 251–5, DOI 10.1038/nnano.2010.27.
[58] S. Ronca, T. Igarashi, G. Forte, S. Rastogi, *Polymer* **2017**, *123*, 203–210, DOI 10.1016/j.polymer.2017.07.027.
[59] Y. Xu, D. Kraemer, B. Song, Z. Jiang, J. Zhou, J. Loomis, J. Wang, M. Li, H. Ghasemi, X. Huang, X. Li, G. Chen, *Nature Communications* **2019**, *10*, 1771, DOI 10.1038/s41467-019-09697-7.
[60] J. Zhou, S. Lin, H. Zeng, J. Liu, B. Li, Y. Xu, X. Zhao, G. Chen, *Materials Horizons* **2020**, *7*, 2936–2943, DOI 10.1039/d0mh00735h.
[61] H. Zheng, K. Wu, Y. Zhan, K. Wang, J. Shi, *Journal of Polymer Science* **2023**, *61*, 1622–1633, DOI 10.1002/pol.20230105.
[62] G.-H. Kim, D. Lee, A. Shanker, L. Shao, M. S. Kwon, D. Gidley, J. Kim, K. P. Pipe, *Nature Materials* **2015**, *14*, 295–300, DOI 10.1038/nmat4141.
[63] L. Zhang, M. Ruesch, X. Zhang, Z. Bai, L. Liu, *RSC Advances* **2015**, *5*, 87981–87986, DOI 10.1039/c5ra18519j.
[64] T. Meng, P. Zhang, H. Zhong, H. Zhu, H. Zhang, D. Xu, Y. Zhao, *Nano Letters* **2024**, *24*, 14095–14101, DOI 10.1021/acs.nanolett.4c04306.
[65] R. Takehara, N. Kubo, M. Ryu, S. Kitani, S. Imajo, Y. Shoji, H. Kawaji, J. Morikawa, T. Fukushima, *Journal of the American Chemical Society* **2023**, *145*, 22115–22121, DOI 10.1021/jacs.3c07921.
[66] R. Takehara, T. Fukui, T. Tano, M. Ryu, S. Kitani, H. Kawaji, J. Morikawa, T. Fukushima, *Journal of the American Chemical Society* **2024**, *146*, 30548–30552, DOI 10.1021/jacs.4c11849.
[67] W. M. Haynes, D. R. Lide, T. J. Bruno, *CRC Handbook of Chemistry and Physics*, 97th ed., CRC Press, Boca Raton, FL, **2016**, DOI 10.1201/9781315380476.
[68] H. Chen, V. V. Ginzburg, J. Yang, Y. Yang, W. Liu, Y. Huang, L. Du, B. Chen, *Progress in Polymer Science* **2016**, *59*, 41–85, DOI 10.1016/j.progpolymsci.2016.03.001.

[69] Y. Tao, Z. Yang, X. Lu, G. Tao, Y. Xia, H. Wu, *Science China Technological Sciences* **2012**, *55*, 28–33, DOI 10.1007/s11431-011-4651-2.
[70] R. F. Hill, P. H. Supancic, *Journal of the American Ceramic Society* **2002**, *85*, 851–857, DOI 10.1111/j.1151-2916.2002.tb00183.x.
[71] S. Bagatella, L. Castoldi, M. Cavallaro, E. Gariboldi, R. Suriano, M. Levi, *Journal of Applied Polymer Science* **2025**, *142*, e57316, DOI 10.1002/app.57316.
[72] Y. Zhou, R. Ciarla, A. Boonkird, S. Raza, T. Nguyen, J. Zhou, N. C. Osti, E. Mamontov, Z. Jiang, X. Zuo, J. Ranasinghe, W. Hu, B. Scott, J. Chen, D. K. Hensley, S. Huang, J. Liu, M. Li, Y. Xu, *Science Advances* **2025**, *11*, eadp6516, DOI 10.1126/sciadv.adp6516.
[73] M. Zhou, G. Wan, P. Mou, S. Teng, S. Lin, G. Wang, *Journal of Materials Chemistry C* **2021**, *9*, 869–880, DOI 10.1039/d0tc04388e.
[74] X. Chen, D. Parker, D. J. Singh, *Physical Review B* **2013**, *87*, 045317, DOI 10.1103/PhysRevB.87.045317.
[75] Y. Zhou, D. Hertog-Raz, S. Raza, J. Transtamar, B. Abarca, Y. Wang, J. Liu, Y. Xu, *ASME Journal of Heat and Mass Transfer* **2025**, *147*, 031402, DOI 10.1115/1.4067734.
[76] J. Chen, X. Xu, J. Zhou, B. Li, *Reviews of Modern Physics* **2022**, *94*, 025002, DOI 10.1103/RevModPhys.94.025002.
[77] X. Zhao, C. Huang, Q. Liu, I. I. Smalyukh, R. Yang, *Journal of Applied Physics* **2018**, *123*, 085103, DOI 10.1063/1.5008582.
[78] A. N. Volkov, L. V. Zhigilei, *International Journal of Heat and Mass Transfer* **2025**, *239*, 126517, DOI 10.1016/j.ijheatmasstransfer.2024.126517.
[79] C. Gaunand, Y. De Wilde, A. François, V. Grigorova-Moutiers, K. Joulain, *Physical Review Applied* **2025**, *23*, 034084, DOI 10.1103/PhysRevApplied.23.034084.
[80] Q. Gao, B. A. F. Kopera, J. Zhu, X. Liao, C. Gao, M. Retsch, S. Agarwal, A. Greiner, *Advanced Functional Materials* **2020**, *30*, 1907555, DOI 10.1002/adfm.201907555.
[81] A. A. Candadai, J. A. Weibel, A. M. Marconnet, *ACS Applied Polymer Materials* **2019**, *2*, 437–447, DOI 10.1021/acsapm.9b00900.
[82] S. Krimm, *Fortschritte der Hochpolymeren-Forschung* **1960**, *2*, 51–172, DOI 10.1007/BFb0050351.
[83] Y. J. Lee, *Journal of the Optical Society of America A* **2025**, *42*, 102–112, DOI 10.1364/josaa.542283.
[84] J. Bolze, M. Gateshki, *Review of Scientific Instruments* **2019**, *90*, 123103, DOI 10.1063/1.5130061.
[85] W. H. Bragg, W. L. Bragg, *Proceedings of the Royal Society of London. Series A Containing Papers of a Mathematical and Physical Character* **1913**, *88*, 428–438, DOI 10.1098/rspa.1913.0040.
[86] S. S. Ray, R. Banerjee in *Sustainable Polylactide-Based Composites*, (Eds.: S. S. Ray, R. Banerjee), Elsevier, **2023**, pp. 69–107, DOI 10.1016/B978-0-323-99640-2.00002-7.
[87] R. Jenkins, R. L. Snyder, *Introduction to X-ray Powder Diffractometry*, 1., John Wiley & Sons, New York, NY, **1996**, p. 403, DOI 10.1002/9781118520994.
[88] R. S. Stein, *Journal of Polymer Science* **1958**, *31*, 327–334, DOI 10.1002/pol.1958.1203112309.
[89] J. L. White, K. C. Dharod, E. S. Clark, *Journal of Applied Polymer Science* **1974**, *18*, 2539–2568, DOI 10.1002/app.1974.070180901.
[90] C. M. Jeffries, J. Ilavsky, A. Martel, S. Hinrichs, A. Meyer, J. S. Pedersen, A. V. Sokolova, D. I. Svergun, *Nature Reviews Methods Primers* **2021**, *1*, 70, DOI 10.1038/s43586-021-00064-9.

[91] T. Feller, Thesis, University of Bayreuth, **2023**, DOI 10.15495/EPub_UBT_00007232.
[92] Abbe, *Journal of the Royal Microscopical Society* **1882**, *2*, 460–473.
[93] A. Garitagoitia Cid, R. Rosenkranz, E. Zschech, *Advanced Engineering Materials* **2015**, *18*, 185–193, DOI 10.1002/adem.201500161.
[94] M. Schöttle, M. Theis, T. Lauster, S. Hauschild, M. Retsch, *Advanced Optical Materials* **2023**, *11*, 2300095, DOI 10.1002/adom.202300095.
[95] M. Schöttle, T. Lauster, L. J. Roemling, N. Vogel, M. Retsch, *Advanced Materials* **2023**, *35*, 2208745, DOI 10.1002/adma.202208745.
[96] J. Xu, Y. Zhang, *Fibers and Polymers* **2017**, *18*, 2146–2152, DOI 10.1007/s12221-017-7478-z.
[97] Y. Zhao, M. L. Fitzgerald, Y. Tao, Z. Pan, G. Sauti, D. Xu, Y. Q. Xu, D. Li, *Nano Letters* **2020**, *20*, 7389–7396, DOI 10.1021/acs.nanolett.0c02014.
[98] M. Schöttle, Thesis, University of Bayreuth, **2023**, DOI 10.15495/EPub_UBT_00007214.
[99] Olympus Corporation, Olympus LEXT OLS5000 3D Measuring Laser Microscope, Manufacturer's technical Brochure, Tokyo, **2017**.
[100] N.-G. GmbH, LFA 467 HyperFlash Light Flash Apparatus – Thermal Diffusivity and Conductivity Measurement, Web Page.
[101] W. J. Parker, R. J. Jenkins, C. P. Butler, G. L. Abbott, *Journal of Applied Physics* **1961**, *32*, 1679–1684, DOI 10.1063/1.1728417.
[102] A. Philipp, J. F. Eichinger, R. C. Aydin, A. Georgiadis, C. J. Cyron, M. Retsch, *Heat and Mass Transfer* **2020**, *56*, 811–823, DOI 10.1007/s00231-019-02742-7.
[103] J. A. Cape, G. W. Lehman, *Journal of Applied Physics* **1963**, *34*, 1909–1913, DOI 10.1063/1.1729711.
[104] A. Mendioroz, R. Fuente-Dacal, E. Apinaniz, A. Salazar, *Review of Scientific Instruments* **2009**, *80*, 074904, DOI 10.1063/1.3176467.
[105] T. Q. V. Tran, Thesis, University of Bayreuth, **2023**, DOI 10.15495/EPub_UBT_00007210.
[106] A. Salazar, A. Mendioroz, R. Fuente, R. Celorrio, *Journal of Applied Physics* **2010**, *107*, 043508, DOI 10.1063/1.3309328.
[107] T. Tran, C. Kodisch, M. Schöttle, N. W. Pech-May, M. Retsch, *The Journal of Physical Chemistry C* **2022**, *126*, 14003–14010, DOI 10.1021/acs.jpcc.2c04254.

Part II

Outline

Synopsis

4

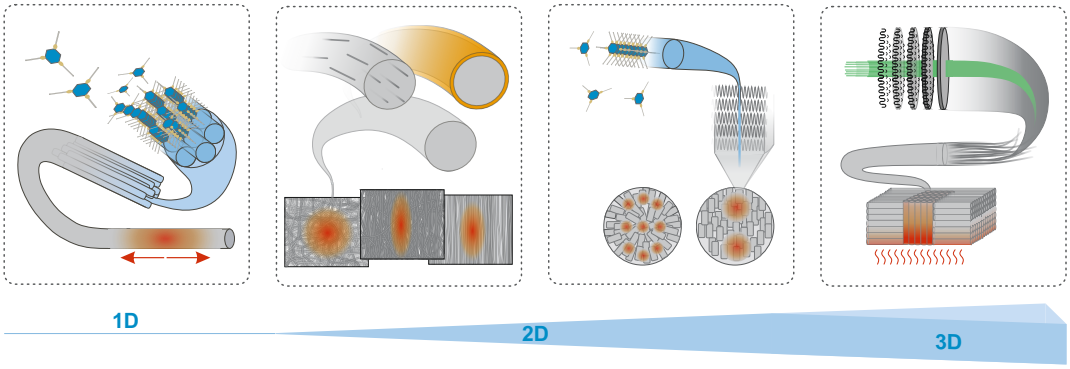

Figure 4.1: Graphical Abstract.

This thesis consists of four interconnected projects that explore thermal transport in hierarchical materials composed of polymers, benzene-1,3,5-tricarboxamides (BTAs), or a combination of both. Each project focuses on how structural features affect the thermal conduction, with particular emphasis on anisotropy. The sequence of the presented projects moves from one-dimensional (1D) fibers to two-dimensional (2D) films and ultimately to three-dimensional (3D) architectures. At the same time, this order reflects a shift from fundamental research questions to more application-driven investigations.

Chapter 7 examines thermal transport in self-assembled BTA fibers and contributes to the broader understanding of how heat flows across supramolecular interactions such as π-π stacking and hydrogen bonding. By comparing the thermal diffusivity of fibers based on a systematically varied set of BTA derivatives, this work provides valuable insight into structure–property relationships at the molecular level. In Chapter 8, the focus shifts from how molecular structures influence heat transport within single fibers to how fiber organization affects thermal transport in nonwovens. We investigated electrospun polystyrene fibers arranged into nonwovens with varying degrees of alignment. In addition to this structural anisotropy, the samples underwent post-processing treatments and metal functionalization. These variations allowed us to analyze how different interfacial and compositional features influence thermal transport with a particular focus on anisotropic heat conduction in fibrous systems. In Chapter 9 we take a step further toward practical applications by studying how BTAs, used as nucleating agents in polypropylene, affect thermal transport. We examined how processing-induced orientation of self-assembled BTA fibrils can lead to crystallite alignment in polypropylene, and whether this structural anisotropy impacts thermal diffusivity. Thin films and 3D discs were prepared to assess the influence of the nucleating agent under different processing conditions. Chapter 10 focuses on well-recyclable pure polyethylene with varying molecular weights, where high structural anisotropy was deliberately introduced using additive manufacturing. During printing, mechanical forces promote the formation of fiber-like extended-chain nanocrystals, which serve as efficient pathways for heat transport in the printed objects. The freely definable printing direction combined with anisotropic thermal conduction provides control over heat flow and offers an opportunity for efficient heat dissipation.

I begin this progression from 1D to 3D architectures by discussing thermal transport in the smallest hierarchical structures. Chapter 7 provides a fundamental look at 1D fibers formed by self-assembled BTA molecules. A wide variety of BTAs with differing side groups, and symmetries exist and several of them form intermolecular bonds that lead to well-defined, self-assembled fibers through solution crystallization. This demonstrates that BTAs offer an outstanding system to analyze heat transport via intermolecular interactions. In the long run, and in combination with theoretical studies, the active phonons, individual contributions of supramolecular interactions to thermal transport, and the dominant influencing factors for transport efficiency may be identified.

My aim was to take a first step in this extensive project by measuring the thermal transport properties on representatives of this material class. Achieving this goal posed significant experimental challenges: fibers just tens of micrometers in diameter had to be handled, and methods to characterize thermal transport in such small, individual structures are limited. Fortunately, fibers from nine different BTA derivatives were successfully prepared, suitable for LIT measurements. These differed either in their side group chemistry (*Hex-C3, iOc-C3, brOC-C3; Am-C3, Su-C3*) or in amide bond orientation (*tBu-N3, tBu-C1N2, tBu-C2N1; Hex-C2N1, Hex-C3*), allowing for a systematic analysis.

Preliminary LIT measurements revealed that selecting a single suitable power was not viable due to varying fiber thicknesses: thicker fibers led to poor signal-to-noise ratios, while thinner ones heated up, falsifying the thermal diffusivity values. To address this, three power sweeps, instead of individual measurements, were applied for each BTA derivative. For every power sweep, the peak values of the amplitude data were compared, and the power that brought this value closest to $175\,\mathrm{mK}$ was selected for the evaluation and comparison of the thermal diffusivity values (Figure 4.2). Crucially, LIT provided 1D thermal diffusivity in the fiber direction. As there are no contributions from covalent bonds in this direction, heat transport is governed solely by supramolecular interactions, presumably a combination of Van der Waals forces, π-π stacking, and especially hydrogen bonding.

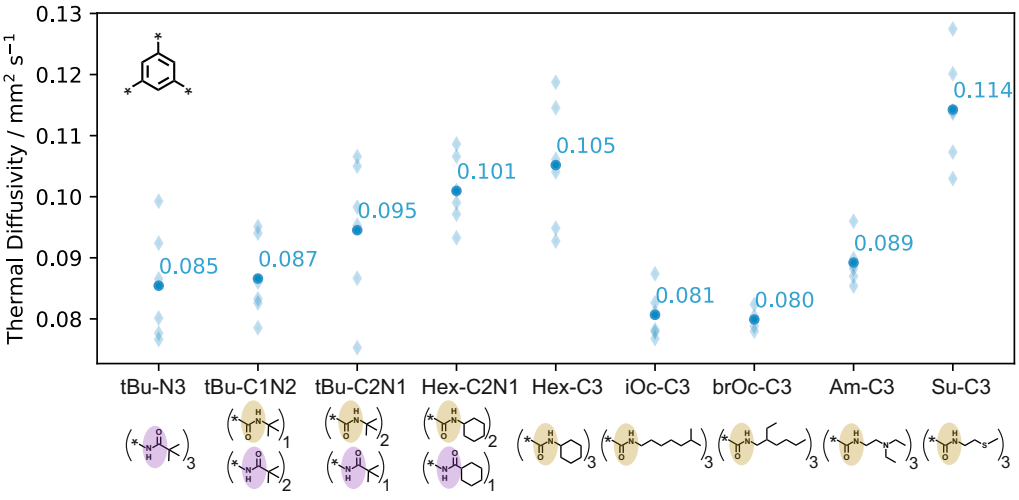

Figure 4.2: Thermal diffusivity values of fibers formed from different BTA derivatives, measured using LIT at a frequency of 0.27 Hz. For each BTA derivative, three measurements were performed, each providing two data points by evaluating both sides of the laser spot (diamonds). Sample-specific laser powers were used to account for differences in fiber thickness. Average diffusivity values are indicated by circles and annotated with corresponding numerical values. The molecular structures of the side groups for each derivative are shown along the x-axis.

The results showed that an increasing number of N-centered side groups and long aliphatic side groups lead to lower thermal diffusivity values, while the rather bulky *Hex*-group does not negatively affect thermal transport. Interestingly, the short chained linear *Su-C3* derivative, which contains a sulfur heteroatom exhibited the highest thermal diffusivity.

To obtain some first clues on structure-property relationships, IR spectra of the BTA derivatives were compared, with specific focus on the N–H and C=O stretching modes as indicators for the hydrogen bonding strength (Figure 4.3). The bands of derivatives with identical side group chemistry but varying orientation of the amide bonds, indicated stronger hydrogen bonding with an increasing ratio of C-centered side groups. This aligned with expectations, given that N-centering reduces the distance between the aromatic cores and weakens the hydrogen bonding.[1–3] As the thermal diffusivity also increased with an increasing ratio of C-centered side groups, we presumed a correlation between hydrogen bonding strength and thermal transport efficiency. Furthermore, we found a strong influence of side group chemistry on thermal diffusivity, also aligning mostly well with the hydrogen bonding strengths derived from IR spectra: *Hex-C3* > *Am-C3* > *iOc-C3* ≈ *brOc-C3*. We linked this correlation to lattice stiffening, reducing phonon-scattering and allowing for transport of higher-frequency phonons.

However, our investigations also revealed exceptions from this relationship. Despite its higher thermal diffusivity compared to *iOc-C3* and *brOC-C3*, the fully N-centered *tBu-N3* showed the N–H band at a higher wavenumber. We attributed this to the long aliphatic chains of *iOc-C3* and *brOc-C3*. Their substantial lengths could impair defect-free self-assembly and fewer fibrils forming the fiber might render thermal transport more susceptible to crystal imperfections. Remarkably, the short-chained *Su-C3* derivative stood out by exhibiting the highest thermal diffusivity, although IR data indicated stronger hydrogen bonding for *Hex-C3*. We suggested that the sulfur heteroatom modified the dipole moment of the structure in a way that is favorable for the self-assembly process, and therefore reduced the defect density.

These findings indicated that additional factors, beyond hydrogen bonding strength, such as susceptibility to defects and defect density, may also play an important role for thermal transport in BTA fibers. Moreover, we considered that stronger hydrogen bonds promote both, direct lattice stiffening and reduction in structural defects via improved self-assembly. Hence, this direct and indirect impact of hydrogen bonding strength could contribute collectively to the observed structure–thermal property relationship.

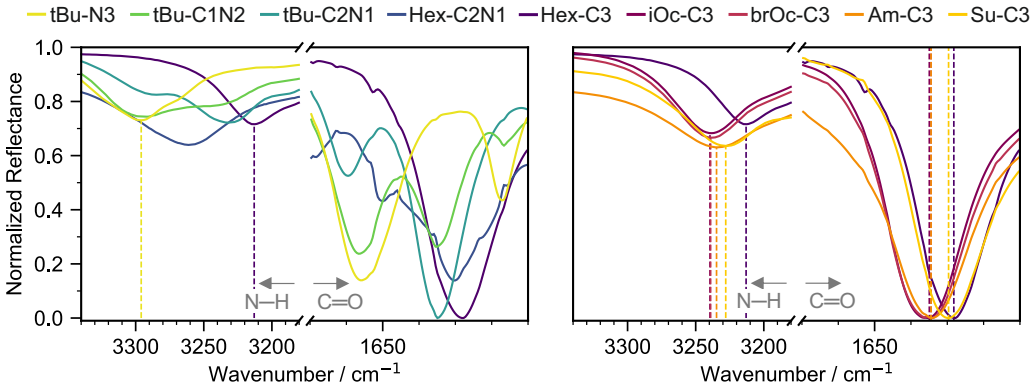

Figure 4.3: Normalized FT-IR spectra of BTA fibers, illustrating the influence of amide bond orientation (left panel) and side group chemistry (right panel). Dashed lines indicate the N–H or C=O stretch bands.

While ongoing theoretical calculations and crystallographic analyses aim to deepen the knowledge on the thermal transport processes, I successfully provided the thermal diffusivity values across molecular BTA assemblies. This offers experimental quantitative data on thermal transport mediated by supramolecular interactions.

Having explored thermal transport at the molecular level within 1D BTA fibers, we now ascend the structural hierarchy. In the next contribution (Chapter 8), we shifted our focus from individual fibers to fiber organizations within 2D nonwoven architectures. The aim of this project was to analyze how interfacial features and compositional modifications influence thermal transport in fibrous systems, with a particular focus on anisotropy. To better understand the parameters relevant for heat conduction in such systems, and ultimately support the development of materials with tailored thermal properties, a systematic experimental approach was taken. My colleague Sophie E. Fritze prepared electrospun polystyrene nonwovens with varying degrees of fiber alignment: random, oriented and highly aligned SJES nonwovens. These three sample types were post-processed either by cold-pressing or by annealing for 3 h or 24 h to investigate the impact of structural and interfacial changes (Figure 4.4 a).

To quantify the degree of orientation, I calculated an orientational order parameter S_{2D} for each nonwoven.[4,5] By analyzing LSCM images and processing the data with a custom $Python$ script, an increasing degree of orientation from random to oriented to SJES nonwovens was confirmed (Table 4.1).

Table 4.1: Average S_{2D} parameters of the electrospun nonwovens quantifying the fiber alignment.

Sample Properties	Random	Oriented	SJES
Cold-pressed	0.19 ± 0.09	0.86 ± 0.04	0.95 ± 0.3
Annealed 3 h	0.21 ± 0.09	0.67 ± 0.10	0.87 ± 0.09
Annealed 24 h	0.27 ± 0.07	0.81 ± 0.04	0.89 ± 0.03

To compare the thermal diffusivity of the nine nonwoven types, which varied either in degree of orientation or post-processing conditions, I used LIT (Figure 4.4 b). The ellipsoidal shape of the phase data for the oriented and SJES nonwovens, along with the two strongly differing thermal diffusivity values in the preferred and the cross-direction clearly showed that the structural anisotropy was reflected in thermal anisotropy. We attributed this to the uneven distribution of the inter-fiber contact points and gaps. These increased thermal resistance in the cross-direction, whereas transport along the fibers enhanced thermal diffusivity in the preferred direction. In contrast, the random nonwovens exhibited a more uniform contact-point distribution, resulting in single diffusivity values that lay between those of the oriented and SJES samples.

In line with the S_{2D} parameters, the cold-pressed SJES nonwoven had a higher thermal diffusivity in the preferred direction than the corresponding oriented nonwoven. Interestingly, the SJES nonwoven also showed significantly higher thermal diffusivity in the cross-direction compared to the oriented sample. In the SJES nonwoven, the highly aligned fibers had large portions of their lengths in direct contact, creating more efficient thermal pathways. Conversely, slight misalignments in the oriented nonwovens reduced inter-fiber contact in the cross-direction. As a result, the thermal anisotropy of the SJES nonwoven (2.8) was considerably lower than that of the oriented sample (8.6), despite its higher degree of orientation. This revealed an important insight for tuning the thermal properties of fibrous systems: while promoting fiber

alignment generally enhances thermal anisotropy, this enhancement is limited by the increasing fiber contact area in the cross direction.

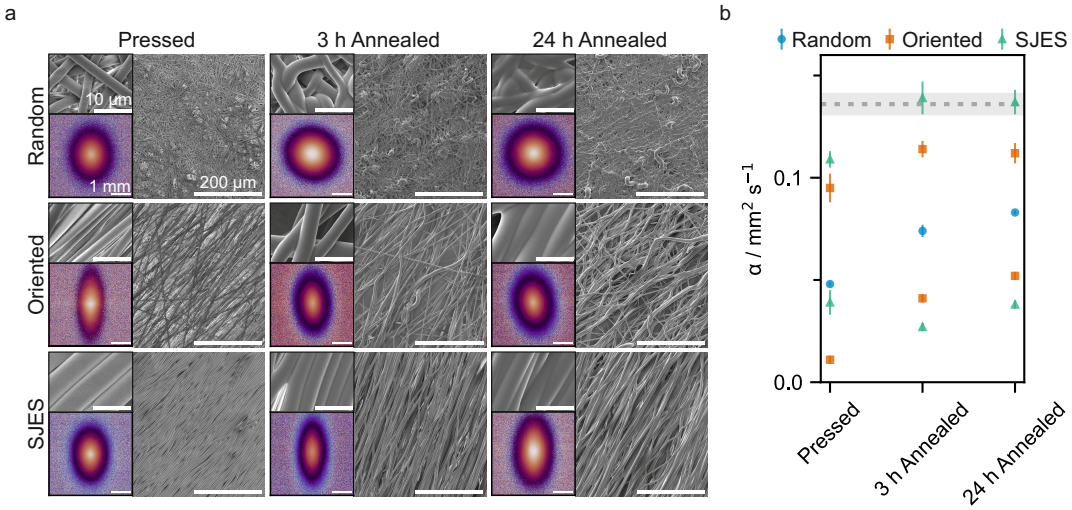

Figure 4.4: Electrospun nonwovens after pressing at room temperature, annealing at $115\,^{\circ}\mathrm{C}$ for 3 h or annealing at $115\,^{\circ}\mathrm{C}$ for 24 h. a) SEM images (Scale bars are $200\,\mu\mathrm{m}$ and $10\,\mu\mathrm{m}$) and the LIT phase data. b) Thermal diffusivity values obtained from measurements at ten positions per sample. The grey line represents the thermal diffusivity of a hot-pressed PS film. Reproduced from[6].

Annealing induced two major structural changes across all nonwoven types, sample shrinkage and fiber fusion. In the random nonwoven, shrinkage occurred isotropically, increasing the density of inter-fiber contact points. At the same time, fusion of fibers at their contact points reduced the contact resistance. Together, these two effects explained the strong increase in thermal diffusivity observed in the random samples after annealing. In the preferred direction, thermal diffusivity also increased for both the oriented and SJES nonwovens. The diffusivity of the annealed SJES samples even approached that of a hot-pressed PS reference film. To better understand the origin of this enhancement, we investigated several possible contributing factors. The S_{2D} parameters indicated no improved fiber alignment upon annealing. Moreover, polarized Raman spectroscopy measurements on the SJES samples ruled out any significant change in molecular orientation. Annealing did lead to increased waviness of the fibers, suggesting some degree of chain relaxation. However, this transition from a slightly stretched to a more relaxed state would typically reduce, rather than enhance, thermal diffusivity. We therefore attributed the improved thermal diffusivity in the preferred direction to the fusion of misaligned fibers. Their reduced thermal contact resistance led to less interference with heat transport along the main alignment direction.

In the cross-direction, annealing had opposing effects on the two aligned nonwovens: it increased the thermal diffusivity of the oriented sample but decreased that of the SJES sample. These seemingly contradictory observations were explained by the distinct roles of fiber fusion and annealing-induced waviness. In the oriented samples, the initial fiber alignment was moderate, so the waviness introduced during annealing had little impact on the contact area. At the same time, fiber fusion effectively reduced interfacial resistance, which enhanced thermal transport in the cross-direction—a conclusion supported by the observed increase in diffusivity with longer annealing times. In contrast, the highly aligned SJES samples were more sensitive to the induced waviness, as their initially large contact area in the cross-direction was strongly

reduced. Here, fiber fusion appeared to play only a subordinate role. These results demonstrate that reducing inter-fiber contact resistance improves thermal transport, but they also reaffirm that the extent of contact area is the decisive parameter.

Motivated by these findings, we further expanded our set of nonwovens to investigate how compositional modifications affect thermal transport in fibrous systems. Sophie E. Fritze functionalized random and oriented nonwovens by incorporating silver nanowires into the PS fibers or by coating the fibers with a thin copper layer. The silver nanowires aligned along the fiber direction but remained isolated, without forming a percolating network. In contrast, the copper coating enwrapped the individual fibers and their contact points, forming a continuous conductive network in both nonwoven types (Figure 4.5 b). However, despite identical treatment, the copper layer formed uniformly in the random nonwoven, while in the oriented nonwoven, it became increasingly sparse toward the center, leaving roughly one-third of its interior uncoated (Figure 4.5 a). We attributed this difference to the fiber arrangement: the isotropic interconnected cavities in the random sample allowed the functionalization solution to infiltrate efficiently, whereas in the oriented sample fiber bundles led to aligned cavities, fewer in number, hindering uniform copper deposition.

I analyzed these samples using LIT to investigate how the different functionalization strategies affect the thermal transport within the fibrous structures (Figure 4.5 c). Incorporating silver nanowires into the PS fibers yielded only a modest enhancement of thermal diffusivity. Despite their excellent intrinsic thermal conductivity, the random sample showed a 1.9-fold increase, while the oriented sample saw a 1.6-fold increase along the preferred direction and a more substantial 3.8-fold increase in the cross-direction. The stronger enhancement in the cross-direction was attributed to a notable decrease in fiber alignment upon functionalization (from an S_{2D} of 0.86 to 0.58), as misaligned fibers facilitate heat flow perpendicular to the primary orientation. These findings showed that phonon scattering at the fiber interfaces significantly constrains the performance of highly conductive fillers. Therefore, strategies aiming to fully exploit such fillers in composite systems must prioritize the reduction of interfacial scattering losses.

In the copper-coated nonwovens, the formation of a percolating metal network allowed not only contributions from both PS and copper to thermal transport, but also enabled measurable electrical transport. Using a four-point probe setup we approximated the electrical conductivities, accounting for the observed differences in copper coating. The resulting electrical conductivities were 2405 $\mathrm{S\,cm^{-1}}$ for the random nonwoven, 2168 $\mathrm{S\,cm^{-1}}$ and 2436 $\mathrm{S\,cm^{-1}}$ for the oriented nonwoven in the cross- and preferred direction, respectively. As expected, the value for the random sample lay between those of the oriented one. Surprisingly, however, the oriented nonwoven displayed a low degree of electrical anisotropy. The limited, elongated cavities apparently do not significantly hinder electron transport across the inter-fiber contacts; an effect comparable to what was observed in the cold-pressed SJES nonwovens, where high inter-fiber contact supported cross-directional transport.

The measured thermal diffusivity values of the copper-coated nonwovens were significantly higher than those of the pure PS nonwovens. This strong increase was attributed to the higher volume fraction of metal, compared to the silver nanowire samples, and the formation of a percolating network. We therefore concluded that most of the heat is conducted through the copper. Interestingly, however, the LIT measurements revealed that thermal transport behaves differently than electrical transport. While the electrical anisotropy of the copper coated oriented

nonwoven was nearly isotropic (1.1), its structural anisotropy was clearly reflected in a thermal anisotropy (2.8). Nevertheless, the thermal anisotropy for the copper coated nonwoven was significantly smaller than for the uncoated nonwoven (2.8 vs. 8.6), despite comparable S_{2D} parameters (0.86 and 0.77). This demonstrated that the cross-direction electric transport mitigated the thermal anisotropy. Although both thermal and electron transport are dictated by the copper-coated fibers, the results reveal that the degree of anisotropy depends on the type of transport.

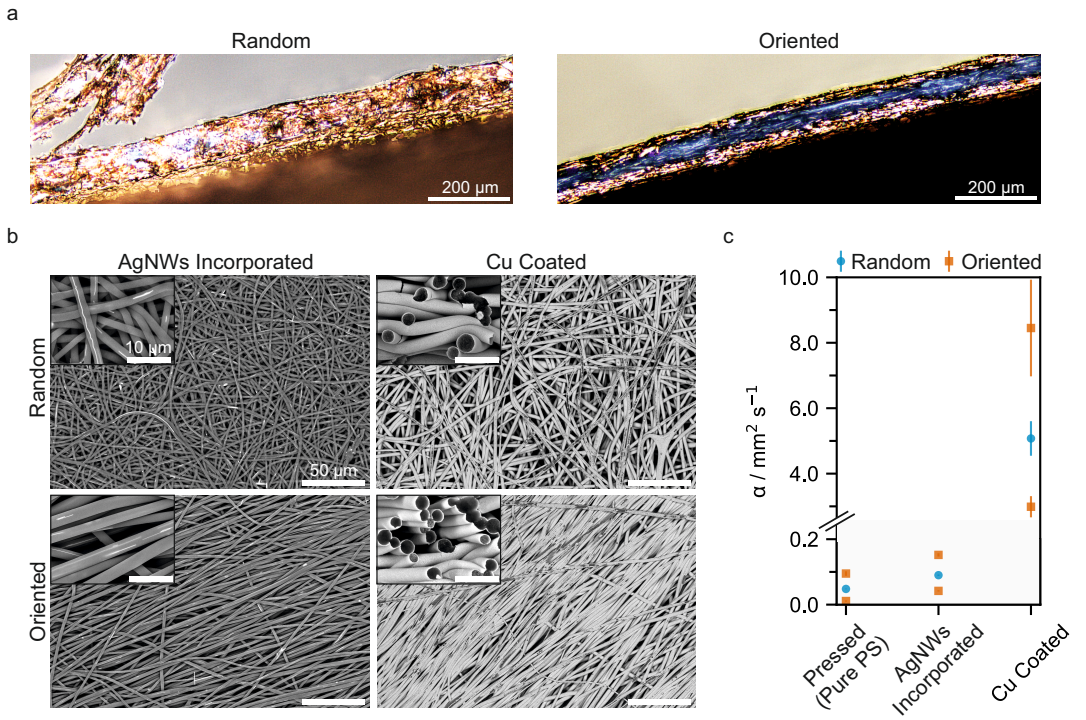

Figure 4.5: Electrospun nonwovens after incorporation of AgNW or coating with copper. a) LSCM cross-section images of the random copper coated nonwoven, showing that the copper coating is present throughout the nonwoven, and the oriented copper coated nonwoven, showing that the copper content is reduced towards the center of the sample (Scale bars are $200\,\mu m$). b) BSE-SEM images highlighting the features of the functionalization (Scale bars are $50\,\mu m$ and $10\,\mu m$). c) Thermal diffusivity values obtained from measurements at a minimum of ten positions per sample. Adapted from[6]. Figures were merged.

Taken together, this project provided valuable insight into how structure and composition affect thermal transport in fibrous systems, offering a systematic foundation for designing their properties in future applications. In the next contribution (Chapter 9) the focus shifts from fiber-based architectures to a nucleated semicrystalline polymer, relevant to industrial applications. Here, we explore the potential for anisotropic thermal transport to arise not from fiber alignment but from crystallite orientation.

BTA derivatives are widely used as nucleating agents for polypropylene, as they significantly enhance optical properties such as transparency and clarity, even at very low weight fractions.[7,8] Similar to Chapter 7, where thermal transport in self-assembled BTA fibers was investigated, the key lies in their self-assembly. During cooling of the polymer melt, the BTAs form fibrillar structures that act as efficient nucleation sites for polymer crystallization (Figure 4.6 a).[9–11] We hypothesized that alignment of these BTA fibrils could direct the orientation of the polymer crystallites, potentially inducing anisotropic thermal transport. Motivated by the widespread use of polypropylene and its copolymers in fields where thermal properties are relevant (e.g.,

electronic housings, automotive components, food packaging), and the likelihood of BTA fibril alignment during common processing, we investigated the link between structural and thermal behavior in these systems.

Cylindrical injection-molded specimens of polypropylene with a small ethylene content (racoPP) were prepared, each containing either $0.5\,\mathrm{wt\%}$, $0.1\,\mathrm{wt\%}$ or $0.05\,\mathrm{wt\%}$ iPe-BTA, a known and efficient nucleating agent.[7,8] For comparison, a corresponding concentration series was produced using nBu-BTA, a structurally similar compound with a low nucleation capability (Figure 4.6 b).[10] A neat racoPP sample without additives served as reference. Since structural characterizations revealed only minor differences across the full concentration range, we focused on the highest BTA concentrations for structural comparison.

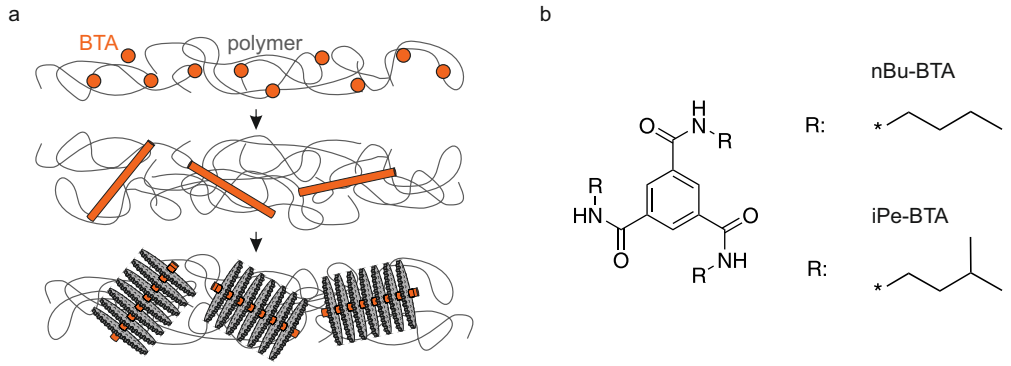

Figure 4.6: a) Nucleation mechanism of BTA additives. Upon cooling the BTA molecules self-assemble into nanofibrils that act as nucleation sites for polypropylene crystallization. b) Molecular structure of the utilized BTA derivatives. Adapted from[12]. A selected portion is shown.

XRD measurements characterized the resulting structures. Both additive types showed reflections below 10°, confirming BTA self-assembly rather than molecular dispersion in the polymer matrix. The calculated crystallinity values differed only slightly but followed the expected trend: racoPP containing iPe-BTA showed the highest relative crystallinity, followed by racoPP with nBu-BTA, and neat racoPP. The superior performance of iPe-BTA was attributed to its better lattice match with racoPP, which is a key requirement for effective nucleation.[10,13]

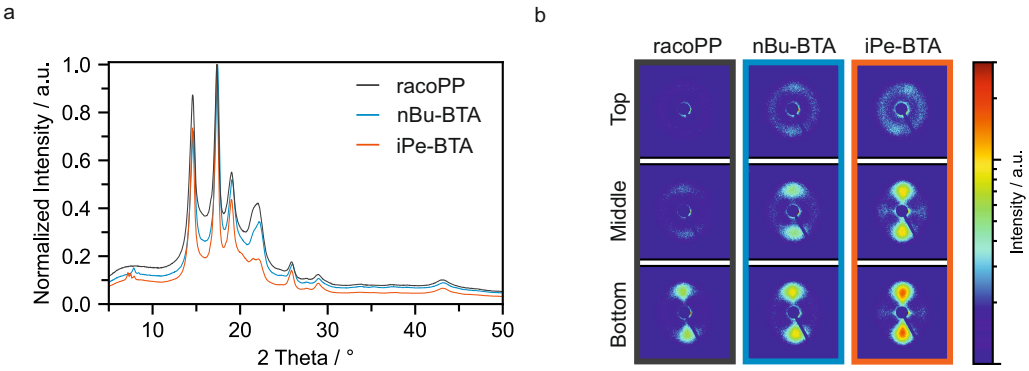

Figure 4.7: Structural characterization of injection-molded neat racoPP (grey), racoPP with $0.5\,\mathrm{wt\%}$ nBu-BTA (blue) and with $0.5\,\mathrm{wt\%}$ iPe-BTA (orange). a) XRD patterns. Intensities are normalized to the highest peak. b) 2D SAXS patterns recorded at different sample positions. Adapted from[12]. A selected portion is shown. Colors were modified.

SAXS measurements complemented the structural analysis by providing insights into the orientation of the lamellar polypropylene structures across three sample positions (top, middle,

and bottom), which experienced varying shear rates during injection molding. The bottom position was closest to the mold inlet, while the top was furthest away. Broad meridional maxima in the SAXS patterns consistently indicated that the polypropylene lamellae were oriented perpendicular to the flow direction in all samples. (Figure 4.7 b). During injection molding of the BTA-containing samples, the BTA molecules self-assembled into columnar structures, aligning with the flow direction and subsequently nucleating epitaxial crystallization of racoPP.[9–11] As the shear forces were highest near the inlet, they induced the strongest orientation of the BTA assemblies at the bottom of the sample. Consequently, the lamellae orientation was most pronounced at the bottom and gradually decreased towards the top. The crystallite orientation in neat racoPP was attributed to shear alignment of chain segments in the melt. These segments formed small oriented clusters that served as primary nuclei for secondary crystallization into perpendicularly oriented lamellae.[14] Nevertheless, BTA additives enhanced lamellar PP structure orientation, and based on its superior nucleation capability, iPe-BTA produced the most pronounced reflexes at the bottom and middle positions of the sample.

Building on the structural characterization, we investigated whether these features influence through-plane thermal transport using LFA on cylindrical specimens from the top and bottom of each injection-molded sample. No correlation between thermal diffusivity and sample position was found, which we attributed to the SAXS-observed anisotropy being an in-plane property while LFA probes through-plane transport. Likewise, no clear trend in thermal diffusivity was observed with varying BTA concentration, aligning with the crystallographic results. Even between neat racoPP, racoPP with $0.5\,\mathrm{wt\%}$ nBu-BTA, and racoPP with $0.5\,\mathrm{wt\%}$ iPe-BTA, the measured values differed only slightly, despite differences in crystallinity. We ascribed this to the dominant role of the amorphous phase in limiting phonon propagation, which suppressed potential enhancement from increased crystallinity. This observation echoes findings from the study on nonwovens (Chapter 8), where the inter-fiber contact area was decisive for thermal transport. Both results highlight how small amounts of thermally hindering components can strongly suppress overall transport. Accordingly, the through-plane thermal diffusivity in the injection-molded racoPP samples was unaffected by sample position, BTA concentration, or BTA type.

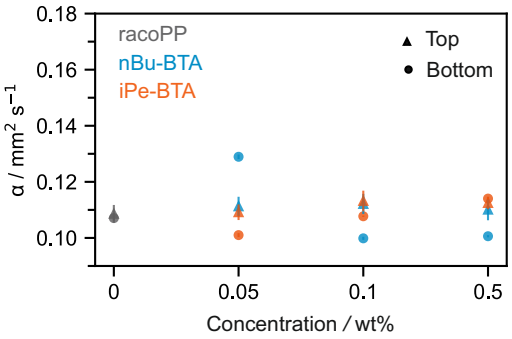

Figure 4.8: Thermal diffusivity α of an injection-molded neat racoPP specimen and racoPP specimens with varying content of nBu-BTA and iPe-BTA, obtained by LFA. Measurements were performed on cylinders measuring $1\,\mathrm{cm}$ in diameter cut from the top and bottom half of the original injection-molded samples. Adapted from[12]. Colors were modified.

In the second part of the project, we transformed the injection-molded samples into thin films via compression-molding. This allowed us to study how different flow conditions and slower cooling affect structure compared to injection-molding. Additionally, compression molding

enabled extended structural characterization by examining polymer chain orientation with polarized IR spectroscopy. Crucially, LIT measurements were possible, allowing us to link structural features with in-plane thermal diffusivity.

Comparing the XRD results, all thin films exhibited a higher crystallinity than their injection-molded counterparts, consistent with enhanced crystal growth due to slower cooling rates (Figure 4.9 a). Polarized IR spectroscopy and 2D SAXS of racoPP containing $0.5\,\mathrm{wt\%}$ iPe-BTA revealed distinct polymer chain and crystallite orientations (Figure 4.9 b and c). Neat racoPP and racoPP with $0.5\,\mathrm{wt\%}$ nBu-BTA showed isotropic polymer chain and crystallite orientations, indicating that compression-molding eliminated any structural anisotropy. We attributed this to the slow cooling rate and nBu-BTA's low nucleation capability, allowing competitive intrinsic self-nucleation of racoPP. In contrast, racoPP with $0.5\,\mathrm{wt\%}$ iPe-BTA exhibited a coplanar crystallite orientation aligned with the sample edge (Figure 4.9 b, c). We ascribed this to outward melt flow during processing, which oriented the BTA fibrils accordingly. Epitaxial growth of racoPP from these nucleation sites resulted in the observable lamellae alignment.[9–11]

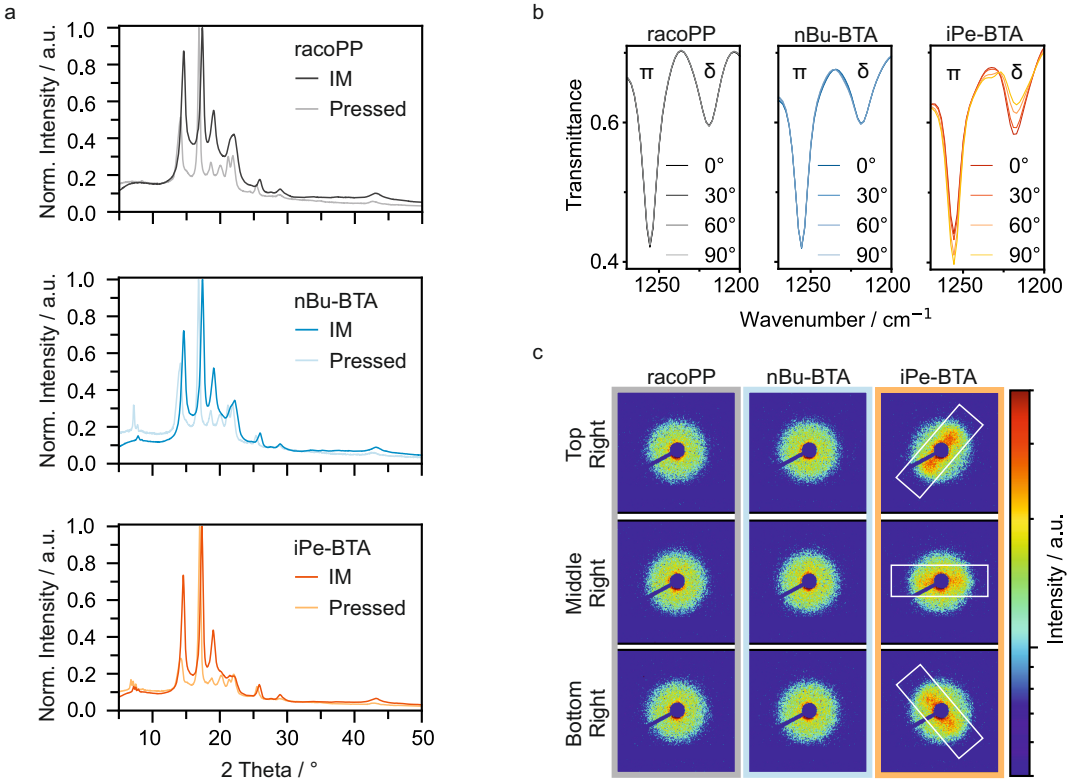

Figure 4.9: Structural characterization of neat racoPP (grey), racoPP with $0.5\,\mathrm{wt\%}$ nBu-BTA (blue) and with $0.5\,\mathrm{wt\%}$ iPe-BTA (orange). a) XRD patterns comparing the injection-molded and compression-molded samples. Intensities are normalized to the highest peaks. b) IR spectra of the compression-molded samples at the bottom-middle position using polarized incident IR radiation. c) 2D SAXS patterns of the compression-molded samples at the designated positions (white boxes indicating the orientation of intensity maxima). Adapted from[12]. Colors were modified.

To probe potential structure - property relationships, LIT measurements were performed on neat racoPP, racoPP with $0.5\,\mathrm{wt\%}$ nBu-BTA, and racoPP with $0.5\,\mathrm{wt\%}$ iPe-BTA. Interestingly, all measurements yielded isotropic amplitude and phase signals, exemplified by the bottom third of the sample with iPe-BTA (Figure 4.10 a). Consequently, the structural anisotropy observed via IR spectroscopy and SAXS in compression-molded racoPP with iPe-BTA was not

reflected in the thermal transport properties. Even when crystallites are arranged with a clear preferred orientation, amorphous regions remain present in all directions, acting as bottlenecks for phonon propagation and uniformly limiting thermal transport.

While racoPP with $0.5\,\mathrm{wt\%}$ iPe-BTA showed slightly higher absolute diffusivity values compared to neat racoPP and racoPP with nBu-BTA, these differences were too minor to be deemed significant. Moreover, for each sample type, the thermal diffusivity remained consistent across all probing positions (Figure 4.10 b). Overall, we found that thermal diffusivity was unaffected by the choice of nucleating agent or sample position in these systems.

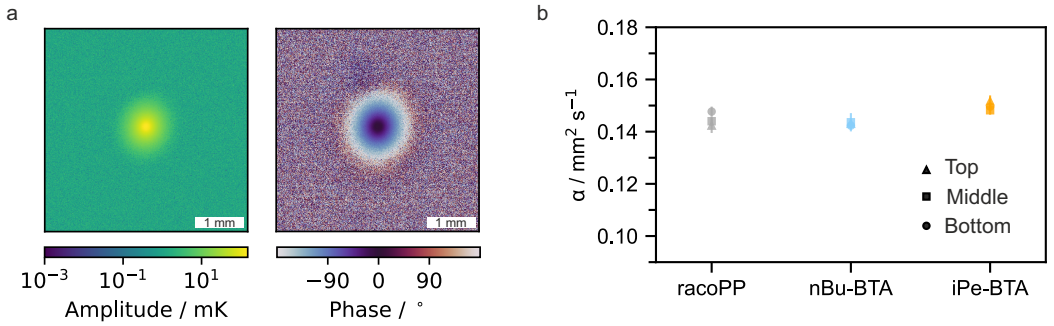

Figure 4.10: LIT of compression-molded samples with a thickness of 0.1 mm. a) Amplitude and phase signal obtained for compression-molded racoPP containing $0.5\,\mathrm{wt\%}$ iPe-BTA. b) Thermal diffusivity α of an injection-molded neat racoPP specimen and racoPP specimens with $0.5\,\mathrm{wt\%}$ nBu-BTA and $0.5\,\mathrm{wt\%}$ iPe-BTA. Five locations on each sample part (Top, Middle, Bottom) were probed. Reproduced from[12].

Comparing the two processing methods, slightly higher values were observed for the compression-molded samples. This may be due to their higher crystallinity or simply reflect inherent differences between the measurement techniques. More importantly, however, the presence of amorphous regions prevented the anisotropic crystallite orientation from manifesting as thermal anisotropy in both cases. In conclusion, this project demonstrates that thermal transport in racoPP is remarkably resilient to structural variations and remains largely unaffected by nucleating agents or processing conditions.

While this robustness benefits industrial applications that demand stable and isotropic thermal behavior, it also sparked our curiosity about whether thermal anisotropy could be intentionally induced by creating continuous crystalline pathways. Such an attribute would be valuable for applications requiring efficient, directional heat dissipation. Moreover, achieving tunable anisotropic thermal transport without the need for filler materials would represent an important step toward sustainable thermal management solutions, as pure materials offer significantly better recyclability than composites. A promising candidate for this purpose is an all-PE system developed by the FMF research center, composed exclusively of HDPE wax, HDPE and, most notably disentangled UHMWPE. The latter is known to form fiber-like, extended-chain nanocrystals (shish structures) during fused filament fabrication (FFF), an extrusion-based 3D printing technique. These shish structures then nucleate lamellar HDPE crystallization (kebab structures).[15] In Chapter 10, we therefore set out not only to conduct a detailed analysis of the relationship between structure and thermal transport in this material, but also to explore how 3D printing could be used to fabricate objects with designed, spatially controlled heat flow.

In the first step, the printed all-PE samples were structurally characterized across multiple length scales. Polarized IR spectroscopy revealed molecular-level orientation of the polyethylene chains along the print direction (Figure 4.11 a). In contrast, the benchmark HDPE reference

sample showed identical spectra for both polarizations, confirming that the observed molecular orientation in the printed all-PE material originates from the presence of disentangled UHMWPE.

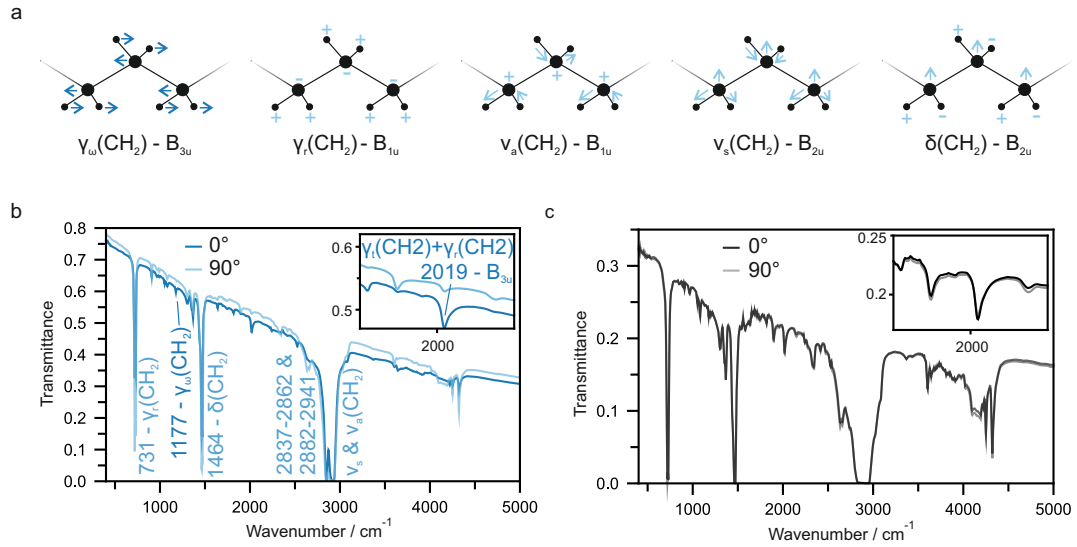

Figure 4.11: a) Fundamental vibrational modes of polyethylene chains. Parallel modes are shown in dark blue, perpendicular modes in light blue. b) Polarized IR spectra of the all-PE material using light polarized at 0° (dark blue) and 90° (light blue) relative to the 3D print direction with the assignment at $2019\,\mathrm{cm}^{-1}$. c) Corresponding spectra of benchmark HDPE. 0° polarization is shown in dark gray and 90° in light gray. Adapted from[16]. A selected portion is shown.

To gain structural insights on the Ånström and nanometer length scales, we performed X-ray scattering measurements on printed all-PE specimens, the unprinted all-PE filament, printed benchmark HDPE, and unprinted HDPE filament. These reference measurements were essential for identifying the conditions required for the formation of shish-kebab structures.

WAXS demonstrated that the benchmark HDPE exhibited isotropic short-range order in both forms, while the unit cells in the all-PE samples displayed a preferred orientation regardless of processing state. However, the intensity distributions and calculated Hermans orientation factor revealed that printing strongly increases the degree of anisotropy in the all-PE material (Table 4.2, Figure 4.12 a).

Table 4.2: Hermans orientation factors calculated from WAXS intensity distributions.

Sample	HDPE Filament	HDPE Printed	All-PE Filament	All-PE Printed
f_H	0.06	0.05	0.16	0.37

SAXS data further showed that the extrusion process used to prepare the all-PE filament induces a slight preferential alignment of the lamellar structures. Additionally, printing the benchmark HDPE also introduced a weak but detectable orientation. However, the characteristic vertical streak in the SAXS patterns, indicating the presence of chain-extended shish structures, was only observed for the printed all-PE material. The corresponding equatorial reflections were attributed to strongly oriented lamellar kebab structures that crystallized from the shish crystal surface (Figure 4.12 b and c). This confirmed that both the presence of UHMWPE and the high shear and elongational forces during 3D printing are required for shish-kebab formation.

To visualize these structures directly, we selectively etched the HDPE matrix from a printed all-PE sample. The resulting SEM images clearly revealed the presence of shish-kebab crystals, providing compelling visual evidence of their formation (Figure 4.12 d).

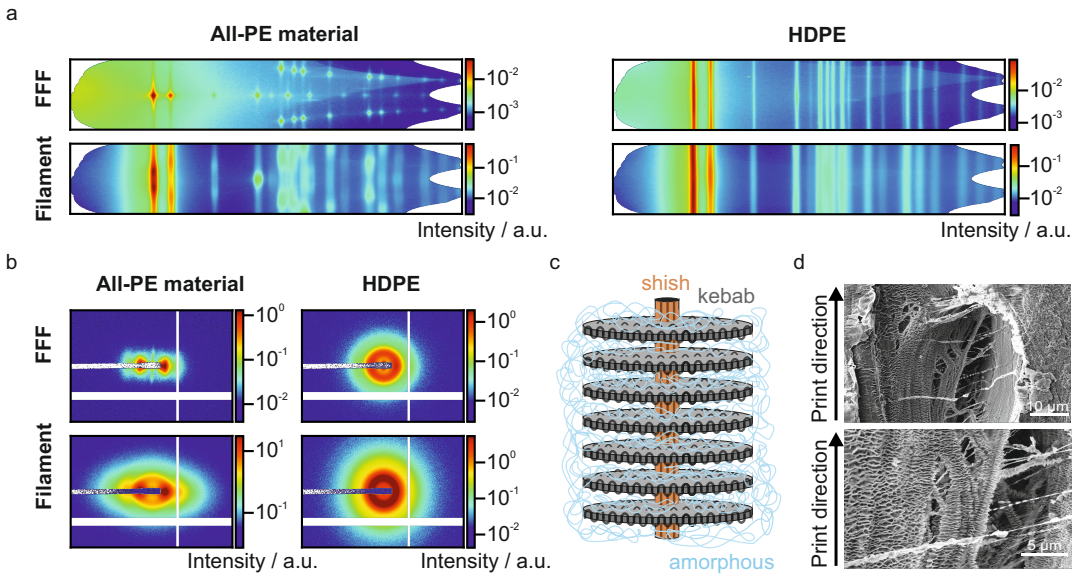

Figure 4.12: Comparison of all-PE filament and benchmark HDPE filament and therewith printed samples obtained by fused filament fabrication (FFF). a) Azimuthal representation of 2D WAXS (azimuth vs. momentum transfer q). b) 2D SAXS (q_y vs. q_x). c) Schematic illustration of a shish-kebab structure surrounded by amorphous PE. d) SEM image of an all-PE sample prepared by FFF and etched with hot xylene. Reproduced from[16].

After confirming that FFF of the all-PE material induces shish-kebab structures, we next investigated how print parameters influence thermal transport properties to identify optimal conditions for controlled directional heat conduction. LIT measurements were performed on single-layered all-PE, printed with varying speeds and temperatures, and a benchmark HDPE reference. The circular amplitude and phase signals obtained for the reference sample confirmed that the deposition of adjacent strands alone does not lead to anisotropic thermal transport. In contrast, the ellipsoidal 2D data of the all-PE samples, clearly revealed anisotropic heat transport (Figure 4.13 a).

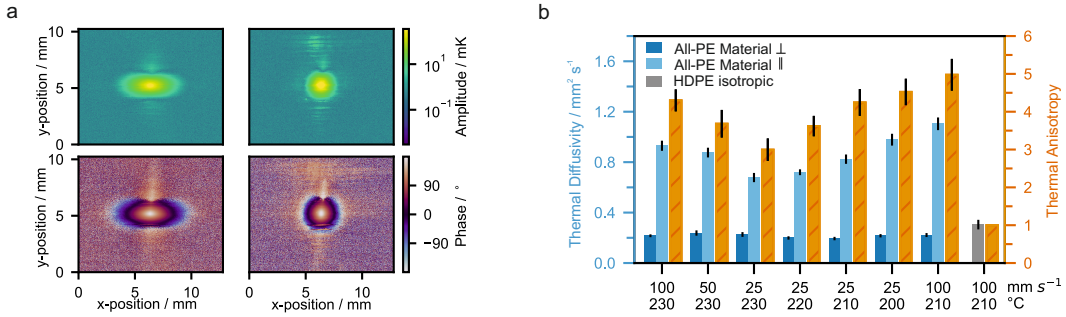

Figure 4.13: LIT for determination of the thermal diffusivity of HDPE and all-PE material processed by FFF. a) Amplitude and phase signals for all-PE and benchmark HDPE printed at 210 °C and 100 mm s^{-1}. b) Thermal diffusivity and thermal anisotropy for all-PE and benchmark HDPE printed at differing print speeds and print temperatures. Reproduced from[16].

Quantitative evaluation showed that this anisotropy increased with higher print speeds and lower print temperatures. Notably, the increase was due to enhanced diffusivity along the print direction, while the perpendicular component remained nearly unchanged (Figure 4.13 b). This confirms that the shish structures function as continuous thermally conductive pathways. The continuous shish-kebab structures offer a direct counterpoint to the nonwovens in Chapter 8 and racoPP in Chapter 9, where transport limiting gaps or amorphous areas prevented continuity and thereby severely hindered thermal transport. The pathways are similar to fibrous fillers in composites but unlike composites, the use of a single material offers two key advantages: improved interfacial linkage due to identical chemistry throughout, and the absence of a percolation threshold, as the transport pathway is governed by the printing process rather than filler volume fraction. As trends in chain orientation, crystal morphology, and overall crystallinity were excluded by SAXS, WAXS and DSC analyses, we attributed the observed parameter dependence to an increase in the macroscopic length of the shish-kebab structures with higher print speed and lower print temperature.

As outlined above, this project not only aimed to reveal and explain structure-property relationships, but also to apply these findings to achieve defined temperature distributions by tailoring the print directions of a specimen. To verify this concept and enable comparison between theory and experiment, we performed a steady-state FEM simulation on a specimen schematically shown in Figure 4.14 a. The input parameters corresponded to the measured thermal diffusivity values of a sample printed at $25\,\mathrm{mm\,s^{-1}}$ and $200\,^{\circ}\mathrm{C}$. The shape of the isotherms clearly revealed that heat preferentially propagates along the direction resembling the print direction, leading to different temperatures at equivalent distances from the heat source.

To validate this experimentally, we printed and heated a corresponding sample. Monitoring the heating process with an IR camera confirmed that the steady-state temperature distribution matches the simulation, especially near the heat source (Figure 4.14 b). The anisotropy was even more pronounced during the heating phase: the right-hand side of the sample heated up significantly slower than the left-hand side, due to the digitally defined print directions and resulting alignment of the shish structures.

Encouraged by the successful demonstration of controlled temperature distributions in quasi-2D samples, we extended our approach to 3D structures. However, printing 3D geometries with the all-PE material proved challenging due to warping and delamination at layer interfaces. Nevertheless, I was able to fabricate the specimen schematically shown in Figure 4.14 c. The asymmetric design not only improved printability but also ensured that any temperature differences could be unambiguously attributed to the print direction rather than geometry-related effects. The sample was placed on a heat plate at $75\,^{\circ}\mathrm{C}$, and its surface temperature evolution was monitored over time (Figure 4.14 d). As intended, the cuboidal section printed with a vertical orientation relative to the heat plate warmed significantly faster than the horizontally printed sections. Furthermore, under steady-state conditions ($500\,\mathrm{sec}$), this part also exhibited a higher temperature.

These results demonstrated that asymmetric temperature distributions can be digitally predefined through the choice of printing paths. With further optimization of the FFF process, 3D printing offers substantial design flexibility in defining the external geometry and in tailoring the orientation distribution of anisotropically conducting regions. In conclusion, 3D printing of all-PE material shows great potential for enabling efficient heat dissipation by a single-component material, supporting sustainable approaches for thermal management.

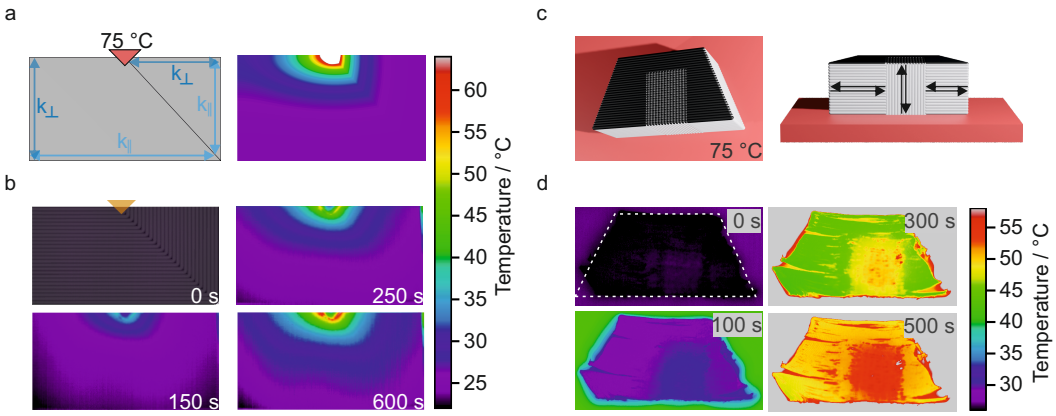

Figure 4.14: Directed heat flow in a single-layered (a, b) and a multi-layered (c, d) sample with respective heat sources at $75\,^{\circ}\mathrm{C}$. a) Geometry and steady-state FEM simulation of the designed 2D sample. Thermal conductivities were defined according to measured values of a sample printed by FFF parallel ($k_{\parallel}$) and perpendicular ($k_{\perp}$) to the print direction. b) Evolution of the surface temperature distribution on the 2D sample monitored via IR camera. The image at $0\,\mathrm{sec}$ includes a semi-transparent overlay with the print direction scheme. c) Visualization of the all-PE sample (top and side view) on a heat plate with print directions indicated by arrows. d) Evolution of the surface temperature distribution on the 3D sample monitored via IR camera. Adapted from[16]. Figures were cropped and merged.

With this I have summarized the trajectory of my work on thermal transport in 1D, 2D, and 3D hierarchical structures. The projects progressed from fundamental studies to application-oriented research, and I believe that this clarity of purpose should also guide future investigations.

The work in Chapter 7 and Chapter 8 provided foundational insights into structure–property relationships in thermal transport. Future work could extend these findings through theoretical and computational studies. For the BTA fibers, this includes identifying the key factors governing transport efficiency and clarifying the underlying mechanisms. For the nonwovens, graph-theoretical approaches and FEM simulations could build upon my findings and push toward decoupling thermal and electrical transport. Complementary experiments on additional copper-coated fiber systems with varying anisotropy could further support this aim. The resilience of thermal transport in racoPP (Chapter 9) already provides a rather complete picture with potential relevance for industrial applications. Finally, Chapter 10 lays important groundwork for implementing the recyclable all-PE material in thermal management. Future efforts should focus on optimizing 3D printing hardware and parameters specifically for this material to enhance its printability and increase the thermal anisotropy even further. Together, my thesis deepens the understanding of structure – property relationships in thermal transport across hierarchical architectures and establishes a strong foundation for both, fundamental research and practical innovations.

5 Individual Contributions to Joint Publications

This thesis consists of four scientific publications, that were prepared in collaboration with colleagues. The individual contributions of all authors are designated below.

Thermal Transport Across Supramolecular Bonds in Self-Assembled BTA Fibers

Ina Klein, Melina Weber, Hans-Werner Schmidt, Markus Retsch

This article contributes to the thesis as an unpublished manuscript.

I conceptualized the project together with Markus Retsch and was responsible for the methodology and investigation. Melina Weber performed the sample fabrication by solution crystallization. Based on preliminary IR spectroscopy results by Melina Weber, I conducted the IR spectroscopy analysis. I also prepared the individual samples for LIT, and performed the LIT measurements. I evaluated, interpreted, and visualized the resulting data, and wrote the original manuscript. The project was supervised by Hans-Werner Schmidt and Markus Retsch. Markus Retsch also reviewed and edited the manuscript.

Thermal Transport in Polystyrene Nonwovens: Influence of Anisotropy, Structural Modification, and Functionalization

Ina Klein*, Sophie E. Fritze*, Alexander Berger, Holger Schmalz, Andreas Greiner, Markus Retsch

* *These authors contributed equally to this work.*

We published this article in *ACS Applied Polymer Materials*, **2026**, *8*, 1954–1963, DOI 10.1021/acsapm.5c03952.

Sophie E. Fritze and I conceptualized the project with Andreas Greiner and Markus Retsch. Sophie E. Fritze and I were responsible for the methodology and investigation. Sophie E. Fritze fabricated the samples by electrospinning, performed the copper coating process, and characterized the samples by SEM. We both performed post-processing of the samples. I was responsible for further structural characterization and thermal property analyses of the samples, including LSCM, calculation of the S_{2D} parameters, and LIT measurements. Alexander Berger was responsible for the four-point probe measurements. Holger Schmalz performed Raman spectroscopy. Sophie E. Fritze and I evaluated, interpreted, and visualized the resulting data, and wrote the original manuscript. Andreas Greiner and Markus Retsch supervised the project and reviewed and edited the manuscript.

Do Nucleating Agents or Processing Methods Affect the Thermal Transport in RacoPP?

Ina Klein, Maria Ester Marroquin Lacayo, Thomas Blesch, Sabine Rosenfeldt, Patrick Länger, Klaus Kreger, Stefan Rettinger, Jürgen Senker, Hans-Werner Schmidt, Markus Retsch

We published this article in *Journal of Polymer Science*, **2025**, *63*, 4516-4524, DOI 10.1002/pol.20241079.

I conceptualized the project with Markus Retsch and led the methodology and investigation. Thomas Blesch fabricated the samples. Maria Ester Marroquin Lacayo and Sabine Rosenfeldt performed the SAXS measurements. Patrick Länger measured XRD and calculated the crystallinity values. Stefan Rettinger conducted the DSC measurements. Maria Ester Marroquin Lacayo and I performed polarized IR spectroscopy, LFA, and LIT measurements. We also evaluated and interpreted the resulting data together with Klaus Kreger. I visualized the data and wrote the original manuscript. The project was supervised by Jürgen Senker, Hans-Werner Schmidt and Markus Retsch. Klaus Kreger, Sabine Rosenfeldt and Markus Retsch reviewed and edited the manuscript.

High and Tuneable Anisotropic Thermal Conductivity Controls the Temperature Distribution of 3D Printed All-Polyethylene Objects

Ina Klein, Thomas Tran, Réne Reiser, Maximilian Theis, Sabine Rosenfeldt, Marius Schöttle, Carl Schirmeister, Peter Bösecke, Stefan Rettinger, Rolf Mülhaupt, Markus Retsch

We published this article in *Journal of Materials Chemistry A*, **2023**, *11*, 22492-22502, DOI 10.1039/d3ta04483a.

I conceptualized the project with Markus Retsch and led the methodology and investigation. Réne Reiser and Carl Schirmeister developed and fabricated the material for sample preparation. Maximilian Theis and I fabricated the samples. I performed the polarized IR spectroscopy analysis. Sabine Rosenfeldt, Peter Bösecke and I were responsible for the WAXS and SAXS measurements, and I calculated the Hermans orientation factors. Marius Schöttle conducted the SEM measurements and Stefan Rettinger performed the DSC measurements. Based on preliminary simulations by Maximilian Theis, I performed the FEM simulation. I evaluated, interpreted and visualized the resulting data, and wrote the original manuscript. The project was supervised by Rolf Mülhaupt, Carl Schirmeister, and Markus Retsch. Sabine Rosenfeldt, Carl Schirmeister, and Markus Retsch reviewed and edited the manuscript.

References

6

[1] C. Kulkarni, E. W. Meijer, A. R. A. Palmans, *Accounts of Chemical Research* **2017**, *50*, 1928–1936, DOI 10.1021/acs.accounts.7b00176.

[2] R. Q. Albuquerque, A. Timme, R. Kress, J. Senker, H. W. Schmidt, *Chemistry – A European Journal* **2013**, *19*, 1647–57, DOI 10.1002/chem.201202507.

[3] S. Cantekin, T. F. de Greef, A. R. Palmans, *Chemical Society Reviews* **2012**, *41*, 6125–37, DOI 10.1039/c2cs35156k.

[4] N. E. Persson, M. A. McBride, M. A. Grover, E. Reichmanis, *Chemistry of Materials* **2017**, *29*, 3–14, DOI 10.1021/acs.chemmater.6b01825.

[5] Q. Gao, B. A. F. Kopera, J. Zhu, X. Liao, C. Gao, M. Retsch, S. Agarwal, A. Greiner, *Advanced Functional Materials* **2020**, *30*, 1907555, DOI 10.1002/adfm.201907555.

[6] I. Klein, S. E. Fritze, A. Berger, H. Schmalz, M. Retsch, A. Greiner, *ACS Applied Polymer Materials* **2026**, *8*, 1954–1963, DOI 10.1021/acsapm.5c03952.

[7] M. Blomenhofer, S. Ganzleben, D. Hanft, H.-W. Schmidt, M. Kristiansen, P. Smith, K. Stoll, D. Mäder, K. Hoffmann, *Macromolecules* **2005**, *38*, 3688–3695, DOI 10.1021/ma0473317.

[8] P. M. Kristiansen, A. Gress, P. Smith, D. Hanft, H.-W. Schmidt, *Polymer* **2006**, *47*, 249–253, DOI 10.1016/j.polymer.2005.08.053.

[9] P. M. Kristiansen, Thesis, Eidgenössische Technische Hochschule (ETH), **2004**, DOI 10.13140/RG.2.1.2653.3369.

[10] J. Wang, Q. Dou, X. Chen, D. Li, *Journal of Polymer Science Part B: Polymer Physics* **2008**, *46*, 1067–1078, DOI 10.1002/polb.21440.

[11] F. Abraham, S. Ganzleben, D. Hanft, P. Smith, H.-W. Schmidt, *Macromolecular Chemistry and Physics* **2010**, *211*, 171–181, DOI 10.1002/macp.200900409.

[12] I. Klein, M. E. Marroquin Lacayo, T. Blesch, S. Rosenfeldt, P. Länger, K. Kreger, S. Rettinger, J. Senker, H.-W. Schmidt, M. Retsch, *Journal of Polymer Science* **2025**, *63*, 4516–4524, DOI 10.1002/pol.20241079.

[13] J. C. Wittmann, B. Lotz, *Progress in Polymer Science* **1990**, *15*, 909–948, DOI 10.1016/0079-6700(90)90025-V.

[14] R. H. Somani, B. S. Hsiao, A. Nogales, S. Srinivas, A. H. Tsou, I. Sics, F. J. Balta-Calleja, T. A. Ezquerra, *Macromolecules* **2000**, *33*, 9385–9394, DOI 10.1021/ma001124z.

[15] C. G. Schirmeister, T. Hees, O. Dolynchuk, E. H. Licht, T. Thurn-Albrecht, R. Muelhaupt, *ACS Applied Polymer Materials* **2021**, *3*, 1675–1686, DOI 10.1021/acsapm.1c00174.

[16] I. Klein, T. Tran, R. Reiser, M. Theis, S. Rosenfeldt, M. Schöttle, C. Schirmeister, P. Bösecke, S. Rettinger, R. Mülhaupt, M. Retsch, *Journal of Materials Chemistry A* **2023**, *11*, 22492–22502, DOI 10.1039/d3ta04483a.

Part III

Publications

7

Thermal Transport Across Supramolecular Bonds in Self-Assembled BTA Fibers

Ina Klein[1], Melina Weber[2], Hans-Werner Schmidt[2,3], Markus Retsch[1,3,4]

Manuscript.

[1] Department of Chemistry, Physical Chemistry I, University of Bayreuth, 95447 Bayreuth, Germany.
[2] Department of Chemistry, Macromolecular Chemistry II, University of Bayreuth, 95447 Bayreuth, Germany.
[3] Bavarian Polymer Institute (BPI), Bayreuth Center of Colloids and Interfaces (BZKG), University of Bayreuth, 95447 Bayreuth, Germany.
[4] Bavarian Center for Battery Technology (BayBatt), University of Bayreuth, 95447 Bayreuth, Germany.

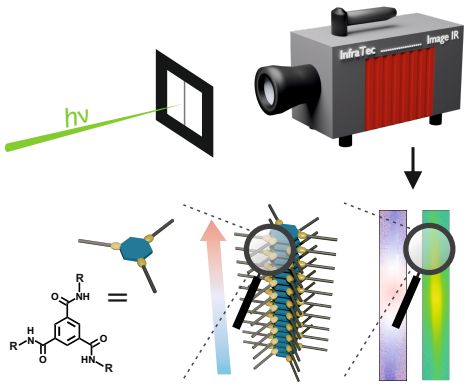

Thermal Transport Across Supramolecular Bonds in Self-Assembled BTA Fibers

Abstract

Supramolecular interactions can enhance thermal transport in otherwise poor thermal conductors by stiffening the lattice and reducing structural defects. However, the transport mechanisms across supramolecular interactions are complex, measurement options are limited, and suitable model systems are scarce. Benzene-1,3,5-tricarboxamides (BTAs) are an exceptionally versatile material class that self-assemble into large, crystalline fiber structures. This makes them an ideal platform for systematically studying thermal transport mediated by supramolecular interactions and identifying underlying trends and correlations. Here, we report thermal diffusivity values for supramolecular fibers formed by nine different BTA derivatives. Using lock-in thermography, we measure thermal transport along the fiber axis, a direction governed exclusively by non-covalent interactions – specifically π-π stacking and hydrogen bonding. Systematic variation of side group chemistry and amide bond orientation reveals correlations between IR spectroscopic features of hydrogen bonding strength and thermal transport efficiency. Our results lay the groundwork for a more fundamental understanding of how supramolecular interactions govern thermal transport in BTAs.

Introduction

Phonons represent the dominant heat carrier type in dielectric crystals, and their frequencies and scattering events dictate thermal transport. The correlation between phonon group velocity and the force constants between adjacent crystal lattice planes highlights the crucial role of atomic interactions in defining thermal transport properties.[1] Consequently, highly crystalline materials with strong covalent bonds, such as diamond, exhibit high thermal conductivity. In contrast, polymers, even those with high crystallinity, typically demonstrate low thermal transport efficiencies, due to amorphous regions limiting phonon propagation, and phonon scattering promoted by grain boundaries, defects or torsion of the polymer chains.[2–4]

Supramolecular interactions can be used to improve thermal transport in materials with low intrinsic conductivity.[2,5–9] These non-covalent interactions can contribute to lattice stiffening, serve as additional pathways for phonon transport or improve lattice ordering, which reduces phonon scattering.[2,9] Molecular dynamics simulations on covalent organic frameworks, for instance, illustrate the significant impact of intermolecular interactions. The thermal conductivity of three interpenetrating frameworks, forming supramolecular bonds, was found to be substantially higher than that of an identical structure lacking these non-covalent bonds, and six times greater than for an individual framework. The supramolecular interactions within the interpenetrating structures, including Van der Waals forces, hydrogen bonding, electrostatic and host-guest interactions, led to phonon hardening and reduced vibrational scattering.[10] Another theoretical study on helical protein structures revealed a strong correlation between thermal transport and hydrogen bond strength. The isomer with the strongest hydrogen bonds exhibited higher phonon group velocities, a pronounced blueshift in key vibrational frequencies, reduced scattering, and thus the highest thermal conductivity.[11]

Experimental measurements on self-assembled supramolecular polymer fibers of melamine and hydroxybenzoic acid isomers further confirmed the key role of hydrogen bonding strength for thermal transport. Unlike the previously discussed systems, here, covalent bonds are not present throughout the entire structure; instead, heat must be transferred across intermolecular interactions. In this system, stronger hydrogen bonding in combination with higher π-stacking efficiency reduced defects, stabilized thermal transport pathways, suppressed phonon scattering, and ultimately enhanced the thermal conductivity.[12]

Although hydrogen bonding is the strongest among supramolecular interactions, the role of π-π stacking should not be underestimated. In a highly ordered π-stacked assembly of a triphenylene derivative without any hydrogen bonding, a thermal diffusivity of approximately $0.21\,\mathrm{mm^2\,s^{-1}}$ was measured along the π-stacking direction.[13] This value surpasses that of many covalently bound polymers.[14] In these stacks, thermal transport across the individual molecules at room temperature is dominated by acoustic phonons and contributions from intramolecular vibrations, through coupling with acoustic phonons, become relevant only below the Debye temperature.[13] Similar insights emerged from a study on an organic material undergoing single-crystal-to-single-crystal topochemical polymerization, which allowed for a direct comparison of thermal transport mediated by Van der Waals interactions versus covalent bonds. At room temperature, the thermal conductivity was only 1.4 times higher in the polymerized structure compared to the depolymerized one, where only supramolecular interactions contributed to heat transport. The deviation became pronounced only at low temperatures, as the formation of covalent bonds increases the Debye temperature, below which the phonon mean free path and scattering time increase exponentially.[15]

These examples underscore the importance and complexity of intermolecular thermal transport, as well as the significant challenges in analyzing individual contributions and fully understanding the interplay of various non-covalent interactions. Despite the growing recognition of supramolecular assemblies in various fields, only a limited number of studies have systematically examined thermal transport across supramolecular bonds. Even fewer reports present systems that allow for the experimental evaluation of heat propagation mediated solely by non-covalent interactions. Addressing this knowledge gap requires a systematic approach combined with a suitable and variable material platform.

Benzene-1,3,5-tricarboxamides (BTAs) are well known self-assembling nucleators for polypropylene and are widely used in industrial applications as clarifying agents.[16] Threefold intermolecular hydrogen bonding between the amide groups of neighboring BTA molecules leads to the formation of self-assembled structures, typically π-π stacked columns with a helical arrangement.[17,18] Depending on the side groups and crystallization conditions these columns assemble hexagonally into fibrils, which further aggregate into macroscopic fibers (Figure 7.1 a).[17–19] Fortunately, supramolecular BTA structures can reach lengths of several millimeters. This enables thermal transport measurements along the fiber axis using lock-in thermography (LIT), a technique that allows us to determine thermal diffusivity in the direction where the structure is held together exclusively by supramolecular interactions. Moreover, the wide variety of BTAs, with differing side groups and symmetries, makes them an excellent material platform for systematically studying thermal transport mediated by supramolecular interactions and for identifying underlying trends and correlations.

In this work, we report the thermal diffusivity of nine selected BTA fibers and identify initial correlations between thermal transport and hydrogen bonding strength, supported by IR

spectroscopy. This lays the groundwork for future investigations into structure–property relationships in BTAs, which will require detailed crystallographic analysis and theoretical modeling. As part of a long-term effort to systematically study BTA derivatives and gain a well-founded, deep understanding of thermal transport via supramolecular interactions, this work represents a first, but substantial, step on the thermal analysis side.

Results and Discussion

To enable reliable thermal measurements of supramolecular BTA structures, several key requirements must be met. First, the fibers must be thermally large to minimize boundary effects, meaning their length should significantly exceed the thermal penetration depth. For the BTA samples studied, this depth was calculated to be approximately $300\,\mathrm{nm}$-$370\,\mathrm{nm}$. Second, the fibers must be thermally thin, with a diameter significantly smaller than the thermal penetration depth. Additionally, the fiber surface should be as smooth as possible, which requires well-assembled fibrils forming compact fiber structures without protruding smaller fibrils or fibril aggregates.

To obtain fibers meeting these criteria, a broad set of BTAs with various side groups was dissolved in DMF or DMSO, and the solvent was slowly evaporated over at least one week to promote self-assembly. From this large set, supramolecular fibers with the desired properties were successfully formed by nine BTA derivatives, which could then be individually transferred onto the LIT sample holders (Figure 7.1 b). This success provides a solid basis for comparative analysis and for identifying potential trends. Among the nine BTAs, five differ only in their side group chemistry, including two that incorporate heteroatoms (*Hex-C3, iOc-C3, brOC-C3; Am-C3, Su-C3*). Additionally, the set includes BTAs sharing the same side group chemistry but differing in amide bond orientation (*tBu-N3, tBu-C1N2, tBu-C2N1; Hex-C2N1, Hex-C3*). They can either be C-centered with the amide carbon bonded to the benzene ring, or N-centered with the amide nitrogen bonded to the benzene ring. This enables an additional comparison beyond variation in side group chemistry.

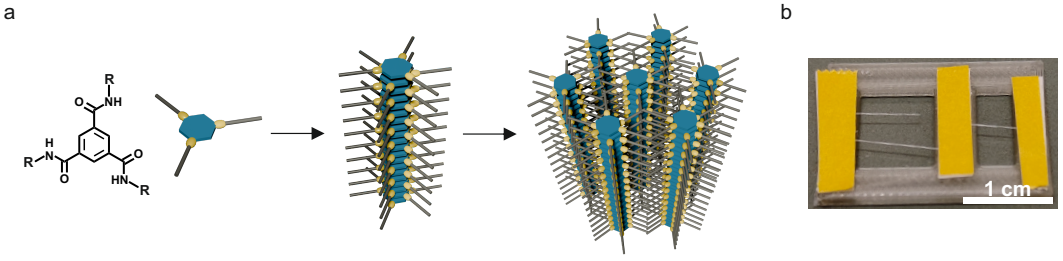

Figure 7.1: Self-assembled benzene-1,3,5-tricarboxamide (BTA) structure a) Schematic illustration of the hierarchical BTA fibrils b) Optical image of macroscopic self-assembled BTA fibers on a lock-in thermography sample holder.

Based on preliminary experiments, a measurement frequency of $0.27\,\mathrm{Hz}$ was selected. However, choosing the laser power proved challenging. Since the fibers form by self-assembly, significant variations in thickness were observed, especially between different BTA derivatives, but also among individual fibers of the same BTA. Using a fixed laser power compromises data quality: thicker fibers yield a poor signal-to-noise ratio, while thinner ones may heat up, leading to inaccurate thermal diffusivity values (Figure S1).[20] To address this, the laser power for each measured fiber position was optimized individually by comparing the peak values of

the amplitude data across 13 measurements with powers ranging from $18\,\mu\mathrm{W}$ to $72\,\mu\mathrm{W}$, and selecting the power that brought this value closest to $175\,\mathrm{mK}$.

The measured thermal diffusivity values are displayed in Figure 7.2. We want to highlight that these values reflect heat transport purely through supramolecular interactions. LIT allows us to probe one-dimensional transport along the fiber axis — a direction without covalent bonds. This approach enables the study of thermal transport without contributions from covalent bonding, which is rarely achievable and offers an exciting opportunity to explore heat conduction governed solely by non-covalent interactions.

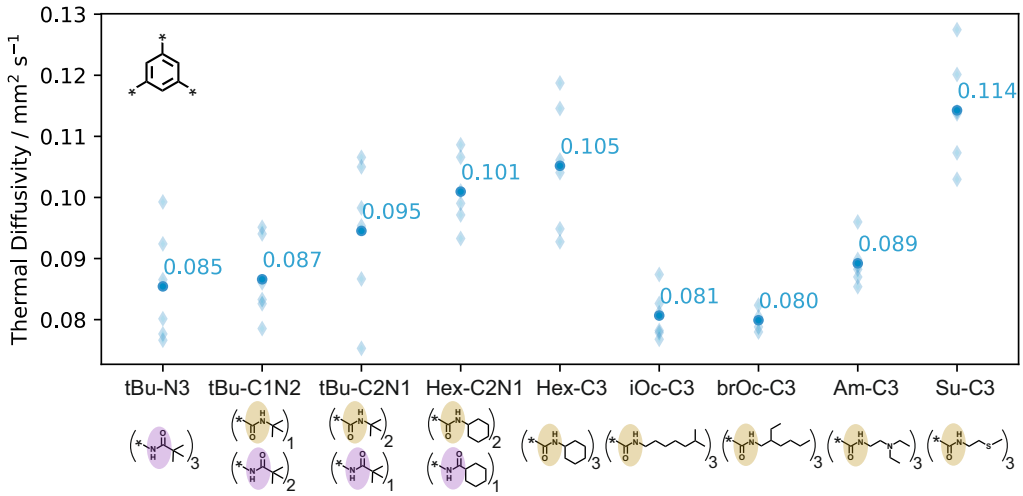

Figure 7.2: Thermal diffusivity values of fibers formed from different BTA derivatives, measured using lock-in thermography at a frequency of $0.27\,\mathrm{Hz}$. For each BTA derivative, three measurements were performed, each providing two data points by evaluating both sides of the laser spot (diamonds). Sample-specific laser powers were used to account for differences in fiber thickness. Average diffusivity values are indicated by circles and annotated with corresponding numerical values. The molecular structures of the side groups for each derivative are shown along the x-axis.

The obtained diffusivity values are comparable to those of polymers, which are typically considered poor thermal conductors. At first glance, this may seem unexpectedly low, given the high crystallinity of the BTA fibers.[21,22] However, unlike polymers, where heat is primarily conducted through strong covalent bonds, these fibers rely solely on supramolecular interactions for phonon transport. These vibrations are said to be more anharmonic than those of covalent bonds, which increases phonon scattering.[5] Compared to previous studies on other supramolecular solids, the obtained thermal diffusivity values fall within a similar range.[13,15] We presume that the heat transfer in BTAs occurs via a combination of van der Waals forces, π–π stacking, and hydrogen bonding. Although these interactions are interdependent, hydrogen bonding, being the strongest, is likely to have the most pronounced and identifiable influence.

A comparison of the thermal diffusivity for BTA derivatives differing only in amide bond orientation, shows that increasing the ratio of N-centered side groups leads to a reduction in thermal diffusivity. Although the absolute differences are small, this consistent trend is observed for both side groups, *tBu* and *Hex*. Examination of the fully C-centered derivatives indicates that long aliphatic side groups lead to lower thermal diffusivity values. In contrast, the rather bulky *Hex*-group does not negatively affect the thermal transport. The only derivative exhibiting even higher thermal diffusivity than *Hex-C3* is the short-chained linear *Su-C3*, which contains a sulfur heteroatom.

Since IR vibrational modes associated with hydrogen bonding typically shift to lower wavenumbers as bonding strength increases, these spectral features can offer insight into the strength of one of the key supramolecular interactions presumed to influence thermal transport in these systems.[18,21] Figure 7.3 provides the IR spectra of BTA fibers, comparing variations in amide bond orientation and side group chemistry.

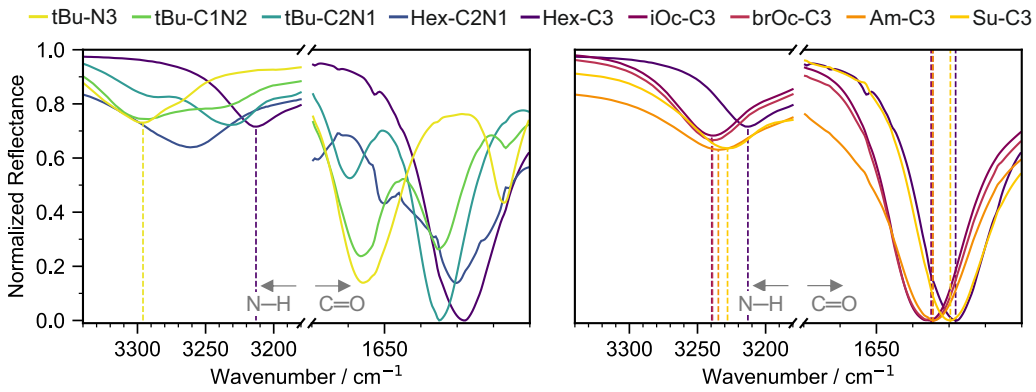

Figure 7.3: Normalized FT-IR spectra of various bulk BTA derivatives. The left panel compares the influence of amide bond orientation, while the right panel shows the effect of side group chemistry. Dashed lines indicate the N–H stretch bands and in the right panel additionally the C=O stretch bands.

First, we compare the effect of C- versus N-centering. Purely C-centered and purely N-centered derivatives exhibit a single band for the N–H and C=O stretching modes, whereas derivatives with mixed centering show a clear splitting of these bands. The intensity distributions within the split bands indicate that the higher-wavenumber components correspond to the N-centered groups, and the lower-wavenumber component to the C-centered ones. This assignment is supported by the N–H and C=O band positions of the purely N-centered *tBu-N3* and the purely C-centered *Hex-C3*. An exception to the splitting is observed in the N–H stretching mode of *Hex-C2N1*: despite its mixed centering, it shows a single band. However, this band is significantly shifted to a higher wavenumber compared to its counterpart *Hex-C3*.

These results indicate stronger hydrogen bonding with an increasing ratio of C-centered side groups. It is consistent with previous reports demonstrating that N-centering leads to planarization of the carbonyl moieties, slightly reduces the distance between the aromatic cores, and weakens the intermolecular hydrogen bonding.[17,19,23] Since the thermal diffusivity also increases with the fraction of C-centered side groups, a correlation between hydrogen bonding strength and thermal transport can be assumed.

The side group chemistry appears to have a strong influence on thermal diffusivity and the correlation with hydrogen bonding strength, as derived from IR spectra, is mostly consistent. *Hex-C3* clearly exhibits the lowest wavenumber for the N–H and the C=O stretch band and a significantly higher thermal diffusivity than *iOc-C3, brOc-C3* and *Am-C3*. Although the differences in N–H stretch wavenumbers among *iOc-C3, brOc-C3* and *Am-C3* are small, they also align well with the trend in thermal diffusivity. Long aliphatic chains are not known to affect the intermolecular distance in the BTA columns.[19] Still, compared to the other fully C-centered derivatives the N–H stretching modes of *iOc-C3* and *brOc-C3* indicate attenuated hydrogen bonding, in line with their low thermal diffusivity values.

We note that the N–H stretch band of *tBu-N3* suggests even weaker hydrogen bonding. This implies that the thermal diffusivity of BTA derivatives with long aliphatic chains is limited by additional factors. Their substantial size may impair the self-assembly process, potentially leading to more structural imperfections. Moreover, the significant volume occupied by these chains might result in fewer fibrils forming the fiber, rendering thermal transport more susceptible to crystal defects.

Comparing these C-centered derivatives with *Su-C3*, it appears that the sulfur heteroatom leads to divergent characteristics. Although the IR data indicates stronger hydrogen bonding for *Hex-C3*, *Su-C3* shows the highest thermal diffusivity. This discrepancy suggests that factors beyond hydrogen bonding strength influence its thermal transport. One possible explanation is that the sulfur heteroatom in *Su-C3* modifies the dipole moment, thereby enhancing the self-assembly process and reducing the defect density within the fiber.

In summary, the observed trends suggest that both the amide bond orientation and the chemical structure of the side groups influence hydrogen bonding strength in the supramolecular BTA fibers. Stronger hydrogen bonding appears to enhance thermal diffusivity, indicating a key role for hydrogen bonds in phonon propagation across the BTA molecules. This aligns with the concept that stronger intermolecular interactions stiffen the lattice, enabling higher-frequency phonon transport and reducing phonon scattering.[2,10]

However, the differences in IR band positions and the mean thermal diffusivity values are relatively small, and some BTA derivatives exhibit a broad distribution of individual measurement results. While many cases demonstrate the correlation between thermal diffusivity and IR band shifts, exceptions suggest that factors beyond hydrogen bonding strength also influence the thermal transport. Specifically, the density and susceptibility to structural defects could play an important role.

We should at least consider that the observed correlation between hydrogen bond strength and thermal diffusivity may not be a causal, but a common-cause relationship. Hydrogen bond strength is known to critically influence the BTA self-assembly process.[17] Therefore, it is plausible that the enhanced thermal diffusivity observed in systems with stronger hydrogen bonding is, at least in part, an indirect consequence of reduced structural defects, rather than solely due to enhanced phonon transport across stronger bonds. Ultimately, it is possible that both factors — direct lattice stiffening from stronger bonds and an indirect reduction in structural defects — collectively contribute to the observed structure–thermal property relationship.

Conclusion

In this study, we demonstrated that BTAs offer a versatile platform to systematically analyze thermal transport across supramolecular bonds using LIT. An initial assessment of hydrogen bonding strengths by IR spectroscopy indicated that these interactions play an important, though not exclusive, role governing heat propagation in BTA fibers. Ongoing work, combining theoretical calculations with detailed crystallographic analysis, aims to further elucidate how supramolecular structure influences heat transport, and to identify the dominant interactions involved. Crucially, we have successfully measured and quantified thermal transport across molecular BTA assemblies, providing a valuable contribution to understanding heat conduction mediated by supramolecular interactions.

Author Contributions

IK: conceptualization, investigation, methodology, formal analysis, writing - original draft, visualization; MW: investigation, methodology; HWS: conceptualization, resources, funding, supervision; MR: conceptualization, resources, funding, writing - review/editing, supervision.

Conflicts of Interest

There are no conflicts to declare.

Acknowledgements

We thankfully acknowledge the support by the Collaborative Research Centre 1585, Project C05 of the German Research Foundation (Grant number 492723217). We also acknowledge support by the Keylabs “Mesoscale Characterization” and “Small Scale Polymer Processing” of the Bavarian Polymer Institute (BPI). We made use of AI-assisted tools to help improve the clarity and language of the manuscript. We take full responsibility for all scientific content and interpretations presented in this work. Additionally, we thank Viktoria Veitengruber and Stefan Rettinger for the design of the schematic BTA structures.

References

[1] C. Kittel, *Introduction to Solid State Physics*, 8., John Wiley & Sons, New York, NY, **2005**.

[2] L. Zhang, M. Ruesch, X. Zhang, Z. Bai, L. Liu, *RSC Advances* **2015**, *5*, 87981–87986, DOI 10.1039/c5ra18519j.

[3] I. Klein, M. E. Marroquin Lacayo, T. Blesch, S. Rosenfeldt, P. Länger, K. Kreger, S. Rettinger, J. Senker, H.-W. Schmidt, M. Retsch, *Journal of Polymer Science* **2025**, *63*, 4516–4524, DOI 10.1002/pol.20241079.

[4] H. Chen, V. V. Ginzburg, J. Yang, Y. Yang, W. Liu, Y. Huang, L. Du, B. Chen, *Progress in Polymer Science* **2016**, *59*, 41–85, DOI 10.1016/j.progpolymsci.2016.03.001.

[5] W. Chen, K. Wu, Z. Qu, M. Lu, *European Polymer Journal* **2019**, *121*, 109275, DOI 10.1016/j.eurpolymj.2019.109275.

[6] C. J. Dionne, M. A. Rahman, P. E. Hopkins, A. Giri, *Nano Letters* **2022**, *22*, 3071–3076, DOI 10.1021/acs.nanolett.2c00420.

[7] G.-H. Kim, D. Lee, A. Shanker, L. Shao, M. S. Kwon, D. Gidley, J. Kim, K. P. Pipe, *Nature Materials* **2015**, *14*, 295–300, DOI 10.1038/nmat4141.

[8] J. Zhou, S. Lin, H. Zeng, J. Liu, B. Li, Y. Xu, X. Zhao, G. Chen, *Materials Horizons* **2020**, *7*, 2936–2943, DOI 10.1039/d0mh00735h.

[9] N. Mehra, M. Jeske, X. Yang, J. Gu, M. A. Kashfipour, Y. Li, J. A. Baughman, J. Zhu, *ACS Applied Polymer Materials* **2019**, *1*, 1291–1300, DOI 10.1021/acsapm.9b00111.

[10] S. Thakur, A. Giri, *Journal of Materials Chemistry A* **2023**, *11*, 18660–18667, DOI 10.1039/d3ta04161a.

[11] J. He, L. Zhang, L. Liu, *Nanoscale* **2021**, *13*, 991–999, DOI 10.1039/d0nr06031c.

[12] T. Meng, P. Zhang, H. Zhong, H. Zhu, H. Zhang, D. Xu, Y. Zhao, *Nano Letters* **2024**, *24*, 14095–14101, DOI 10.1021/acs.nanolett.4c04306.

[13] R. Takehara, N. Kubo, M. Ryu, S. Kitani, S. Imajo, Y. Shoji, H. Kawaji, J. Morikawa, T. Fukushima, *Journal of the American Chemical Society* **2023**, *145*, 22115–22121, DOI 10.1021/jacs.3c07921.

[14] W. M. Haynes, D. R. Lide, T. J. Bruno, *CRC Handbook of Chemistry and Physics*, 97th ed., CRC Press, Boca Raton, FL, **2016**, DOI 10.1201/9781315380476.

[15] R. Takehara, T. Fukui, T. Tano, M. Ryu, S. Kitani, H. Kawaji, J. Morikawa, T. Fukushima, *Journal of the American Chemical Society* **2024**, *146*, 30548–30552, DOI 10.1021/jacs.4c11849.

[16] P. M. Kristiansen, A. Gress, P. Smith, D. Hanft, H.-W. Schmidt, *Polymer* **2006**, *47*, 249–253, DOI 10.1016/j.polymer.2005.08.053.

[17] C. Kulkarni, E. W. Meijer, A. R. A. Palmans, *Accounts of Chemical Research* **2017**, *50*, 1928–1936, DOI 10.1021/acs.accounts.7b00176.

[18] P. J. Stals, M. M. Smulders, R. Martin-Rapun, A. R. Palmans, E. W. Meijer, *Chemistry – A European Journal* **2009**, *15*, 2071–80, DOI 10.1002/chem.200802196.

[19] R. Q. Albuquerque, A. Timme, R. Kress, J. Senker, H. W. Schmidt, *Chemistry – A European Journal* **2013**, *19*, 1647–57, DOI 10.1002/chem.201202507.

[20] T. Tran, C. Kodisch, M. Schöttle, N. W. Pech-May, M. Retsch, *The Journal of Physical Chemistry C* **2022**, *126*, 14003–14010, DOI 10.1021/acs.jpcc.2c04254.

[21] P. J. Stals, J. C. Everts, R. de Bruijn, I. A. Filot, M. M. Smulders, R. Martin-Rapun, E. A. Pidko, T. F. de Greef, A. R. Palmans, E. W. Meijer, *Chemistry – A European Journal* **2010**, *16*, 810–21, DOI 10.1002/chem.200902635.

[22] C. S. Zehe, J. A. Hill, N. P. Funnell, K. Kreger, K. P. van der Zwan, A. L. Goodwin, H. W. Schmidt, J. Senker, *Angewandte Chemie International Edition* **2017**, *56*, 4432–4437, DOI 10.1002/anie.201612122.

[23] S. Cantekin, T. F. de Greef, A. R. Palmans, *Chemical Society Reviews* **2012**, *41*, 6125–37, DOI 10.1039/c2cs35156k.

Supporting Information

Thermal Transport Across Supramolecular Bonds in Self-Assembled BTA Fibers

Experimental

Fourier transform infrared spectra were obtained with a *Vertex 70 FT-IR spectrometer (Bruker Corp.)* equipped with an ATR accessory at a resolution of $1\,\mathrm{cm}^{-1}$ in the range of $4000\,\mathrm{cm}^{-1}$ to $650\,\mathrm{cm}^{-1}$.

BTA fibers were prepared by self-assembly under ambient conditions. The BTA derivatives were first dissolved in DMF (or in DMSO for *Am-C3*) at elevated temperatures. The hot solution was poured into a petri dish lined with aluminum foil and covered with a crystallization dish. Slow solvent evaporation over at least one week enabled fiber formation suitable for lock-in thermography measurements.

The BTA fibers were carefully removed from the aluminum foil using fine tweezers and spatulas, fixed on a 3D-printed sample holder with double-sided tape, and coated on both sides with a thin ($\sim 10\,\mathrm{nm}$) carbon layer. The LIT measurements were performed in a vacuum chamber ($p \leqslant 0.01\,\mathrm{mbar}$) to minimize convective heat losses. The fibers were excited periodically with a frequency of $0.27\,\mathrm{Hz}$ using a point laser (*51nano-N-5200.9-O05P124280150, Schäfter + Kirchhoff GmbH*). The power was adjusted individually for each measured fiber by comparing the peak values of the amplitude data across 13 measurements per sample with powers ranging from $18\,\mu\mathrm{W}$ to $72\,\mu\mathrm{W}$, and selecting the power that brought this value closest to $175\,\mathrm{mK}$. The temperature evolution was monitored with an *ImageIR 9430* research IR camera (*InfraTec GmbH*) with a spectral window ranging from $1.5\,\mu\mathrm{m}$ to $5.5\,\mu\mathrm{m}$. It was mounted with an M = 8.0x microscopy objective. The time–temperature data were converted to an amplitude and phase signal by the software *IRBIS* (*InfraTec GmbH*). The linearized amplitude and phase data as a function of the distance from the excitation point of the laser were used to calculate the thermal diffusivity values (slope method).

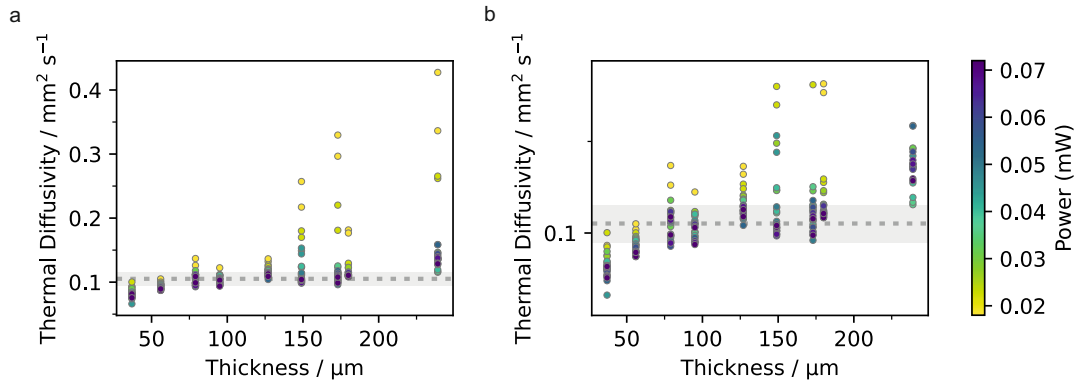

Figure 7.4: Thermal diffusivity values of fibers formed from *Hex-C3*, measured using lock-in thermography at $0.27\,\mathrm{Hz}$ across a wide range of fiber diameters. Each data point corresponds to one of 13 different heating powers ranging from $18\,\mu\mathrm{W}$ to $72\,\mu\mathrm{W}$, as indicated by the color scale. The grey line shows the average thermal diffusivity (reference) and standard deviation obtained from three measurements using a sample-specific power that resulted in a peak amplitude signal closest to $175\,\mathrm{mK}$. a) All data points. b) Zoomed-in view of the y-axis to better visualize the differences near the reference value.

8

Thermal Transport in Polystyrene Nonwovens: Influence of Anisotropy, Structural Modification, and Functionalization

Ina Klein[1]*, Sophie Edith Fritze[2]*, Alexander Berger[1], Holger Schmalz[2], Markus Retsch[1,3], Andreas Greiner[2]

* *These authors contributed equally to this work.*

Published in *ACS Applied Polymer Materials*, **2026**, *8*, 1954-1963.
Reproduced with permission from American Chemical Society.

[1] Department of Chemistry, Physical Chemistry I, University of Bayreuth, 95447 Bayreuth, Germany.
[2] Department of Chemistry, Macromolecular Chemistry II, University of Bayreuth, 95447 Bayreuth, Germany.
[3] Bavarian Polymer Institute (BPI), Bayreuth Center of Colloids and Interfaces (BZKG), University of Bayreuth, 95447 Bayreuth, Germany.

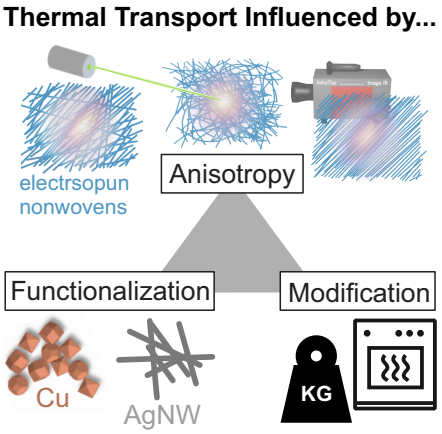

ACS APPLIED POLYMER MATERIALS

pubs.acs.org/acsapm Article

Thermal Transport in Polystyrene Nonwovens: Influence of Anisotropy, Structural Modification, and Functionalization

Ina Klein,[#] Sophie E. Fritze,[#] Alexander Berger, Holger Schmalz, Markus Retsch,[*] and Andreas Greiner[*]

Cite This: *ACS Appl. Polym. Mater.* 2026, 8, 1954−1963 Read Online

ACCESS | Metrics & More | Article Recommendations | Supporting Information

ABSTRACT: Understanding heat transport in hierarchical materials is essential for the rational design of next-generation thermal management systems. In this study, we utilize a combination of electrospinning and functionalization techniques to fabricate a series of polystyrene (PS) nonwovens with defined variations in fiber alignment and fusion, as well as functionalization with metals. Using lock-in thermography, we analyze in-plane thermal transport with directional sensitivity and correlate the results with morphological characteristics. We show that increasing fiber alignment enhances thermal anisotropy only up to a certain threshold, beyond which the quality of interfiber contact becomes the dominant factor. The incorporation of nonpercolating silver nanowires is only effective when phonon scattering is minimized. Otherwise, fiber boundaries significantly limit the potential transport enhancement offered by these costly additives. In contrast, copper coatings form percolating networks that markedly enhance thermal transport, yet they remain governed by the global architecture of the fiber network. Altogether, this work experimentally highlights that minimizing phonon scattering and controlling structural features are more critical than maximizing fiber or filler alignment. The insights contribute to a deeper understanding of heat conduction in fibrous systems and offer guidance for designing such materials with targeted performance.

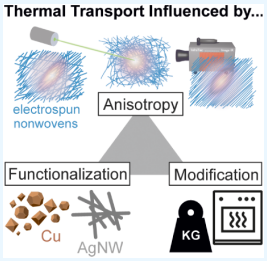

KEYWORDS: *electrospinning, thermal transport, anisotropy, metallic functionalization, polymer nonwoven, lock-in thermography*

INTRODUCTION

The interconnected global challenges of population growth, climate change, and the energy crisis demand an understanding of, control over, and optimization of thermal transport to regulate energy use and mitigate adverse effects efficiently.[1] The importance of thermal transport processes spans multiple length scales, influencing systems from the microscopic to the macroscopic. At the microscale, the continuous miniaturization and increasing integration density in microelectronics give significant challenges for heat dissipation.[2] Therefore, efficient thermal management is crucial for the performance, service life, and safety of electronic devices, such as batteries[3,4] and semiconductor chips.[5−7] At the macroscopic scale, thermal transport plays a critical role in personal thermal management, with the aim of optimizing heat exchange between the human body and the environment to increase thermal comfort and reduce energy consumption.[8,9]

A key approach for the development of so-called thermal interface materials is the use of composite materials that unite the properties of soft polymer matrices with the advantages of inorganic fillers.[10] This enables freedom in the design of the desired flexible, thermally stable structures with tailored thermal and electrical conductivity.[11] Architectures based on one-dimensional fibers, therefore, seem appealing. Their high aspect ratio and large surface area provide further potential for functionalization.[12] Metallic nanowires such as silver nanowires (AgNWs) in turn also prove to be promising nanofillers for thermal management, as they allow efficient thermal conduction paths due to their high thermal conductivity and mechanical flexibility resulting from their one-dimensional nature.[10] Various incorporation strategies can be employed, such as homogeneous dispersion in polymer matrices to form thermal networks, directional arrangement to control anisotropic heat conduction, or as thermal bridges in hybrid filler systems to enhance their overall conductivity.[13−15] The integration into textiles, fiber mats, or 3D-printed structures creates a wide range of applications, including personalized thermal management solutions and flexible electronics.[16] However, the systematic development of such materials requires a renewed understanding of the underlying transport mechanisms, as nanostructures deviate from classical models due to interfacial thermal resistance, phonon scattering, and anisotropic thermal conductivity.[17] Interfaces in nanocomposites significantly influence heat transfer, as phonons are scattered at material junctions, making the efficiency of thermal conduction highly dependent on the specific interactions between the filler and matrix.[18] The formation of percolating networks of nanofillers enhances thermal transport, while their

Received: November 3, 2025
Revised: January 13, 2026
Accepted: January 13, 2026
Published: February 2, 2026

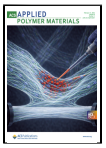

spatial arrangement and synergies with other fillers, such as graphene or boron nitride, play a crucial role.[19]

At the same time, size effects and structural hierarchies in materials such as fiber membranes, porous materials, or 3D-printed architectures lead to complex transport behaviors.[12,20] These are often studied through simulations, which aim to identify key parameters influencing thermal transport. Furthermore, finite element modeling of low-conducting isotropic particles mixed with thermally anisotropic ones has shown that the formation of heat-conducting pathways, essential for efficient heat transport, requires a very high fraction of the particles to be anisotropic.[21] Graph theory has been applied to identify a microstructural parameter that relates to thermal anisotropy in various thermal networks. Specifically, three contact attributes—particle connectivity, contact quality, and contact orientation—were used to derive the so-called "directed network thermal resistance". It correlates with the anisotropic effective thermal conductivity.[22] In addition, models have been developed to predict thermal conduction in fibrous 3D networks, recognizing the average number of contacts per fiber as a key factor.[23] These theoretical studies all indicate that the pathways formed by contact points between thermally conductive elements are the decisive factor governing thermal transport in networked hierarchical systems.[21−23]

While many studies either focus on developing high-performance materials for thermal management or on theoretical and computational analysis of heat transfer, relatively few adopt an experimental approach with the primary goal of elucidating influence of the mesostructure on the overall transport properties. Systematic, experiment-driven investigations that disentangle which structural features most critically influence thermal transport remain scarce. To address this challenge, electrospinning emerges as a powerful and versatile tool for creating controllable fiber architectures with tunable functionality and anisotropy.[20] For instance, A. Chen et al. demonstrated that combining electrospinning with hot-stretching aligns both poly(vinyl alcohol) fibers and their polymer chains, yielding a nanostructured film with high thermal conductivity and thermal stability.[24] The mechanical properties of electrospun materials cover a broad range and depend on multiple parameters, including the solution composition and concentration, fiber diameter, orientation, crystallinity and packing density.[25−27] The large surface area and controllable pore structure of the electrospun membranes make electrospinning a promising approach for the fabrication of carbon capture and air filtration materials.[28,29] In addition, these features, combined with the high specific capacitance of transition metal oxide additives, have been exploited to produce electrospun electrodes for supercapacitor applications.[30] The versatility and tunability of electrospinning further enable the fabrication of biomimetic structures that resemble the natural, fibrous extracellular matrix, rendering the technique highly attractive for tissue engineering scaffolds.[31] Furthermore, wettability can be tailored through processing conditions and solution composition, allowing the development of electrospun membranes for oil/water separation.[32]

In this study, electrospinning is employed to fabricate polystyrene (PS) nonwovens with varying degrees of fiber orientation. To achieve highly aligned PS fibers, the technique of stable jet electrospinning (SJES) is applied.[33−35] Utilizing electrospinning not only enables precise control over fiber alignment but also facilitates the incorporation of highly conductive AgNWs as fillers within the polymer matrix.[36] Additionally, individual fibers within the nonwoven structure can be externally coated with copper using a previously reported method, further expanding the range of achievable material properties.[37] Polystyrene (PS) was deliberately chosen as the matrix material due to its amorphous nature, ensuring that crystallinity does not introduce an additional variable in the study. The selection aims to isolate the effects of fiber orientation, structural, and surface modifications on thermal transport. To achieve this, an appropriate technique for measuring thermal transport in thin films is required. Lock-in thermography (LIT) is well-suited for this purpose. The nonwoven is heated periodically using a laser, and its temperature response is monitored with an infrared (IR) camera. A Fourier transformation is applied to extract amplitude and phase data, which are linearized to finally calculate the sample's in-plane thermal diffusivity.[38,39] As LIT enables direction-dependent analysis in anisotropic thin films, it allows for the investigation of how in-plane structural variations, such as anisotropy, influence thermal transport. This study provides a comprehensive foundation for investigating in-plane thermal transport within fiber-based systems. It provides a systematic evaluation of the various parameters that influence heat conduction in these complex structures. As understanding is the foundation for improvement, we believe that conclusions drawn from this study will be valuable for advancing research on thermal management materials.

RESULTS AND DISCUSSION

PS nonwovens with different fiber orientations were obtained by electrospinning utilizing a high-speed rotating drum as collector (Figure 1). The latter is essential for achieving a preferential orientation of the fibers during deposition. In the classical electrospinning setup, the drum collector is placed between the solution-filled syringe that is subjected to a positive voltage and a back electrode that is subjected to a

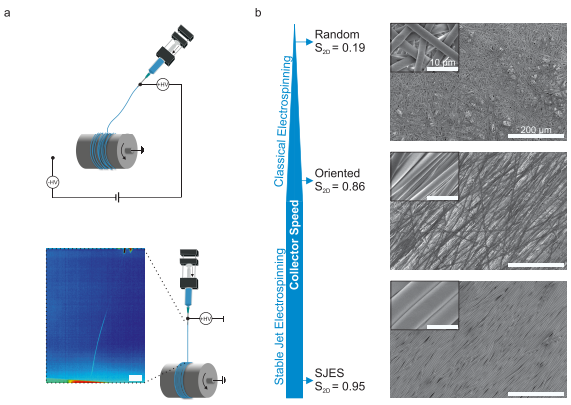

Figure 1. Influence of collector speed on fiber orientation in electrospun nonwovens. a) Schemes of the electrospinning setups and a high-speed camera image that shows the unsplit fiber jet during the SJES process (scale bar is 1 cm). b) The S_{2D} parameters used to quantify fiber orientation and corresponding SEM images are provided (scale bars are 200 and 10 μm). The classical electrospinning setup yields PS nonwovens with a random or oriented fiber arrangement, and the SJES setup leads to highly aligned PS fibers. This is confirmed by the corresponding S_{2D} parameters and SEM images.

https://doi.org/10.1021/acsapm.5c03952
ACS Appl. Polym. Mater. 2026, 8, 1954−1963

negative voltage. This creates an additional driving force for the fiber jet to travel toward the grounded collector during electrospinning. The collector-syringe distance is kept at 24 cm, and the degree of anisotropy is regulated simply by varying the rotational speed (from 30 to 3000 rpm). This results in random and oriented PS nonwovens. To achieve an even higher degree of orientation, SJES is utilized.[33,34] This technique has been adapted to match the solution concentrations that were used to obtain the random and oriented nonwovens via the classical electrospinning approach. In the SJES setup, the back electrode is removed, and the syringe is placed 15 cm above the high-speed drum, which is operated at 3000 rpm. The high-speed camera images in Figure 1b reveal the travel of the stable and unsplit jet that overcomes the typically occurring bending instabilities. The combination of a "low moving velocity jet"[34] and collection on a high-speed rotating drum finally enables highly aligned PS nonwovens, which we will refer to as SJES nonwovens in the following. For clarity, we term the direction in which the majority of fibers in oriented or SJES nonwovens are aligned as the "preferred orientation" or 'preferred direction. The perpendicular direction is referred to as the "cross-orientation" or "cross-direction".

To validate and quantify the orientation obtained by the different electrospinning methods and enable well-grounded discussions on structure−property relationships, we calculate an orientational order parameter (S_{2D} parameter)[40,41] for every nonwoven from the orientation angles α_i in the range of −90° to 90° of fiber segments i and the area ratio of the fiber segments ω_i.

$$S_{2D} = 2\left[\sum_{i=1}^{N} \cos^2(\alpha_i - \overline{\alpha})\omega_i\right] - 1 \quad (1)$$

The parameter ranges from 0 to 1, where 0 corresponds to complete randomness in orientation and 1 to perfect alignment of the fiber segments. To achieve comparable results, the microscopy images used for the calculation were rotated so that the mean fiber orientation becomes 0°. The average S_{2D} parameter across ten images was taken for every sample type. Further details on the calculation of the S_{2D} parameters are provided in the Supporting Information (Figure S1).

Figure 2a presents SEM images of the nonwoven samples. The corresponding fiber diameters are summarized in Table S1. Qualitative evaluation of these images aligns with the calculated S_{2D} parameters for all samples. The degree of orientation increases from the random nonwoven, through the oriented, to the SJES nonwoven, which exhibits nearly perfect fiber alignment. The three sample types were either cold pressed at 2 t to ensure they were sufficiently flat and compact for LIT analysis or annealed at 115 °C for 3 or 24 h. These procedures allow investigation of structural changes and the resulting relationships with thermal transport properties. Thermal stability at the annealing temperature was ensured via TGA (Figure S2). During annealing, all nonwovens shrink significantly. The shrinkage of the random sample is isotropic, while the oriented and SJES samples primarily shrink along the preferred orientation (Figure S3). SEM images also reveal that the fibers transition from straight to wavy shapes upon annealing. Both observations indicate relaxation of the PS chains during the annealing process. All films are subjected to LIT for characterizing their in-plane thermal diffusivity. The bottom-left inset in Figure 2a shows the phase data for the random, oriented, and SJES PS nonwovens after pressing or annealing. The corresponding S_{2D} parameters are provided in the Supporting Information (Table S1). The resulting thermal diffusivities are summarized in Figure 2b.

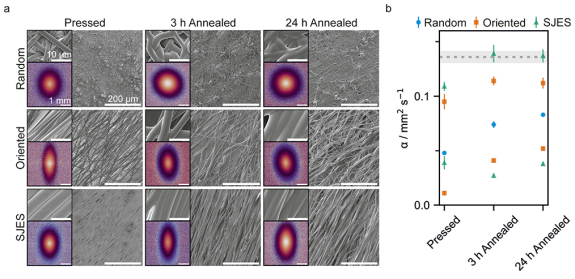

Figure 2. Electrospun nonwovens after pressing at room temperature, annealing at 115 °C for 3 h or annealing at 115 °C for 24 h. a) SEM images (scale bars are 200 and 10 μm) and the lock-in thermography phase data. b) Thermal diffusivity values obtained from measurements at ten positions per sample. The gray line represents the thermal diffusivity of a hot-pressed PS film.

The ellipsoidal shape of the 2D phase data for the oriented and SJES nonwovens, along with the corresponding two strongly differing thermal diffusivity values, clearly demonstrates that the structural anisotropy introduced by fiber orientation results in thermal anisotropy. The higher thermal diffusivity values correspond to the preferred direction, while the lower values correspond to the cross-direction. It must be noted that the phase data for the pressed random sample show a slight but noticeable thermal anisotropy, while the corresponding annealed samples appear isotropic. This suggests that some accidental fiber orientation occurred during fiber collection on the slowly rotating drum roll, but the anisotropy is too weak to be detected by the S_{2D} parameter calculations. Given the minimal anisotropy, a single overall thermal diffusivity value is reported. Regardless of the postprocessing treatments, the thermal diffusivity values for the random nonwovens lay between those of the oriented sample. We rationalize this by the even distribution of contact points and gaps between neighboring fibers, as seen both qualitatively in the SEM images and quantitatively in the low S_{2D} parameter. In contrast, the oriented sample has most of its gaps and interfiber contact points perpendicular to the preferred orientation, increasing thermal resistance in this direction, while transport along the fibers enhances the thermal diffusivity in the preferred direction. The SJES sample exhibits a higher thermal diffusivity in the preferred direction compared to the oriented sample. The SEM image and the higher S_{2D} parameter validate the improved fiber alignment, which reduces hindrance to thermal transport in the preferred direction. Interestingly, the SJES sample also shows higher thermal diffusivity in the cross-direction. This is not immediately explained by its higher S_{2D} parameter, as a higher degree of orientation is expected to reduce thermal transport across the fibers. Nevertheless, this can be attributed to the exceptional degree of alignment in the SJES nonwoven: the fibers are so well aligned that a substantial portion of their lengths are in direct contact, creating a significantly larger contact area. In contrast, the oriented nonwoven sample exhibits some misalignment, which disrupts interfiber contact and reduces cross-directional heat transfer. This difference

https://doi.org/10.1021/acsapm.5c03952
ACS Appl. Polym. Mater. 2026, 8, 1954−1963

becomes even more apparent when comparing the thermal anisotropy, defined as the ratio of thermal diffusivity in the preferred direction to that in the cross-direction. For the SJES sample, this ratio is 2.8. Meanwhile, the very low cross-direction diffusivity of the oriented nonwoven results in a much higher thermal anisotropy of 8.6.

Annealing has notable effects on the thermal diffusivities of the electrospun samples. In randomly oriented specimens, thermal diffusivity increases by more than 50% after 3 h of annealing, and by over 70% after 24 h. This enhancement is likely due to a combination of shrinkage and fiber fusion. Shrinkage increases the interfiber contact density, improving thermal transport. In parallel, SEM images show that annealing causes fibers to fuse at their contact points, which significantly reduces thermal contact resistance and further facilitates heat transfer across fiber interfaces. The longer the fibers are annealed, the more extensive the fusion appears to be, resulting in lower contact resistance and higher thermal diffusivity.

In the preferred direction, both the annealed oriented and SJES samples exhibit higher thermal diffusivities than the random sample. Notably, the values for the SJES sample approach those of a hot-pressed reference PS film, indicated by the gray line in Figure 2b. These enhancements are not due to improved alignment, as confirmed by S_{2D} parameters (Table S1). To explore possible changes at the molecular level, polarized Raman spectroscopy was applied, but no significant differences in polymer chain orientation were observed (Figure S4). The increase in fiber waviness after annealing, however, suggests PS chain relaxation, indicating a transition from a less coiled, possibly even slightly stretched conformation to a more relaxed, amorphous state. Since this structural change would typically be expected to reduce thermal diffusivity rather than enhance it, the observed increase in thermal transport is more likely due to improved contact quality between fibers. Misaligned fibers, which previously disrupted orientation and hindered transport along the preferred direction, fuse with the aligned fibers during annealing. As a result, they interfere less with heat transport in the preferred direction.

In the cross-direction, the thermal diffusivity of the oriented nonwoven increases significantly after 3 or 24 h of annealing. This reduces the thermal anisotropies from 8.6 to 2.8 and 2.2, respectively. While shrinkage may contribute by increasing the total contact area, this effect is likely limited, as shrinkage primarily occurs in the preferred direction and thus does not significantly increase the number of cross-fiber contact points. In contrast, fiber fusion is clearly visible in SEM images of the annealed oriented nonwovens and becomes more pronounced with longer annealing times. Since the cross-direction thermal diffusivity also increases with annealing time, we conclude that fiber fusion and the resulting reduction in thermal contact resistance are the main driving forces of this enhancement.

In contrast, the cross-direction thermal diffusivity of the SJES samples decreases upon annealing for 3 h, despite SEM evidence of fiber fusion at contact points. However, these images also reveal a reduced contact area between neighboring fibers. The loss of the straight fiber shape, originally enabling nearly perfect close-packing in the pressed SJES samples, introduces gaps between fibers that were previously in contact. This explains the reduced thermal diffusivity in the cross-direction for the SJES sample annealed for 3 h. Combined with increased diffusivity in the preferred direction, this results in higher thermal anisotropy (5.1) compared to the pressed SJES nonwoven (2.8). In the SJES sample annealed for 24 h, the cross-direction thermal diffusivity returns to a value close to that of the pressed sample. Since the long-range structure remains similar to that of the 3 h annealed specimen, this cannot be attributed to differences in contact area size. Instead, it is possible that more extensive fiber fusion in the 24 h annealed nonwoven compensates for the loss of initial contact area by significantly reducing thermal resistance at those fused sites. Nevertheless, the cross-direction thermal diffusivities of the annealed SJES samples remain lower than those of the corresponding oriented samples. This implies that increased fiber waviness in the oriented nonwoven does not significantly reduce the number of contact points, as the initial orientation was already only moderate. In contrast, the highly aligned SJES samples are severely affected by the introduction of the gaps.

In conclusion, random fiber orientation in nonwovens leads to isotropic thermal transport on a macroscopic length scale. The thermal diffusivity in such nonwovens lies between those observed in the preferred and cross-direction. Also, a higher degree of orientation enhances thermal diffusivity in the preferred direction and suppresses transport in the cross direction, as long as the interfiber contact is not significantly enhanced by the alignment. In such cases of near-perfect alignment, the resulting large contact area can also promote heat transfer across fibers. The annealing experiments, together with the behavior of the pressed oriented sample, show that even small gaps between fibers are sufficient to significantly hinder thermal transport in the cross-direction. Thus, achieving high thermal anisotropy depends not on perfect alignment, but on reducing contact between neighboring fibers while preserving a high degree of orientation.

In the next step, the material series is expanded by the introduction of metallic conductors to the PS fiber architectures. We elucidate this influence by two distinct strategies. First, by a preprocessing incorporation of AgNWs[36] into the electrospinning feedstock. Second, by using an electroless plating solution of copper on an already formed nonwoven. The AgNWs were synthesized according to the polyol method,[42] resulting in NWs with a high aspect ratio, a diameter of approximately 100 nm, and 5 to 23 μm in length (Figure S5). The AgNWs form a stable dispersion in water, which is then freeze-dried before being redispersed in DMF and mixed with PS (Figure 3a). This solution is then processed by electrospinning to form PS-AgNW composite nonwovens with a random as well as oriented fiber orientation resulting

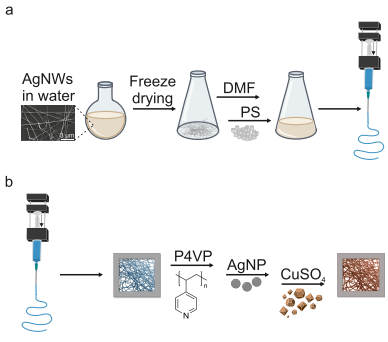

Figure 3. Schematic illustrations of both functionalization routes a) Steps of the preprocessing functionalization of PS nonwovens with AgNWs shown in a BSE-SEM image (scale bar is 3 μm). b) Steps of the postprocessing functionalization of PS nonwovens with copper.

https://doi.org/10.1021/acsapm.5c03952
ACS Appl. Polym. Mater. 2026, 8, 1954−1963

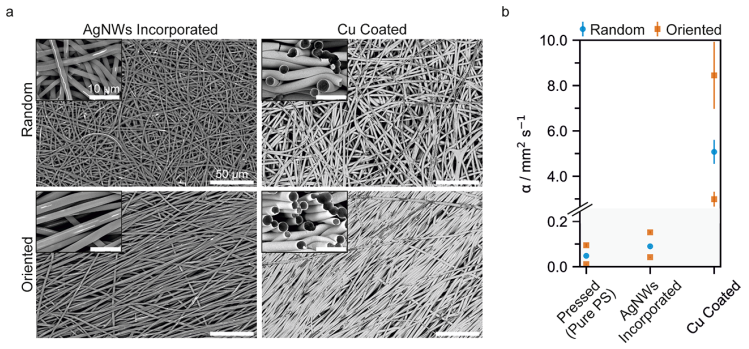

Figure 4. Electrospun nonwovens after incorporation of AgNW or coating with copper a) BSE-SEM images highlighting the features of the functionalization (scale bars are 50 and 10 μm). b) Thermal diffusivity values obtained from measurements at a minimum of ten positions per sample.

from the setup in Figure 1a. The prepared fiber nonwovens show a yellowish-brown color that was already observed for the electrospinning solution (Figure S5). The proof of the location of the AgNWs in the PS fiber matrix is given by SEM. With the use of an SE detector, only the surface of the PS fibers is imaged, showing no traces of AgNWs on the outside of the fibers (Figure S6). Using a BSE detector, the AgNWs embedded in the PS fibers can be visualized, where they align with the fiber axis (Figure 4a, Figure S7). The ratio of silver in PS was determined by ICP-OES to be 2.6 wt %, corresponding to about 0.27 vol %.[43] This also marks the maximum concentration of AgNWs that is still compatible with electrospinning.[36] As shown in the BSE-SEM images, this amount is insufficient for the AgNWs to form a percolating network, but the AgNWs are strongly coaligned with the orientation of the polymer fiber.

The second metallized structure is achieved by means of a wet chemical impregnation. A copper coating is deposited around the individual fibers of pressed random and pressed oriented PS nonwovens (Figure 3b). This postprocessing metallization follows a three-step procedure starting with coating of the membranes with poly(4-vinylpyridine) (P4VP) that acts as an anchor group for the silver nanoparticles (AgNPs) that are seeded in the next step. The AgNPs then form the nuclei for the electroless deposition of copper, resulting in a copper layer covering the individual PS fibers (Figure S8).[37] After this final step, the nonwovens appear with a coppery finish (Figure S9).

The BSE-SEM images of Figure 4a show the well-defined copper shells. In the cross-section images, it becomes evident that the thin copper coating enwraps the individual fibers with contact points between individual fibers allowing for the formation of a percolating network. Although random and oriented nonwovens were treated simultaneously in the same reaction container (Figure S9), the copper layer is more uniformly distributed in the random nonwoven compared to the oriented nonwoven. While the copper layer in the random nonwoven is about 50 to 100 nm thick, the coating in the oriented nonwoven becomes increasingly sparse toward the center (Figure S10). This comparison showcases that the fiber arrangement can significantly influence the electroless plating and, consequently the distribution of the coating. In the random nonwoven, the isotropic fiber orientation creates numerous interconnected cavities with random shape and distribution, allowing the functionalization solutions to efficiently penetrate the entire membrane. In contrast, the aligned fibers in the oriented nonwoven tend to form bundles of several fibers leading to denser layers. The gaps between such bundles, caused by misalignment and imperfections, are predominantly oriented along the preferred direction. These elongated cavities are larger but less frequent compared to the random nonwoven case. As a consequence, the anisotropic cavities in the oriented nonwoven case do not form an interconnected cavity network. This hinders imbibing of the metallization solution. Moreover, during copper deposition, the growing metal layer can further narrow or close these already limited cavities, aggravating the difficulty of coating the membrane's interior.

These structures are analyzed using LIT to investigate how the presence, geometry, and concentration of highly conductive materials affect thermal transport in the nonwovens. As shown in Figure 4a and Figure S7, the AgNWs do not form a percolating network but remain as individual wires aligned in the same direction as the PS fibers. Comparing the random PS nonwoven with its counterpart containing 0.27 vol % AgNWs, the thermal diffusivity increases from 0.048 $mm^2\ s^{-1}$ to 0.090 $mm^2\ s^{-1}$. Considering the excellent thermal transport properties of AgNWs ($\sim$191 − 332 W $(m\ K)^{-1}$)[44,45] this increase is relatively modest. It shows that the high contact resistance between the PS fibers significantly limits the potential impact of the AgNWs even when they align with the fiber axes. In accordance with the previously discussed samples, the thermal diffusivity of the random nonwoven with AgNWs lies between the preferred direction and cross-direction diffusivities of the corresponding oriented sample. Interestingly, the incorporation of AgNWs results in a 1.6-fold increase in thermal diffusivity along the preferred direction (from 0.095 $mm^2\ s^{-1}$ to 0.152 $mm^2\ s^{-1}$), while diffusivity in the cross direction increases by a factor of 3.8 (from 0.011 $mm^2\ s^{-1}$ to 0.042 $mm^2\ s^{-1}$). Since the AgNWs are embedded within the PS fibers, they cannot reduce interfiber contact resistance. However, the S_{2D} parameter of the oriented pure PS sample is 0.86, whereas that of the AgNW containing oriented sample is considerably lower at 0.58 (Table S1, Figure S11). This lower degree of alignment likely contributes to the more pronounced effect of AgNWs on the thermal diffusivity in the cross direction. A higher proportion of fibers misaligned from the preferred direction enhances thermal transport perpendicular to it, while reducing transport along it. Overall, these results show that phonon scattering at the fiber boundaries, as primary

https://doi.org/10.1021/acsapm.5c03952
ACS Appl. Polym. Mater. 2026, 8, 1954−1963

bottleneck for the thermal transport, diminishes the effectiveness of highly conductive fillers also in the preferred direction. Minimization of scattering is therefore essential to harness the full potential of conductive fillers in composite materials.

In contrast to the AgNW nonwovens, the copper coated samples form an electrically percolating network. The conductance of the samples is estimated using the four-point probe method, assuming square geometry and applying a correction factor to account for the relatively small sample size. For the random sample we obtain a sheet conductance (26.2 S sq^{-1} ± 2.6 S sq^{-1}), which is significantly higher compared to the oriented nonwoven. The electrical sheet conductance of the oriented sample is slightly lower in the cross-direction (7.4 S sq^{-1} ± 0.1 S sq^{-1}) compared to the preferred direction (8.3 S sq^{-1} ± 0.3 S sq^{-1}).[46] This difference can be explained by the structural characteristics of the samples. The copper coating is homogeneously distributed throughout the entire random nonwoven, such that all fibers contribute to electrical transport. In contrast, the oriented nonwoven was coated with copper only near the interfaces, leaving about one-third of the interior thickness uncoated. To account for this in the conductivity calculation, the full thickness is used for the random sample, while only one-third of the thickness is considered for the oriented sample.[46] With this adjustment, the resulting conductivity values are comparable: 2405 S cm^{-1} for the random sample, 2168 S cm^{-1} in the cross-direction, and 2436 S cm^{-1} in the preferred direction of the oriented sample. The low degree of electrical anisotropy is surprising in the case of the oriented copper coated sample. Apparently, the fiber bundles and their copper coating lead to an electric conductivity in the cross-direction, which is only slightly lower compared to the preferred direction. The presence of few elongated cavities only slightly obstructs the effective electric transport across the interfiber contacts. This observation can be understood similarly to the SJES sample, where the cross-orientation thermal diffusivity was found to be remarkably high (Figure 2b) due to the high interfiber contact areas.

Measuring the thermal diffusivity of copper-coated nonwovens using LIT presents challenges, as the reflectivity of the copper leads to low signal-to-noise ratios even after coating the samples with carbon. Hence, the absolute values should be interpreted with caution (Figure S12). Nevertheless, the comparison of the anisotropy allows relevant insights into the interplay of nonwoven structure and the observed heat transport. Here, the measured thermal diffusivities are significantly higher compared to pure PS nonwovens. Consequently, the copper network transports the majority of heat in this system. In contrast to the AgNW nonwovens, the copper-coated specimens comprise a higher metal volume fraction and form a percolating copper network, enabling more efficient heat propagation. Analogously to the unfunctionalized PS samples the random nonwoven's diffusivity falls between the values measured along and perpendicular to the preferred direction in the oriented one. This indicates that the different degree of copper functionalization plays a subordinate role for the effective thermal diffusivity. In contrast to the electric measurements, the structural anisotropy is preserved for the heat transport. The oriented copper coated nonwoven exhibits a thermal anisotropy of ∼2.8, whereas the electrical anisotropy (1.1) is almost isotropic. Nevertheless, the introduction of cross-direction electric transport attenuates the thermal anisotropy. Considering the order parameters of the oriented PS nonwoven (0.86) and the oriented copper coated nonwoven (0.77) it is noteworthy that the thermal anisotropy decreased from about 8.2 to 2.8. Since both, the electric and thermal transport, are governed by the copper coated fibers it is interesting to conclude that even though the underlying nonwoven structure is identical in both cases, different degrees of anisotropy can be observed depending on the type of transport.

CONCLUSION

This study systematically investigates thermal transport in polymer nonwovens, focusing on how anisotropy, structural modifications, and functionalization influence heat conduction. Through the controlled fabrication of a set of nonwovens, varying in fiber orientation, processing history, and functionalization, we establish a framework for analyzing how specific design parameters affect thermal transport in fibrous materials.

The results validate that random fiber arrangements lead to isotropic thermal transport, whereas oriented or SJES nonwovens exhibit pronounced thermal anisotropy. However, the enhancement of anisotropy through increased orientation is limited. As fiber alignment approaches perfection, the resulting increase in contact area between fibers can actually promote cross-directional heat transfer. Annealing was found to fuse fibers at contact points, reducing thermal resistance and increasing thermal diffusivity. However, the emergence of gaps between fibers or fused fiber bundles can substantially hinder cross-directional conduction. Both results highlight that limited contact between fibers, rather than perfect alignment, is key to achieving high thermal anisotropy.

AgNWs embedded within the nonwoven fibers yield only a moderate increase in thermal transport, not only due to the lack of percolation but also because of phonon scattering at the fiber boundaries. Copper coatings deposited around the fibers, on the other hand, form percolating networks that significantly enhance thermal diffusivity. The results also suggest that thermal transport is more influenced by the overall fiber architecture, whereas electrical conductance is more sensitive to local structural variations. This observation clearly warrants further investigation and highlights metal-coated nonwovens as a promising system for exploring and potentially decoupling electrical and thermal conduction, an important step toward the targeted design of multifunctional materials. In conclusion, minimizing phonon scattering and controlling structural features, rather than solely maximizing fiber or filler alignment, are key to tailoring thermal transport for optimal performance of fiber-based materials. These insights establish a strong foundation for the rational design of next-generation thermal management materials.

EXPERIMENTAL SECTION

Materials

In this study, polystyrene (*Sigma-Aldrich*, M_n 119 000, M_w 193 000), poly(vinylpyrrolidone) (*Sigma-Aldrich*, M_w 1 300 000 by LS), poly(4-vinylpyridine) (*Sigma-Aldrich*, M_n 160 000), polyethylene glycol 400 (*Sigma-Aldrich*), silver nitrate (*VWR Chemical*, 99−100.5% Ph. Eur.), iron(III) chloride (*Fisher Chemical*, ≥97.0%), sodium chloride (*Bernd Kraft*, p.a.), sodium citrate (*Fisher Chemical*, 98%), sodium borohydride (*Fluka*, ≥96%), sodium hydroxide (*Fisher Chemical*, p.a.), copper(II) sulfate pentahydrate (*Alfa Aesar*, 99%), potassium sodium tartrate tetrahydrate (*Alfa Aesar*, 99%), formaldehyde

https://doi.org/10.1021/acsapm.5c03952
ACS Appl. Polym. Mater. 2026, 8, 1954−1963

(*Alfa Aesar*, 37 wt %, w/w aq. soln. stab. with 7−8% methanol), pyridine (*Fisher Scientific*, ≥99.5%), ethylene glycol (*Fisher Scientific*, p.a. ≥ 99.5%), and dimethylformamide (*Fisher Chemical*, p.a. 99.5%) were used as obtained. Other solvents like acetone and methanol (tech.) were distilled before further use.

Aqueous dispersions of AgNWs were synthesized according to the polyol method.[42]

Preparation of Unfunctionalized PS Film

The homogeneous PS film was prepared by hot-pressing (*hot press 2518 Mod. 25-12-2 HC, Carver, Inc.*, Indiana, USA). The PS was evenly distributed in a mold of 100 μm thickness and molten for 3 min at 220 °C before 2 t were applied for 2 min. The hot film was then pressed (*press, PO Weber GmbH*, Germany) until it cooled down to room temperature.

Preparation of Unfunctionalized PS Nonwovens

A 28 wt % solution of PS in DMF was prepared and filled in a syringe equipped with a 21G cannula. This syringe was placed in the electrospinning setup (Figure 1a) 35 cm apart from the back electrode and 24 cm apart from the grounded drum collector (diameter: 5 cm). For the isotropic nonwovens a rotation speed of 30 rpm was used, while the anisotropic fiber orientation was created with a speed of 3000 rpm. The solution was processed with a feed of 0.6 mL/h while being subjected to a voltage of +22 kV. To the back electrode a voltage of −3 kV was applied to create a driving force for the fiber jet to travel toward the collector. The spinning time was fixed at 2 h while keeping a temperature of 21 °C and a humidity level of ∼40%. After removal of the nonwovens, one part of the membranes was compression molded (*hot press 2518 Mod. 25-12-2 HC, Carver, Inc.*, Indiana, USA) at 2 t for 1 min, while the other part was subjected to thermal annealing. For this purpose, the samples were heated to 115 °C within 11 min in an oven (*Heratherm OGS60, Thermo Scientific GmbH*, Germany) and held at this temperature for 3 or 24 h. The samples were then cooled within 55 min to below 80 °C, before taking them out of the oven.

Preparation of Unfunctionalized PS Nonwovens via Stable Jet Electrospinning (SJES)

A 28 wt % solution of PS in DMF was prepared and filled in a syringe equipped with a 21G cannula. This syringe was placed in the electrospinning setup (Figure 1b) 15 cm apart from the grounded drum collector. For the highly anisotropic nonwovens a rotation speed of 3000 rpm was used. The solution was processed with a feed of 0.9 mL/h while being subjected to a voltage of +18 kV. The spinning time was fixed at 1 h while keeping a temperature of 21 °C and a humidity level of ∼40%. After removal of the nonwovens, one part of the membranes was compression molded (*hot press 2518 Mod. 25-12-2 HC, Carver, Inc.*, Indiana, USA) at 2 t for 1 min, while the other part was subjected to thermal annealing following the same procedure as described above.

Preparation of AgNW Functionalized PS Nonwovens

The functionalization was adapted from Chen et al.[36] The AgNWs have diameters of approximately 100 nm and lengths ranging from 5 to 23 μm. 2.0 mL of a 2.2 wt % aqueous AgNW dispersion were freeze-dried. The residue was redispersed in 3.88 mL DMF. The solution was put in an ultrasound bath for 5 min. Then, 1.5 g PS pellets were added, and the solution was homogenized in a shaker (*Multi Reax, Heidolph Instruments GmbH & Co. KG*, Germany) overnight. Before processing, the solution was stirred for 1 h at room temperature before being filled in a syringe equipped with a 27G cannula. This syringe was placed in the electrospinning setup (Figure 1a) 35 cm apart from the back electrode and 24 cm apart from the grounded drum collector. For the isotropic nonwovens, a rotation speed of 30 rpm was used, while the anisotropic fiber orientation was created with a speed of 3000 rpm. The solution was processed with a feed of 0.6 mL/h while being subjected to a voltage of +22 kV. To the back electrode a voltage of −3 kV was applied to create a driving force for the fiber jet to travel toward the collector. The spinning time was fixed at 2 h while keeping a temperature of 21 °C and a humidity level of ∼40%. After removal of the nonwovens, they were compression molded (*hot press 2518 Mod. 25-12-2 HC, Carver Inc.*, Indiana, USA) at 2 t for 1 min.

Preparation of Copper Functionalized PS Nonwovens

The metallization was adapted from Langner et al.[37] Pieces of pressed unfunctionalized PS nonwoven (3 × 4 cm) were clamped between two PP frame parts that were glued together by heat. The loaded frames were placed in 90 mL of a P4VP solution in methanol (6.6 mg/mL) in a bespoke made Teflon reaction container (Figure S9) and stirred for 5 min. After a short draining, the nonwovens were dried overnight at 80 °C in vacuum. The dried nonwovens were immersed in 90 mL of a 0.2×10^{-3} M AgNP dispersion. For preparation of the AgNP solution, an amount of 42 mg (0.247 mmol) $AgNO_3$ and 65 mg (0.252 mmol) sodium citrate were dissolved in 1000 mL distilled water. Subsequently, 0.55 mg (0.015 mmol) $NaBH_4$ dissolved in 3 mL water were added. The nonwoven loaded AgNP solution was degassed twice at 1 mbar until the solution began to boil. The samples were left in the AgNP dispersion for 24 h under shaking at 60 rpm before being rinsed with distilled water. For the deposition of copper on the nonwovens, 90 mL of the solution prepared as described in the following was used to immerse the nonwovens. An amount of 1.0 g (4 mmol) $CuSO_4 \cdot 5H_2O$ was dissolved in 40 mL water, followed by dissolution of 2.5 g (8.8 mmol) potassium sodium tartrate tetrahydrate. Subsequently, 1.5 g (24.8 mmol) NaOH, 0.2 g (4.54 mmol) PEG 400, 6.1 μL pyridine, and 3.0 mL formaldehyde were dissolved in the solution. The flask was filled up to 100 mL. The loaded reaction container was placed in a water bath with a temperature of 45 °C for 30 min while stirring slowly. Nonwoven samples were taken and rinsed with water. The wet nonwovens were then placed on filter papers for predrying, followed by drying at 80 °C in vacuum overnight.

Analytical Instruments and Methods

Images of the fiber jet were taken with a *CR5000 × 2* Ultra Highspeed camera (*Optronis GmbH*, Germany), equipped with a *Sigma 24−70 mm f/2.8 EX DG lens* (*Sigma Corporation*, Japan).

An *FEI Quanta FEG 250* (*Thermo Fisher Scientific Inc.*, Oregon, USA) was used for SEM characterization of the polystyrene nonwovens. Besides an ETD-detector, a CBS-detector was used for the visualization of the functionalization. Before measuring, the samples were sputtered with platinum by a *208HR* sputter coater (*Cressington Scientific Instruments Ltd.*, UK). The layer thickness lied around 1.6 nm.

The metal content of the used AgNW dispersion and composite nonwovens was determined from *ICP-OES* (*Avio 200, PerkinElmer*, Massachusetts, USA) equipped with a *PerkinElmer S10* autosampler, echelle polychromator, argon

https://doi.org/10.1021/acsapm.5c03952
ACS Appl. Polym. Mater. 2026, 8, 1954−1963

nebulizer and CCD semiconductor detector. For calibration of the respective sample matrix a single silver element standard (*PerkinElmer*, Massachusetts, USA, 1000 μg/mL) was used. Before measurement, 0.1 mL of the AgNW dispersion, respectively 0.02 g of the AgNW functionalized PS nonwovens were dissolved in 5 mL nitric acid. The solutions were then placed in the glass inlays for Teflon reactors. The microwave assisted digestion took place in an *Anton Paar Multiwave GO* (Austria). In the program, the samples were digested twice for 15 min at 185 °C. The digested solutions were diluted to 100 mL with deionized water (*Millipore Milli-Q Plus system, QPAK*2* purification cartridge, *Merck KGaA*, Germany).

Microscopy images and topographic reconstructions were obtained with a laser scanning confocal microscope (*LEXT OLS5000, Olympus Corp.*, Japan) in reflection geometry with a white light source and a 405 nm laser. For the determination of the orientational order parameters ten images were taken with overexposure and converted into grey scale images. The orientations, diameters and lengths of fiber segments were obtained using the software *MountainsLab* by *Digital Surf* (Figure S1). The images were turned by adding or subtracting angles to all segment orientation angles until their average orientation was 0°. Then the orientation angles between 90° and −90° were used to calculate the S_{2D} parameters according to Formula 1. For the calculation of electrical conductivity values the area and thickness of the copper coated samples were determined to 166.7 mm^2 and 109.1 μm for the random sample and 122.4 mm^2 and 102.0 μm for the oriented sample using the data analysis software corresponding to the confocal microscope (*Olympus Corp.*, Japan).

Electrical conductivity was measured using a custom-built four-point probe setup. This setup consists of four spring-loaded pin electrodes, evenly spaced at a distance of 1 mm, with spherical (0.42 mm) rhodium-coated gold tips (*NPS8-N, MISUMI Europa GmbH*, Germany). The electrodes are mounted on a 3D-printed head connected to a force-pressure sensor (*Series-4, MARK-10 Corp.*, New York, USA). Measurements were carried out under constant current and auto mode using a *Keithley 2400* multimeter (*Tektronix Inc.*, Oregon, USA) with an applied pressure force of 0.34 N−0.44 N. Three measurements, each comprising 500 data points, were conducted at different positions on each copper coated nonwoven to obtain the average electrical resistance values and corresponding standard deviations. The square roots of the sample areas were used to estimate the effective side lengths. Correction factors corresponding to these side lengths were then obtained by interpolating values reported in the literature.[46] These factors were subsequently applied to calculate the electrical sheet conductance. To calculate the electrical conductivity the sheet conductance was multiplied by the sample thickness. For the random sample, the measured thickness was used, while for the oriented sample, the measured thickness was divided by three prior to multiplication to account for the partial copper coating.

Prior to LIT measurements the nonwovens were coated on both sides with a thin carbon layer (10 nm−40 nm) to enhance surface emissivity (*EM ACE600 Carbon Thread Coater, Leica Microsystems GmbH*, Austria). Then periodic thermal excitation was applied using a point laser (*model 51nano-N520-0.9-O05-P-12-4-28-0-150, Schäfter + Kirchhoff GmbH*, Germany) at a maximum power of 0.9 mW. To account for variations in thermal penetration depth, different excitation frequencies were used: 0.18 Hz for pressed and annealed nonwovens, 0.3 Hz for nonwovens containing AgNWs, and 1.0 Hz for copper-coated nonwovens. 0.1 Hz was used for the homogeneous pressed PS thin film. The thermal response was monitored with an *ImageIR 9430* research IR camera (*InfraTec GmbH*, Germany) with a spectral window of 1.5 to 5.5 μm and equipped with a M = 1.0× objective. All measurements were carried out under vacuum conditions (pressure <10^{-5} bar) in a chamber with an optically transparent N-BK7 glass window to minimize convective heat losses. The time−temperature data were processed using the *IRBIS* software (*InfraTec GmbH*, Germany), which extracts amplitude and phase data via Fourier transformation. From the linearized amplitude and phase data as a function of the spatial distance from the laser excitation point, the thermal diffusivity values were calculated using the slope method.

Polarized Raman measurements were performed on a confocal *WITec Alpha RA+* Raman imaging system, equipped with an *UHTS 300* spectrometer and a back-illuminated *Andor Newton 970 EMCCD* camera (*Suite SEVEN 7.0* software package, *WITec GmbH*, Germany). Raman spectra were recorded with an excitation wavelength of λ = 532 nm and a 50× long working distance objective (*LD EC Epiplan-Neofluar DIC, Zeiss AG*, Germany, NA = 0.55), employing a laser intensity of 12 mW and an integration time of 0.5 s (50 accumulations). All spectra were subjected to a background removal routine.

■ ASSOCIATED CONTENT

Supporting Information

The Supporting Information is available free of charge at https://pubs.acs.org/doi/10.1021/acsapm.5c03952.

Fiber diameter and orientation parameters of all specimens; optical microscopy images and details of orientation parameter determination; TGA characterization; macroscopic photographs; polarized Raman spectra; Ag nanowire SEM24 (PDF)

■ AUTHOR INFORMATION

Corresponding Authors

Markus Retsch − *Department of Chemistry, Physical Chemistry I, University of Bayreuth, Bayreuth 95447, Germany; Bavarian Polymer Institute, University of Bayreuth, Bayreuth 95447, Germany; Bayreuth Center for Colloids and Interfaces, Bayreuther Institut für Makromolekülforschung, and Bavarian Center for Battery Technology (BayBatt), University of Bayreuth, 95447 Bayreuth, Germany;* orcid.org/0000-0003-2629-8450; Email: markus.retsch@uni-bayreuth.de

Andreas Greiner − *Department of Chemistry, Macromolecular Chemistry II, University of Bayreuth, Bayreuth 95447, Germany; Bavarian Polymer Institute, University of Bayreuth, Bayreuth 95447, Germany*; Email: greiner@uni-bayreuth.de

Authors

Ina Klein − *Department of Chemistry, Physical Chemistry I, University of Bayreuth, Bayreuth 95447, Germany;* orcid.org/0009-0005-9451-0080

Sophie E. Fritze − *Department of Chemistry, Macromolecular Chemistry II, University of Bayreuth, Bayreuth 95447, Germany*

https://doi.org/10.1021/acsapm.5c03952
ACS Appl. Polym. Mater. 2026, 8, 1954−1963

Alexander Berger − *Department of Chemistry, Physical Chemistry I, University of Bayreuth, Bayreuth 95447, Germany*

Holger Schmalz − *Department of Chemistry, Macromolecular Chemistry II, University of Bayreuth, Bayreuth 95447, Germany; Bavarian Polymer Institute, University of Bayreuth, Bayreuth 95447, Germany;* orcid.org/0000-0002-4876-0450

Complete contact information is available at: https://pubs.acs.org/10.1021/acsapm.5c03952

Author Contributions

#I.K. and S.E.F. contributed equally to this work. I.K.: conceptualization, investigation, methodology, formal analysis, writing—original draft, visualization; S.E.F.: conceptualization, investigation, methodology, formal analysis, writing—original draft, visualization; A.B.: investigation; H.S.: investigation; A.G.: conceptualization, resources, funding, writing—review/editing, supervision; M.R.: conceptualization, resources, funding, writing—review/editing, supervision

Notes

The authors declare no competing financial interest.

■ ACKNOWLEDGMENTS

We thank the Collaborative Research Centre 1585 (Project C05) of the German Research Foundation (grant number: 492723217) for financial support and the Bavarian Polymer Institute (BPI) for the use of the infrastructure of the KeyLabs "Small Scale Polymer Processing," "Synthesis and Molecular Characterization," and "Electron and Optical Microscopy". We also thank Stefan Rettinger and Simon Knorr for their valuable support and contributions to the conducted measurements. We acknowledge the use of AI tools to improve the readability and expression of the manuscript. The scientific content, analysis, and conclusions were developed entirely by us, and we take full responsibility for the work.

■ REFERENCES

(1) Das, M.; Knapczyk-Korczak, J.; Moradi, A.; Pichor, W.; Stachewicz, U. Enhanced thermal management of mats and yarns from polystyrene fibers through incorporation of exfoliated graphite. *Mater. Adv.* **2025**, *6* (6), 1859−1868.

(2) Moore, A. L.; Shi, L. Emerging challenges and materials for thermal management of electronics. *Mater. Today* **2014**, *17* (4), 163−174.

(3) Fu, L.; Wu, Z.; Wu, K.; Chen, W.; Zhang, M.; Huang, X.; Ma, C.; Shao, Y.; Ran, J.; Chua, K. J. A thermally induced flexible composite phase change material with boron nitride nanosheets/carbon nanotubes modified skeleton for battery thermal management. *Applied Energy* **2024**, *373*, 123899.

(4) Piggott, A. J.; Allen, J. S.; Pesaran, A. A. High-heat transfer lithium-ion batteries: A new era in battery thermal management. *Appl. Therm. Eng.* **2025**, *272*, 126347.

(5) Li, M.; Li, S.; Zhang, Z.; Su, C.; Wong, B.; Hu, Y. Advancing Thermal Management Technology for Power Semiconductors through Materials and Interface Engineering. *Acc. Mater. Res.* **2025**, *6* (5), 563−576.

(6) Rangarajan, S.; Schiffres, S. N.; Sammakia, B. A Review of Recent Developments in "On-Chip" Embedded Cooling Technologies for Heterogeneous Integrated Applications. *Engineering* **2023**, *26*, 185−197.

(7) Kim, M.; Kim, J.; Park, W.; Kang, J. S. A review in thermal management for advanced chip packaging from chip to heat sink. *Microelectron. Reliab.* **2025**, *170*, 115782.

(8) Ghahari, S. A.; Mohsenzadeh, E.; Oguz Gouillart, Y.; Gidik Vanderberck, H. A review of body radiant infrared control for personal thermal management with electrospun membranes. *Sol. Energy Mater. Sol. Cells* **2024**, *278*, 113149.

(9) Peng, Y.; Cui, Y. Thermal management with innovative fibers and textiles: Manipulating heat transport, storage and conversion. *Natl. Sci. Rev.* **2024**, *11* (10), nwae295.

(10) Liang, C.; Hong, J.; Wan, C.; Ma, X.; Wang, Z.; Zhao, X.; Hou, A.; Nika, D.; Huo, Y.; Zhang, G. A perspective on mechanism of heat transfer and performance optimization in advanced thermal interface materials. *Appl. Phys. Lett.* **2025**, *126* (7), 070501.

(11) Liao, X.; Denk, J.; Tran, T.; Miyajima, N.; Benker, L.; Rosenfeldt, S.; Schaffoner, S.; Retsch, M.; Greiner, A.; Motz, G.; et al. Extremely low thermal conductivity and high electrical conductivity of sustainable carbon-ceramic electrospun nonwoven materials. *Sci. Adv.* **2023**, *9* (13), No. eade6066.

(12) Han, W. H.; Wang, Q. Y.; Kang, Y. Y.; Zhou, X.; Hao, C. C. Electrospun polymer nanocomposites for thermal management: A review. *Nanoscale* **2023**, *15* (5), 2003−2017.

(13) Cheng, S.; Guo, X.; Cai, W.; Zhang, Y.; Zhang, X.-A. Enhanced thermal management in electronic devices through control-oriented structures. *J. Mater. Chem. A* **2024**, *12* (15), 8640−8662.

(14) Sun, Z.; Li, J.; Yu, M.; Kathaperumal, M.; Wong, C.-P. A review of the thermal conductivity of silver-epoxy nanocomposites as encapsulation material for packaging applications. *Chem. Eng. J.* **2022**, *446*, 137319.

(15) Ying, J.; Tan, X.; Lv, L.; Wang, X.; Gao, J.; Yan, Q.; Ma, H.; Nishimura, K.; Li, H.; Yu, J.; Liu, T. H.; Xiang, R.; Sun, R.; Jiang, N.; Wong, C.; Maruyama, S.; Lin, C. T.; Dai, W. Tailoring Highly Ordered Graphene Framework in Epoxy for High-Performance Polymer-Based Heat Dissipation Plates. *ACS Nano* **2021**, *15* (8), 12922−12934.

(16) Yun, J. Recent progress in thermal management for flexible/wearable devices. *Soft Sci.* **2023**, *3* (2), 12.

(17) Burger, N.; Laachachi, A.; Ferriol, M.; Lutz, M.; Toniazzo, V.; Ruch, D. Review of thermal conductivity in composites: Mechanisms, parameters and theory. *Prog. Polym. Sci.* **2016**, *61*, 1−28.

(18) Fitzgerald, M. L.; Zhao, Y.; Pan, Z.; Yang, L.; Lin, S.; Sauti, G.; Li, D. Contact Thermal Resistance between Silver Nanowires with Poly(vinylpyrrolidone) Interlayers. *Nano Lett.* **2021**, *21* (10), 4388−4393.

(19) Liang, X.; Chen, G.; Wu, Q.; Zhang, H.; Zhong, R.; Zeng, X.; Hu, D.; Lin, J. Highly thermally conductive composite films by the rational assembly of aramid nanofibers with low-dimensional nanofillers. *J. Mater. Res. Technol.* **2024**, *30*, 4003−4023.

(20) Gao, Q.; Agarwal, S.; Greiner, A.; Zhang, T. Electrospun fiber-based flexible electronics: Fiber fabrication, device platform, functionality integration and applications. *Prog. Mater. Sci.* **2023**, *137*, 101139.

(21) Lebeda, F.; Lebeda, T.; Retsch, M. Evaluation of Effective Heat Transport and Temperature Gradients in Thermally Anisotropic Particulate Arrangements. *ACS Appl. Eng. Mater.* **2023**, *1* (11), 3099−3107.

(22) Fei, W.; Ma, Q.; Soga, K.; Narsilio, G. A. A graph-theory based directed network feature for thermal anisotropy. *Int. J. Heat Mass Transfer* **2022**, *194*, 122987.

(23) Gaunand, C.; De Wilde, Y.; François, A.; Grigorova-Moutiers, V.; Joulain, K. Modeling conductive thermal transport in three-dimensional fibrous media with fiber-to-fiber contacts. *Phys. Rev. Appl.* **2025**, *23* (3), 034084.

(24) Chen, A.; Wu, Y.; Zhou, S.; Xu, W.; Jiang, W.; Lv, Y.; Guo, W.; Chi, K.; Sun, Q.; Fu, T.; Xie, T.; Zhu, Y.; Liang, X.-G. High thermal conductivity polymer chains with reactive groups: A step towards true application. *Mater. Adv.* **2020**, *1* (6), 1996−2002.

(25) Chavoshnejad, P.; Razavi, M. J. Effect of the Interfiber Bonding on the Mechanical Behavior of Electrospun Fibrous Mats. *Sci. Rep.* **2020**, *10* (1), 7709.

(26) Conte, A. A.; Sun, K.; Hu, X.; Beachley, V. Z. Effects of Fiber Density and Strain Rate on the Mechanical Properties of Electrospun Polycaprolactone Nanofiber Mats. *Front Chem.* **2020**, *8*, 610.
(27) Rashid, T. U.; Gorga, R. E.; Krause, W. E. Mechanical Properties of Electrospun Fibers—A Critical Review. *Adv. Eng. Mater.* **2021**, *23* (9), 2100153.
(28) Hong, W.; Lian, Z.; Jiang, H.; Chen, J.; Zhang, Z.; Ni, Z. Progress in advanced electrospun membranes for CO(2) capture: Feedstock, design, and trend. *J. Environ. Manage.* **2024**, *352*, 120026.
(29) Lu, T.; Cui, J.; Qu, Q.; Wang, Y.; Zhang, J.; Xiong, R.; Ma, W.; Huang, C. Multistructured Electrospun Nanofibers for Air Filtration: A Review. *ACS Appl. Mater. Interfaces* **2021**, *13* (20), 23293−23313.
(30) Pullanchiyodan, A.; Joy, R.; Sreeram, P.; Raphael, L. R.; Das, A.; Balakrishnan, N. T. M.; Ahn, J.-H.; Vlad, A.; Sreejith, S.; Raghavan, P. Recent advances in electrospun fibers based on transition metal oxides for supercapacitor applications: A review. *Energy Adv.* **2023**, *2* (7), 922−947.
(31) Xie, X.; Chen, Y.; Wang, X.; Xu, X.; Shen, Y.; Khan, A. U. R.; Aldalbahi, A.; Fetz, A. E.; Bowlin, G. L.; El-Newehy, M.; Mo, X. Electrospinning nanofiber scaffolds for soft and hard tissue regeneration. *J. Mater. Sci. Technol.* **2020**, *59*, 243−261.
(32) Yan, X.; Xiao, X.; Au, C.; Mathur, S.; Huang, L.; Wang, Y.; Zhang, Z.; Zhu, Z.; Kipper, M. J.; Tang, J.; Chen, J. Electrospinning nanofibers and nanomembranes for oil/water separation. *J. Mater. Chem. A* **2021**, *9* (38), 21659−21684.
(33) Kiselev, P.; Rosell-Llompart, J. Highly aligned electrospun nanofibers by elimination of the whipping motion. *J. Appl. Polym. Sci.* **2012**, *125* (3), 2433−2441.
(34) Xu, J.; Zhang, Y. Uniaxially well-aligned nanofiber arrays fabricated by electrospinning with a stable and low moving velocity jet. *Fibers Polym.* **2017**, *18* (11), 2146−2152.
(35) Yuan, H.; Zhao, S.; Tu, H.; Li, B.; Li, Q.; Feng, B.; Peng, H.; Zhang, Y. Stable jet electrospinning for easy fabrication of aligned ultrafine fibers. *J. Mater. Chem.* **2012**, *22* (37), 19634.
(36) Chen, S.; Ding, C.; Lin, Y.; Wu, X.; Yuan, W.; Meng, X.; Su, W.; Zhang, K. Q. SERS-active substrate assembled by Ag NW-embedded porous polystyrene fibers. *RSC Adv.* **2020**, *10* (37), 21845−21851.
(37) Langner, M.; Agarwal, S.; Baudler, A.; Schröder, U.; Greiner, A. Large Multipurpose Exceptionally Conductive Polymer Sponges Obtained by Efficient Wet-Chemical Metallization. *Adv. Funct. Mater.* **2015**, *25* (39), 6182−6188.
(38) Mendioroz, A.; Fuente-Dacal, R.; Apinaniz, E.; Salazar, A. Thermal diffusivity measurements of thin plates and filaments using lock-in thermography. *Rev. Sci. Instrum.* **2009**, *80* (7), 074904.
(39) Salazar, A.; Mendioroz, A.; Fuente, R. The strong influence of heat losses on the accurate measurement of thermal diffusivity using lock-in thermography. *Appl. Phys. Lett.* **2009**, *95* (12), 121905.
(40) Gao, Q.; Kopera, B. A. F.; Zhu, J.; Liao, X.; Gao, C.; Retsch, M.; Agarwal, S.; Greiner, A. Breathable and Flexible Polymer Membranes with Mechanoresponsive Electric Resistance. *Adv. Funct. Mater.* **2020**, *30* (26), 1907555.
(41) Persson, N. E.; McBride, M. A.; Grover, M. A.; Reichmanis, E. Automated Analysis of Orientational Order in Images of Fibrillar Materials. *Chem. Mater.* **2017**, *29* (1), 3−14.
(42) Reich, S.; Burgard, M.; Langner, M.; Jiang, S.; Wang, X.; Agarwal, S.; Ding, B.; Yu, J.; Greiner, A. Polymer nanofibre composite nonwovens with metal-like electrical conductivity. *Npj Flex. Electron.* **2018**, *2* (1), 5.
(43) Haynes, W. M.; Lide, D. R.; Bruno, T. J. *CRC Handbook of Chemistry and Physics*; CRC Press, 2016. .
(44) Cheng, Z.; Liu, L.; Xu, S.; Lu, M.; Wang, X. Temperature dependence of electrical and thermal conduction in single silver nanowire. *Sci. Rep.* **2015**, *5*, 10718.
(45) Zhao, Y.; Fitzgerald, M. L.; Tao, Y.; Pan, Z.; Sauti, G.; Xu, D.; Xu, Y. Q.; Li, D. Electrical and Thermal Transport through Silver Nanowires and Their Contacts: Effects of Elastic Stiffening. *Nano Lett.* **2020**, *20* (10), 7389−7396.
(46) Topsøe, H. *Geometric Factors in Four Point Resistivity Measurement; Bulletin No 472−13*; Haldor Topsøe, Semiconductor Division, Vedbæk, Denmark, 1966.

https://doi.org/10.1021/acsapm.5c03952
ACS Appl. Polym. Mater. 2026, 8, 1954−1963

Supporting Information

Thermal Transport in Polystyrene Nonwovens: Influence of Anisotropy, Structural Modification, and Functionalization

Ina Klein[1§], Sophie E. Fritze[2§], Alexander Berger[1], Holger Schmalz[2,3], Markus Retsch[1,3,4*], Andreas Greiner[2,3*]

[§] These authors contributed equally to this work

[1] Department of Chemistry, Physical Chemistry I, University of Bayreuth, 95447 Bayreuth, Germany

[2] Department of Chemistry, Macromolecular Chemistry II, University of Bayreuth, 95447 Bayreuth, Germany

[3] Bavarian Polymer Institute, University of Bayreuth, 95447 Bayreuth, Germany

[4] Bayreuth Center for Colloids and Interfaces, Bayreuther Institut für Makromolekülforschung, and Bavarian Center for Battery Technology (BayBatt) University of Bayreuth, 95447 Bayreuth, Germany

* Markus Retsch: markus.retsch@uni-bayreuth.de

* Andreas Greiner: greiner@uni-bayreuth.de

Table S1: Fiber diameter of the different (functionalized) PS nonwovens determined by evaluation of respective SEM images using the software *ImageJ* and the corresponding orientational order (S2D) parameters determined from microscopy images using the software *Mountainslab*.

Sample	**Diameter [µm]**	**Orientational order parameter S_{2D}**
PS random pressed	2.70 ± 0.45	0.19 ± 0.09
PS random annealed 3h	3.27 ± 0.64	0.21 ± 0.09
PS random annealed 24h	3.52 ± 0.92	0.27 ± 0.07
PS oriented pressed	2.78 ± 0.35	0.86 ± 0.04
PS oriented annealed 3h	4.87 ± 1.18	0.67 ± 0.10
PS oriented annealed 24h	4.70 ± 1.38	0.81 ± 0.04
PS SJES pressed	3.98 ± 0.49	0.95 ± 0.03
PS SJES annealed 3h	4.39 ± 0.43	0.87 ± 0.09
PS SJES annealed 24h	5.09 ± 0.57	0.89 ± 0.03

PS random AgNWs incorporated	2.06 ± 0.27	0.25 ± 0.16
PS oriented AgNWs incorporated	1.04 ± 0.18	0.58 ± 0.04
PS random copper coated	2.72 ± 0.32	0.10 ± 0.11
PS oriented copper coated	2.77 ± 0.31	0.77 ± 0.05

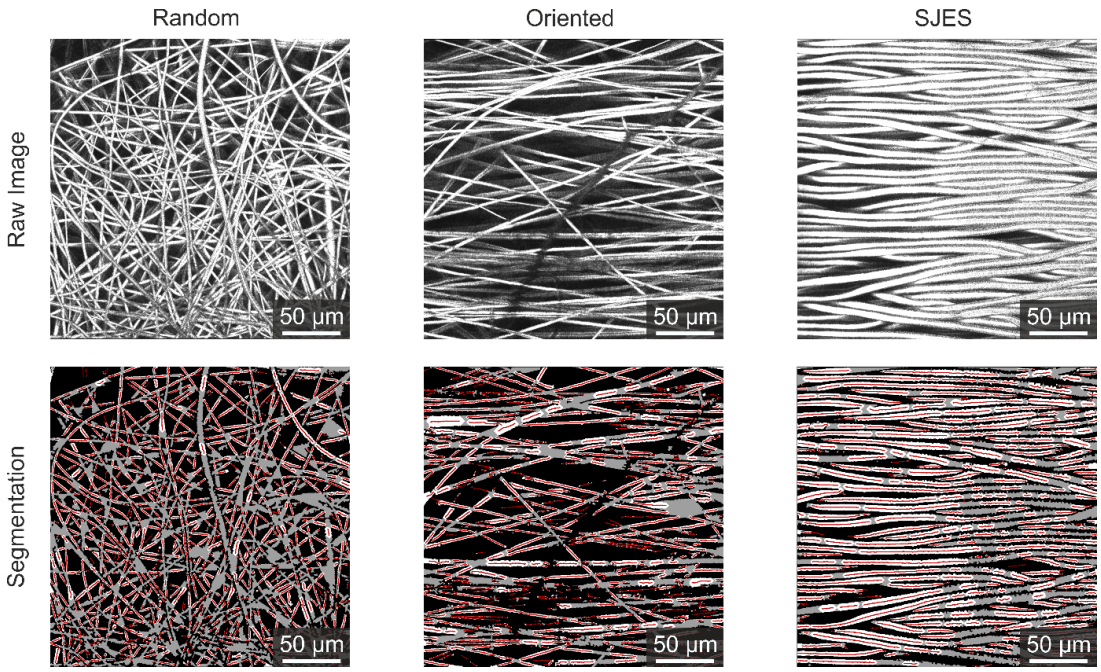

Figure S1: Exemplary optical microscopy images used to determine the orientational order parameters (S_{2D} parameters). Detection and segmentation of the fibers is performed with the software *MountainsLab*. Individual fiber segments are presented in white, each with a red line in its center showing the orientation (Scale bars are 50 µm).

After segmentation *MountainsLab* provides a table including the segment diameter *d*, length *l* and orientation of each segment. We calculated the weighing factor for each segment as in Formula S1.

$$\omega_i = \frac{l_i \, d_i}{\sum_{k=1}^{N} l_k \, d_k} \qquad \text{(S1)}$$

As angles between -90° and 90° are used for the calculation of the S_{2D} parameter the orientation of the sample under the light microscope can impact the results. To prevent this, each image was iteratively turned by subtracting the mean orientation angle from all fiber segment orientations and recalculating the mean orientation angle until the average orientation was 0°. The S_{2D} parameters are calculated for every image using Formula 1 presented in the main text. Per sample, ten microscopy images were used to obtain the average S_{2D} parameter and the corresponding standard deviation.

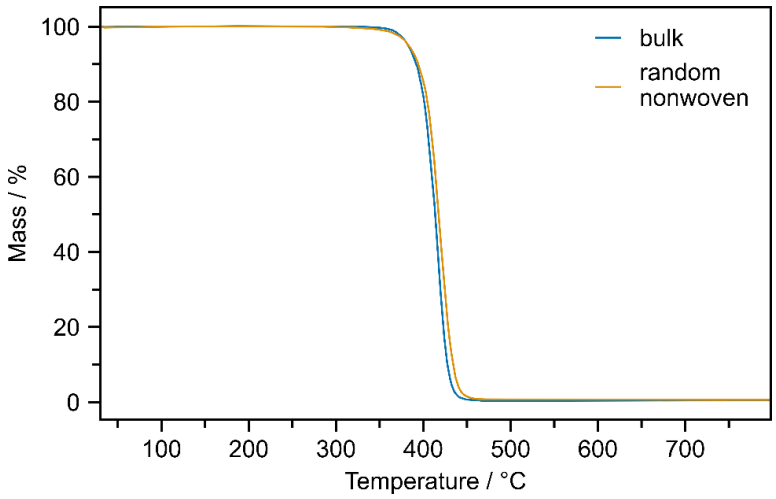

Figure S2: TGA of bulk PS (onset temperature at 398 °C) and random PS nonwoven (onset temperature at 401 °C), demonstrating thermal stability at the annealing temperature of 115 °C. There is no significant difference in thermal stability between the two sample types.

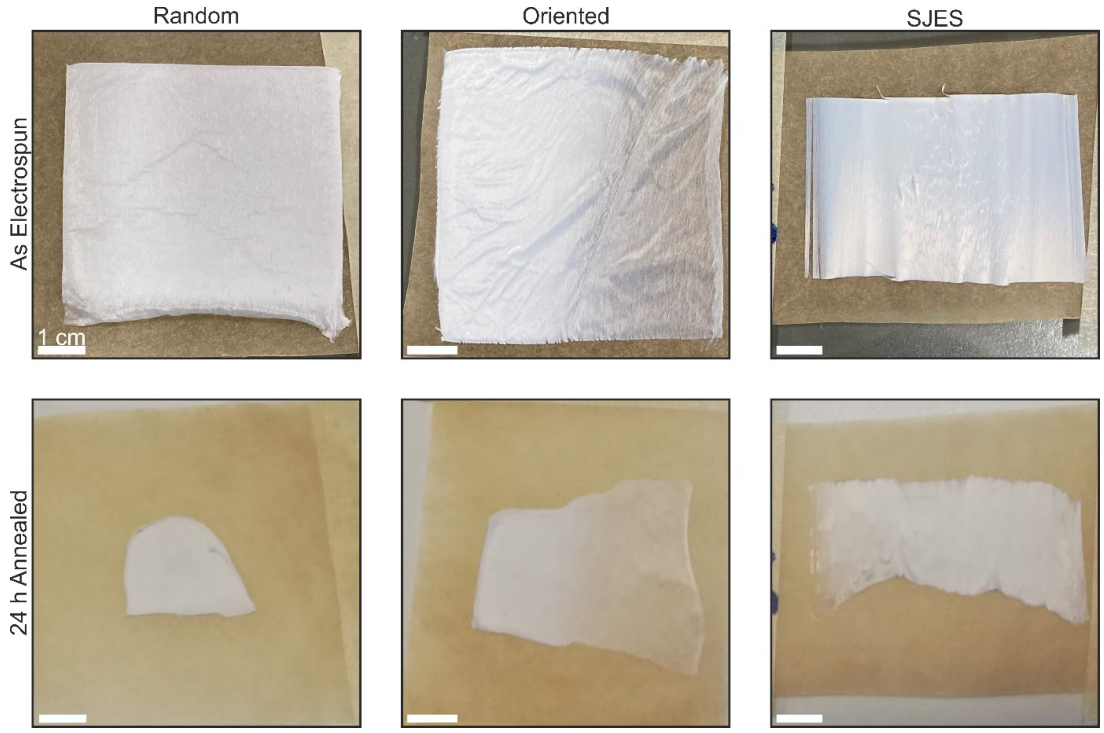

Figure S3: Pictures of the electrospun nonwovens with different degrees of orientation before and after annealing them for 24 h at 115 °C (Scale bars are 1 cm).

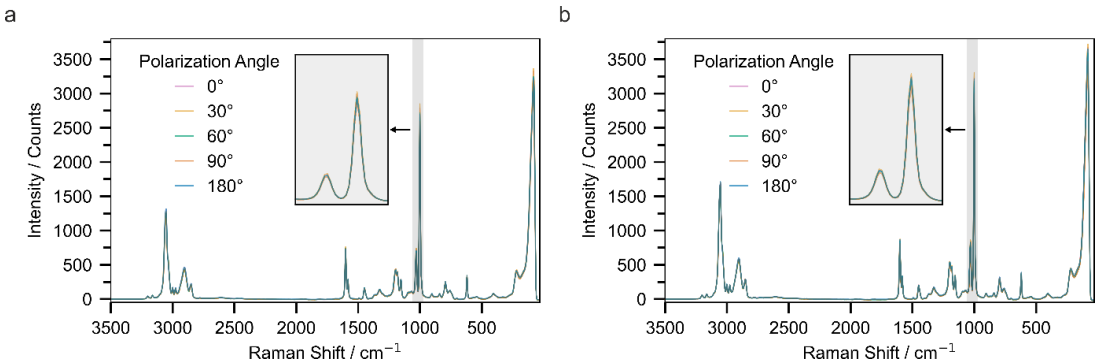

Figure S4: Raman spectra using polarized incident radiation with angles ranging from 0° to 180° of a) pressed SJES nonwoven and b) SJES nonwoven annealed at 115 °C for 3 h.

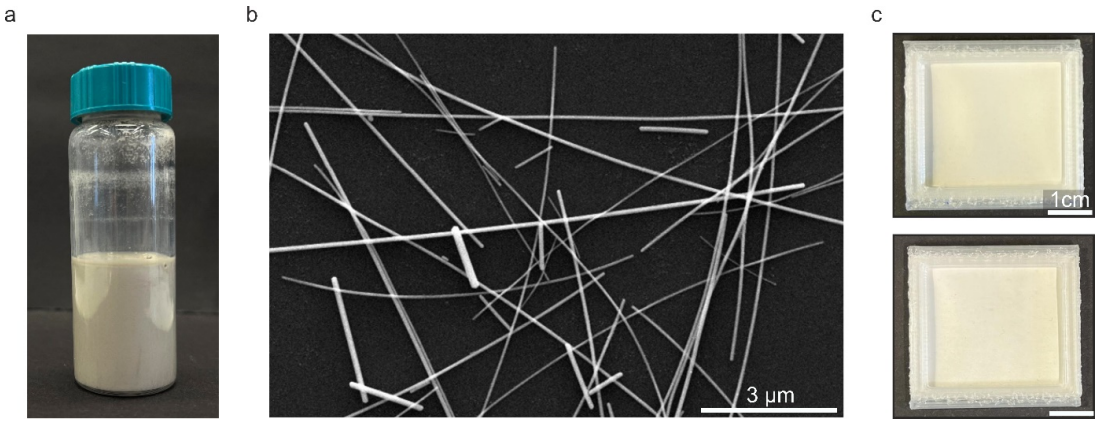

Figure S5: a) Picture of the silver nanowire dispersion (22 mg mL^{-1}). b) SEM image of silver nanowires used for the nonwoven functionalization. c) Picture of the random nonwoven (top) and oriented nonwoven (bottom) with incorporated silver nanowires (Scale bars are 1 cm).

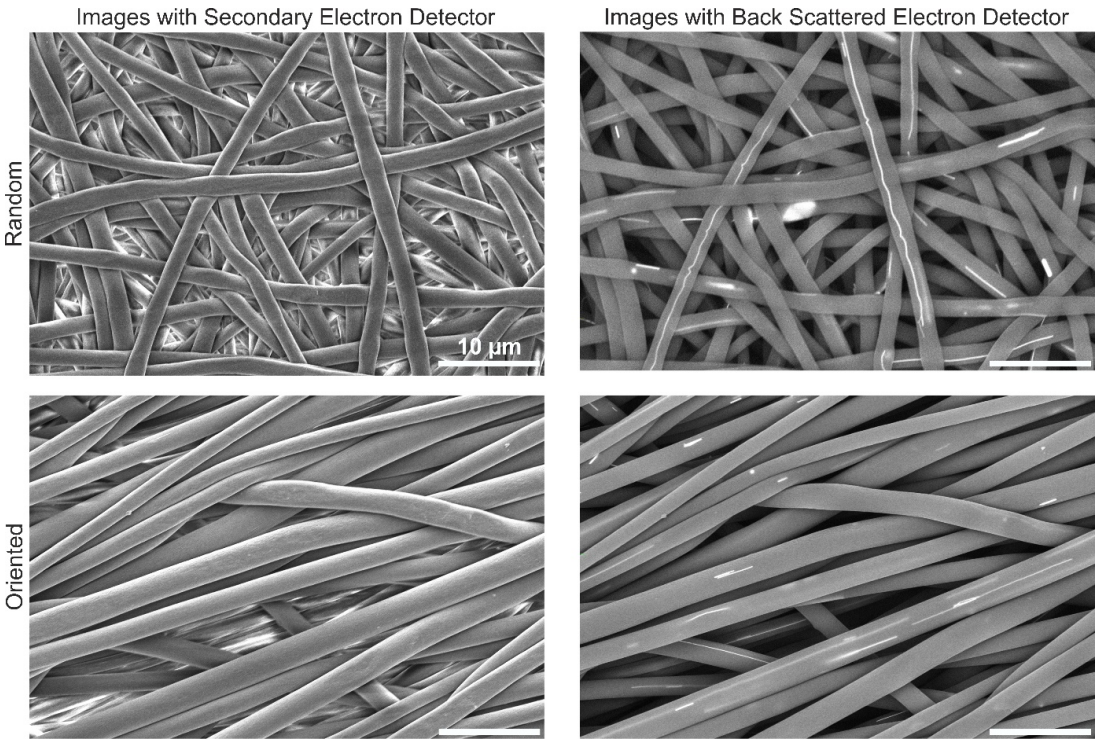

Figure S6: SEM images of nonwovens containing silver nanowires, captured using a secondary electron detector and a backscattered electron detector. The images confirm the incorporation of silver nanowires into the PS fibers (Scale bars are 10 µm).

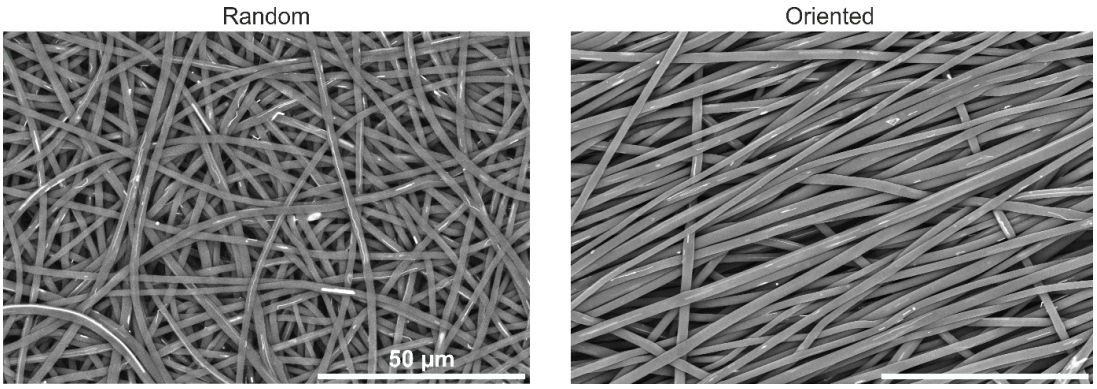

Figure S7: SEM images of nonwovens containing silver nanowires, captured using a backscattered electron detector. The images confirm the incorporation of silver nanowires into the PS fibers (Scale bars are 50 µm).

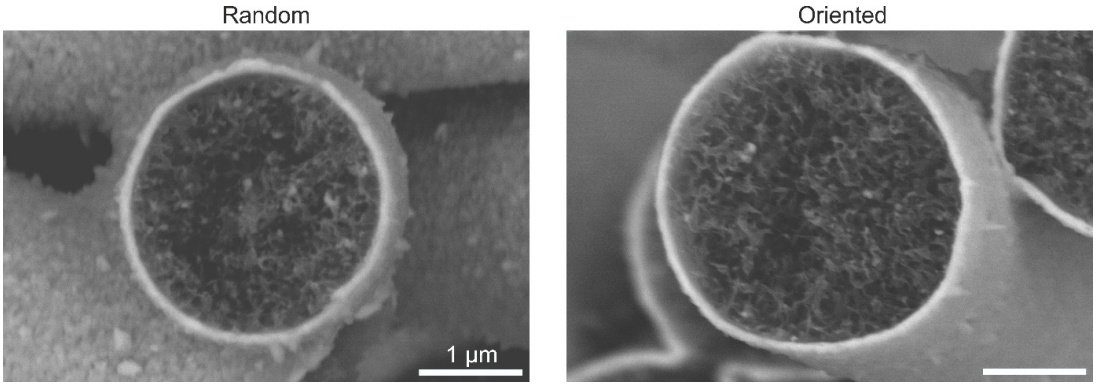

Figure S8: Cross section SEM images of the copper coated nonwovens obtained with a backscattered electron detector at high magnification (Scale bars are 1 µm).

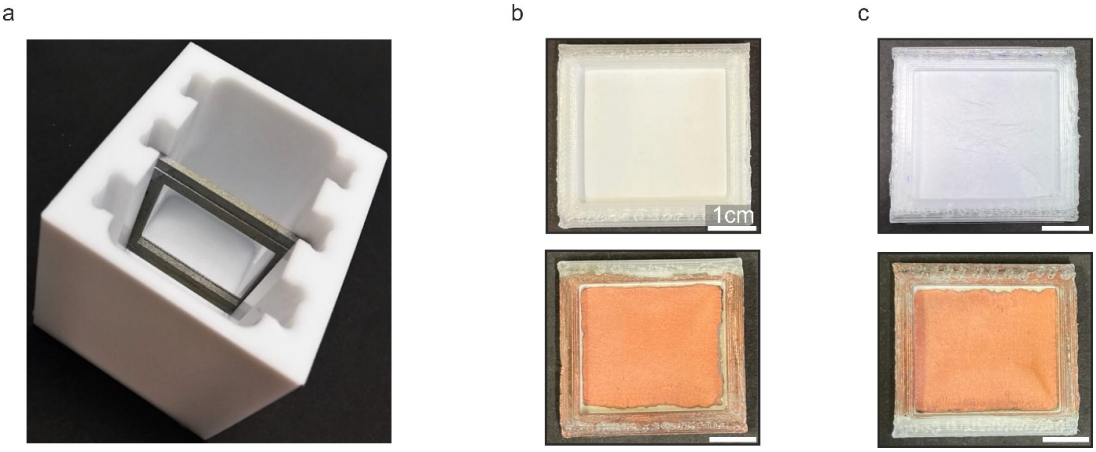

Figure S9: Pictures of a) the metallization bath used for the copper coating process of PS nonwovens, b) the random PS nonwoven, and c) the oriented PS nonwoven before and after copper coating (Scale bars are 1 cm).

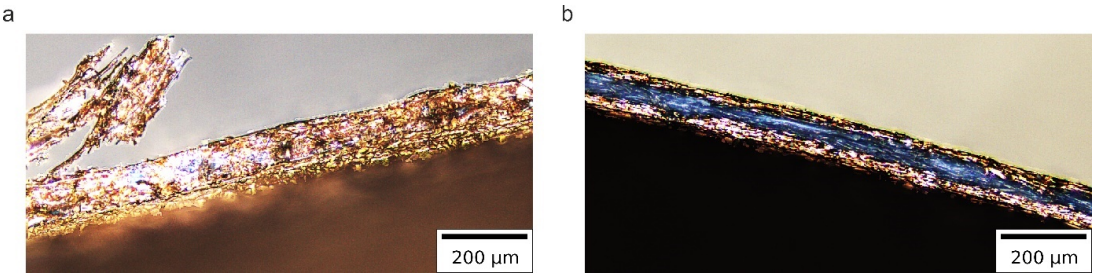

Figure S10: Optical microscopy cross-section images taken in reflection geometry of a) the random copper coated nonwoven, showing that the copper coating is present throughout the nonwoven and b) the oriented copper coated nonwoven, showing that the copper content is reduced towards the center of the sample (Scale bars are 200 µm).

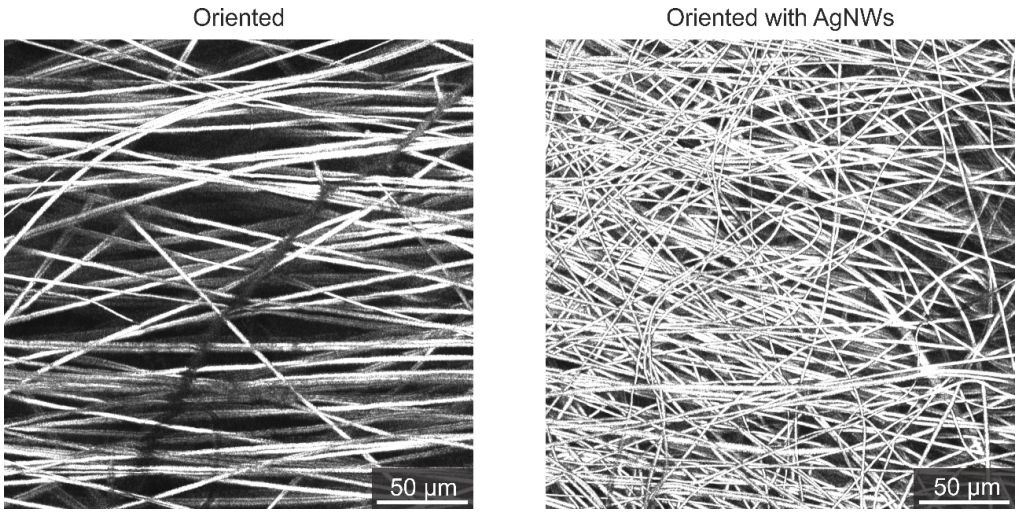

Figure S11: Exemplary optical microscopy images of an oriented nonwoven and an oriented nonwoven containing silver nanowires used to determine the S2D parameters (Scale bars are 50 µm).

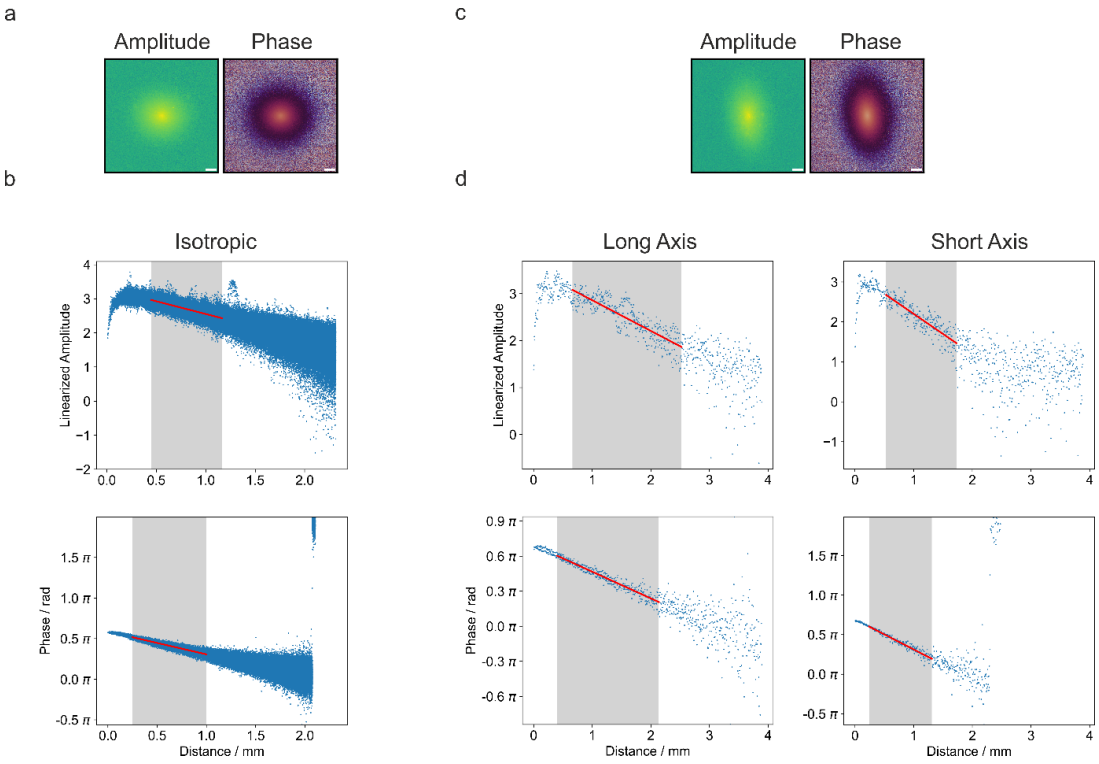

Figure S12: Exemplary Lock-In Thermography data of copper coated nonwovens to visualize the analysis difficulty. a) 2D data of the random nonwoven (Scale bars are 1 mm). b) Linearized 1D plots for the random nonwoven. c) 2D data of the oriented nonwoven (Scale bars are 1 mm). d) Linearized 1D plots for the oriented nonwoven in the preferred direction and in the cross-direction.

9

Do Nucleating Agents or Processing Methods Affect the Thermal Transport in RacoPP?

Ina Klein[1], Maria Ester Marroquin Lacayo[1], Thomas Blesch[2], Sabine Rosenfeldt[1], Patrick Länger[3], Klaus Kreger[2], Stefan Rettinger[1], Jürgen Senker[3,4,5], Hans-Werner Schmidt[2,4], Markus Retsch[1,4,5]

Published in *Journal of Polymer Science*, **2025**, *63*, 4516-4524.
Reproduced with permission from Wiley VCH.

[1] Department of Chemistry, Physical Chemistry I, University of Bayreuth, 95447 Bayreuth, Germany.
[2] Department of Chemistry, Macromolecular Chemistry II, University of Bayreuth, 95447 Bayreuth, Germany.
[3] Department of Chemistry, Inorganic Chemistry III, University of Bayreuth, 95447 Bayreuth, Germany.
[4] Bavarian Polymer Institute (BPI), Bayreuth Center of Colloids and Interfaces (BZKG), University of Bayreuth, 95447 Bayreuth, Germany.
[5] Bavarian Center for Battery Technology (BayBatt), University of Bayreuth, 95447 Bayreuth, Germany.

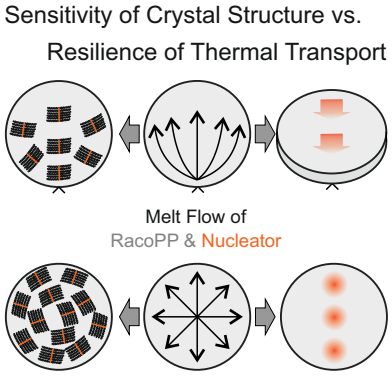

Journal of Polymer Science

WILEY

JOURNAL OF POLYMER SCIENCE

RESEARCH ARTICLE OPEN ACCESS

Do Nucleating Agents or Processing Methods Affect the Thermal Transport in RacoPP?

Ina Klein[1] | María Ester Marroquin Lacayo[1] | Thomas Blesch[2] | Sabine Rosenfeldt[1] | Patrick Länger[3] | Klaus Kreger[2] | Stefan Rettinger[1] | Jürgen Senker[3,4,5] | Hans-Werner Schmidt[2,4] | Markus Retsch[1,4,5]

[1]Department of Chemistry, Physical Chemistry I, University of Bayreuth, Bayreuth, Germany | [2]Department of Chemistry, Macromolecular Chemistry I, University of Bayreuth, Bayreuth, Germany | [3]Department of Chemistry, Inorganic Chemistry III, University of Bayreuth, Bayreuth, Germany | [4]Bavarian Polymer Institute (BPI), Bayreuth Center for Colloids and Interfaces, University of Bayreuth, Bayreuth, Germany | [5]Bavarian Center for Battery Technology (BayBatt), University of Bayreuth, Bayreuth, Germany

Correspondence: Markus Retsch (markus.retsch@uni-bayreuth.de)

Received: 19 November 2024 | **Revised:** 27 January 2025 | **Accepted:** 30 January 2025

Funding: This work was supported by Collaborative Research Centre 1585, Projects A04 and C05 of the German Research Foundation (grant number: 492723217).

Keywords: compression molding | injection molding | nucleating agent | polypropylene | thermal transport

ABSTRACT

Polypropylene (PP) homopolymers and copolymers play a pivotal role in the plastics industry. With applications spanning automotive components, electronic housings, construction materials, and food packaging, understanding their thermal transport properties is essential. This study investigates the impact of a highly efficient 1,3,5-benzenetrisamide (BTA) nucleator (N,N′,N″-tris(3-methylbutyl)benzene-1,3,5-tricarboxamide) on the thermal diffusivity of injection- and compression-molded propylene-ethylene random copolymer (racoPP). Results are compared with those for a less efficient BTA (N,N′,N″-tris(n-butyl) benzene-1,3,5-tricarboxamide) and a control sample without additives. We supplement our thermal characterizations with x-ray diffraction (XRD) and small-angle x-ray scattering (SAXS) analyses and demonstrate that the processing method and the presence of BTAs can impact the crystallinity and orientation of the PP lamellae. However, the thermal diffusivity of racoPP exhibits remarkable resilience to these changes, ensuring the consistent performance that is often required in industrial applications.

1 | Introduction

Polypropylene (PP) is one of the most widely applied plastics worldwide [1]. It shows low density, great mechanical properties, and thermal resistance at low costs. These properties strongly depend on the microstructure and morphology of the PP object, which can be controlled by the processing parameters and by the addition of suitable additives and fillers [1, 2]. Controlling and promoting the nucleation in PP and in related copolymers is used to reduce the cycle time during processing and to improve its mechanical and optical properties [3]. This includes the increase of flexural strength and modulus, tensile strength and modulus, impact resistance, rigidity, clarity, reduction of haze, and even the enhancement of charge-storage properties [4–9]. Injection molding represents one of the most applied industrial manufacturing methods for PP. The polymer is heated until melting and injected into a cold mold, where it solidifies into the shape of the mold [1, 10]. Thereby, the process parameters, such as temperature, shear force, cooling rate, and pressure, all affect the properties of the obtained PP product. Owing to the semicrystalline nature of iso-tactic PP (iPP), this includes the ratio of the crystal modifications (α, β, γ), the ratio of the amorphous to crystalline phase, the presence and size of three-dimensional spherulites, oriented lamellar crystallites, shish-kebab structures, and gradients and blends of such morphologies [2, 10–14]. Due to these numerous levers affecting the polymer's microstructure and thereby its properties, many papers address injection-molded

PP and, thereby, add another important aspect to the complex topic [8, 11, 13, 15–19]. Particularly, the temperature evolution upon cooling an iPP melt is critical for the crystal nucleation and crystal growth rate and, therefore, decisive for the crystallite microstructure [2, 10, 11]. Increasing the cooling rate, for instance via thermally conductive fillers, can significantly increase the number of nucleation sites [2, 10]. A similar effect can be achieved by adding nucleating agents to the polymer melt. The nucleators raise the crystallization temperature and accelerate crystal nucleation by providing numerous heterogeneous nucleation sites in the melt. This leads to smaller spherulite sizes [5–7, 19]. In addition to the nucleation via heterogeneous additives, shear can induce orientation-induced primary iPP nuclei. They lead to accelerated crystallization and oriented lamellar structures (kebab structures) perpendicular to the flow direction. Note that the primary nuclei may be long fibrillar extended chain crystals (shish structures), but they may also be small clusters of aligned chains. Hence, the evolution of shish structures is not necessary for the formation of oriented kebab structures. Furthermore, the extent of crystal orientation is dependent on factors such as the molecular weight distribution, the strain, and the shear rate [12].

1,3,5-Benzenetrisamide (BTA) derivatives represent an excellent and versatile family of nucleating agents. The good solubility of several BTA types in an iPP melt ensures a homogeneous distribution of the additive. Even at very low weight fractions, these additives can significantly enhance nucleation and induce high transparency and clarity of iPP [4, 7, 20–22]. Furthermore, depending on the chosen BTA, different crystal modifications of iPP can be selectively induced [20, 23]. Here, we focus specifically on their nucleation effect in a propylene-ethylene random copolymer (racoPP). RacoPPs contain a small amount of ethylene as a comonomer and can be regarded as iPP, with the comonomer acting as defects in the polymer chain sequence [24]. As a result, racoPPs have a lower melting point, higher transparency, and improved toughness compared with iPP, while supramolecular nucleating agents, such as distinct BTAs, remain similarly effective [1, 21]. As the polymer melt cools, the BTA molecules crystallize into finely dispersed, highly ordered fibrils. Based on lattice matching, BTA crystals serve as efficient nucleation sites for the racoPP, fostering epitaxial growth [21, 22, 25, 26]. Consequently, BTAs represent a highly interesting additive in various applications, and their influence on the melt temperature, optical, and mechanical properties is intensively studied, along with desired effects. The influence of the PP microstructure on the thermal conductivity of the resulting macroscopic objects has, however, been scarcely studied up to now. The widespread utilization of PP copolymers in electronic housings, automotive components, or food packaging necessitates an understanding of its thermal transport properties. One must be aware that processing, post-processing, and the addition of nucleating agents may impact the thermal transport characteristics. Herein, it is our objective to provide clarity on this matter. We investigate how the presence of N,N′,N″-tris(isopentyl)benzene-1,3,5-tricarboxamide (iPe-BTA), which is known to efficiently nucleate iPP, affects the thermal diffusivity of injection-molded racoPP. It is compared with N,N′,N″-tris(n-butyl)benzene-1,3,5-tricarboxamide (nBu-BTA), a structurally similar BTA additive that has a low nucleation capability, and with no additive at all [20, 21]. The chemical structure of the chosen BTAs is shown in Figure 1a. Moreover, we explore the influence of further processing by pressing the injection-molded samples into thin films and subsequently compare the thermal diffusivities once again. These assessments are supported by structural analyses to unveil the potential presence of an underlying structure–property relationship.

2 | Results and Discussion

2.1 | Injection-Molded Samples

To comprehensively study the influence of the BTAs on the racoPP morphology, a series of injection-molded samples were prepared with a diameter of approximately 27.0 mm and a thickness of about 1.1 mm. Three BTA concentrations were selected: 0.5 wt%, 0.1 wt%, and 0.05 wt%, which ensure a sufficient amount of BTA for the formation of nanofibrils in the racoPP while maintaining good processability for injection-molding. X-ray diffraction (XRD) analysis was performed to assess the impact of the BTAs on the polymer's crystallinity. The results for a concentration of 0.5 wt% are exemplarily shown in Figure 1b. Although the difference in the calculated crystallinities is small, and the absolute values should be interpreted with caution, their comparison follows the expected trend: RacoPP with iPe-BTA exhibits the highest relative crystallinity (46%), followed by racoPP containing nBu-BTA (41%), and finally neat racoPP (38%) (Figure S1). The reflections below 10°, visible for the samples containing nBu-BTA or iPe-BTA, correspond to the most intense reflections of BTA nanocrystallites. They demonstrate that the BTA molecules are self-assembled rather than being molecularly dispersed within the polymer. These supramolecular nano-objects of either BTA type function as nucleation sites in the polymer melt, hereby lowering the energy barrier for the polymer nucleation [21, 22]. The differences between the two types of BTA may be reasoned by a superior nucleation performance of iPe-BTA compared with nBu-BTA. We confirm this by studying the crystallization behavior of racoPP in the presence of the additives, showing a higher crystallization temperature of racoPP with iPe-BTA than with nBu-BTA (Figure S3). It is generally acknowledged that lattice matching is a prerequisite for the nucleation capability of additives; thus, we can attribute the difference in nucleation performance to a better lattice match of iPe-BTA with racoPP than nBu-BTA with racoPP [21, 26].

Small-angle x-ray scattering (SAXS) measurements of injection-molded samples supplement the data on the Ångström range by the nanometer length scale. Figure 1c shows the SAXS patterns of three injection-molded racoPP samples with different concentrations of iPe-BTA. Hereby, we distinguish three sample positions, which were exposed to different shear rates during processing. “top” represents a point in the top-third of the sample that is furthest away from the inlet where the material is injected during processing. “middle” represents the center point of the circular sample and “bottom” is in the center of the bottom-third, closest to the inlet. All samples and all sample positions show a pronounced anisotropy in the SAXS pattern, characterized by broad meridional maxima. During injection-molding the BTAs form thin columnar structures, which are oriented in the direction of the flow. These function as nucleation sites for epitaxial growth of racoPP [22, 25]. As a result, kebab structures with

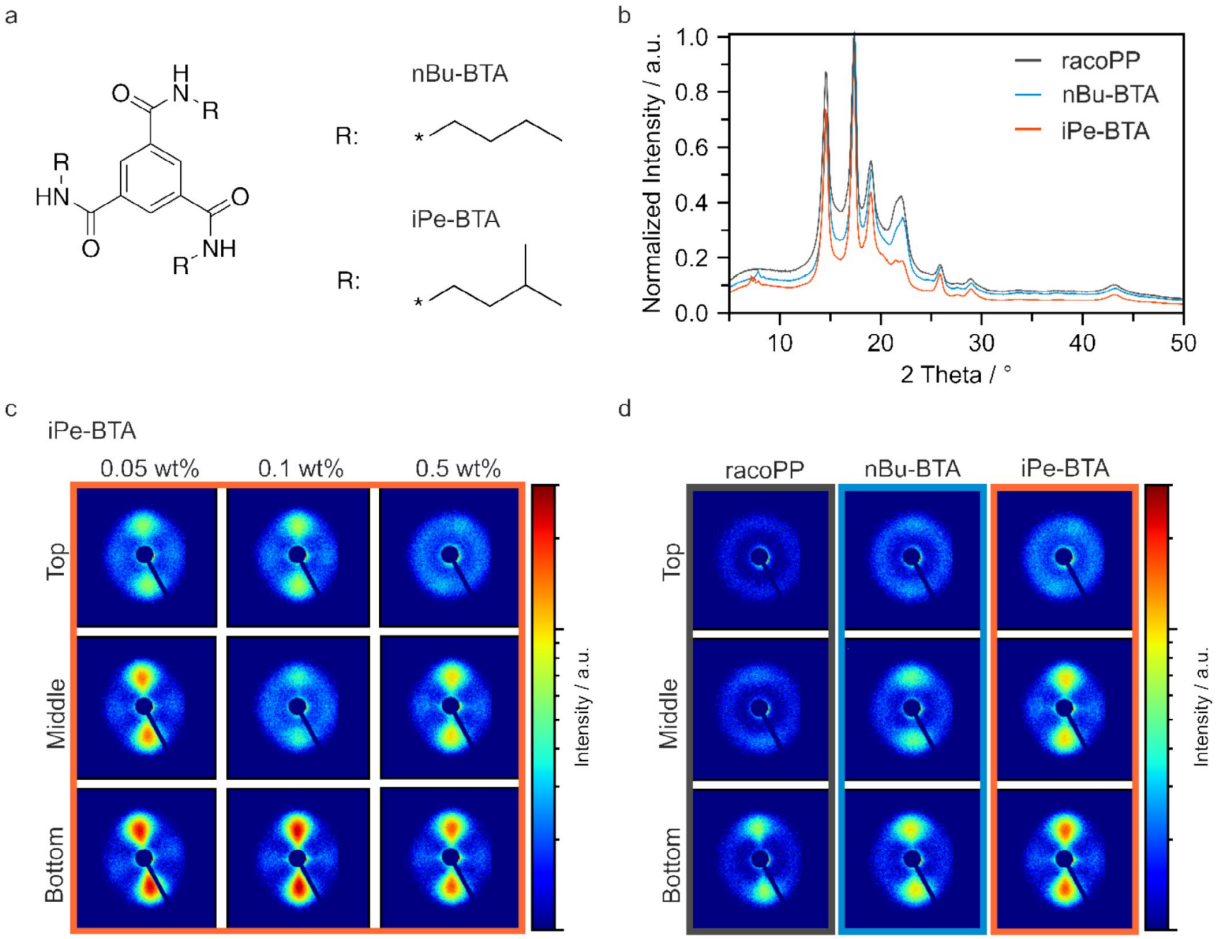

FIGURE 1 | (a) Molecular structure of the utilized nBu-BTA and iPe-BTA. (b) XRD of injection-molded neat racoPP, racoPP with 0.5 wt% nBu-BTA and with 0.5 wt% iPe-BTA. Intensities are normalized to the highest peak. (c) 2D SAXS patterns of injection-molded racoPP with variation in iPe-BTA content and sample position (with "top" furthest from the inlet, "bottom" closest to the inlet and "middle" in between). (d) 2D SAXS patterns of injection-molded neat racoPP, racoPP with 0.5 wt% nBu-BTA and with 0.5 wt% iPe-BTA at different sample positions. The colors are crucial for displaying the results, especially in c and d, to visualize differences in the SAXS patterns. The colors in b and the frames in c and d help to distinguish the sample types.

an orientation perpendicular to the flow direction evolve, which is mirrored in the dumbbell-like intensity distribution of the SAXS patterns. The meridional maxima are most pronounced at positions closest to the inlet for all three concentrations. As the distance increases, their distinctiveness diminishes, giving rise to a more circular intensity distribution. The concentration of 0.1 wt% iPe-BTA initially appears to be an exception, as the top position exhibits a more anisotropic pattern compared with the middle position. However, this initial impression does not hold true. A more detailed examination at various positions across the injection-molded racoPP sample with 0.1 wt% iPe-BTA reveals a general increase in the azimuthal intensity distribution with growing distance from the inlet (Figure S4). Consequently, the deviation observed at the middle position in Figure 1c is likely attributable to a more amorphous region of the sample being probed by the x-ray, which reduces the signal intensity at this specific position and gives the misleading appearance of an outlier. A slightly higher crystallinity at the bottom of the sample (48% for 0.5 wt% iPe-BTA) compared with the top (45% for 0.5 wt% iPe-BTA) implies a higher concentration of orientable lamellar structures near the inlet. More importantly, higher shear flow near the inlet enhances the orientation of the fibrillar nucleation sites. Therefore, with increasing proximity to the inlet, a larger fraction of the existing lamellar crystallites has a preferred orientation. Comparing the different concentrations at the same measurement positions (excluding the apparent outlier) reveals that all samples produce similarly anisotropic patterns. In the case of 0.5 wt%, the absolute scattering intensity is slightly reduced. We do not attribute this observation to the degree of crystallinity, as the values for the samples with 0.05 wt%, 0.1 wt%, and 0.5 wt% iPe-BTA are comparable, at 44%, 46%, and 46%, respectively. Therefore, slight variations in the specimen thickness, the instrumental setting, or the scattering contrast might be the reason for the reduced scattering intensity at 0.5 wt%.

In Figure 1d the patterns of neat racoPP are compared with those containing 0.5 wt% BTA. The results for neat racoPP show that

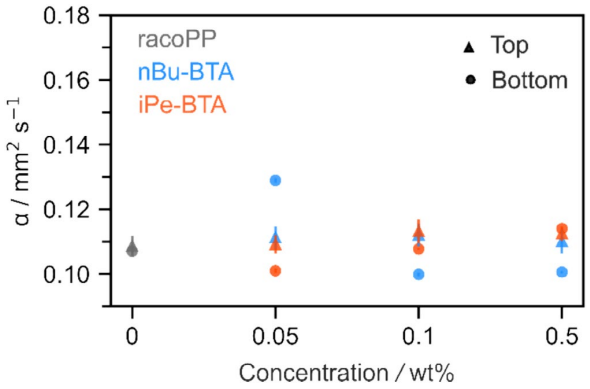

FIGURE 2 | Thermal diffusivity α of an injection-molded neat racoPP specimen and racoPP specimens with varying content of nBu-BTA and iPe-BTA, obtained by LFA. Measurements are performed on cylinders measuring 1 cm in diameter, cut from the top and bottom halves of the original injection-molded samples.

anisotropy is not solely based on the presence of BTA, but the BTA addition merely enhances the orientation of PP crystallites. Especially, the SAXS pattern obtained from the bottom position exhibits reflexes of greater intensity along the meridional direction, suggesting that the lamellar PP crystallites have grown in the perpendicular flow direction. This can be attributed to the alignment of chain segments in the direction of the flow, leading to the formation of primary nuclei. The absence of a horizontal streak indicates that these nuclei are not long fibrillar shish crystals; instead, they likely represent smaller clusters of aligned chains. Lamellar PP structures grow perpendicularly from these oriented nuclei in a secondary crystallization stage [12]. Nevertheless, this orientation of lamellar PP structures is more dominant when a nucleating agent is added to the racoPP melt. The nBu- and iPe-BTA both lead to meridional maxima, which are clearly visible for all measurement positions. The sample containing iPe-BTA leads to the most pronounced high-intensity reflexes at the bottom and middle sample positions. This observation is attributed to the superior nucleation capability of iPe-BTA compared with nBu-BTA, as evidenced by

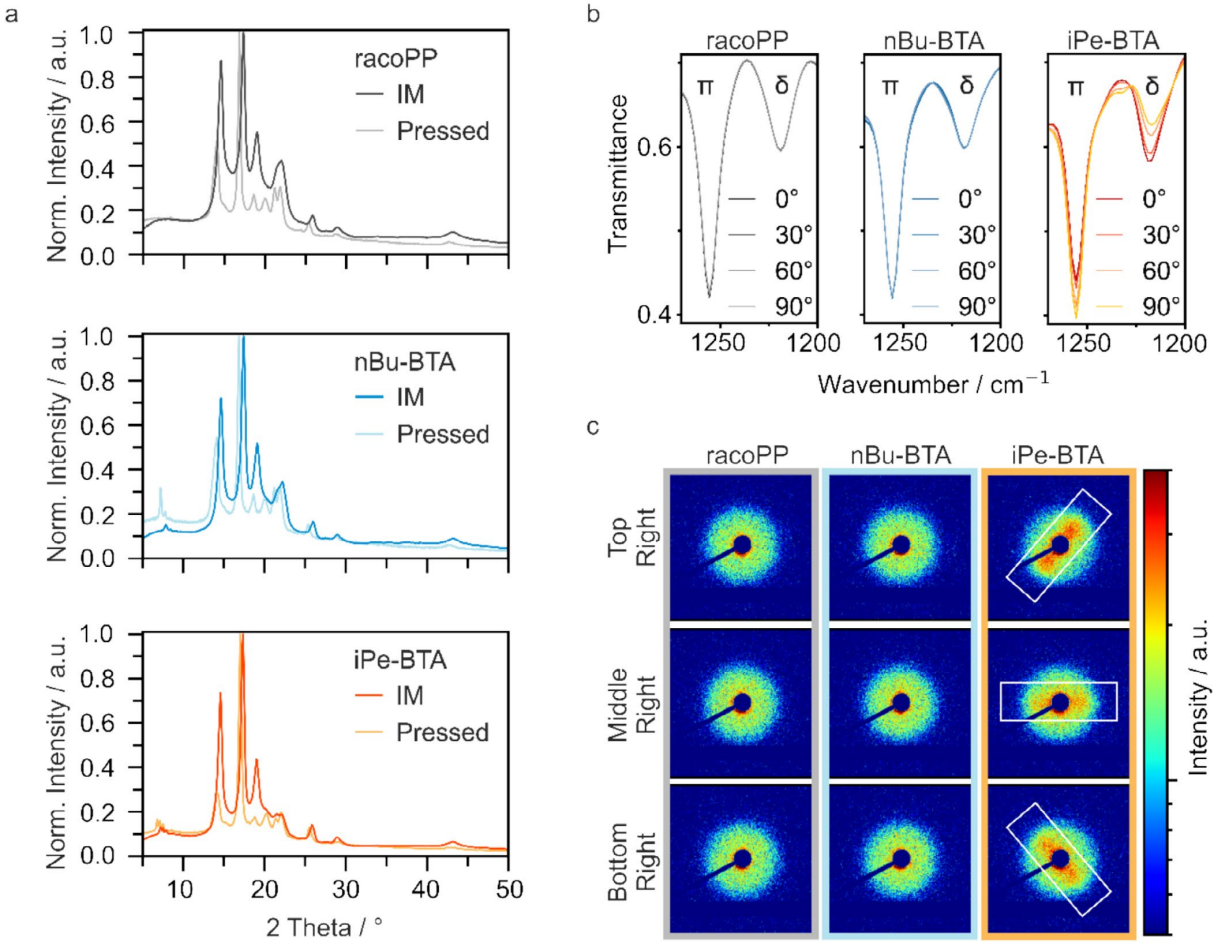

FIGURE 3 | Structural characterization of neat racoPP (gray), racoPP with 0.5 wt% nBu-BTA (blue) and racoPP with 0.5 wt% iPe-BTA (orange). (a) XRD patterns comparing the injection-molded and compression-molded samples. Intensities are normalized to the highest peaks. (b) IR spectra of the compression-molded samples at the bottom-middle position using polarized incident IR radiation. (c) 2D SAXS patterns of the compression-molded samples at the designated positions (white boxes indicating the orientation of intensity maxima).

the higher crystallization temperature of racoPP with iPe-BTA versus nBu-BTA (Figure S3). In summary, the lamellar polymer structures in injection-molded racoPP are oriented perpendicularly to the flow direction. This orientation and its extent, however, depend on the position within the sample and the addition or omission of a BTA nucleating agent.

We verified whether the structural differences between the sample positions and the sample types affect the through-plane thermal diffusivity, using light flash analysis (LFA). Figure 2 shows the obtained results for cylindrical samples with a diameter of 1 cm obtained from the top and bottom halves of each injection-molded specimen.

Comparing the values for the top and bottom of the samples, no correlation between thermal diffusivity and specimen position can be found, although SAXS determined differences in structural anisotropy. The reason for this could be that the observed structural anisotropy reflects an in-plane crystallite orientation, whereas LFA probes the through-plane thermal diffusivity of the samples perpendicular to the flow direction during injection molding. Also, there is no discernible trend in thermal diffusivity with varying BTA concentrations. This aligns with the consistency observed in the XRD measurements conducted across different BTA concentrations (Figure S2). The variations in thermal diffusivity among neat racoPP, racoPP with 0.5 wt% nBu-BTA, and racoPP with 0.5 wt% iPe-BTA are also subtle, below 0.04 $mm^2 s^{-1}$, despite the differences in crystallinity. It appears that these differences are not sufficient to induce notable changes in through-plane thermal transport. We suspect that the amorphous components predominantly govern phonon propagation and, therefore, limit thermal diffusivity, even for samples with high crystallinity [27]. All in all, through-plane thermal diffusivity of the injection-molded samples is independent of factors such as sample position, BTA concentration, or BTA type.

2.2 | Compression-Molded Samples

To obtain thin films from the injection-molded specimens, we performed compression molding at a temperature of 180°C, which is well above the melting point of racoPP. After gradually cooling the samples to 90°C under pressure, films with a thickness of approximately 0.1 mm were obtained. Infrared (IR) spectroscopy, XRD, and SAXS measurements were conducted to analyze the effect of the pressing process on the racoPP structure (Figure 3).

Figure 3a compares the XRD results before and after compression molding of the neat racoPP, racoPP with 0.5 wt% nBu-BTA, and racoPP with 0.5 wt% iPe-BTA. Due to the slower cooling rate of the pressed specimens in contrast to the injection-molded samples, all thin films exhibit an increased degree of crystallinity compared with their injection-molded counterparts. For racoPP with iPe-BTA and neat racoPP, the crystallinities increased to 57% and 54%, respectively, which can be well explained by enhanced crystal growth for slow cooling rates. The crystallinity of compression-molded racoPP with nBu-BTA lies beneath those values at 50%. In addition, the presence of an additional reflex at about 20° shows the formation of a certain fraction of the γ modification of racoPP, caused by the shear stress and low cooling rate during compression molding [28]. The persistence of the peaks below 10° for the samples containing a BTA nucleating agent verifies that the BTA crystal structures are present within these compression-molded samples.

Polarized IR spectroscopy offers insights into the orientation of the polymer chains. Since specific vibrational modes of PP are polarized, the absorption of the corresponding frequencies relies on the polarization angle of the incident radiation [29]. The full spectra of all measured samples and sample positions with light polarized by 0°, 30°, 60°, and 90° are provided in Figure S5. The IR spectra of neat racoPP and racoPP containing 0.5 wt% nBu-BTA do not show a dependency on the polarization angle of incident radiation (Figure 3b). This points towards an isotropic orientation of the PP chains in these samples. In the spectra of racoPP with 0.5 wt% iPe-BTA, slight differences can be seen when utilizing light polarizations ranging from 0° to 90°. As the polarization angle of the incident light decreases, the absorption of parallel-polarized frequencies (π) increases, whereas the absorption of perpendicular-polarized frequencies (δ) decreases. Although these changes are subtle, the example bands in Figure 3b, corresponding to the perpendicular-polarized mode at 1218 cm^{-1} and the parallel-polarized mode at 1256 cm^{-1}, demonstrate the dependence on incident light polarization [29]. Similar observations are noted across the other sample positions of racoPP containing 0.5 wt% iPe-BTA. This result indicates that the presence of iPe-BTA leads to a weak but observable preference for the orientation of the PP chains and thus of the lamellar crystallites. IR spectroscopy is supplemented by 2D SAXS at 11 measurement positions per sample, evenly distributed to cover the top, center, and bottom of the specimen. In Figure 3c, a representative selection of three measurement points taken from the right-hand side of each sample is shown (top-right, middle-right, bottom-right). Details on the locations of the measurement points and the SAXS patterns for all sample positions are provided inFigures S6 and S7. The 2D SAXS data corresponding to neat racoPP and racoPP with nBu-BTA show consistent intensity maxima across the entire azimuthal angle range, resulting in a circular SAXS pattern. This demonstrates an isotropic distribution of the lamellar crystallites, which is consistent with the isotropic orientation of the PP chains revealed by IR spectroscopy. Although the PP chains are aligned within the individual crystallites, the crystallites themselves are small relative to the area analyzed by IR spectroscopy and are oriented randomly. This results in an overall appearance of isotropic PP chain orientation when examined using IR spectroscopy. As discussed, the XRD data show crystalline nBu-BTA after pressing the samples. However, the preferential spatial orientation of the PP crystallites was lost during the compression-molding step. Several possible reasons must be considered: Either the nBu-BTA assemblies are not aligned during compression molding, or the nBu-BTA assemblies are oriented, but the supramolecular additive does not dominate the nucleation process. Looking at the iPe-BTA, we may gain some clues on the most relevant contribution to this loss of orientation. The measurements conducted on racoPP with 0.5 wt% iPe-BTA reveal broad meridional maxima, being distinctly different from the neat racoPP and the case of nBu-BTA. These results are consistent with the IR spectroscopic data. Considering the similarity between nBu-BTA and iPe-BTA in inducing crystallite orientation within the injection-molded samples, no difference in the orientation of the supramolecular

assemblies consisting of nBu-BTA or iPe-BTA is expected in the compression-molded specimens. However, the cooling kinetics is much slower in this case, allowing for significant differences in the nucleation and growth mechanism of racoPP. Since nBu-BTA is a less effective nucleating agent for PP and shear is absent during polymer crystallization, we suspect that the intrinsic self-nucleation of racoPP plays a dominant role [20, 21]. This leads to randomly oriented crystallites and competes with the nBu-BTA nucleation sites, leading to an isotropic SAXS pattern.

The orientations of the dumbbell-like maxima determined for racoPP with 0.5 wt% iPe-BTA are highlighted by white rectangles (Figure 3c). They are all oriented perpendicularly to the sample edge, indicating a respective coplanar orientation of the PP lamellae. This result is attributed to the outward flow of the PP melt during the pressing process. The flow profile orients the BTA fibrils outwards to the center. As the lamellae grow perpendicularly to the BTA nuclei, they result in a coplanar arrangement with respect to the sample edge, which we observe in the SAXS patterns.

The low thickness of the samples allows measuring the in-plane thermal diffusivities using lock-in thermography (LIT). This technique is based on periodic heating of the thin film using a focused point laser, while the temperature distribution is monitored with an IR camera. Fourier Transformation is applied, and the obtained amplitude and phase data are linearized relative to the distance from the center of the heat source. The thermal diffusivity is then calculated using the so-called slope method [30, 31]. The compression-molded racoPP films without BTA, with 0.5 wt% nBu-BTA, and with 0.5 wt% iPe-BTA are measured in the bottom third, middle third, and top third of the samples. All measurements yield an isotropic amplitude and phase signal, as exemplified by the bottom segment of the racoPP sample containing 0.5 wt% iPe-BTA (Figure 4a). This shows that the preferential orientation of lamellar structures, as confirmed by 2D SAXS, does not result in anisotropic thermal transport. Amorphous regions between the crystalline PP lamellae act as a bottleneck for thermal transport [27]. Apparently, even for high crystallinities, amorphous regions persist in all directions and uniformly limit phonon propagation. Within the boundaries of the processing parameters explored in this study, processing racoPP with or without a nucleating agent does not result in anisotropic heat transport.

In Figure 4b the obtained thermal diffusivity values are presented. Given that structural anisotropy does not dictate a preferred direction for heat transport, it is unsurprising that the diffusivity remains consistent across different sample positions. Slightly elevated values are observed in the sample containing 0.5 wt% iPe-BTA compared to those with nBu-BTA or neat racoPP. However, the difference is too marginal to be deemed significant. Overall, a consistent thermal diffusivity is apparent across variations in nucleating agent and sample position.

Careful consideration is needed when comparing the through-plane thermal diffusivity obtained by LFA with the in-plane thermal diffusivity measured via LIT, as these methods are inherently based on different measurement principles. Despite the limitations of LFA to the thick injection-molded specimens and LIT to thin films, the ability to measure both provides valuable insights. It is notable that the thermal diffusivity of the injection-molded samples is slightly lower than the thermal diffusivity of the pressed samples. This may be attributed to the higher crystallinity of the compression molded (50%–57%) compared with the injection-molded samples (38%–46%), but may also be reasoned by the inherent differences of the measurement techniques. More importantly, it is evident that the results of all performed thermal diffusivity measurements lay within the small range of 0.10–0.15 $mm^2 s^{-1}$. Taking the heat capacity and density of racoPP into account, this leads to thermal conduction values between 0.15 and 0.22 $W (m K)^{-1}$, regardless of the processing or the addition of BTA. Furthermore, the structural anisotropy, driven by the in-plane orientation preference of the PP lamellae, is not reflected in either the through-plane or in-plane thermal transport direction. This can be attributed to the amorphous regions, which uniformly limit the phonon propagation and, therefore, function as bottlenecks for thermal transport [27]. For industrial applications of racoPP, this resilience of thermal transport represents a practical advantage. Whether the material is injection-molded, pressed into thin films, or whether BTAs are added to alter optical and mechanical properties, there is no need to be concerned about a preferred direction of heat

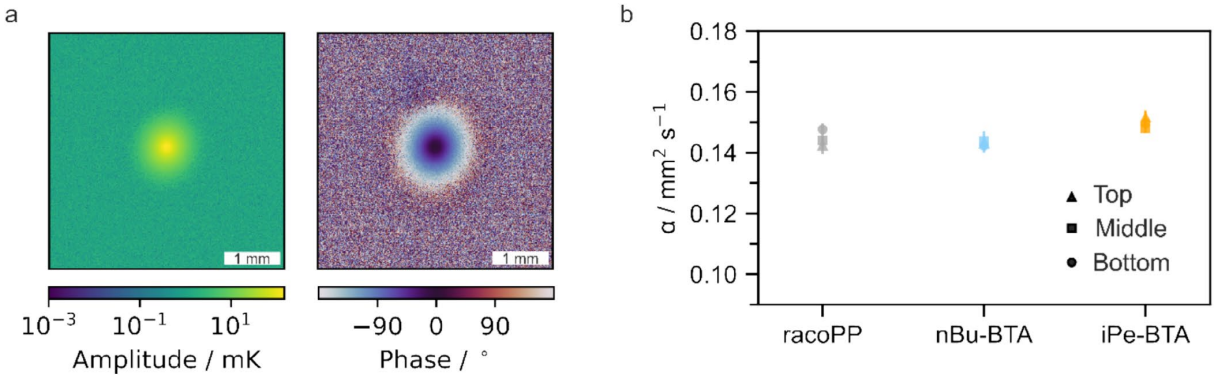

FIGURE 4 | LIT of compression-molded samples with a thickness of 0.1 mm. (a) Amplitude and phase signal obtained for compression-molded racoPP containing 0.5 wt% iPe-BTA. (b) Thermal diffusivity α of an injection-molded neat racoPP specimen and racoPP specimens with 0.5 wt% nBu-BTA and 0.5 wt% iPe-BTA. Five locations on each sample part (top, middle, and bottom) were probed.

transport or significant changes in the magnitude of thermal conduction.

3 | Conclusion

The impact of BTA additives on the thermal diffusivity of racoPP was assessed. Hereby, neat racoPP was compared with racoPP containing the efficient nucleating agent iPe-BTA and racoPP containing the less efficient nucleating agent nBu-BTA. The specimens were additionally classified into injection-molded and compression-molded samples to analyze potential processing effects. Structural information was obtained using XRD, SAXS, and IR spectroscopy. The results demonstrate that the crystal structure of racoPP is notably influenced by both processing method and the presence of BTAs. Differences in crystallinity and orientation of the PP lamellae were determined. On the contrary, the thermal diffusivity of racoPP exhibits remarkable resilience to such changes. Although it limits the ability to easily tune thermal transport, it also ensures the consistent performance that is often required in industrial applications.

4 | Experimental

4.1 | Sample Preparations

N,N′,N″-tris(3-methylbutyl)benzene-1,3,5-tricarboxamide (iPe-BTA) and N,N′,N″-tris(n-butyl) benzene-1,3,5-tricarboxamide (nBu-BTA) were synthesized and characterized as described previously [32]. *RD208CF* (Borealis AG), a random polypropylene copolymer (racoPP), was obtained as a fine powder and used as received. Two powder masterbatches containing 2 wt% of the supramolecular additives were prepared by carefully mixing 23.52 g of the racoPP with 0.48 g of the respective additive in a mortar.

Compounding was carried out at 230°C with a corotating twin-screw microcompounder (*Xplore 15 mL*, [*DSM*]) under nitrogen atmosphere at a residence time of 5 min and a rotational speed of 40 rpm. Three different concentrations of each of the supramolecular additives in racoPP (0.5, 0.1, and 0.05 wt.%) were achieved by a dilution series. In the first step of this dilution series, 12.5 g of a master batch with a concentration of 2.0 wt.% of the additive was compounded until a homogeneous polymer melt was obtained. After discharging the polymer melt, approximately 4.49 g of the molten polymer-additive mixture remained in the compounder, which was then diluted to the selected concentration by adding a corresponding amount of neat racoPP.

Injection molding was carried out using a microinjection-molding machine, *Xplore 12 mL* (*DSM*). The barrel temperature of the injection-molding unit was set to 230°C. The homogeneous polymer melt was transferred from the compounder to the microinjection-molding machine and then injected into a polished mold at an injection pressure of 6 bar for the duration of 20 s, resulting in round-shaped platelets with a diameter of 27 mm and a thickness of 1.1 mm. For each polymer-additive concentration, about five round specimens were obtained. Several neat racoPP round specimens were produced in the same way and used as references.

For the thin film preparation, we selected injection-molded racoPP specimens with additive concentrations of 0.05 wt%, 0.1 wt%, and 0.5 wt% and a neat racoPP specimen as a reference. To produce homogeneous thin films, an injection-molded platelet was placed in the center of a Teflon spacer with a diameter of 90 mm and a thickness of 0.1 mm and sandwiched between two Kapton foils. The sandwich was placed in a two-column lab press (*PW 20 H HKP300-ø165*, *PO Weber GmbH*) at 180°C and loaded with a force of 2.5 kN for 3 min. The force was then increased to 15 kN, and the press was slowly cooled to 90°C within approximately 35 min before the thin sample was removed from the press. The resulting samples have a diameter of 89.5 mm and a thickness of 0.1 mm.

4.2 | Characterization by XRD, SAXS, IR Spectroscopy, Differential Scanning Calorimetry, and Helium Pycnometer

XRD was performed via a Bragg–Brentano geometry *Empyrean* diffractometer by *Malvern Panalytical BV* in spinning mode. It is equipped with a pixel detector using a copper K_α ($\lambda = 1.54$ Å) radiation source. The instrument provides the software *Pananlytical's Highscore Plus* for data analysis. The crystallinity of the processed racoPP samples was estimated by integrating the relative intensities of the Bragg reflections and amorphous halos [33]. Examples are given in Figure S1.

SAXS measurements were performed on a lab-based *Double Ganesha AIR* system by *SAXSLAB/Xenocs*. This system is equipped with a copper rotating anode (*MicroMax 007HF* by *Rigaku Corporation* $\lambda = 1.54$ Å) and position-sensitive *Pilatus* detectors from *Dectris Ltd* (300 K for SAXS).

Polarized broadband IR spectroscopy was applied with a *Vertex 70* by *Bruker Corporation* in combination with a corresponding polarizer.

DSC measurements were performed on a *Discovery DSC 2500* by *TA Instruments Inc*. The heat capacity of racoPP was determined to be 1.819 ± 0.004 J $(\mathrm{g\,K})^{-1}$. It was calculated from three measurements, all according to the American Society for Testing and Materials (ASTM) E1269 standard. The crystallization peak temperatures of racoPP were determined during cooling at a rate of 20°C/min, under nitrogen, after holding at 230°C for 15 min.

To determine the density of racoPP, a small amount of the injection-molded sample was measured with an *Ultrapyc 1200e* helium pycnometer by *Quantachrome Instruments*. The average density was calculated to be $0.815 \pm 0.003\,\mathrm{g\,cm^{-3}}$ using 25 individual measurement results.

4.3 | Lock-In Thermography

Each compression-molded sample was coated with a thin layer of carbon (10–20 nm) on both sides. They were excited periodically with a frequency of 1.3 Hz using a point laser (*51nano-N520-0.9-O05-P-12-4-28-0-150*) by *Schäfter + Kirchhoff GmbH* with a power of 0.9 mW. The temperature evolution was monitored with an *ImageIR 9430* research IR camera *by InfraTec*

GmbH, with a spectral window ranging from 1.5 to 5.5 µm. It was mounted with an $M = 1.0\times$ microscopy objective. The experiments were performed in a vacuum chamber ($p \leq 0.02$ mbar) containing an optically transparent N-BK7 glass window to minimize convective heat losses. The time–temperature data were converted by Fourier transformation to an amplitude and phase signal via the *IRBIS* software provided by *InfraTec GmbH*. The linearized amplitude and phase signals as a function of the distance from the excitation point of the laser were then used to obtain the thermal diffusivity (slope method).

Acknowledgments

We thankfully acknowledge the support of the Collaborative Research Centre 1585, Projects A04 and C05 of the German Research Foundation (grant number: 492723217). We acknowledge support from the Keylabs "Mesoscale Characterization" and "Small Scale Polymer Processing" of the Bavarian Polymer Institute (BPI). This research benefited from SAXS instrumentation funded by Deutsche Forschungsgemeinschaft (grant number INST 91/38-41).

Conflicts of Interest

The authors declare no conflicts of interest.

References

1. H. A. Maddah, "Polypropylene as a Promising Plastic: A Review," *American Journal of Polymer Science* 6 (2016): 1–11.

2. S. Radhakrishnan and P. S. Sonawane, "Role of Heat Transfer and Thermal Conductivity in the Crystallization Behavior of Polypropylene-Containing Additives: A Phenomenological Model," *Journal of Applied Polymer Science* 89 (2003): 2994–2999.

3. M. Gahleitner, C. Grein, S. Kheirandish, and J. Wolfschwenger, "Nucleation of Polypropylene Homo- and Copolymers," *International Polymer Processing* 26 (2011): 2–20.

4. P. M. Kristiansen, A. Gress, P. Smith, D. Hanft, and H.-W. Schmidt, "Phase Behavior, Nucleation and Optical Properties of the Binary System Isotactic Polypropylene/N,N′,N″-Tris-Isopentyl-1,3,5-Benzene-Tricarboxamide," *Polymer* 47 (2006): 249–253.

5. N. Mohmeyer, B. Müller, N. Behrendt, et al., "Nucleation of Isotactic Polypropylene by Triphenylamine-Based Trisamide Derivatives and Their Influence on Charge-Storage Properties," *Polymer* 45 (2004): 6655–6663.

6. Y.-F. Zhang, H. Chen, B.-B. Liu, Y.-H. Gu, and X.-X. Li, "Isothermal and Non-Isothermal Crystallization of Isotactic Polypropylene Nucleated With 1,3,5-Benzenetricarboxylic Acid Tris(Cyclohexylamide)," *Thermochimica Acta* 590 (2014): 226–231, https://doi.org/10.1016/j.tca.2014.07.007.

7. Y.-f. Zhang and H. Chen, "Effects of Nucleating Agent 1,3,5-Benzenetricarboxylic Acid Tris(Cyclohexylamide) on Properties and Crystallization Behaviors of Isotactic Polypropylene," *Colloid and Polymer Science* 292 (2013): 493–498.

8. A. A. Abreu, S. I. Talabi, and A. de Almeida Lucas, "Influence of Nucleating Agents on Morphology and Properties of Injection-Molded Polypropylene," *Polymer Advances in Technology* 32 (2021): 2197–2206.

9. Z. Horváth, A. Menyhárd, P. Doshev, et al., "Improvement of the Impact Strength of Ethylene-Propylene Random Copolymers by Nucleation," *Journal of Applied Polymer Science* 133 (2016): 43823.

10. R. Pantani, I. Coccorullo, V. Speranza, and G. Titomanlio, "Modeling of Morphology Evolution in the Injection Molding Process of Thermoplastic Polymers," *Progress in Polymer Science* 30 (2005): 1185–1222.

11. B. Yang, J.-Z. Lin, R. Xia, et al., "Correlation Between Solidification Behavior and Melt Crystallization Kinetics of IsotacticPolypropylene (iPP) During Injection Molding," *Journal of Macromolecular Science, Part B* 53 (2014): 462–473.

12. R. H. Somani, B. S. Hsiao, A. Nogales, et al., "Structure Development During Shear Flow-Induced Crystallization of i-PP: In-Situ Small-Angle X-Ray Scattering Study," *Macromolecules* 33 (2000): 9385–9394.

13. M. Kandemir, İ. Karagöz, and H. Sepetcioglu, "Experimental Investigation of Effects of the Nucleating Agent on Mechanical and Crystallization Behavior of Injection-Molded Isotactic Polypropylene," *El-Cezeri Fen Ve Mühendislik Dergisi* 10 (2022): 110–120.

14. R. Čermák, M. Obadal, P. Ponížil, M. Polášková, K. Stoklasa, and A. Lengálová, "Injection-Moulded α- and β-Polypropylenes: I. Structure vs. Processing Parameters," *European Polymer Journal* 41 (2005): 1838–1845.

15. G. Kalay and M. J. Bevis, "Processing and Physical Property Relationships in Injection-Molded Isotactic Polypropylene. 1. Mechanical Properties," *Journal of Polymer Science. Part B, Polymer Physics* 35 (1997): 241–263.

16. B. Purgleitner, D. Viljoen, I. Kühnert, and C. Burgstaller, "Influence of Injection Molding Parameters, Melt Flow Rate, and Reinforcing Material on the Weld-Line Characteristics of Polypropylene," *Polymer Engineering and Science* 63 (2023): 1551–1566.

17. D. R. Fitchmun and Z. Mencik, "Morphology of Injection-Molded Polypropylene," *Journal of Polymer Science: Polymer Physics Edition* 11, no. 5 (2003): 951–971, https://doi.org/10.1002/pol.1973.180110512.

18. F. Liu, C. Guo, X. Wu, X. Qian, H. Liu, and J. Zhang, "Morphological Comparison of Isotactic Polypropylene Parts Prepared by Micro-Injection Molding and Conventional Injection Molding," *Polymer Advances in Technology* 23 (2011): 686–694.

19. D. Libster, A. Aserin, and N. Garti, "Advanced Nucleating Agents for Polypropylene," *Polymers for Advanced Technologies* 18 (2007): 685–695.

20. M. Blomenhofer, S. Ganzleben, D. Hanft, et al., "'Designer' Nucleating Agents for Polypropylene," *Macromolecules* 38 (2005): 3688–3695.

21. J. Wang, Q. Dou, X. Chen, and D. Li, "Crystal Structure and Morphologies of Polypropylene Homopolymer and Propylene-Ethylene Random Copolymer: Effect of the Substituted 1,3,5-Benzenetrisamides," *Journal of Polymer Science. Part B, Polymer Physics* 46 (2008): 1067–1078.

22. F. Abraham, S. Ganzleben, D. Hanft, P. Smith, and H. W. Schmidt, "Synthesis and Structure–Efficiency Relations of 1,3,5-Benzenetrisamides as Nucleating Agents and Clarifiers for Isotactic Poly(Propylene)," *Macromolecular Chemistry and Physics* 211 (2010): 171–181.

23. Y.-F. Zhang, P.-Z. Zhou, Y.-Z. Jiang, and X. Yang, "The Relationship Between Side Chain Isomerism of Aliphatic C4 Substituted 1,3,5-Benzenetricarboxylamides and Nucleation Effects in Isotactic Polypropylene," *Thermochimica Acta* 655 (2017): 219–225.

24. T. Bárány and J. Karger-Kocsis, *Polypropylene Handbook: Morphology, Blends and Composites* (Springer International Publishing, 2019).

25. P. M. Kristiansen, "PhD Thesis," (2004), Eidgenössische Technische Hochschule (ETH), Zürich.

26. J. C. Wittmann and B. Lotz, "Epitaxial Crystallization of Polymers on Organic and Polymeric Substrates," *Progress in Polymer Science* 15 (1990): 909–948.

27. K. Herrmann, S. Freund, F. Eller, et al., "Microstructural and Thermal Transport Properties of Regioregular Poly(3-Hexylthiophene-2,5-Diyl) Thin Films," *Materials* 15 (2022): 7700.

28. Y. Wang, J. Zhao, M. Qu, et al., "An Unusual Promotion of γ-Crystals in Metallocene-Made Isotactic Polypropylene From Orientational Relaxation and Favorable Temperature Window Induced by Shear," *Polymer* 134 (2018): 196–203.

29. S. Krimm, *Fortschritte der Hochpolymeren-Forschung* (Springer, 1960), 51–172.

30. A. Salazar, A. Mendioroz, and R. Fuente, "The Strong Influence of Heat Losses on the Accurate Measurement of Thermal Diffusivity Using Lock-In Thermography," *Applied Physics Letters* 95 (2009): 121905.

31. A. Salazar, A. Mendioroz, R. Fuente, and R. Celorrio, "Accurate Measurements of the Thermal Diffusivity of Thin Filaments by Lock-In Thermography," *Journal of Applied Physics* 107 (2010): 043508.

32. A. Timme, R. Kress, R. Q. Albuquerque, and H. W. Schmidt, "Phase Behavior and Mesophase Structures of 1,3,5-Benzene- and 1,3,5-Cycl ohexanetricarboxamides: Towards an Understanding of the Losing Order at the Transition Into the Isotropic Phase," *Chemistry* 18 (2012): 8329–8339.

33. G. W. Becker, *Kunststoff-Handbuch. 3, Technische Thermoplaste: 4. Polyamide* (Hanser, 1998).

Supporting Information

Additional supporting information can be found online in the Supporting Information section.

Supporting Information

Do Nucleating Agents or Processing Methods Affect the Thermal Transport in RacoPP?

Ina Klein, María Ester Marroquin Lacayo, Thomas Blesch, Sabine Rosenfeldt, Patrick Länger, Klaus Kreger, Stefan Rettinger, Jürgen Senker, Hans-Werner Schmidt, Markus Retsch*

Injection-Molded Specimens

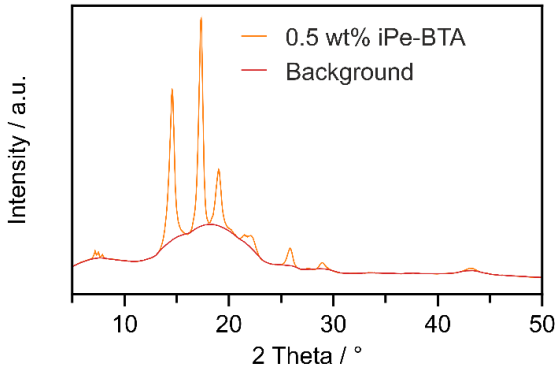

Figure S1: XRD of injection-molded racoPP specimens with 0.5 wt% BTA with the applied background.

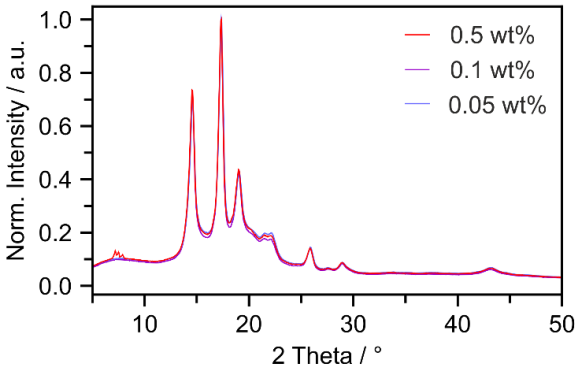

Figure S2: XRD of injection-molded racoPP specimens with various concentrations of iPe-BTA. Intensities are normalized to the highest peak.

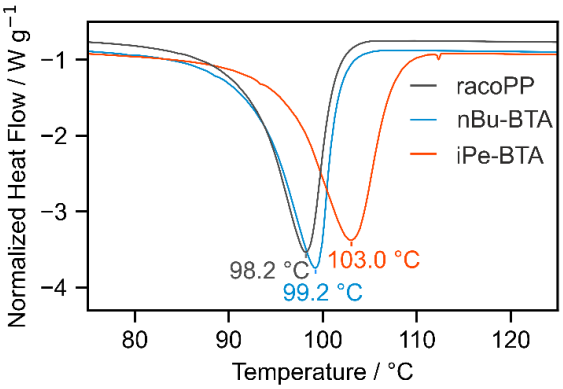

Figure S3: DSC measurements of neat racoPP (grey), racoPP with 0.5 wt% nBu-BTA (blue) and racoPP with 0.5 wt% iPe-BTA (orange) showing the corresponding crystallization peaks. Cooling was perforemd at a rate of 20 °C min^{-1}.

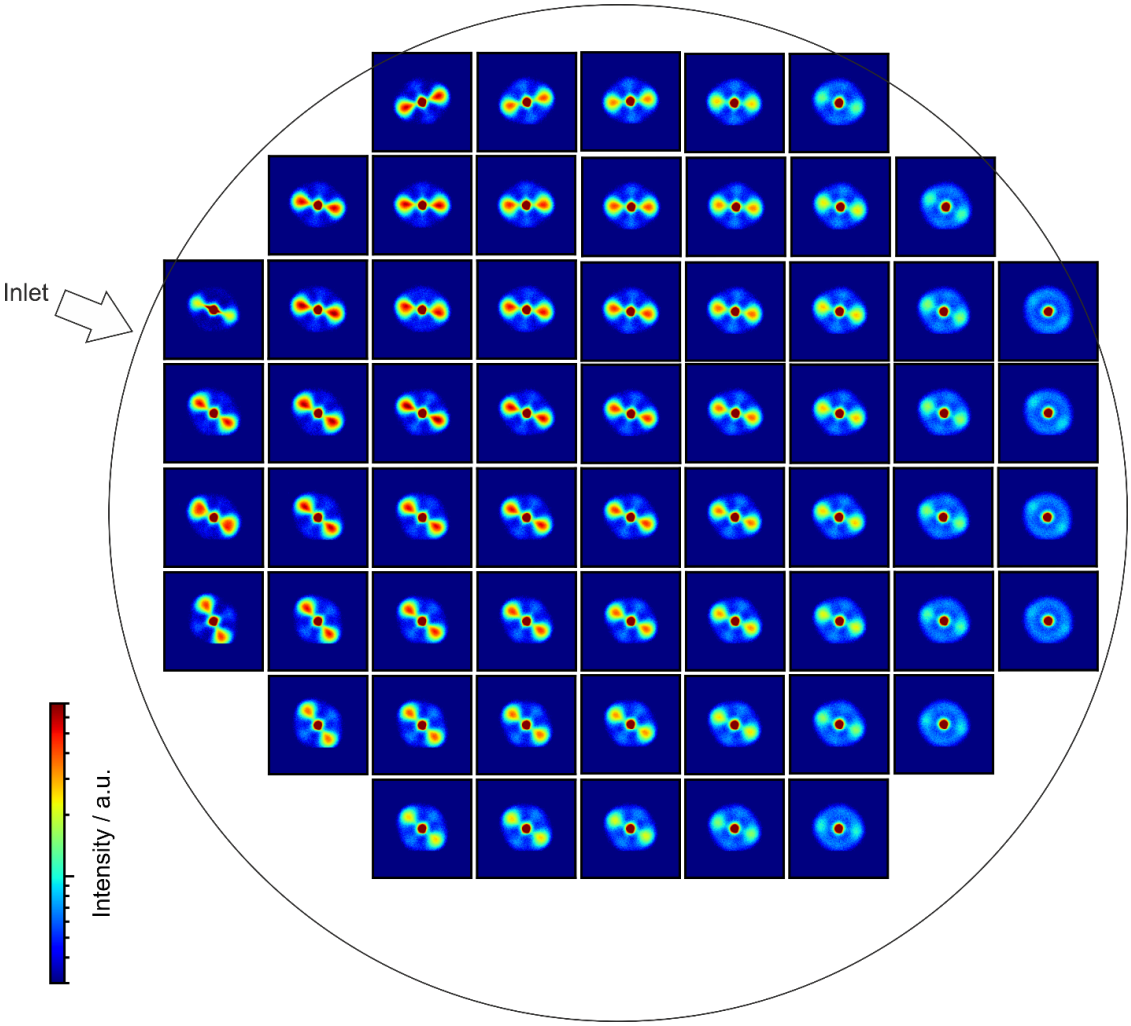

Figure S4: 2D SAXS patterns of the injection-molded racoPP sample with 0.1 wt% iPe-BTA. The approximate positions of the 60 SAXS measurements on the injection-molded sample with a diameter of 27 mm correspond to the positions shown within the circle.

Figure S4 clearly shows that also for the injection-molded sample containing 0.1 wt% iPe-BTA the azimuthal intensity distribution increases with growing distance from the inlet.

When using the raster containing 3 measurement positions to obtain the patterns for Figure 1 c, the middle position showed a more amorphous region of the sample being probed by the X-ray. This specific position was apparently not probed using the raster to obtain the 60 measurement positions shown here.

Compression-Molded Thin Films

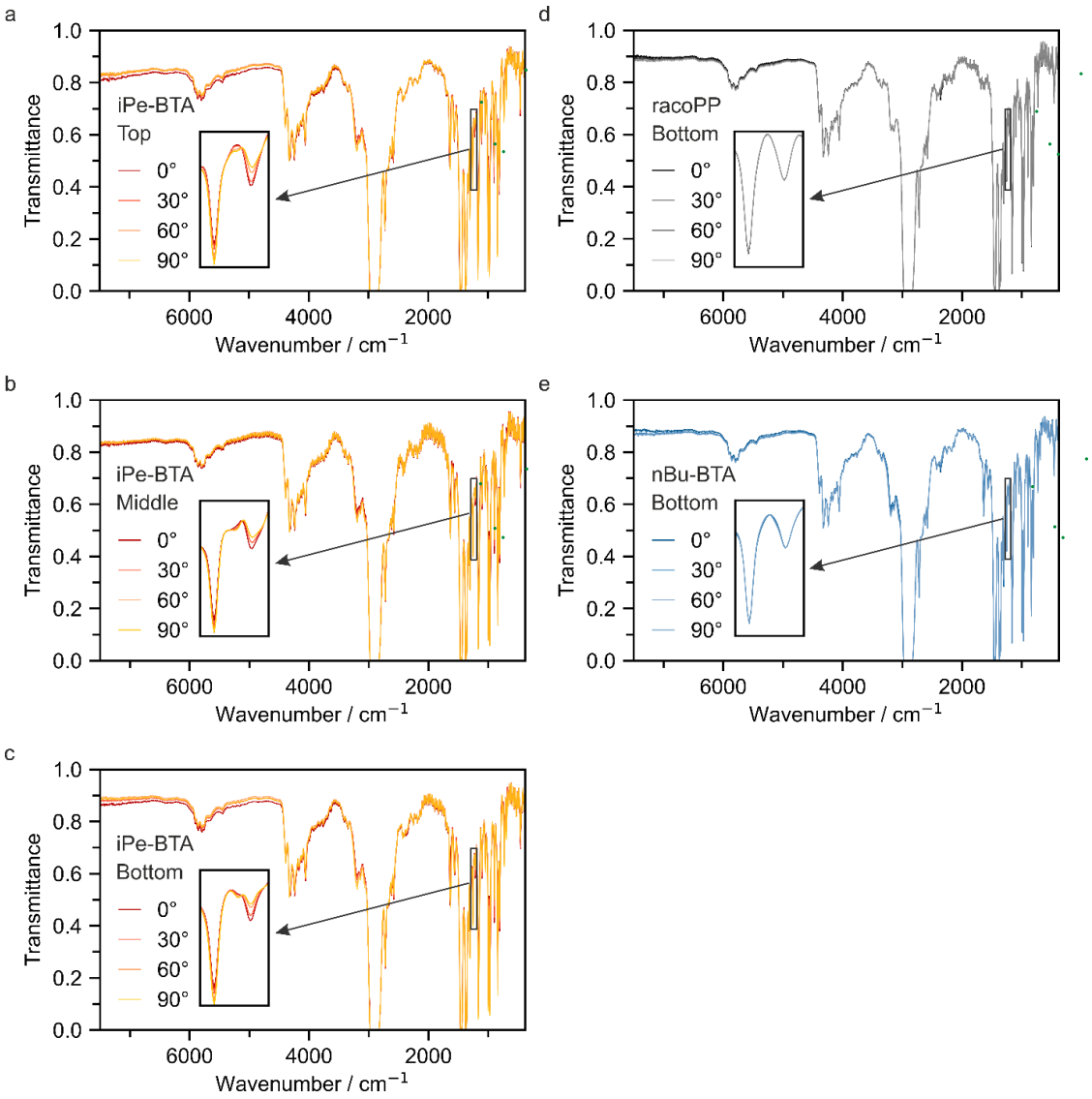

Figure S5: IR spectra using polarized incident IR radiation from 0° to 90°. The inlets correspond to a parallel polarized γ_w(CH) mode at 1256 cm^{-1} and a perpendicular polarized γ_w(CH) mode at 1218 cm^{-1}.[1] (a-c) RacoPP with 0.5 wt% iPe-BTA at the top, middle and bottom position, d) neat racoPP at the bottom position and e) racoPP with 0.5 wt% nBu-BTA at the bottom position.

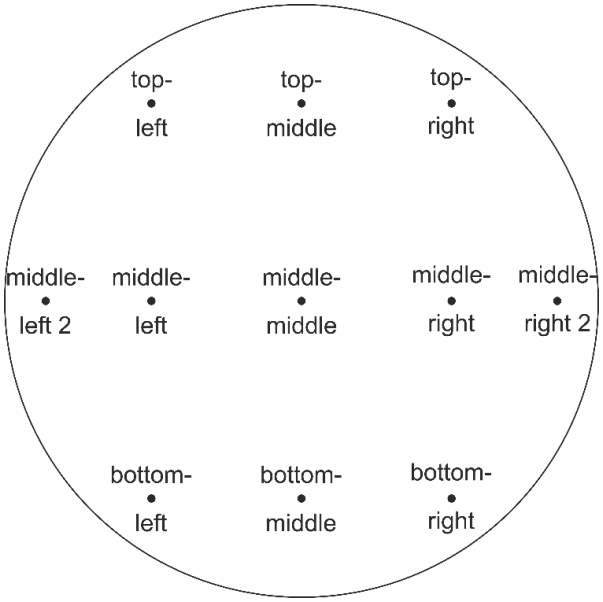

Figure S6: Schematic illustration showing the positions on the compression-molded thin films with a diameter of 89.5 mm chosen for SAXS measurements. Hereby 'bottom-middle' is closest to the inlet.

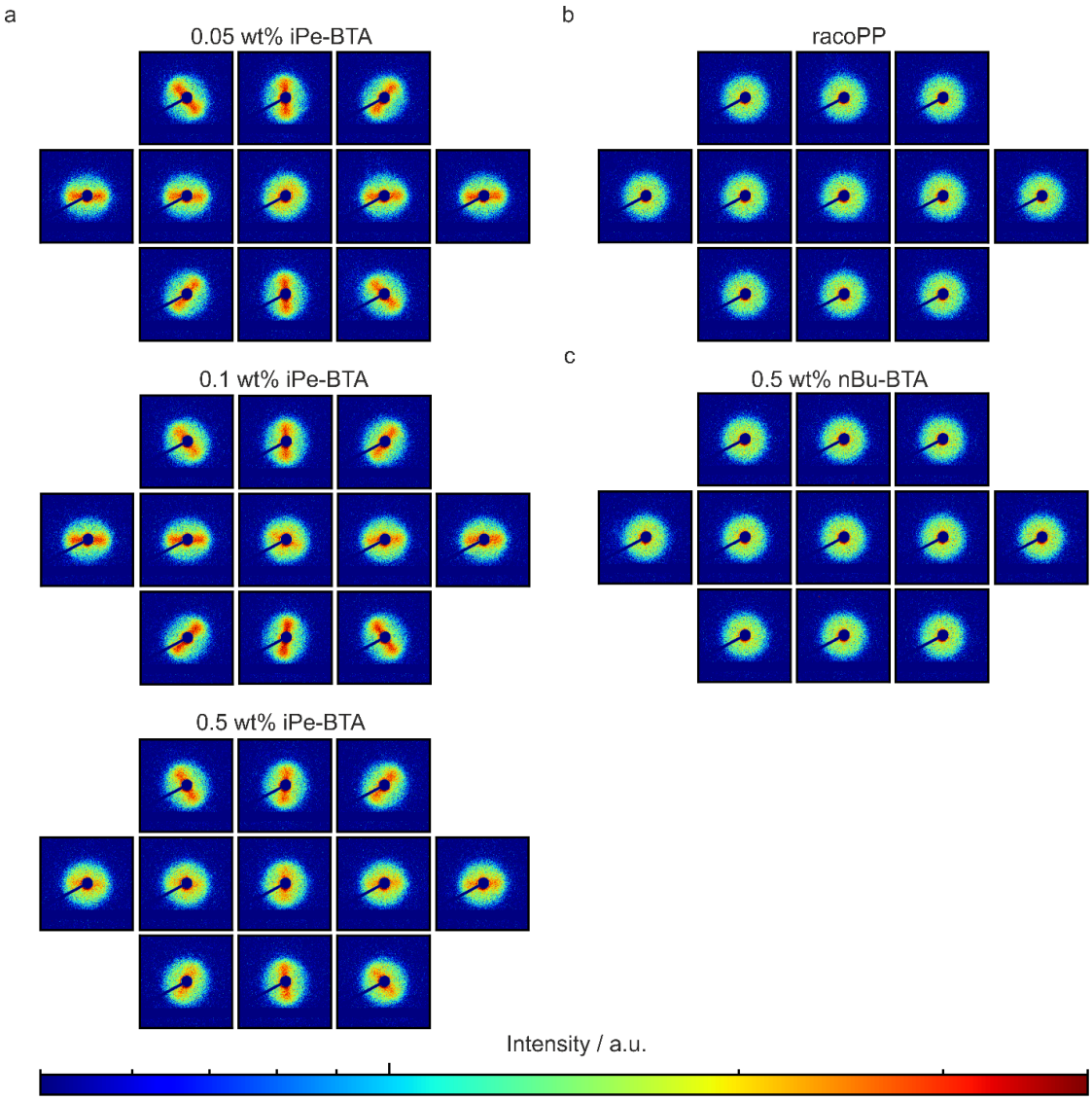

Figure S7: 2D SAXS patterns of compression-molded samples at 11 sample positions a) RacoPP with various concentrations of iPe-BTA, b) neat racoPP and c) racoPP with 0.5 wt% nBu-BTA.

References

[1] S. Krimm. *Fortschritte der Hochpolymeren-Forschung* **1960**, *2*, 51-172.

10

High and Tuneable Anisotropic Thermal Conductivity Controls the Temperature Distribution of 3D Printed All-Polyethylene Objects

Ina Klein[1], Thomas Tran[1], Réne Reiser[2,3], Maximilian Theis[1], Sabine Rosenfeldt[1], Marius Schöttle[1], Carl Schirmeister[2,3], Peter Bösecke[4], Stefan Rettinger[1], Rolf Mülhaupt[2], Markus Retsch[1,5]

Published in *Journal of Materials Chemistry A*, **2023**, *11*, 22492-22502.
Reproduced with permission from Royal Society of Chemistry.

[1] Department of Chemistry, Physical Chemistry I, University of Bayreuth, 95447 Bayreuth Germany.
[2] Freiburg Materials Research Center FMF, Albert-Ludwigs-University Freiburg, 79104 Freiburg, Germany.
[3] LyondellBasell Industries, Industriepark Höchst, 65926 Frankfurt am Main, Germany
[4] European Synchrotron Radiation Facility (ESRF), 71 Avenue des Martyrs, CS 40220, 38043 Grenoble Cedex 9, France.
[5] Bavarian Polymer Institute (BPI), Bayreuth Center for Colloids and Interfaces (BZKG), Bavarian Center for Battery Technology (BayBatt), University of Bayreuth, 95447 Bayreuth, Germany.

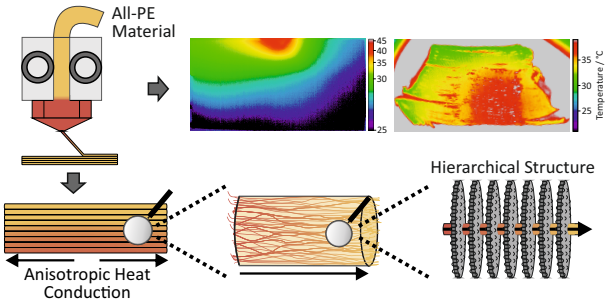

Journal of Materials Chemistry A

ROYAL SOCIETY OF CHEMISTRY

PAPER

View Article Online
View Journal

Cite this: DOI: 10.1039/d3ta04483a

High and tuneable anisotropic thermal conductivity controls the temperature distribution of 3D printed all-polyethylene objects†

Ina Klein,[a] Thomas Tran,[a] René Reiser,[bc] Maximilian Theis,[a] Sabine Rosenfeldt,[a] Marius Schöttle,[a] Carl Schirmeister,[bc] Peter Bösecke,[d] Stefan Rettinger,[a] Rolf Mülhaupt[b] and Markus Retsch *[ae]

Received 28th July 2023
Accepted 9th October 2023

DOI: 10.1039/d3ta04483a

rsc.li/materials-a

With ongoing miniaturization and weight reduction of portable electronic devices, effective heat dissipation is essential to inhibit malfunctions and premature failure. The application of fillers in a polymer matrix enhances the thermal conductivity of lightweight materials but impedes recyclability. All-polyethylene (all-PE) materials represent a sustainable and easy-to-recycle single-material alternative, whereby high and tunable thermal conductivity is provided by process-induced hierarchical PE nanostructures. Essential for this type of composite-free high-performance material is the specific PE composition containing high amounts of ultra-high molecular weight PE that form ultrastrong extended-chain nanostructures induced by shear and elongational flow during processing. This results in self-reinforcing fibre-like shish-kebab nanostructures with a high thermal conductivity parallel to the extended PE chains. Extrusion-based 3D printing enables tuning the orientation of the PE nanostructure to tailor the orientation and magnitude of the thermal conductivity. Thus, this material class highlights the possibility of combining digitally programmable heat management in 3D printed materials with sustainable material concepts.

Introduction

Over the last several decades, progress in the development of electronic devices has been omnipresent. Not only a constantly improved performance but also practicability is demanded from all kinds of portable electronic devices, ranging from mobile phones to laptops to wearable electronic devices.[1,2] The miniaturization and weight reduction of electronics represent increasingly decisive endeavors.[3,4] However, reducing the size of such devices implies a great challenge, as the flow of electric current inevitably leads to the generation of heat, increasing the risk of overheating, malfunctions, or even premature failure.[2–8] To inhibit temperature-induced failures, effective heat dissipation is essential.[2,6–9] Generated heat must be directed away from sensitive parts towards heat sinks or alternative cooling systems. A common approach is the use of thermal interface materials. Thermally conductive filler materials are added to a polymer matrix, which bridges the heat source and cooling system. Thereby, the softness of the polymer matrix is essential, as adhesion to the rigid solid interfaces reduces the thermal interface resistance. Concomitantly, the low weight of polymers represents a further advantage. Unfortunately, polymers commonly exhibit a low thermal conductivity; thus fillers with high thermal conductivity are necessary to enhance the material's functionality.[10,11] Applied fillers include various sizes and shapes of metals, carbon-based structures, ceramics and different combinations of the mentioned.[9,10,12–14] However, the interfacial thermal resistance of filler and matrix represents an omnipresent drawback of such materials. Scattering of the heat carriers at the interface limits the positive effect of the conductive filler. To target this issue, high filler loadings are often needed to evoke heat conducting paths.[9,10,12–14] This, however, entails increasing costs and impairs the weight advantage of polymers. Also, the mechanical properties can suffer from high loadings, impeding processability.[9,10,14] Alternative approaches include the functionalization of filler materials to reduce the interfacial resistance and enhance the dispersion of the filler.[8,10,15,16] High thermal conductivity in an epoxy/poly-*p*-phenylene benzobisoxazole (PBO) bulk material was achieved by using a hierarchical spiral and weaving structure in combination with thermal bridging between crystalline

[a]Department of Chemistry, Physical Chemistry I, University of Bayreuth, 95447 Bayreuth, Germany. E-mail: markus.retsch@uni-bayreuth.de
[b]Freiburg Materials Research Center FMF, Albert-Ludwigs-University Freiburg, 79104 Freiburg, Germany
[c]LyondellBasell Industries, Industriepark Höchst, 65926 Frankfurt am Main, Germany
[d]European Synchrotron Radiation Facility (ESRF), 71 Avenue des Martyrs, CS 40220, 38043 Grenoble Cedex 9, France
[e]Bavarian Polymer Institute, Bayreuth Center for Colloids and Interfaces, Bavarian Center for Battery Technology (BayBatt), University of Bayreuth, 95447, Germany

† Electronic supplementary information (ESI) available. See DOI: https://doi.org/10.1039/d3ta04483a

and amorphous PBO regions.[17] Also, networks of filler material, into which the polymer is incorporated subsequently, can be prefabricated to ensure continuous thermally conductive paths.[6,10,18,19] Moreover, multiple fillers have been combined to achieve synergistic effects.[10,16,20] However, the related preparation methods commonly contain multiple steps and can be rather laborious. Furthermore, multi-component composites hamper the prospect of a circular economy due to their inherent heterogeneity.[21] The recovery of matrix and filler material is complex, expensive, and energy-consuming; thus most end-of-life composite products are still disposed of by landfilling and incineration.[21–23] This circumstance strongly conflicts with the demand for sustainability, which represents an increasingly decisive argument for the selection of materials. With limited resources and partly energy-intensive acquirement of raw materials, efforts towards a circular economy are essential.[24] In the beginning of the 21st century, Mülhaupt *et al.* developed easy to recycle single material composites based on polyethylene (PE)-based multisite catalysis.[25,26] The robust catalyst design allows producing PE reactor blends with a high content of nanophase-separated disentangled ultra-high molecular weight PE (UHMWPE). Due to the UHMWPE nanophase separation and the absence of massive UHMWPE entanglement, high UHMWPE contents are tolerated in conventional injection moulding and extrusion-based 3D printing. During melt processing, the flow-induced crystallization of the disentangled UHMWPE, controlled by extensional flow and shear force, induces the formation of fibre-like extended-chain nanostructures to create an all-PE material. These *in situ*-formed fibre-like nanostructures (shish) nucleate the crystallization of high density PE (HDPE) to yield shish-kebab structures as reinforcing phases. Therefore, the injection moulded as well as the 3D-printed all-PE material exhibit substantially enhanced mechanical properties and high wear resistance. As the reinforcing phase and the matrix are made of the same polymer and the reinforcing nanostructure can be repeatedly formed by melt processing, all-PE material is designed for mechanical as well as chemical recycling. This material designed for a circular economy represents a great advantage in terms of sustainability.[27,28]

As extensional flow and shear force are essential for the *in situ* formation of the desired nanofibres, the choice of a suitable extrusion-based processing technique is required, such as injection moulding and extrusion-based 3D printing, *e.g.* fused filament fabrication (FFF).[27] FFF is a 3D printing technique based on heating a filament above its glass transition or melting temperature and extruding the polymer layer by layer through a nozzle.[29] In contrast to injection moulding, where the flow-induced crystallization is restricted by the mould design, FFF provides full control over orientation and degree of reinforcement by extended-chain UHMWPE nanostructures *via* the printing parameters.[27] Besides the improvement of mechanical properties, the extended-chain UHMWPE nanostructures are expected to efficiently conduct heat along the fibre axes, increasing the thermal conductivity in the related direction. Such high anisotropic thermal conductivities are known from chain-oriented polymer fibres with a stiff polymer backbone.[30] A thermal conductivity of 104 W (m K)$^{-1}$ was reported in ultra-drawn PE nanofibers and high chain alignment combined with low chain entanglement enabled a conductivity of 62 W (m K)$^{-1}$ in PE films.[31,32] An anisotropic thermal conductivity can be expected in the all-PE material introduced here, offering great potential for directing heat without the need for multi-material composites. Efficient thermal management may, thus, be combined with a material designed for circular economy. This pending issue is addressed in our work by presenting the material's structure on various length scales, prior and post-processing *via* FFF and in comparison to benchmark HDPE. We demonstrate that structural anisotropy allows for tailoring the thermal conductivity of 3D-printed all-PE materials, being controlled by the print parameters. Finally, we use the findings to provide an example of digitally defined control of temperature distributions in 3D-printed all-PE specimens.

Results and discussion

Structural analysis on various length scales

The microstructure of the all-PE material formed *in situ* during melt processing induced by shear and elongational flow comprises several length-scales starting from the molecular orientation of the PE macromolecules, which was characterized by infrared (IR) spectroscopy. A single layer of all-PE material and a single layer of benchmark HDPE were printed unidirectionally using basic print parameters (200 °C, 25 mm s^{-1}). Each sample was measured using infrared light polarized by 0° and 90° relative to the print direction at identical positions. Polarization of the IR active modes is dependent on the symmetry of vibrational modes. Whereas most vibrational mode symmetries of PE are not polarized, two irreducible representations (B_{1u} and B_{2u}) show polarization perpendicular to the PE chain axis.[33] Hence, they are excited by light polarized in the according direction. In addition, PE exhibits vibrational modes with a symmetry leading to an increased absorption of parallel polarized light (B_{3u}).[33] The obtained spectra for printed all-PE material are shown in Fig. 1b. A more detailed assignment of all acquired absorption bands and the polarization of corresponding modes are provided in the ESI (Table S1†).[33,34] For most parts of the spectra light polarized with 0° relative to the print direction is absorbed slightly stronger than light polarized by 90°. However, the spectrum for light polarized with 90° shows increased absorption for perpendicularly polarized modes, for instance at 719 cm^{-1}. Accordingly, light polarized with 0° relative to the print direction gives rise to the absorption of parallelly polarized modes for example at 1051 cm^{-1}. This verifies that PE chains in the 3D-printed all-PE material are predominantly oriented along the print direction. The spectra pertaining to the benchmark HDPE specimen (Fig. 1c) show no noteworthy difference between the two measurements. Bands corresponding to both, perpendicularly and parallelly polarized modes, are equivalent for both light polarizations. Consequently, the presence of UHMWPE in all-PE material represents a prerequisite for the molecular orientation of PE chains. Without UHMWPE the HDPE chains do not align preferably in print direction, but randomly.

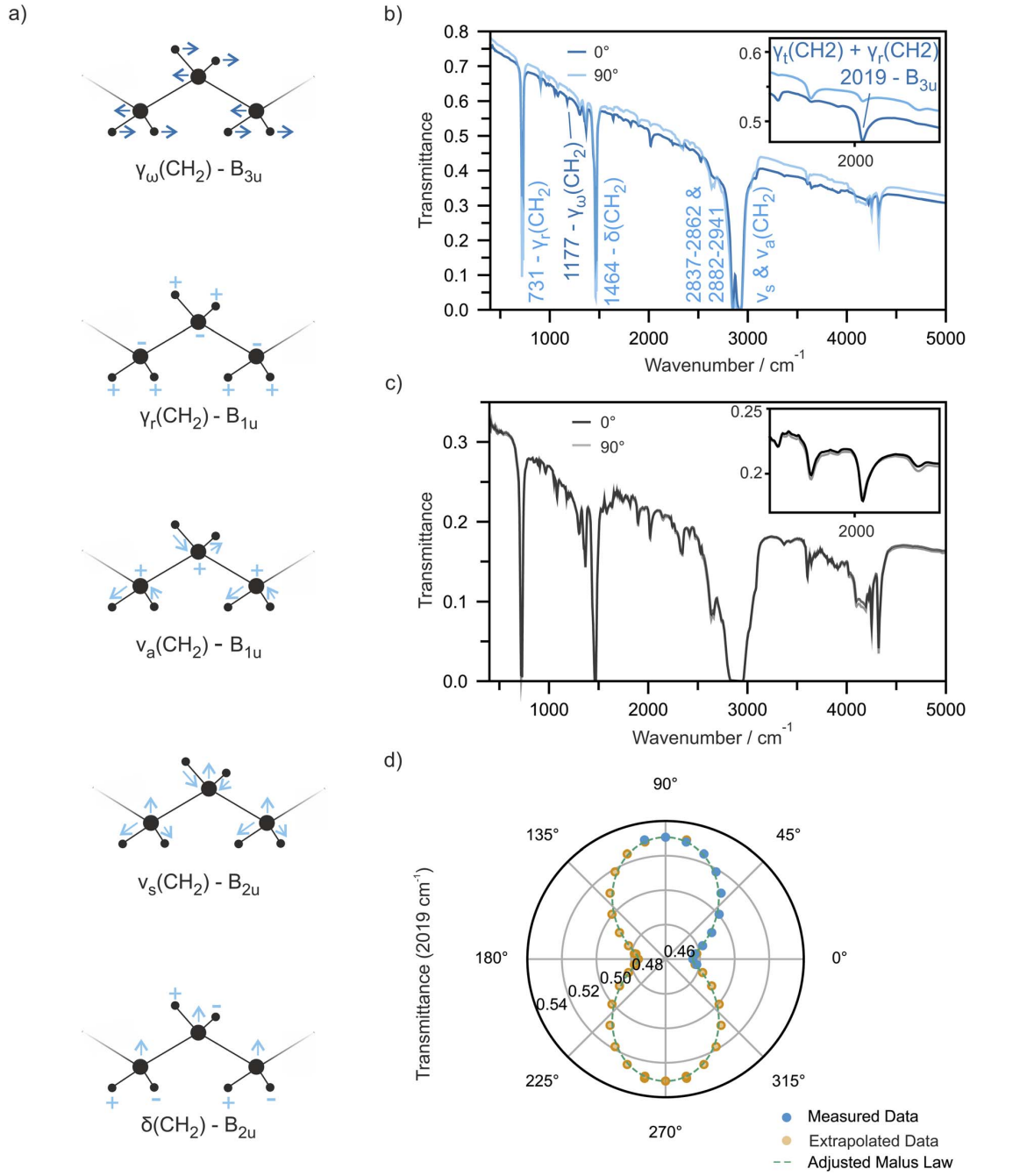

Fig. 1 (a) Polyethylene chain fundamental frequencies. IR spectra using light polarized by 0° and 90° relative to the 3D print direction of (b) all-PE material with the assignment at 2019 cm^{-1} and (c) benchmark HDPE. (d) Angle-dependent transmittance of all PE-material at 2019 cm^{-1}, the results are fitted with an adjusted form of Malus' law.

To supplement the IR results for light polarized by 0° and 90° relative to the print direction, additional spectra at intermediate angles were obtained in 10° steps from −10° to 100° (Fig. 1d – measured data). The parallel polarized mode of 2019 cm^{-1} was chosen as representative of the polarized IR modes of all-PE material in general.[34] The measured transmission values are displayed by the radial distance in a polar coordinate system and extrapolated to the remaining angles from 90° to 360° (Fig. 1d – extrapolated data). The resulting peanut shape is typical for the display of Malus' law, which is commonly used to

describe the transmission of polarized light by analysers in relation to the angle between the plane of transmission and the polarization angle. The correlation is slightly modified, as the transmission of the polarized IR frequencies ranges between a minimum and maximum transmission (Formula (S1) and (S2)†). The adjusted Malus law results in a good fit for the obtained angle-dependent transmission values (Fig. 1d – dashed line). It has been shown that print direction and PE chain orientation are parallel to each other; thus, the adjusted Malus' law can link the angle dependent transmission of the polarized light to the PE chain orientation.

The findings on chain orientation on the molecular scale are complemented by information on the ångström and nanometer length scale *via* two-dimensional wide-angle X-ray scattering (2D WAXS) and 2D small-angle X-ray scattering (2D SAXS). The all-PE filament and 3D-printed samples based on the identical filament were both analysed to determine the influence of the FFF process on the UHMWPE nanostructure formation. Benchmark HDPE filament and a corresponding printed sample functioned as references. In all cases, the positions of the Bragg reflexes in the 1D WAXS spectra indicate mainly orthorhombic crystals of the space group *Pnma* (Fig. S1†). No significant dependency of the lattice parameters on the processing method or the applied print speed (25–100 mm s^{-1}) or temperature (200–230 °C) was observed (Fig. S3a†). Whereas the 2D WAXS patterns showed a mainly isotropic short-range order for the benchmark HDPE samples, slight anisotropy was apparent for the all-PE filament and strong anisotropy for the corresponding printed samples (Fig. 2a). These readily visible qualitative results, were supplemented by calculation of the Hermans orientation factors.[35,36] For the printed benchmark HDPE sample and the HDPE filament, Hermans factors of 0.05 and 0.06 were obtained, respectively, indicating that the PE chain orientation is almost fully isotropic. The all-PE filament resulted in a higher Hermans factor of 0.16 and the highest anisotropy was obtained for the printed all-PE material with a Hermans factor of 0.37. A more detailed elaboration of the orientation parameters is provided in the ESI.† The results indicate that UHMWPE represents a necessity for a preferred spatial orientation of the PE unit cells in the printed material, which is in good agreement with the conclusions drawn from IR spectroscopy. The 2D WAXS patterns also revealed that processing the filament by FFF strongly increased the spatial orientation of the PE unit cells in the all-PE material; hence, the orientation of the PE chains was intensified by the printing process. The applied print parameters, on the contrary, *i.e.*, print speed (25, 50, 100 mm s^{-1}) and print temperature (200–230 °C), did not significantly influence the anisotropy of the obtained WAXS patterns and their calculated orientation factors within this narrow processing range (Fig. S3b and Table S4†).

SAXS provides information on the crystal morphologies on the nanometer length scale. During HDPE crystallization, the chains organize to form lamellar structures matching this size range.[37] The 2D SAXS data, shown in Fig. 2b, are isotropic for the HDPE filament but slightly elliptical for HDPE processed by FFF, elliptical for the filament of all-PE material, and strongly anisotropic for the 3D-printed all-PE material, reflecting the different spatial arrangements of the lamellar structures. A

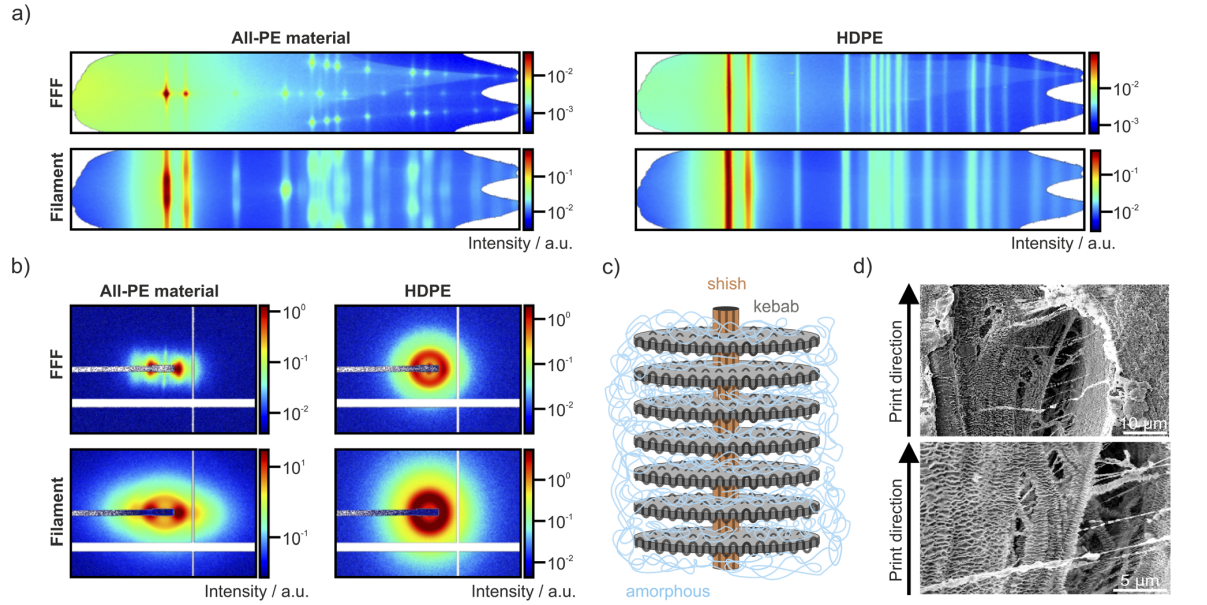

Fig. 2 Comparison of all-PE filament and benchmark HDPE filament and therewith printed samples obtained by fused filament fabrication (FFF). (a) Azimuthal representation of 2D wide angle X-ray scattering (azimuth *vs.* momentum transfer q). (b) 2D small angle X-ray scattering (detector position q_y *vs.* detector position q_x). (c) Schematic illustration of a shish-kebab structure surrounded by amorphous PE. (d) Scanning electron microscopy image of an all-PE sample prepared by FFF and etched with hot xylene.

comparison of the two non-printed filament samples showed that the lamellar structures in benchmark HDPE oriented randomly, whereas the presence of UHMWPE enhances the organization of these lamellar structures along the 3D-printing direction. Furthermore, the results revealed a very weak but observable orientation of the lamellar structures in 3D printed benchmark HDPE, even though an orientation of the PE chains in the corresponding sample could not be measured by IR spectroscopy or WAXS. A significant anisotropy, on the other hand, is observable for the pattern of unidirectionally printed all-PE specimens. The flow-induced coil-stretch transition of UHMWPE chains was provoked by the shear and elongational forces during the printing process. As a result, chain-extended fibre-like shish crystals evolved, which correlate to the distinctive vertical streak in the 2D SAXS pattern. The extended-chain shish guide the crystallization of HDPE, leading to strongly oriented lamellar structures around the shish nanofibres. These lamellar kebab structures are abundant in the SAXS pattern as equatorial reflections. Their thickness was estimated to 13 nm from the intensity minimum at around 0.48 nm^{-1}. The diffraction maximum at 0.26 nm^{-1} indicated an inter-lamellar distance of approximately 24 nm. Although these features slightly vary with changes in print speed and temperature, no explicit trend for the print parameter variation was identified (Fig. S4 and Table S5†) for the given set of print speed and temperatures (25–100 mm s^{-1}; 200–230 °C). In conclusion, 2D SAXS indicated that either the presence of UHMWPE in the extruded material or processing by FFF is sufficient to obtain at least a weak orientation of the lamellar structures. The formation of shish-kebab crystals, on the other hand, requires both: presence of UHMWPE and high shear and elongation forces exerted by FFF.

The appearance of these shish-kebab structures was further validated by scanning electron microscopy (SEM) (Fig. 2d). The etching of a printed all-PE material with hot xylene removes the amorphous PE, surrounding the shish-kebab crystals. This reveals the crystals, making their structure visible in the SEM images. The elongated fibre-like UHMWPE shish crystals are encircled by the lamellar HDPE kebab formations. Furthermore, the SEM images clearly display the predominant alignment of the shish-kebab structures in the print direction.

Effect of print parameters on the thermal diffusivity

The extended-chain UHWMPE nanostructures function as reinforcing phases and significantly improve the mechanical properties of HDPE.[27,28] This improvement was found to be dependent on the printing conditions.[27] Clear differences were discovered between specimens printed parallel and perpendicular to the tensile and impact test direction. Furthermore, the reduction of print temperature and increase of print speed were found to enhance the structural and mechanical properties significantly thus allowing for digitally tuning the material properties *via* the 3D-printing parameters.[27] The in-plane elastic modulus, shear modulus, and Poisson's ratio are known to correlate directly with the velocity of sound waves or acoustic phonons.[38–40] Hence, a correlation between the mechanical properties and thermal conductivity can be conjectured. Lock-in thermography was applied to determine the in-plane thermal diffusivity perpendicular and parallel to the print direction of a selection of unidirectionally printed specimens. The method is based on periodic heating of the printed specimen *via* a focused laser, whereby the temperature distribution is monitored by an IR-camera. The thermal diffusivity was then calculated *via* the so-called slope method from the linearized relation of the amplitude and phase data to the distance from the centre of the laser beam.[41–43] Measurements corresponding to the printed all-PE specimens resulted in ellipsoidal phase and amplitude signals, whereas a circular signal was obtained for the benchmark HDPE sample (Fig. 3a). The isotropic patterns obtained from the benchmark HDPE specimen proved that adjacent deposition of strands alone does not lead to anisotropic thermal characteristics. In line with the results on structural anisotropy, thermal anisotropy requires the presence of UHMWPE inducing the formation of extended-chain nanostructures. Moreover, the faint preferred orientation of lamellar structures in 3D-printed HDPE, observed in the 2D SAXS pattern, did not induce thermal anisotropy.

Fig. 3b provides the obtained thermal diffusivity values of specimens prepared using a variety of print speeds and print temperatures. Diffusivities parallel and perpendicular to the printing direction were compared, as well as their ratio, termed thermal anisotropy. It was notable that the diffusivity of printed benchmark HDPE (0.3 mm s^{-1}) is similar to the diffusivities obtained for the all-PE material perpendicular to the print direction (0.2 mm^2 s^{-1}), whereas the thermal diffusivity of all-PE material parallel to the print direction is significantly higher (0.7–1.1 mm^2 s^{-1}). Hence, not only did the shish-kebab formation lead to thermal anisotropy, it also strongly increased the thermal diffusivity in the print direction. Comparable to fibres functioning as filler material in multi-material composites, the shish structures may be regarded as conducting paths that transfer heat efficiently. This reasons for the diffusivity enhancement in the print direction, while the diffusivity in the perpendicular direction is not significantly affected. In contrast to alien fillers, there are two major advantages of the all-PE material. Firstly, we expect a strong interfacial linking between the crystalline nanophase and the amorphous parts of the polymer film, owing to the identical materials' chemistry. Secondly, macroscopic pathways along the crystalline backbone are not controlled by the volume fraction and hence by a percolation threshold but rather by the 3D-printing process itself, which defines the orientation and crystallization of the shish structures. The direction in which heat is primarily conducted can, therefore, be digitally defined by adjusting the print direction. The influence of the 3D printing parameters on the thermal diffusivity in print direction, and therewith on the thermal anisotropy, is also displayed in Fig. 3b. The dependence on the print parameters may be caused by four distinct effects: (1) orientation, (2) morphology of the shish-kebab structures formed during the 3D printing process, (3) degree of crystallization and (4) macroscopic length of the shish-kebab structures. As described above, extensive SAXS and WAXS analysis did not reveal any significant

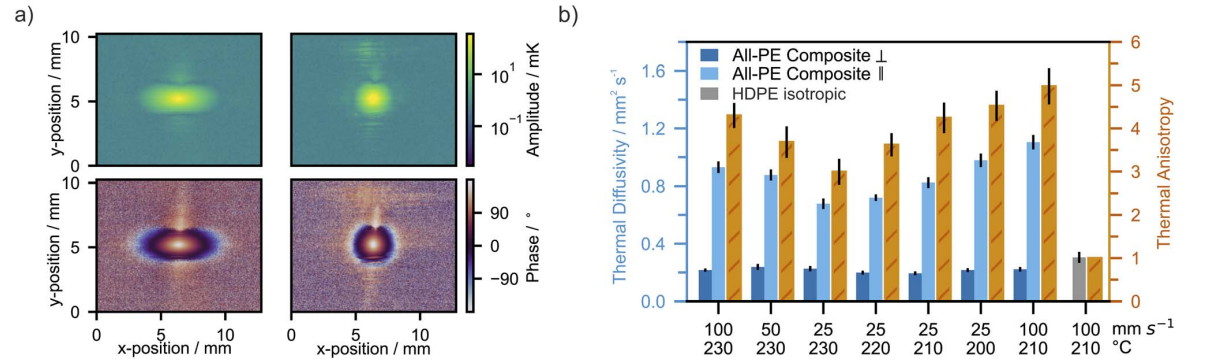

Fig. 3 Lock-in thermography for determination of the thermal diffusivity of HDPE and all-PE material processed by FFF. (a) Amplitude and phase signal obtained for an all-PE and a benchmark HDPE sample prepared with a print temperature of 210 °C and a print speed of 100 mm s^{-1}. The difference in shape shows that anisotropy of printed all-PE samples is not based on the printing process itself, but UHMWPE in the material is influential. (b) Thermal diffusivity and thermal anisotropy of all-PE samples and a benchmark HDPE sample, prepared with differing print speeds and print temperatures. Anisotropy is enhanced by reduced print temperatures and increased print speeds.

dependence of the shish-kebab orientation or morphology on the print speed or temperature (Fig. S3 and S4†). Analysis of the first heating cycle of the single-layered samples *via* differential scanning calorimetry (DSC) resulted in crystallinities between 63% and 68% (Fig. S5†). However, the DSC measurements did not display the shish-kebab content, and no trend considering the total degree of crystallization with respect to the print parameters can be identified. The last mentioned hypothesis, the macroscopic length of the shish-kebab crystals, goes hand in hand with the length of the individual fibre-like shish structures. As shear and extensional flow rate correlate with the print speed, high print speeds promote coil-stretch transitions of disentangled UHMWPE and the formation of extended-chain shish nanostructures. Increasing the temperature favours the opposite effect, promoting stretch-coil relaxation. Potentially, these effects cause longer shish structures and, therefore, enhanced continuity of the heat conducting paths. However, evaluation on the length scale of the individual shish structures represents a challenging task, and confirmation of this hypothesis remains open to future investigations. Nevertheless, it is evident that increased 3D printing speed and reduced 3D printing temperature both give rise to higher thermal diffusivity in the print direction. Even though the material processability limits the parameter settings for the given setup to a temperature of 210 °C and a speed of 100 mm s^{-1}, we achieved a high thermal conductivity, calculated from the materials density, heat capacity, and diffusivity, of up to 1.30 W $(m\ K)^{-1}$ in print direction. This is 2.8 times higher than the thermal conductivity of 0.46 W $(m\ K)^{-1}$, obtained for benchmark HDPE, which matches literature values for the thermal conductivity of HDPE well.[44–46] We are confident that even higher thermal conductivities in print direction of all-PE material are accessible by optimizing the printing conditions and the 3D printer to overcome the current processing limitation. Remarkably high metal-like thermal conductivities for PE have already been achieved in ultra-drawn nanofibers,[31,32] which represents an upper limit of what is possible with PE as a material. Moreover, the thermal conductivity in our all-PE material is 5 times higher in the print direction than perpendicular to it (0.26 W $m^{-1}\ K^{-1}$); thus, a high thermal anisotropy of up to 5 is achieved in our case using a conventional FFF 3D printer. In a broader context, our observed thermal conductivities can also be achieved by other material classes, *e.g.* ceramics,[47–49] metallic foams,[50,51] or other composite materials. Depending on the desired field of application and processing methods at hand, such other material classes can also be tuned for optimum performance with respect to their anisotropy, usable temperature range, or environmental resilience. A major advantage of the all-PE materials discussed here is their comparatively high thermal conductivity, while being soft and electrically insulating at the same time. In addition, the absence of a second compound eases the processability, while preserving the anisotropy of heat transport. FFF is, therefore, suitable to fabricate specimens with complex and computer aided distributions of anisotropic heat transport.

Digitally controlled temperature distribution

The orientation of the shish-kebab structures can be digitally tuned by the print direction. Also, the thermal diffusivity correlates with the shish-kebab orientation. Consequently, the digital control over the print direction can be used to define the temperature distribution in a 3D-printed all-PE specimen. A simulation based on Comsol Multiphysics was used to verify this concept in a first approach. For this purpose, a cuboid-shaped specimen (24 mm × 13 mm × 0.2 mm) was constructed using the computer aided design (CAD) software FreeCAD. The applied thickness of 0.2 mm corresponds to the height of a single printed layer. For a realistic simulation, the density and heat capacity of printed all-PE material was used to calculate the thermal conductivity. A density of 0.913 g cm^{-3} ± 0.004 g cm^{-3} was measured by helium pycnometry and a heat capacity of 1.28 ± 0.03 J $(g\ K)^{-1}$ was obtained by differential scanning calorimetry (DSC). Using the thermal diffusivity value known from lock-in thermography, the thermal conductivity of the all-PE material printed with a print temperature of 200 °C

and a print speed of 25 mm s^{-1} was calculated in the print direction (1.14 W m^{-1} K^{-1}) and perpendicular to the print direction (0.25 W m^{-1} K^{-1}) (Formula (S8)†). In Comsol Multiphysics the calculated thermal conductivity values parallel and perpendicular to the print direction were assigned to different segments of the constructed sample as visualized in Fig. 4a. According to the figure, a heat source at 75 °C is located on the top and below the specimen. The finite element method (FEM) provided the steady state temperature distribution for such a specimen. The shape of the isotherms clearly indicated that heat originating from the heat source is transferred preferably in the direction resembling the print direction. Therefore, the decrease in temperature is significantly enhanced in the perpendicular direction. As a result, different temperatures are obtained at equivalent distances to the heat source depending on the theoretical 3D printing directions.

To validate the findings of the simulation, the designed sample was 3D-printed by FFF from the all-PE filament with printing parameters (200 °C, 25 mm s^{-1}) according to the simulation (Fig. 4b). The heating of the sample was tracked using an IR camera, and the obtained temperature evolution is shown in Fig. 4c. After 600 s of heating, the printed sample was in a steady state. Although the absolute temperature distribution was not identical to the simulated steady state, the isotherm shapes are similar, especially in proximity to the heat source. As the thermal energy is transported preferably in the print direction, an anisotropic temperature distribution is clearly observable. This effect is even more pronounced during the heating process. The temperature differences between the right and left-hand side of the heat source were induced by digitally defining the print directions, thus controlling the orientation of the shish-kebab crystals.

Having verified the possibility to control the temperature distributions in a single-layered specimen, the concept is further advanced to a higher, multi-layered sample. It consisted of two parts, exhibiting print directions vertically to one another: a cuboidal part and a part surrounding the cuboid (Fig. 5a). The sample is printed from all-PE filament using the same 3D printing parameters as for the single-layered sample (200 °C, 25 mm s^{-1}). It must be noted that warping and associated splitting at layer boundaries represented a challenge during the 3D printing process, which should be addressed in the future by further engineering of 3D printing parameters and the 3D printer itself. Nonetheless, for the purpose of demonstrating controlled heat flow, the obtained specimen was sufficiently well 3D printed (Fig. S7†). The specimen's shape was selected for two reasons. On the one hand, the inclination helps to evade print failure based on warping, and on the other hand, asymmetry ensures that the design can be excluded as a reason for potential temperature differences. The specimen was placed on a hot plate at 75 °C so the 3D printing direction of the cuboidal part is vertical to a heat source. The temperature evolution on the specimen's surface was monitored *via* IR camera (Fig. 5b). It was clearly observable that the surface of the cuboidal part warms up much faster than its surrounding with a 3D printing direction parallel to the heat source. Furthermore, the surface corresponding to the vertical part was significantly warmer in the equilibrium state (after 500 s). Both observations were valid for the entire sample surface, thus for the inner area as well as for the sample boundaries that are more strongly

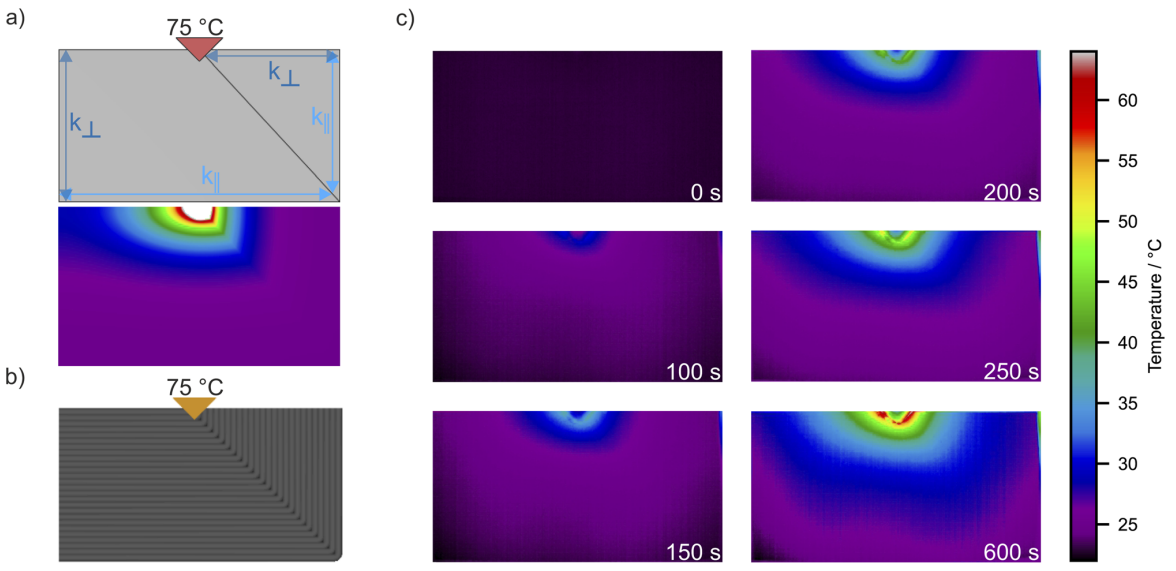

Fig. 4 Surface temperature distributions of a single-layered sample, printed by FFF using two different print directions and heated by a point-like heat source at 75 °C. (a) Designed sample for the simulation of the temperature distribution. The thermal conductivities of the sample are defined according to the thermal conductivity of a sample printed by FFF in the print direction ($k_{\parallel}$) and perpendicular to the print direction ($k_{\perp}$). The steady-state result of the simulation is provided. (b) Visualization of the 3D printed sample with two different print directions and the position of a copper heat source at 75 °C. (c) Evolution of the surface temperature distribution monitored *via* an IR camera.

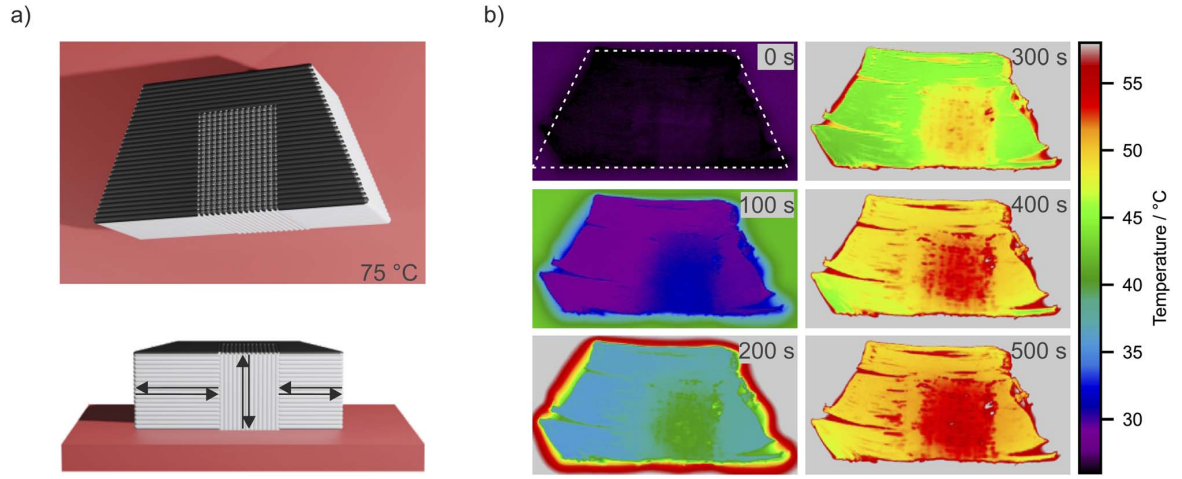

Fig. 5 Surface temperature distributions of a multi-layered sample, printed by FFF using two different print directions and placed on a hot plate at 75 °C. (a) Visualization of the all-PE sample (top and side view). Print directions are indicated by arrows. (b) Evolution of the surface temperature distribution monitored *via* IR camera.

affected by convective cooling. The results demonstrated that the anisotropic thermal diffusivity of all-PE material can be used to tailor the temperature distributions also in multi-layered parts by digitally tuning the 3D printing directions. Consequently, the all-PE material comprises a substantial potential for effective heat dissipation by a single-component material.

Conclusions

Thermal anisotropy of 3D-printed all-PE material containing high amounts of disentangled UHMWPE was investigated and evaluated in the context of heat management applications. A combination of polarized IR spectroscopy, WAXS, SAXS, and SEM showed that processing of all-PE material by FFF leads to the alignment of extended-chain UHMWPE forming shish-kebab structures with preferred orientation in the 3D printing direction. 3D-printed benchmark HDPE, lacking the UHMWPE, and filament of the benchmark HDPE and all-PE material were used as reference materials. A comparison of the references to 3D-printed all-PE samples revealed that shish-kebab evolution requires both: high shear and elongation forces exerted by FFF and elongated UHMWPE, to form nanofibre-like shish crystals, nucleating the kebab crystallization. The structural anisotropy of the printed all-PE material is linked to its significant thermal anisotropy. Whereas 3D-printed benchmark HDPE exhibited an isotropic thermal diffusivity, the thermal diffusivity of the printed all-PE material was significantly enhanced parallel to the 3D printing direction. As the increased thermal diffusivity was only observable in all-PE material along the 3D printing direction, it is evident that the shish-kebab formation induced by extended-chain UHMWPE is responsible for the effect. It is plausible that the fibre-like shish crystals function as continuous heat conducting paths, leading to enhanced thermal diffusivity along the fibre axes. The result was further proven by the correlation of the thermal diffusivities of 3D-printed all-PE samples and the applied 3D printing parameters. Increased print speed and reduced print temperature improved the thermal diffusivity along the 3D printing direction. A thermal anisotropy of up to 5 was achieved with a conventional home use FFF printer and we are confident that even higher anisotropies are accessible in combination with an optimized 3D printer setup. Anisotropic thermal conductivity combined with a freely definable 3D printing direction provided control over the temperature distribution in 3D printed all-PE specimens. This was validated by a FEM simulation, single-layered, and multi-layered all-PE specimens produced by FFF. In all cases, an asymmetric temperature distribution was achieved digitally predefined by the 3D printing parameters. With further optimization of the FFF printing process, great freedom in design is in prospect, considering both the specimen morphology itself and the orientation distribution of anisotropic heat conducting sections. In conclusion, the results obtained in the scope of this work revealed the potential of 3D-printed all-PE material as a low-weight, low cost, and highly sustainable recyclable material for digitally tuning heat flow and an efficient heat dissipation.

Experimental

Materials

For the preparation of all-PE material a nanophase separated reactor blend consisting of disentangled UHMWPE ($M_W > 10^6$ g mol^{-1}, 14 wt%) and HDPE wax ($M_W < 5 \times 10^3$ g mol^{-1}, 4 wt%) was melt compounded with benchmark HDPE at a ratio of 7 to 3 by the Freiburg Materials Research Center FMF according to the procedure previously reported by T. Hees *et al.*[28] HDPE Hostalen GC7260 (10^3–10^5 g mol^{-1}), used as the benchmark material and as matrix component in all-PE material, was provided by LyondellBasell. The filaments of benchmark HDPE and all-PE

material with diameters of 2.74 mm and 2.68 mm, respectively, were kindly supplied by the Freiburg Materials Research Center FMF. They were obtained by extruding powder of all-PE material or the pure HDPE benchmark using the single-screw extruder RCP-MT250 by Randcastle equipped with a 2.30 mm nozzle at an extrusion temperature of 200 °C and a screw speed of 100 rpm. The extruded polymer strands were water-cooled, pulled off with a takeoff speed of 7 mm s^{-1} and collected on a spool.

Fused filament fabrication (FFF)

CAD models were designed using the software FreeCAD 0.19. They were imported as stl data files into the software Ultimaker Cura 4.11. This software was applied to define the print parameters and subsequently generate gcode files of the prints. The print temperature and print speed was varied, whereas the print bed temperature was constantly set to 60 °C. A line width of 0.7 mm, layer height of 0.2 mm and a distance between the lines of 0.5 mm was applied. Samples were printed by FFF using an Ultimaker 3 FFF printer and the print core AA with a nozzle diameter of 0.8 mm, both by Ultimaker BV. The samples prepared for IR spectroscopy, SAXS, WAXS and lock-in thermography measurements were printed as a single layer with a height of 0.2 mm. For the IR measurements the corresponding print parameters were 210 °C and 100 mm s^{-1}. For WAXS, SAXS and lock-in thermography measurements, the print parameters were varied between 200 °C and 230 °C and between 25 mm s^{-1} and 100 mm s^{-1}. The sample used for SEM was printed multi-layered with a print temperature of 200 °C and a print speed of 25 mm s^{-1}. For the analysis of temperature evolution and distribution on the surface of printed specimens by IR camera one single- and one multi-layered sample was prepared, both printed with a temperature of 200 °C and print speed of 25 mm s^{-1}. The cuboid shaped single-layered specimen consisted of two parts with print directions perpendicular to one another, as shown in Fig. 4b. The multi-layered sample was printed according to Fig. 5a. The inclinations were included as they diminish the risk of the nozzle hitting the specimen and inducing print failure, due to warpage.

Characterization by IR, X-ray scattering, SEM, DSC and helium pycnometer

Polarized broadband IR spectroscopy was applied using Vertex 70 by Bruker Corporation in combination with a polarizer.

Preliminary SAXS and WAXS experiments were performed on single-layer samples printed *via* FFF on a lab-based Double Ganesha AIR system by SAXSLAB/Xenocs. This system is equipped with a copper rotating anode MicroMax 007HF by Rigaku Corporation with a wavelength of $\lambda = 1.54$ Å and position-sensitive Pilatus detectors from Dectris Ltd (300 K for SAXS, 100 K for WAXS). Additionally, we are grateful for measurements performed at the beamline IDO2 at ESRF in Grenoble, France. The corresponding beam energy was set to 12.2 keV and simultaneous SAXS/WAXS measurements were performed using an Eiger2-4M for SAXS and a Rayonix LX170 for WAXS, spanning together a q range from 0.07 nm^{-1} to 46.53 nm^{-1}. Data reduction and azimuthal integration were performed with a software provided by ID02, including the software packages SAXSutilities2 and PyFAI.[52–54] If needed, the 2D scattering patterns were converted to 1D profiles of $I(q)$ *vs.* q, where q is given as $q = 4\pi/\lambda \sin(\theta/2)$ with θ being the scattering angle.

Additionally, powder X-ray (XRD) experiments were carried out with a Bragg–Brentano geometry Empyrean diffractometer equipped with a pixel detector in spinning mode using copper K_α ($\lambda = 0.15406$ nm) radiation by Malvern Panalytical BV. The instrument provides the Pananlytical's Highscore Plus software for data analysis.

To obtain SEM images the multi-layered all-PE material was split into smaller pieces after cooling with liquid nitrogen. The pieces were etched by xylene at 100 °C to 130 °C and dried by compressed air multiple times. After sputtering 2 nm platinum on the pieces, images were obtained with a Zeiss Leo 1530 by Carl Zeiss AG at an operating voltage of 3 kV and a secondary electron detector.

DSC measurements were applied using a Discovery DSC 2500 by TA Instruments Inc. The heat capacity of all-PE material was determined according to the American Society for Testing and Materials (ASTM) E1269 standard. The sample was heated from −10 °C to 160 °C with a heating rate of 20 °C min^{-1}. It was kept at 160 °C for 10 min and then cooled to −10 °C with a rate of 10 °C min^{-1}, where it was held for 10 min. The heat flux was recorded while heating to 160 °C with a rate of 20 °C min^{-1} in a second heating cycle and the recorded heat flux was used to calculate the heat capacity. The measurement was repeated for 3 samples and the mean heat capacity at 25 °C with the corresponding standard deviation was acquired (1.28 J $(g\ K)^{-1} \pm 0.03$ J $(g\ K)^{-1}$). The heat flows of the first heating cycle of printed single layer samples were acquired using a heating rate of 10 °C min^{-1}. The degrees of crystallization were calculated using the software TRIOS 5.1.1 by TA Instruments and the heat of fusion for 100% crystalline HDPE of 293 J g^{-1}.[55]

The densities of printed single-layered all-PE samples were obtained from a Ultrapyc 1200e helium pycnometer by Quantachrome Instruments. To determine the average density and corresponding standard deviation 25 individual measurement results were used.

Lock-in thermography

The single-layered samples were coated with a thin layer of carbon (10–20 nm) on both sides before performing lock-in thermography. Lock-in thermography is used to measure the temperature evolution of a theoretically infinitely thin sample. The samples were excited periodically with a frequency of 0.8 Hz using a continuous wave Coherent Genesis MX532-1000 laser with powers between 8 mW and 11 mW. The temperature evolution was monitored with an ImageIR 9430 research IR camera by InfraTec GmbH, exhibiting a spectral window from 1.5 μm to 5.5 μm and mounted with an $M = 1.0\times$ microscopy objective. Convective heat losses were minimized by performing the experiment in a vacuum chamber ($p < 10^{-2}$ mbar) containing an optically transparent N-BK7 glass window for the laser to pass through. The time–temperature data were converted by

Fourier transformation to an amplitude and phase signal using the IRBIS software provided by the manufacturer.[41–43,56] For samples with an anisotropic amplitude and phase signal an ellipse was fitted to the respective signals. The slope method for thin films was applied to the long and the short axis of the fitted ellipse to obtain the maximum and minimum thermal diffusivity of the sample. For the isotropic sample the slope method was applied to all data points within the same concentric distance from the laser heating spot to obtain the thermal diffusivity.

Simulation of the steady state heat distribution

A specimen (24 mm × 13 mm × 0.2 mm) composed of two parts was designed in the general-purpose CAD software FreeCAD (Version 0.19). Also, two right-angled triangles (hypotenuse: 4 mm) contacting the specimens from the top and the bottom were designed. All 4 parts were imported into the software Comsol Multiphysics (Version 6.0) as step data files, organized as in Fig. 4a. The material properties of copper were provided by the software and were assigned to the triangles, whereas the thermal properties (heat capacity, density and thermal conductivity) of an all-PE sample printed with 200 °C and 25 mm s^{-1} were assigned to the remaining two parts. Thereby the thermal conductivity in print direction was assigned to the thermal conductivity in the direction of the *x*-axis. The thermal conductivity known for the perpendicular direction was assigned to the direction of the *y*-axis. Although the conductivity in the build direction has not been measured, heat transport in this direction is also perpendicular to the shish-kebab orientation. Hence, the value set for the thermal conductivity in the *y*-axis direction was adopted for the thermal conductivity in the *z*-axis direction. To resemble two sections with perpendicular print directions the thermal properties of one of the two all-PE material parts were turned by 90° by applying turning matrices.[57] A room temperature of 25 °C and a heat transfer coefficient of 5 W $(m^2\ K)^{-1}$ was assumed. Radiative heat losses were neglected. The temperature of the triangles resembling copper were set to 75 °C and the steady state of the set-up was simulated by FEM.

Monitoring of the temperature evolution

For analyzing the temperature distribution with time of a heated single-layered 3D printed all-PE material sample, a cuboid of copper was placed on silver heating block controlled by a mK2000 Precision Temperature Controller by InStec Inc. The sample was coated with a thin layer of graphite and placed on the corner of the copper cuboid. It was weighted with another copper piece according to Fig. 4b. On the areas of contact between copper piece and heat plate, as well as sample and copper piece, Thermal Joint Compound Type 120 by Wakefield Solutions, Inc. was applied to ensure good thermal contact. A VarioCAM HD research IR camera by InfraTec GmbH with a spectral window of 7.5 μm to 14 μm was positioned above the set up. The heat plate was set to 75 °C and recording of the temperature evolution on the sample surface was begun simultaneously. Images were taken with a frequency of 1 s^{-1} until a steady state was reached.

For the analysis of the time-dependent temperature distribution of the surface of a multi-layered 3D printed all-PE sample, two sides of the sample were ground to ensure a homogeneous surface contact with the heat plate and to diminish any roughness influence on the IR images. The IR camera facing side was coated with graphite and placed on a silver heating block controlled by a mK2000 Precision Temperature Controller by InStec Inc. The thermal contact was increased *via* Thermal Joint Compound Type 120 by Wakefield Solutions, Inc. A VarioCAM HD research IR camera by InfraTec GmbH was positioned above the setup. The heat plate was set to 75 °C, and the temperature evolution on the sample surface was recorded simultaneously. Images were taken with a frequency of 0.5 s^{-1} until a steady state was reached.

Author contributions

IK: conceptualization, investigation, methodology, writing-original draft, visualization; TT: investigation, methodology, writing – review/editing; RR: writing – review/editing, resources; MT: investigation, methodology; SR: investigation, methodology, writing – review/editing, supervision; MS: investigation, writing – review/editing; CS: conceptualization, resources, writing – review/editing; PB: methodology, writing – review/editing; SR: investigation; RM: resources, writing – review/editing; MR: conceptualization, resources, funding, writing – review/editing, supervision.

Conflicts of interest

There are no conflicts to declare.

Acknowledgements

We thankfully acknowledge the supply of polymeric material by LyondellBasell Industries. Additionally, we are grateful for the measurements performed at the beamline ID02 at ESRF in Grenoble, France. This work has been supported by Collaborative Research Center 1585, Project C05 of the German Research Foundation (Grant number 492723217).

References

1 Y. Guo, C. Dun, J. Xu, J. Mu, P. Li, L. Gu, C. Hou, C. A. Hewitt, Q. Zhang, Y. Li, D. L. Carroll and H. Wang, *Small*, 2017, **13**, 1702645.
2 Y. Cui, Z. Qin, H. Wu, M. Li and Y. Hu, *Nat. Commun.*, 2021, **12**, 1284.
3 Q. Li, L. Chen, M. R. Gadinski, S. Zhang, G. Zhang, U. Li, E. Iagodkine, A. Haque, L. Q. Chen, N. Jackson and Q. Wang, *Nature*, 2015, **523**, 576–579.
4 J. Chen, X. Huang, Y. Zhu and P. Jiang, *Adv. Funct. Mater.*, 2017, **27**, 1604754.
5 J. Chen, X. Huang, B. Sun and P. Jiang, *ACS Nano*, 2019, **13**, 337–345.

6 Z. Liu, Y. Chen, Y. Li, W. Dai, Q. Yan, F. E. Alam, S. Du, Z. Wang, K. Nishimura, N. Jiang, C. T. Lin and J. Yu, *Nanoscale*, 2019, **11**, 17600–17606.
7 N. Wang, M. K. Samani, H. Li, L. Dong, Z. Zhang, P. Su, S. Chen, J. Chen, S. Huang, G. Yuan, X. Xu, B. Li, K. Leifer, L. Ye and J. Liu, *Small*, 2018, **14**, e1801346.
8 H. Oh and J. Kim, *Compos. Sci. Technol.*, 2019, **172**, 153–162.
9 W.-Y. Zhou, S.-H. Qi, H.-Z. Zhao and N.-L. Liu, *Polym. Compos.*, 2007, **28**, 23–28.
10 H. Ma, B. Gao, M. Wang, Z. Yuan, J. Shen, J. Zhao and Y. Feng, *J. Mater. Sci.*, 2020, **56**, 1064–1086.
11 C.-P. Feng, L.-Y. Yang, J. Yang, L. Bai, R.-Y. Bao, Z.-Y. Liu, M.-B. Yang, H.-B. Lan and W. Yang, *Compos. Commun.*, 2020, **22**, 100528.
12 S. Jasmee, G. Omar, S. S. C. Othaman, N. A. Masripan and H. A. Hamid, *Polym. Compos.*, 2021, **42**, 2629–2652.
13 S. Moradi, Y. Calventus, F. Roman and J. M. Hutchinson, *Polymers*, 2019, **11**, 1156.
14 K. Pashayi, H. R. Fard, F. Lai, S. Iruvanti, J. Plawsky and T. Borca-Tasciuc, *J. Appl. Phys.*, 2012, **111**, 104310.
15 Y. Sun, Y. He, B. Tang, C. Tao, J. Ban and L. Jiang, *RSC Adv.*, 2017, **7**, 55790–55795.
16 K. Yang and M. Gu, *Composites, Part A*, 2010, **41**, 215–221.
17 X. Chen, K. Wu, Y. Zhang, D. Liu, R. Li and Q. Fu, *Adv. Mater.*, 2022, **34**, e2206088.
18 J. Han, G. Du, W. Gao and H. Bai, *Adv. Funct. Mater.*, 2019, **29**, 1900412.
19 Y. Yao, Z. Ye, F. Huang, X. Zeng, T. Zhang, T. Shang, M. Han, W. Zhang, L. Ren, R. Sun, J. B. Xu and C. P. Wong, *ACS Appl. Mater. Interfaces*, 2020, **12**, 2892–2902.
20 X. He, D. Ou, S. Wu, Y. Luo, Y. Ma and J. Sun, *Adv. Compos. Hybrid Mater.*, 2021, **5**, 21–38.
21 Y. Yang, R. Boom, B. Irion, D.-J. van Heerden, P. Kuiper and H. de Wit, *Chem. Eng. Process.*, 2012, **51**, 53–68.
22 G. Chatziparaskeva, I. Papamichael, I. Voukkali, P. Loizia, G. Sourkouni, C. Argirusis and A. A. Zorpas, *Microplastics*, 2022, **1**, 377–392.
23 R. Bernatas, S. Dagreou, A. Despax-Ferreres and A. Barasinski, *Cleaner Engineering and Technology*, 2021, **5**, 100272.
24 C. G. Schirmeister and R. Mulhaupt, *Macromol. Rapid Commun.*, 2022, **43**, e2200247.
25 T. Hees, F. Zhong, M. Sturzel and R. Mulhaupt, *Macromol. Rapid Commun.*, 2019, **40**, e1800608.
26 M. Stürzel, A. G. Kurek, T. Hees, Y. Thomann, H. Blattmann and R. Mülhaupt, *Polymer*, 2016, **102**, 112–118.
27 C. G. Schirmeister, T. Hees, O. Dolynchuk, E. H. Licht, T. Thurn-Albrecht and R. Muelhaupt, *ACS Appl. Polym. Mater.*, 2021, **3**, 1675–1686.
28 T. Hees, F. Zhong, C. Koplin, R. Jaeger and R. Mülhaupt, *Polymer*, 2018, **151**, 47–55.
29 S. C. Ligon, R. Liska, J. Stampfl, M. Gurr and R. Mulhaupt, *Chem. Rev.*, 2017, **117**, 10212–10290.
30 X. Wang, V. Ho, R. A. Segalman and D. G. Cahill, *Macromolecules*, 2013, **46**, 4937–4943.
31 Y. Xu, D. Kraemer, B. Song, Z. Jiang, J. Zhou, J. Loomis, J. Wang, M. Li, H. Ghasemi, X. Huang, X. Li and G. Chen, *Nat. Commun.*, 2019, **10**, 1771.
32 S. Shen, A. Henry, J. Tong, R. Zheng and G. Chen, *Nat. Nanotechnol.*, 2010, **5**, 251–255.
33 S. Krimm, C. Y. Liang and G. B. B. M. Sutherland, *J. Chem. Phys.*, 1956, **25**, 549–562.
34 S. Krimm, *Fortschr. Hochpolym.-Forsch.*, 1960, **2**, 51–172.
35 J. L. White, K. C. Dharod and E. S. Clark, *J. Appl. Polym. Sci.*, 1974, **18**, 2539–2568.
36 R. S. Stein, *J. Polym. Sci.*, 1958, **31**, 327–334.
37 K. Tashiro and H. Yamamoto, *Polymers*, 2019, **11**, 1316.
38 S. Cusack and A. Miller, *J. Mol. Biol.*, 1979, **135**, 39–51.
39 Z. Wang, K. Rolle, T. Schilling, P. Hummel, A. Philipp, B. A. F. Kopera, A. M. Lechner, M. Retsch, J. Breu and G. Fytas, *Angew Chem. Int. Ed. Engl.*, 2020, **59**, 1286–1294.
40 T. Dorres, M. Bartkiewicz, K. Herrmann, M. Schottle, D. Wagner, Z. Wang, O. Ikkala, M. Retsch, G. Fytas and J. Breu, *ACS Appl. Nano Mater.*, 2022, **5**, 4119–4129.
41 A. Mendioroz, R. Fuente-Dacal, E. Apinaniz and A. Salazar, *Rev. Sci. Instrum.*, 2009, **80**, 074904.
42 B. Zhang and R. E. Imhof, *Appl. Phys. A: Mater. Sci. Process.*, 1996, **62**, 323–334.
43 L. Fabbri and P. Fenici, *Rev. Sci. Instrum.*, 1995, **66**, 3593–3600.
44 C.-M. Ye, B.-Q. Shentu and Z.-X. Weng, *J. Appl. Polym. Sci.*, 2006, **101**, 3806–3810.
45 T. A. Osswald, E. Baur, S. Brinkmann, K. Oberbach and E. Schmachtenberg, in *International Plastics Handbook*, 2006, pp. 63–269, DOI: **10.3139/9783446407923.003**.
46 M. D. Lechner, in *Springer Handbook of Condensed Matter and Materials Data*, 2005, ch. 7, pp. 477–522, DOI: **10.1007/3-540-30437-1_7**.
47 Y. Chen, N. Wang, O. Ola, Y. Xia and Y. Zhu, *Mater. Sci. Eng., R*, 2021, **143**, 100589.
48 H. Xiang, Y. Xing, F.-Z. Dai, H. Wang, L. Su, L. Miao, G. Zhang, Y. Wang, X. Qi, L. Yao, H. Wang, B. Zhao, J. Li and Y. Zhou, *J. Adv. Ceram.*, 2021, **10**, 385–441.
49 K. Watari, *J. Ceram. Soc. Jpn.*, 2001, **109**, S7–S16.
50 C. Y. Zhao, *Int. J. Heat Mass Transfer*, 2012, **55**, 3618–3632.
51 M. Fink, O. Andersen, T. Seidel and A. Schlott, *Metals*, 2018, **8**, 554.
52 M. Sztucki, *Zenodo*, 2021, DOI: **10.5281/zenodo.5825707**.
53 T. Narayanan, M. Sztucki, P. Van Vaerenbergh, J. Leonardon, J. Gorini, L. Claustre, F. Sever, J. Morse and P. Boesecke, *J. Appl. Crystallogr.*, 2018, **51**, 1511–1524.
54 J. Kieffer and D. Karkoulis, *J. Phys.: Conf. Ser.*, 2013, **425**, 202012.
55 B. Wunderlich and G. Czornyj, *Macromolecules*, 2002, **10**, 906–913.
56 A. Salazar, A. Mendioroz and R. Fuente, *Appl. Phys. Lett.*, 2009, **95**, 121905.
57 T. L. v. Vuure, *presented in part at the COMSOL2013 Conference Proceedings*, Rotterdam, 2013.

Supporting Information

High and Tuneable Anisotropic Thermal Conductivity Controls the Temperature Distribution of 3D Printed All-Polyethylene Objects

Ina Klein [a], Thomas Tran [a], René Reiser [b,c], Maximilian Theis [a], Sabine Rosenfeldt [a], Marius Schöttle [a], Carl Schirmeister [b,c], Peter Bösecke [d], Stefan Rettinger [a], Rolf Mülhaupt [b] and Markus Retsch [a, e]

[a.] *Department of Chemistry, Physical Chemistry I, University of Bayreuth, 95447 Bayreuth, Germany.*

[b.] *Freiburg Materials Research Center FMF and Institute for Macromolecular Chemistry, Albert-Ludwigs-University Freiburg, 79104 Freiburg, Germany.*

[c.] *LyondellBasell Industries, Industriepark Höchst, 65926 Frankfurt am Main, Germany.*

[d.] *European Synchrotron Radiation Facility (ESRF), 71 Avenue des Martyrs, CS 40220, 38043 Grenoble Cedex 9, France*

[e] *Bavarian Polymer Institute, Bayreuth Center for Colloids and Interfaces, and Bavarian Center for Battery Technology (BayBatt), University of Bayreuth, 95447, Germany*

Infrared Spectroscopy

Table S1: Broad band infrared spectrum and assignments for 3D printed all-PE material.

Wave number / cm^{-1}	Polarization	Assignment
719	σ	$\gamma_r(CH_2)$ [1, 2]
730	σ	$\gamma_r(CH_2)$ [1, 2]
908	σ	$\delta(R–CH{=}CH_2)$ [2]
966	σ	$\gamma_r(CH_3)$, trans RCH=CHR' [2]
991	σ	$RCH{=}CH_2$ [2]
1051	π	$\gamma_t(CH_2)$ [2]
1082	σ	$\nu(C–C)$ [2]
1177	π	$\gamma_w(CH_2)$ [2]
1188	σ	
1304	π	$\gamma_w(CH_2)$, $\gamma_t(CH_2)$, amorphous [1-3]
1352	π	$\gamma_w(CH_2)$, amorphous [1-3]
1367	π	$\gamma_w(CH_2)$[1-3]
1464	σ	$\delta(CH_2)$[1, 2]
1472	σ	$\delta(CH_2)$ [1, 2]
1819	π	$\nu(C–C) + \gamma_r(CH_2)$ $2 \cdot \delta(R–CH{=}CH_2))$ [2]
1898	σ	$2 \cdot \gamma_r(CH_2)$ $2 \cdot RCH{=}CH_2$ (?) [2]
2019	π	$\gamma_t(CH_2) + \gamma_r(CH_2)$ [2]
2243	π	$\gamma_w(CH_2) + \nu(0)$ [2]
2328	σ	$\gamma_w(CH_2) + \gamma_r(CH_3)$ $2 \cdot \gamma_r(CH_2)$ [2]
2345	σ	$2 \cdot \gamma_t(CH_2)$ [2]
2635	σ	$\gamma_r(CH_2) + \delta(CH_2)$ [2]
2660	σ	$\gamma_w(CH_2) + \gamma_t(CH_2)$ [2]
2741	σ	$2 \cdot \gamma_w(CH_2)$ $\delta(CH_2) + \gamma_t(CH_2)$ [2]

~ 2837 – 2862	σ	$\nu_s(CH_2)$ [1, 2]
~ 2882 – 2941	σ	$\nu_a(CH_2)$ [1, 2]
3604	σ	$\nu_a(CH_2) + \gamma_r(CH_2)$ [2]
3643	π	$3 \cdot \gamma_t(CH_2)$ $\delta(CH_2) + \nu(\pi) + \nu(0)$ [2]
~ 4095 - 4195	σ	$\nu_a(B_{1u}) + \gamma_r(A_g)$ $\nu_a(CH_2) + \gamma_t(CH_2)$ [2]
4220	π	$\nu_{as}(CH_2) + \gamma_w(CH_2)$ [4]
4251	σ	$\nu_s(CH_2) + \delta(CH_2)$ [4]
4322	σ	$\nu_{as}(CH_2) + \delta(CH_2)$ [4]
5664	σ	$2 \cdot \nu_s(CH_2)$ [4]
5775	σ	$2 \cdot \nu_a(CH_2)$ [4]

IR spectroscopy of unidirectionally printed all-PE material is applied for polarization angles between 10° and 100°. The values can be extrapolated to angles between 90° and 360°. A peanut shape, typical for the display of Malus' Law, can be fitted.[5] However, the original form of Malus' Law (Formula S1) cannot be fully adopted, as the transmission of the polarized IR frequencies (ν) does not range between 0 and the initial intensity (T_0), but between a minimum (T_{min}) and maximum transmission (T_{max}), thus Malus' Law is adjusted according to Formula S2.1 and S2.2.

Malus' Law	$T(\nu) = T_0(\nu) \cos^2(\sigma)$	Formula S1
Parallel polarized frequencies:	$T(\nu) = [T_{max}(\nu) - T_{min}(\nu)] \cos^2(\sigma + 90\,°) + T_{min}$	Formula S2.1
Perpendicular polarized frequencies:	$T(\nu) = [T_{max}(\nu) - T_{min}(\nu)] \cos^2(\sigma) + T_{min}$	Formula S2.2

The adjusted Malus' Laws show that the change in transmission is proportional to the squared cosine of the angle σ, whereby σ is the deviation between print direction and light polarization.

Wide Angle X-Ray Scattering and X-Ray Diffraction

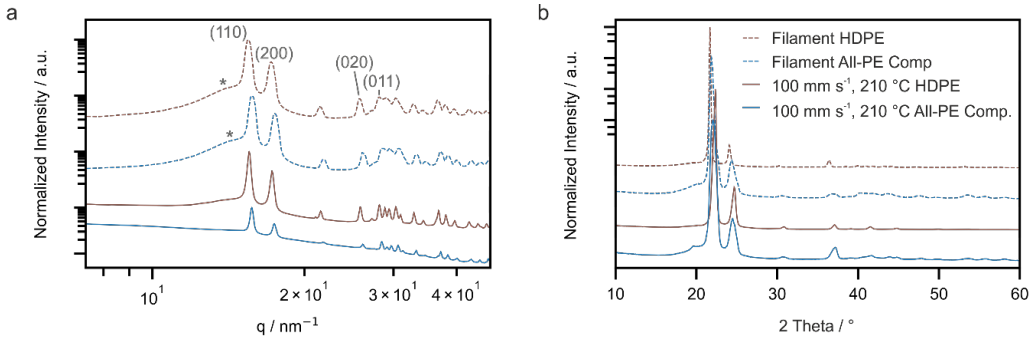

Figure S1: Spectra of the benchmark HDPE filament, all-PE filament and therewith 3D printed samples. The lattice planes (110), (200), (020) and (011) of orthorhombic PE are labeled.[6] a) WAXS measurements performed in transmission geometry b) XRD measurements performed in Bragg-Brentano geometry and spinning mode.

In agreement with the literature, WAXS and XRD spectra reveal mainly orthorhombic PE crystal cells of the space group Pnam.[6] Furthermore, the measured data exhibit a weak signal for both filaments at around 14 nm^{-1} (asteriscs in Fig. S1 a), which diminishes by processing the materials by FFF. The signal can be based on amorphous PE and small amounts of the (010) plane of monoclinic crystallized PE. Both amorphous and monoclinic PE could be converted into the orthorhombic PE phase due to the melting and recrystallization process of FFF.

To describe the orientation of the PE chains more quantitatively the Hermans factor f_H is calculated using the azimuthal angle (ψ) dependent diffraction intensities ($I(\psi)$) corresponding to the hkl planes (200) and (020).[7, 8] The azimuthal plots are exemplary shown for printed all-PE material in Figure S2.

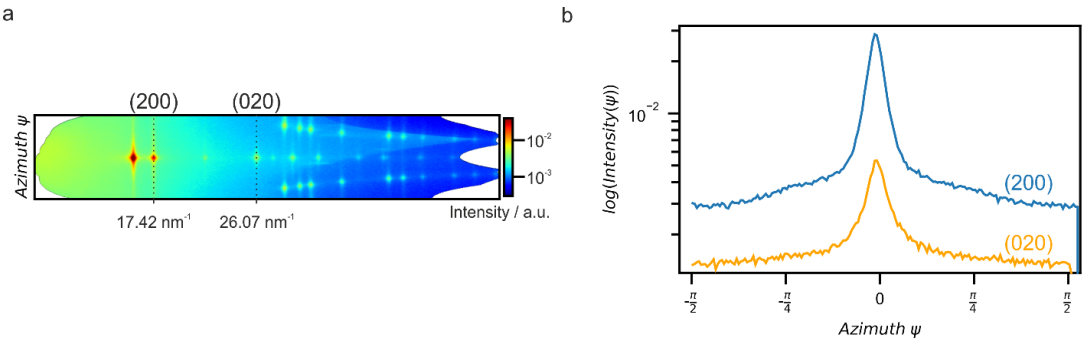

Figure S2: Wide angle X-ray scattering data of all PE material printed with 100 mm s^{-1} and 210 °C a) 2D Azimutal representation with indication of the hkl planes (200) and (020). b) Scattering intensity $I(\psi)$ vs. azimuth angle ψ for the hkl planes (200) and (020).

In a first step $\overline{\cos^2(\phi)}$ is calculated according to Formula S3 and S4. Hereby ϕ are the angles formed by the crystallographic axes a, b and c and θ represents the Bragg angle of the respective hkl plane.

$$\overline{\sin^2(\psi)} = \frac{\int_0^{\pi/2} I(\psi)\sin^2(\psi)\cos(\psi)\ d\psi}{\int_0^{\pi/2} I(\psi)\cos(\psi)\ d\psi} \qquad \text{Formula S3}$$

$$\overline{\cos^2(\phi)} = \cos^2(\theta)\ \overline{\sin^2(\psi)} \qquad \text{Formula S4}$$

The calculations are performed for all-PE filament, HDPE filament and therewith printed samples using a print temperature of 210 °C and a print speed of 100 mm s^{-1}.

Table S2 provides the Bragg angles θ and the values obtained for $\overline{\cos^2(\phi)}$.

Table S2: Bragg angles θ and calculated $cos^2(\phi)$ for all-PE filament and HDPE filament and therewith 3D printed samples.

Sample	hkl	θ / °	$\overline{\cos^2(\phi)}_a$	$\overline{\cos^2(\phi)}_b$
HDPE Filament	200	7.981	0.296	
	020	11.994		0.330
Printed HDPE	200	8.011	0.348	
	020	12.034		0.287
All-PE Filament	200	8.118	0.356	
	020	12.153		0.209
Printed All-PE	200	8.099	0.177	
Material	020	12.172		0.239

In a next step the orientation factors f_a and f_b can be calculated using Formula S5 and finally the Hermans factor f_H, which is equal to f_c, can be obtained *via* Formula S6.

$$f_a = 0.5\left(3\ \overline{\cos^2(\phi)}_a - 1\right)$$

Formula S5

$$f_b = 0.5\left(3\ \overline{\cos^2(\phi)}_b - 1\right)$$

$$f_H = f_c = -f_a - f_b$$

Formula S6

The Hermans orientation factor f_H is - 0.5 in the case of perpendicular orientation, 0 for isotropic conditions and 1 for perfect parallel orientation of the chains in the print direction. The resulting orientation factors, obtained from one thin film specimen per sample, are summarized in Table S3.

Table S3: Orientation factors f_a, f_b and f_c calculated for all-PE filament and benchmark HDPE filament and therewith 3D printed samples.

Sample	f_a	f_b	$f_c = f_H$
HDPE Filament	- 0.06	0.00	0.06
Printed HDPE	0.02	- 0.07	0.05
All-PE Filament	0.03	- 0.19	0.16
Printed All-PE Material	- 0.23	- 0.14	0.37

A comparison of WAXS measurements of printed all-PE material with various print temperatures and print speeds is applied to investigate the effect of print parameters on the crystal structure.

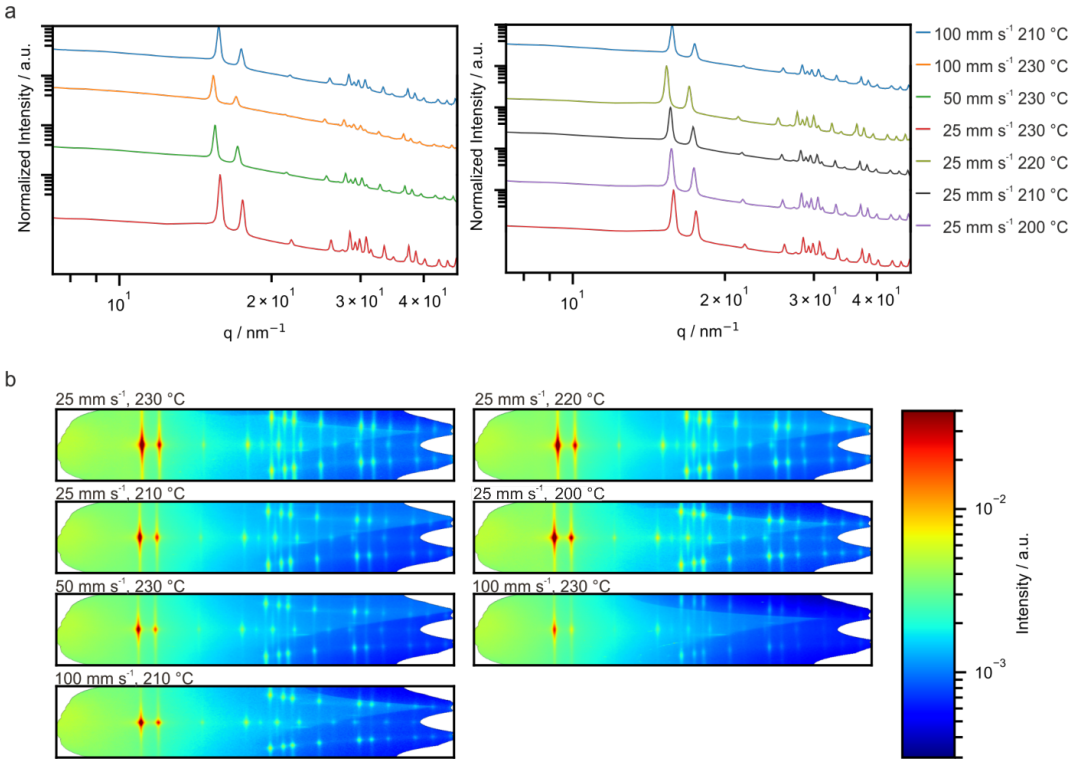

Figure S3: WAXS of all-PE material processed by FFF with various print temperatures and print speeds a) 1D WAXS spectra. b) 2D WAXS patterns (azimuth vs. momentum transfer).

Table S4: Orientation factors f_a, f_b and f_c calculated for all-PE material printed with various print temperatures and print speeds.

Sample	f_a	f_b	$f_c = f_H$
25 mm s^{-1} 230 °C	-0.21	-0.16	0.37
25 mm s^{-1} 220 °C	-0.23	-0.16	0.39
25 mm s^{-1} 210 °C	-0.20	-0.14	0.34
25 mm s^{-1} 200 °C	-0.25	-0.17	0.42
50 mm s^{-1} 230 °C	-0.16	-0.11	0.27
100 mm s^{-1} 230 °C	-0.10	-0.09	0.19
100 mm s^{-1} 210 °C	-0.23	-0.14	0.37

Figure S3 a and b show that neither the position of Bragg reflexes in 1D WAXS spectra, nor the 2D WAXS patterns significantly depend on print speed or print temperature used in our work. Furthermore, the Hermans factors, calculated from the WAXS spectra, do not indicate an unambiguous trend (Table S4). We note that all Hermans factor calculations were based on a single thin film specimen as shown in Fig. S3. Additional specimens for each combination of print speed and temperature should be measured to assess the accuracy of the Hermans factor calculation. Nonetheless, it is observable that the Hermans factors for all printed all-PE material samples indicate a PE chain alignment in the print direction.

The lattice parameters of the orthorhombic crystals are determined *via* Formula S7 for the corresponding lattice planes (110), (200), and (011).[6]

$$\frac{1}{d_{hkl}} = \frac{h^2}{a^2} + \frac{k^2}{b^2} + \frac{l^2}{c^2} \qquad \text{Formula S7}$$

The experimental lattice parameters are determined to a = 0.72 nm – 0.74 nm, b = 0.48 nm – 0.49 nm and c = 0.24 nm – 0.26 nm. These values are in agreement with the results found by Schirmeister *et al.*[9]

Small Angle X-Ray Scattering

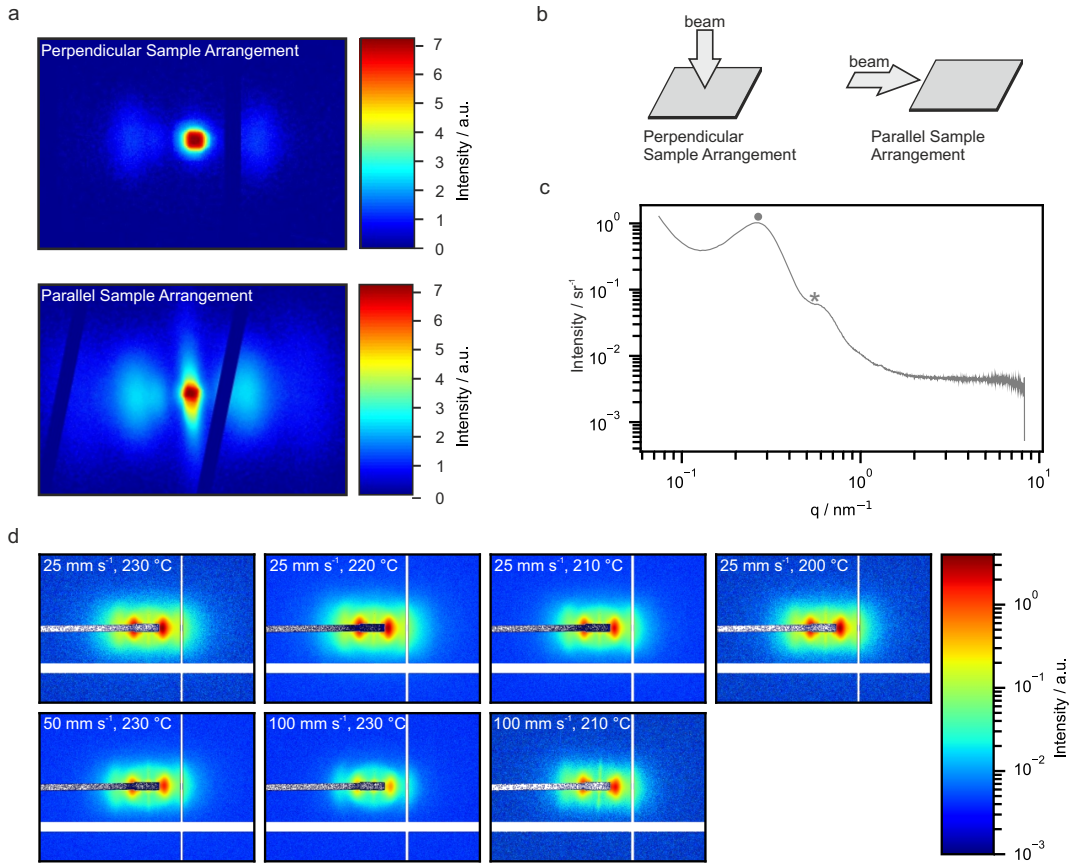

Figure S4: 2D SAXS of all-PE material processed by FFF (detector coordinates q_y vs. q_x) a) with a print speed of 100 mm s^{-1} and a print temperature of 210 °C measured by a lab-based *Double Ganesha AIR* system; Measurements performed perpendicular to the sample and parallel to the sample. b) Schematic illustration of the perpendicular and parallel arrangement of the beam and sample. c) 1D SAXS spectrum of all-PE material printed with 25 mm s^{-1} and 230 °C. The maximum (•) and faintly pronounced minimum (*) used to estimate the lamellar thickness and inter-lamellar distance, respectively, are indicated d) 2D SAXS of all-PE material processed by FFF with various print temperatures and print speeds.

Figure S4 a show the signals obtained with a lab-based system. The reflexes associated with shish-kebab crystal structures are significantly better visible when measured parallel to the printed layer compared to perpendicular arrangement of the beam and the printed layer (Figure S4 b). Note that in the case of perpendicular arrangement, the scattering contribution of the shish structures is not detectable, and the kebab structures solemnly provide a weak signal. Measurements *via* a high brilliance beamline provide a better resolution and allow fast measurements in the perpendicular arrangement. Both scattering

contributions of shish and kebab structures are easily detected. In contrast to our expectations, the 2D SAXS patterns are not significantly dependent on print speed or print temperature in the investigated parameter range (Figure S4 d). The SAXS data are furthermore used to estimate the thickness of the HDPE lamellae from a faintly pronounced local minimum (marked *****) at around 0.48 nm^{-1} and the inter-lamellar distances from a maximum (marked •) at roughly 0.26 nm^{-1}.

Table S5: Lamellar thicknesses and inter-lamellar distances of shish-kebab crystals in all-PE material processed by FFF with various print temperatures and print speeds and in all-PE filament.

Print Parameters	Thickness of lamellae / nm	Inter-lamellar distance / nm
Filament	13	24
100 mm s^{-1} 210 °C	13	24
100 mm s^{-1} 230 °C	13	23
50 mm s^{-1} 230 °C	13	25
25 mm s^{-1} 230 °C	14	27
25 mm s^{-1} 220 °C	13	27
25 mm s^{-1} 210 °C	13	25
25 mm s^{-1} 200 °C	13	26

The inter-lamellar distance appears to decrease slightly with increasing print speed, whereas no significant trend can be observed for the variation of the print temperature.

Differential Scanning Calorimetry

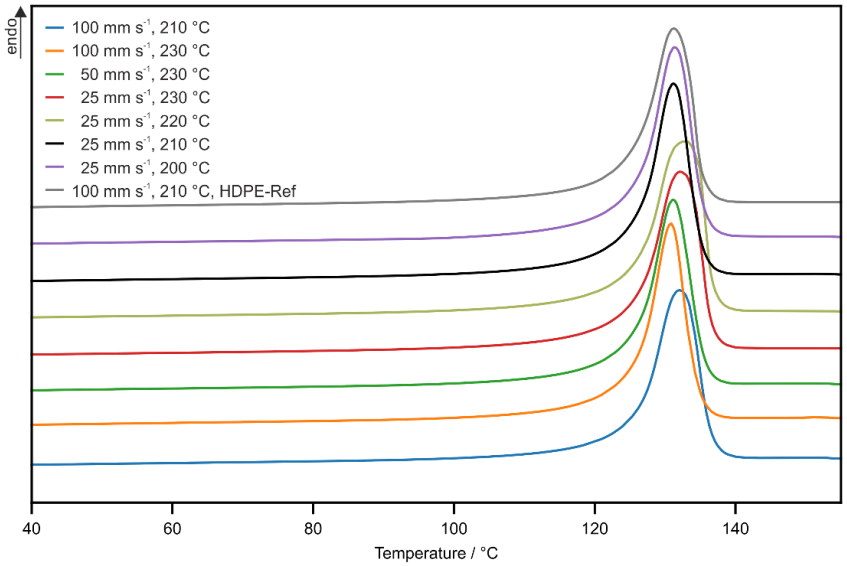

Figure S5: DSC traces of the first heat3D printed single-layered all-PE samples and benchmark HDPE reference.

No significant trend in heat flux can be observed for the variations in print temperature or print speed. Crystallinity of the samples is determined by integration of the melt peak. Table S6 summarizes the results.

Table S6: Degree of crystallinity in HDPE and all-PE material processed by FFF with various print temperatures and print speeds obtained from DSC.

Print Parameters	Melt temperature / °C	Crystallinity / %
HDPE 100 mm s^{-1} 210 °C	131.1	65
All-PE Material 100 mm s^{-1} 210 °C	131.8	63
All-PE Material 100mm s^{-1} 230 °C	130.9	66
All-PE Material 50mm s^{-1} 230 °C	131.1	66
All-PE Material 25 mm s^{-1} 230 °C	131.8	68
All-PE Material 25 mm s^{-1} 220 °C	132.4	68
All-PE Material 25 mm s^{-1} 210 °C	131.1	64
All-PE Material 25 mm s^{-1} 200 °C	131.4	67

Calculation of the thermal conductivity

For the simulation in *Comsol Multiphysics* the thermal conductivity of 3D printed all-PE material in print direction and perpendicular to the print direction is calculated according to Formula S8.

$$k = \alpha \, \varphi \, c_p \qquad \text{Formula S8}$$

The corresponding density φ of 0.913 ± 0.004 g cm^{-3} is measured with a helium pycnometer, the heat capacity c_p of 1.28 ± 0.03 J $(g\ K)^{-1}$ is determined by DSC and the thermal diffusivities α of 0.98 ± 0.05 $mm^2\ s^{-1}$ and 0.22 ± 0.01 $mm^2\ s^{-1}$ are known from lock-in thermography.

3D Printed All-PE Sample

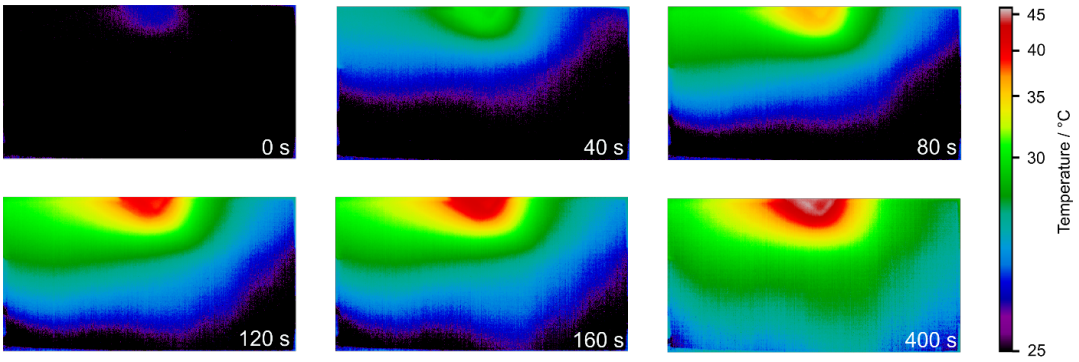

Figure S6: Evolution of the surface temperature of a single-layered sample, printed by FFF using two differing print directions and heated by a point-like heat source at 50 °C monitored *via* an IR camera.

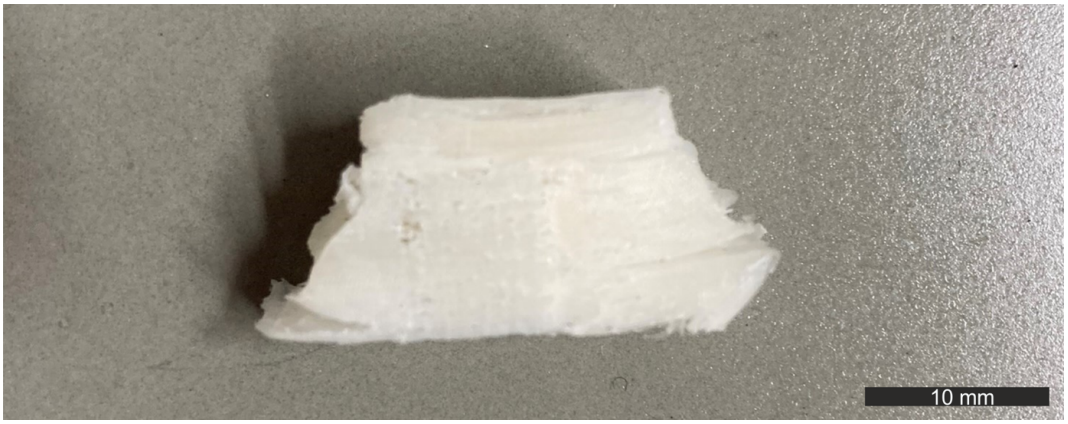

Figure S7: Image of the 3D printed all-PE sample used for demonstrating that defined temperature distributions are obtained by controlling the print direction.

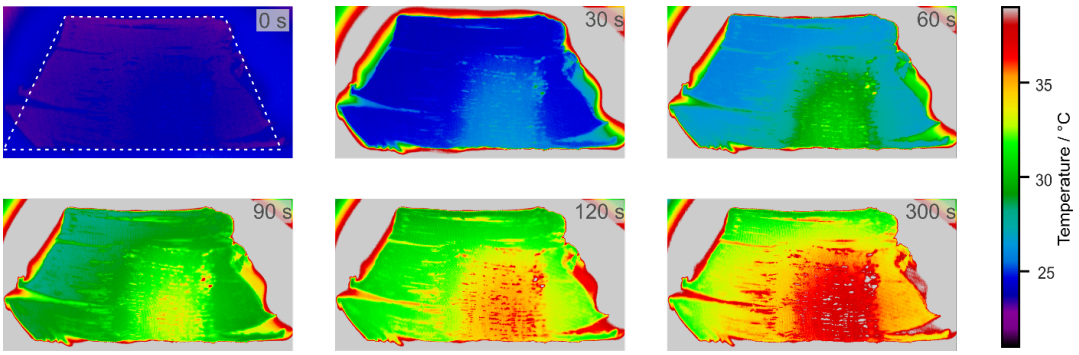

Figure S8: Evolution of the surface temperature of a multi-layered sample, printed by FFF using two differing print directions and placed on a hot plate at 50 °C monitored *via* IR camera.

1. S. Krimm, C. Y. Liang and G. B. B. M. Sutherland, *The Journal of Chemical Physics*, 1956, **25**, 549-562.
2. S. Krimm, *Fortschritte der Hochpolymeren-Forschung*, 1960, **2**, 51-172.
3. A. R. Wedgewood and J. C. Seferis, *Pure Appl. Chem.*, 1983, **55**, 873-892.
4. S. Watanabe, J. Dybal, K. Tashiro and Y. Ozaki, *Polymer*, 2006, **47**, 2010-2017.
5. S. K. Markham, A. Mani, E. A. Korsakova, A. S. Korsakov, L. V. Zhukova, J. Bauer, C. Silien and S. A. M. Tofail, *J. Therm. Anal. Calorim.*, 2020, **142**, 1115-1122.
6. A. A. Alsaygh, J. Al-hamidi, F. D. Alsewailem, I. M. Al-Najjar and V. L. Kuznetsov, *Applied Petrochemical Research*, 2014, **4**, 79-84.
7. J. L. White, K. C. Dharod and E. S. Clark, *J. Appl. Polym. Sci.*, 1974, **18**, 2539-2568.
8. R. S. Stein, *Journal of Polymer Science*, 1958, **31**, 327-334.
9. C. G. Schirmeister, T. Hees, O. Dolynchuk, E. H. Licht, T. Thurn-Albrecht and R. Muelhaupt, *ACS Appl. Polym. Mater.*, 2021, **3**, 1675-1686.

List of Figures

1.1 Schematic illustration of the three heat transfer mechanisms: radiation, convection, and conduction, depicted in a campfire scenario. 4

1.2 Spectral emissive power of a black body at various temperatures. Dotted lines indicate the wavelengths corresponding to the maximum spectral emissive power for each temperature. 5

1.3 Thermal conductivity k versus thermal diffusivity α for a wide variety of homogeneous materials. Adapted with permission from[23]. 7

1.4 Scheme of phonons in a diatomic linear lattice, displayed by the particle displacements for a a) transverse acoustic mode, b) longitudinal acoustic mode, c) transverse optical mode, and d) longitudinal optical mode. 8

1.5 Schematic illustration of phonon scattering mechanisms. a) Normal- and Umklapp-phonon collision process. The square represents the first Brillouin zone. b) Scattering of phonons at boundaries, grain boundaries, defects or impurities. 10

1.6 Schematic illustration of a semicrystalline polymer, with crystalline regions organized into spherulites (left top) or lamellar stacks (left bottom). Upon stretching, the crystalline domains fragment and the chains realign along the tensile axis, ultimately forming fibrillar structures. 12

1.7 Relationship between filler content and thermal conductivity in isotropic epoxy–silver composites with varying silver filler aspect ratios. Reproduced with permission from[69]. 15

2.1 Schematic illustration of polarized infrared (IR) spectroscopy. 17

2.2 Schematic illustration of wide angle X-ray scattering (WAXS). a) Basic experimental setup. b) Illustration of Bragg's law showing constructive and destructive interference depending on the scattering angle. 18

2.3 Schematic illustration of a basic small angle X-ray scattering (SAXS) setup. 20

2.4 Schematic illustration of a scanning electron microscopy (SEM) setup. 22

2.5 Schematic illustration of laser scanning confocal microcopy (LSCM). 24

2.6 Schematic illustration of a light flash analysis (LFA) setup. Adapted with permission from[100] copyright NETZSCH-Gerätebau GmbH. 25

2.7 Illustration of the custom-built lock-in thermography (LIT) setup. a) Schematic of the main components and their interconnections. b) 3D Visualization of the experimental setup. 27

2.8 Exemplary frequency sweep demonstrating the the deviation of thermal diffusivity values at high and low frequencies, and the plateau region in between. 28

4.1 Graphical Abstract. 37

4.2 Thermal diffusivity values of fibers formed from different BTA derivatives, measured using LIT at a frequency of 0.27 Hz. For each BTA derivative, three measurements were performed, each providing two data points by evaluating both sides of the laser spot (diamonds). Sample-specific laser powers were used to account for differences in fiber thickness. Average diffusivity values are indicated by circles and annotated with corresponding numerical values. The molecular structures of the side groups for each derivative are shown along the x-axis. 38

4.3 Normalized FT-IR spectra of BTA fibers, illustrating the influence of amide bond orientation (left panel) and side group chemistry (right panel). Dashed lines indicate the N–H or C=O stretch bands. 39

4.4 Electrospun nonwovens after pressing at room temperature, annealing at $115\,^{\circ}\mathrm{C}$ for 3 h or annealing at $115\,^{\circ}\mathrm{C}$ for 24 h. a) SEM images (Scale bars are $200\,\mu\mathrm{m}$ and $10\,\mu\mathrm{m}$) and the LIT phase data. b) Thermal diffusivity values obtained from measurements at ten positions per sample. The grey line represents the thermal diffusivity of a hot-pressed PS film. Reproduced from[6]. 41

4.5 Electrospun nonwovens after incorporation of AgNW or coating with copper. a) LSCM cross-section images of the random copper coated nonwoven, showing that the copper coating is present throughout the nonwoven, and the oriented copper coated nonwoven, showing that the copper content is reduced towards the center of the sample (Scale bars are $200\,\mu\mathrm{m}$). b) BSE-SEM images highlighting the features of the functionalization (Scale bars are $50\,\mu\mathrm{m}$ and $10\,\mu\mathrm{m}$). c) Thermal diffusivity values obtained from measurements at a minimum of ten positions per sample. Adapted from[6]. Figures were merged. 43

4.6 a) Nucleation mechanism of BTA additives. Upon cooling the BTA molecules self-assemble into nanofibrils that act as nucleation sites for polypropylene crystallization. b) Molecular structure of the utilized BTA derivatives. Adapted from[12]. A selected portion is shown. 44

4.7 Structural characterization of injection-molded neat racoPP (grey), racoPP with $0.5\,\mathrm{wt}\%$ nBu-BTA (blue) and with $0.5\,\mathrm{wt}\%$ iPe-BTA (orange). a) XRD patterns. Intensities are normalized to the highest peak. b) 2D SAXS patterns recorded at different sample positions. Adapted from[12]. A selected portion is shown. Colors were modified. 44

4.8 Thermal diffusivity α of an injection-molded neat racoPP specimen and racoPP specimens with varying content of nBu-BTA and iPe-BTA, obtained by LFA. Measurements were performed on cylinders measuring $1\,\mathrm{cm}$ in diameter cut from the top and bottom half of the original injection-molded samples. Adapted from[12]. Colors were modified. 45

4.9 Structural characterization of neat racoPP (grey), racoPP with $0.5\,\mathrm{wt}\%$ nBu-BTA (blue) and with $0.5\,\mathrm{wt}\%$ iPe-BTA (orange). a) XRD patterns comparing the injection-molded and compression-molded samples. Intensities are normalized to the highest peaks. b) IR spectra of the compression-molded samples at the bottom-middle position using polarized incident IR radiation. c) 2D SAXS patterns of the compression-molded samples at the designated positions (white boxes indicating the orientation of intensity maxima). Adapted from[12]. Colors were modified. 46

4.10 LIT of compression-molded samples with a thickness of 0.1 mm. a) Amplitude and phase signal obtained for compression-molded racoPP containing $0.5\,\mathrm{wt\%}$ iPe-BTA. b) Thermal diffusivity α of an injection-molded neat racoPP specimen and racoPP specimens with $0.5\,\mathrm{wt\%}$ nBu-BTA and $0.5\,\mathrm{wt\%}$ iPe-BTA. Five locations on each sample part (Top, Middle, Bottom) were probed. Reproduced from[12]. . . . 47

4.11 a) Fundamental vibrational modes of polyethylene chains. Parallel modes are shown in dark blue, perpendicular modes in light blue. b) Polarized IR spectra of the all-PE material using light polarized at 0° (dark blue) and 90° (light blue) relative to the 3D print direction with the assignment at $2019\,\mathrm{cm^{-1}}$. c) Corresponding spectra of benchmark HDPE. 0° polarization is shown in dark gray and 90° in light gray. Adapted from[16]. A selected portion is shown. 48

4.12 Comparison of all-PE filament and benchmark HDPE filament and therewith printed samples obtained by fused filament fabrication (FFF). a) Azimuthal representation of 2D WAXS (azimuth vs. momentum transfer q). b) 2D SAXS (q_y vs. q_x). c) Schematic illustration of a shish-kebab structure surrounded by amorphous PE. d) SEM image of an all-PE sample prepared by FFF and etched with hot xylene. Reproduced from[16]. 49

4.13 LIT for determination of the thermal diffusivity of HDPE and all-PE material processed by FFF. a) Amplitude and phase signals for all-PE and benchmark HDPE printed at $210\,^\circ\mathrm{C}$ and $100\,\mathrm{mm\,s^{-1}}$. b) Thermal diffusivity and thermal anisotropy for all-PE and benchmark HDPE printed at differing print speeds and print temperatures. Reproduced from[16]. 49

4.14 Directed heat flow in a single-layered (a, b) and a multi-layered (c, d) sample with respective heat sources at $75\,^\circ\mathrm{C}$. a) Geometry and steady-state FEM simulation of the designed 2D sample. Thermal conductivities were defined according to measured values of a sample printed by FFF parallel ($k_\parallel$) and perpendicular ($k_\perp$) to the print direction. b) Evolution of the surface temperature distribution on the 2D sample monitored via IR camera. The image at $0\,\mathrm{sec}$ includes a semi-transparent overlay with the print direction scheme. c) Visualization of the all-PE sample (top and side view) on a heat plate with print directions indicated by arrows. d) Evolution of the surface temperature distribution on the 3D sample monitored via IR camera. Adapted from[16]. Figures were cropped and merged. 51

7.1 Self-assembled benzene-1,3,5-tricarboxamide (BTA) structure a) Schematic illustration of the hierarchical BTA fibrils b) Optical image of macroscopic self-assembled BTA fibers on a lock-in thermography sample holder. 62

7.2 Thermal diffusivity values of fibers formed from different BTA derivatives, measured using lock-in thermography at a frequency of $0.27\,\mathrm{Hz}$. For each BTA derivative, three measurements were performed, each providing two data points by evaluating both sides of the laser spot (diamonds). Sample-specific laser powers were used to account for differences in fiber thickness. Average diffusivity values are indicated by circles and annotated with corresponding numerical values. The molecular structures of the side groups for each derivative are shown along the x-axis. . . . 63

7.3 Normalized FT-IR spectra of various bulk BTA derivatives. The left panel compares the influence of amide bond orientation, while the right panel shows the effect of side group chemistry. Dashed lines indicate the N–H stretch bands and in the right panel additionally the C=O stretch bands. 64

7.4 Thermal diffusivity values of fibers formed from *Hex-C3*, measured using lock-in thermography at $0.27\,\mathrm{Hz}$ across a wide range of fiber diameters. Each data point corresponds to one of 13 different heating powers ranging from $18\,\mu\mathrm{W}$ to $72\,\mu\mathrm{W}$, as indicated by the color scale. The grey line shows the average thermal diffusivity (reference) and standard deviation obtained from three measurements using a sample-specific power that resulted in a peak amplitude signal closest to $175\,\mathrm{mK}$. a) All data points. b) Zoomed-in view of the y-axis to better visualize the differences near the reference value. 70

List of Tables

4.1 Average S_{2D} parameters of the electrospun nonwovens quantifying the fiber alignment. 40
4.2 Hermans orientation factors calculated from WAXS intensity distributions. 48

Colophon

AI-based language tools were used for stylistic editing. All content and conclusions are my own, and I take full responsibility for them.

This thesis was typeset with LaTeX 2$_\varepsilon$. It uses the *Clean Thesis* style developed by Ricardo Langner. The design of the *Clean Thesis* style is inspired by user guide documents from Apple Inc.

Eidesstattliche Versicherung und Erklärung

§8 Satz 2 Nr. 3 PromoO Fakultät für Biologie, Chemie und Geowissenschaften

Hiermit versichere ich eidesstattlich, dass ich die Arbeit selbstständig verfasst und keine anderen als die von mir angegebenen Quellen und Hilfsmittel benutzt habe (vgl. Art. 97 Abs. 1 Satz 8 BayHIG).

§8 Satz 2 Nr. 3 PromoO Fakultät für Biologie, Chemie und Geowissenschaften

Hiermit erkläre ich, dass ich die Dissertation nicht bereits zur Erlangung eines akademischen Grades eingereicht habe und dass ich nicht bereits diese oder eine gleichartige Doktorprüfung endgültig nicht bestanden habe.

§8 Satz 2 Nr. 4 PromoO Fakultät für Biologie, Chemie und Geowissenschaften

Hiermit erkläre ich, dass ich Hilfe von gewerblichen Promotionsberatern bzw. –vermittlern oder ähnlichen Dienstleistern weder bisher in Anspruch genommen habe noch künftig in Anspruch nehmen werde.

§8 Satz 2 Nr. 7 PromoO Fakultät für Biologie, Chemie und Geowissenschaften

Hiermit erkläre ich mein Einverständnis, dass die elektronische Fassung der Dissertation unter Wahrung meiner Urheberrechte und des Datenschutzes einer gesonderten Überprüfung unterzogen werden kann.

§8 Satz 2 Nr. 8 PromoO Fakultät für Biologie, Chemie und Geowissenschaften

Hiermit erkläre ich mein Einverständnis, dass bei Verdacht wissenschaftlichen Fehlverhaltens Ermittlungen durch universitätsinterne Organe der wissenschaftlichen Selbstkontrolle stattfinden können.

Bayreuth, 5. Mai 2026

Ina Klein

Ina Klein
From Fibers to 3D Architectures:
How Structural Hierarchies Affect Heat Transport
Dissertation, October 2025

University of Bayreuth
Physical Chemistry I -
Colloidal Structures and Energy Materials
Faculty of Biology, Chemistry & Earth Sciences
Universitätsstraße 30
95447 Bayreuth